UNIVERSITY OF PAVIA

DOCTORATE IN BIOMEDICAL SCIENCES

DEPARTMENT OF MOLECULAR MEDICINE

UNIT OF BIOCHEMISTRY

OI zebrafish models and their use to develop new pharmacological treatments

Supervisor:

Prof.ssa Antonella Forlino

Experimental Thesis of Ph.D.

by Francesca Tonelli

XXX Cycle A.Y. 2016/2017

CONTENTS

Introduction 1

Collagen 1

Osteogenesis Imperfecta 6

OI classification 6

Zebrafish 17

Aims 27

Chapter I: Zebrafish collagen type I 32

Zebrafish Collagen type I: Molecular and Biochemical Characterization of the Major Structural Protein in Bone and Skin 36

Chapter II: The chemical chaperone 4 phenylbutyric acid ameliorated OIphenotype in the osteogenesis imperfecta zebrafish model Chihuahua 50

The chaperone activity of 4PBA ameliorates the skeletal phenotype of Chihuahua, a zebrafish models for dominant osteogenensis imperfecta 56

Chapter III: Characterization of bone properties and material composition of the zebrafish Chihuahua 71

Severely impaired bone material quality in *Chihuahua* zebrafish resembles classical dominant human osteogenesis imperfecta 74

Chapter IV: Generation of new zebrafish models for recessive OI 94

Collagen prolyl 3-hydroxylation complex 95

Trimeric Intracellular Cation channel type B (TRIC-B) 99

CRISPR/Cas system 103

Materials and methods.....108

Zebrafish 108

In silico analysis.....108

KO generation 108

Identification of mutation.....113

Morphometric analysis.....113

Alizarin Red skeletal staining 115

x-Ray.....115

µCT 116

Steady state collagen analysis 116

RNA extraction 117

Real time PCR (qPCR) analysis.....117

In situ hybridization 119

Statistical analysis 120

Results.....121

In silico analysis of p3h1, crtap and tmem38b genes in zebrafish.....121

Generation of knock out fish using the CRISPR/Cas9 gene editing system 125

Validation of p3h1 and crtap knock-out fish as OI models 134

Characterization of p3h1 and crtap zebrafish models 144

Reduced swim bladder insufflation characterizes mutant fish models.....148

tmem38b expression in WT zebrafish embryos.....149

Preliminary characterization on adult tmem38b$^{\Delta KEV/\Delta KEV}$ 151

Discussion.....153

Supplementary tables 159

References 165

Introduction

Collagen

Collagens are the most abundant proteins in mammals, representing ~30% of the total protein mass (Ricard-Blum 2011). They can be divided into several subgroups, depending on structural differences: classical fibrillar collagens, FACITs (fibril-associated collagens with interrupted triple helices), network-forming collagens, microfibrillar collagens, MACITs (membrane-associated collagens with interrupted triple helices), and MULTIPLEXINs (multiple triple-helix domains and interruptions) (Shoulders and Raines 2009).

All members of the collagen family, despite the structural diversity among the various subgroups, contain a right-handed triple helix composed of three α polypeptide chains each characterized by the repetitive sequence $(Gly\text{-}X\text{-}Y)_n$. The amino acid glycine is required every third residue to allow the proper folding of the triple helix, since only its small size chain can be properly accommodated in the centre of the helical domain. The X and Y amino acids are often proline and hydroxyproline and they are involved in the triple helix stabilization. The α chains might be identical (homotrimers), like in collagens II, III, VII, VIII, X, or different (heterotrimers) as in collagen types I, IV, V, VI, IX and XI (Gelse et al. 2003).

The fibril-forming collagens, characterized by an uninterrupted central helix flanked by globular domains, are the most abundant in the human body. They include types I, II, III, V, XI, XXIV and XXVII.

Fibrillar collagens type I and type II: the main collagens in the skeletal system

The main collagens in the skeleton are the fibrillar collagen type I and type II. Collagen type I represents more than 90% of the organic mass of bone and it is also the major constituent of tendons, skin, ligaments, cornea, and many interstitial connective tissues (Gelse et al.2003). It provides most tissues and organs with form, stability and connectivity (Hulmes 2008). Collagen type I is typically a heterotrimer composed by two identical α1 chains and one α2 chain coiled around each other in a characteristic triple helix (Gelse et al. 2003).

Although the triple helix is the most representative element of fibril-forming collagens, the non-collagenous domains, known as N- and C- propeptides, flanking the central helical part, are also important structural components. The C-propeptide plays a fundamental role in the initiation of triple helix formation, whereas the N-propeptide is involved in the regulation of fibril diameters (Vranka et al. 2004). Proteolytic removal of the propeptides results in triple-helical collagen molecules that have short telopeptides at both ends and can spontaneously assemble into highly ordered aggregates known as fibrils (Canty and Kadler 2005). The short non-helical C- and N- telopeptides are important for the formation of covalent cross-links among collagen molecules (Eyre et al. 1984) (Figure 1).

Collagen type II is the major component of hyaline cartilage (80% of the total collagen content), but it is also present in the vitreous body, in the corneal epithelium, in the notochord, in the nucleus pulposus of invertebral discs and in the embryonic epithelial-mesenchymal transitions (Gelse et al. 2003). Collagen type II is a homotrimer composed of three α1 chains that form a molecule similar in size and biochemical properties to collagen type I (Gelse et al. 2003) (Figure 1). Compared to collagen type I, collagen type II chains show higher content of hydroxylysine as well as glucosyl and galactosyl residues, which mediate the interaction with proteoglycans, typical components of the highly hydrated matrix of hyaline cartilage (Mayne 1989).

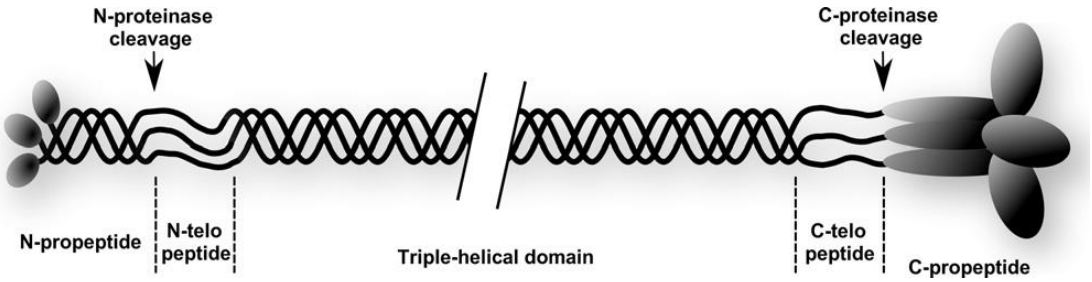

Figure1. **General fibrillar collagen structure** from (Boudko and Bachinger 2012).

Biosynthesis of fibrillar collagen

The biosynthesis of fibrillar collagen is a long and complex multistep process involving α chain association, post-translational modifications, folding, secretion, processing, self-assembly and progressive cross-linking (Ishikawa et al. 2013).

Collagen synthesis starts in the rough endoplasmic reticulum (ER) where specific mRNAs, transcribed from the α chains encoding genes, are translated. The pre-procollagen chains protrude into the lumen of the ER thanks to a signal recognition peptide, that is then proteolitically removed.

Several enzymes and molecular chaperones assist procollagen trimerization and folding. Triple helix assembly begins when the single chains are still anchored to the ER membrane and requires specific recognition domains. In fact, the formation of collagen triple helix requires trimerization domains (250 residues) which are non-collagenous peptides located next to the triple helix forming Gly-X-Y repeats. They prevent the formation of misaligned collagen triple helices and are also required for chain selection, chain arrangement and efficient folding (Boudko and Bachinger 2012). In presence of these domains the triple helix formation starts at defined sites. In fact, it begins at the C-terminal, where a non-collagenous domain was identified as the domain which aligns and registers the three α chains (Bächinger et al. 1978). Moreover, the trimerization domains have also an inhibitory role on premature intracellular fibril formation, process achieved mainly only after procollagen secretion following C-propeptide cleavage (Boudko and Bachinger 2012). Finally, the folding propagation towards the N- terminal end is accompanied by further modifications at some specific amino acid residues (Canty and Kadler 2005).

The hydroxylation of proline and lysine residues, catalysed by prolyl 3-hydroxylase, prolyl 4-hydroxylase, and lysyl 5-hydroxylase, respectively, occurs in the procollagen chain after removal of the signal peptide. Proline residues can be hydroxylated at two different sites by different enzymes, according to their position in the Gly-X-Y triplet. This triplet motif results in a left-handed helix that can wrap two other helices to form a right-handed triple-helical structure (Canty and Kadler 2005). The α chains assemble around a central axis in a way that the side chain of all glycine residues, the smallest amino acid, are directed towards the centre of the triple helix, while the more bulky side chains of the other residues occupy the outer positions, allowing a close packaging along the central axis of the molecule. Proline residues in Y-position are converted to 4-hydroxyproline by the enzyme prolyl 4-hydroxylase, and few proline residues in X-position are converted into 3-hydroxyproline by

prolyl 3-hydroxylase. Approximately 50% of the proline residues contain a hydroxyl group at position 4 (Gelse et al. 2003). The presence of 4-hydroxyproline is fundamental for intra-molecular hydrogen bonds; it contributes to the thermal stability of the triple helical domain, and therefore also to the integrity of the collagen fibril (Gelse et al. 2003)**.** Prolyl 3-hydroxylation contributes to the proper folding, stability and secretion of procollagen, while lysyl hydroxylation contributes to extracellular crosslink stability between molecules and allows collagen glycosylation (Figure 2) (Yamauchi and Sricholpech 2012).

The efficient folding of the procollagen chains depends on the presence of enzymes like peptidyl-prolyl *cis-trans* isomerase (PPI), which catalyzes the *cis-trans* isomerisation of peptide bond, and collagen-specific chaperones like heat shock protein 47 (HSP47) (Ishikawa et al. 2017). In particular, HSP47 preferentially interacts with the procollagen molecules assembled in the triple-helix, stabilizing them from heat denaturation and facilitating the transport from the ER to the Golgi apparatus (Tasab et al. 2000).

After procollagen assembly, the triple helical molecules are transported to the Golgi compartment and released into the extracellular space through coat protein complex II (COPII) vesicles (Malhotra and Erlmann 2015). Recently, it has been proposed that the Src homology 3 (SH3) domain of the transmembrane protein transport and golgi organization 1 (TANGO1), encoded by *MIA3*, interacts with HSP47 in the ER, directing collagen molecules to specific vesicles for extracellular sorting (Ishikawa et al. 2016). Following the secretion, a key step in collagen formation is the cleavage of the globular C- and N-propeptides by the procollagen N-proteinase A Disintegrin And Metalloproteinase with ThromboSpondin motifs 2, (ADAMTS2) and the procollagen C-proteinase Bone morphogenic protein 1 (BMP1), respectively (Rossert and de Crombrugghe 2002).

The fibril-forming collagens spontaneously aggregate after processing of procollagens into ordered fibrillar structures. The collagen molecules are packed in parallel and longitudinally staggered with respect to one another by some multiple of axial repeat distance, called a D period (~ 67 nm). The molecular arrangement into fibrils is additionally stabilized by the formation of covalent cross-links, which finally contribute to the mechanical resilience of collagen fibrils (Yamauchi and Sricholpech 2012) (Figure 2). The hydroxylation state of telopeptide lysine residues is crucial in defining collagen cross-links, which are a prerequisite for the physical and mechanical properties of collagen fibrils and

a stable network formation. Thus, the unique pattern of crosslinking of bone collagen is believed to be important for the normal mineralisation and material strength of bone tissue (Eyre and Weis 2013).

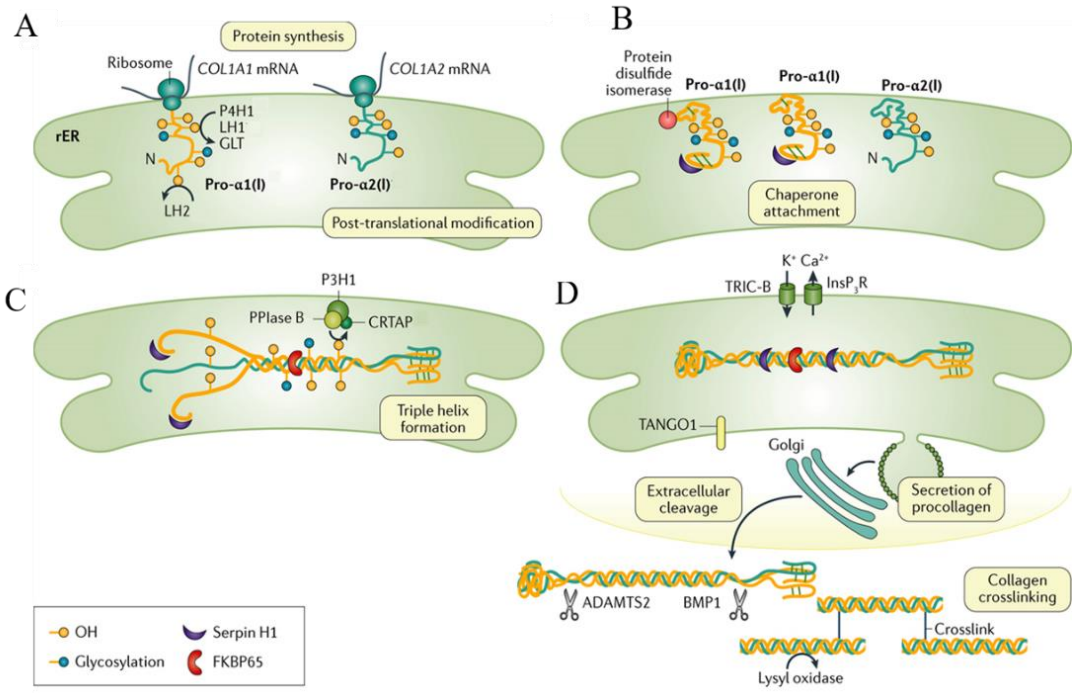

Figure 2. Type I collagen synthesis and processing. (A) Translation and post-translational modifications of pro-α1(I) and pro-α2(I). (**B)** Interactions with molecular chaperones to prevent premature triple helix formation. (**C)** Triple helix formation that comprises the interaction of two pro-α1-chains and one pro-α2-chain. (**D)** Secretion of procollagen, extracellular cleavage to collagen and crosslinking formation. ADAMTS2, a disintegrin and metalloproteinase with thrombospondin motifs 2; BMP1, bone morphogenetic protein 1; CRTAP, cartilage-associated protein; GLT, galactosyltransferase 1; InsP3R, inositol-1,4,5-triphosphate receptor; LH, lysyl hydroxylase; P3H1, prolyl 3-hydroxylase 1; P4H1, prolyl 4-hydroxylase 1; PPIase B, peptidyl-prolyl *cis–trans* isomerase B; ER, rough endoplasmic reticulum; TANGO1, transport and Golgi organization protein 1; TRIC-B, trimeric intracellular cation channel type B (modified from Marini et al. 2017).

Osteogenesis Imperfecta

Osteogenesis imperfecta (OI), also called brittle bone disease, is a heritable rare connective tissue disorder mainly characterized by skeletal fragility and growth deficiency (Forlino and Marini 2016). In the past, OI was known as an autosomal dominant disorder caused by structural or quantitative mutations in *COL1A1* and *COL1A2*, coding for α1 and α2 chains of collagen type I. In 1979 Sillence (Sillence and Rimoin 1979) classification divided OI in four types on the basis of clinical and radiographic features. Mild Sillence OI type I was related to quantitative deficiency of structurally normal collagen, whereas lethal type II, severe type III and moderate type IV forms were caused by mutations altering collagen structure (Marini, Forlino et al. 2007).
In 2006 the first gene for recessive OI was discovered (Barnes et al. 2006), leading to consider OI a more collagen-related disorder. Defects in proteins with different functions, ranging from structural to enzymatic and from intracellular transport to chaperones, have been described in patients with OI (Forlino and Marini 2016).

These new findings required a deeper investigation on the specific molecular basis of each form of the disease, in order to improve clinical diagnosis and stimulate targeted therapeutic approaches (Forlino and Marini 2016). Forlino and Marini proposed a new OI classification subdividing the different forms in five groups on the basis of the metabolic pathways compromised, related to collagen synthesis, structure and processing or to bone forming cell differentiation (Forlino and Marini 2016) (Table 1).

OI classification

Defects in collagen synthesis, structure or processing (group A)

This first group includes both autosomal dominant forms of OI, due to mutations in α1 and α2 chains of collagen type I (OI type I-IV), and one recessive form, caused by defects in the C-protease enzyme Bone Morphogenic Protein 1 (BMP1, OI type XIII).
OI type I, the mildest form, is characterized by fractures, blue sclerae and hearing loss. Patients have minimal bone deformity, near normal stature and rarely dentinogenesis imperfecta. The matrix insufficiency of OI type I generally results from a premature termination codon in *COL1A1* transcript, which activates the nonsense-mediated mRNA (NMD) decay surveillance mechanism. Heterozygous

null *COL1A1* alleles result in synthesis of about half amount of structurally normal collagen (Forlino et al. 2011). Homozygous null mutations in *COL1A2* cause symptoms ranging from severe OI to a mild form of Ehlers-Danlos syndrome-like disease, while heterozygotes have no OI phenotype (de Wet et al. 1983; Malfait et al. 2006).

OI types II-IV are caused by defects in collagen type I structure, most commonly glycine substitutions (80%) and splice site mutations (20%). Glycine substitutions delay helix folding, leading to post-translational overmodifications, which may compromise collagen secretion and/or processing (Marini, Forlino et al. 2007).

OI type II is perinatal lethal. Infants are characterized by short, bowed long bones, blue or grey sclerae and large, soft cranium. Moreover, *in utero* fractures are frequent. The most common cause of death is respiratory failure (Singer et al. 2001).

OI type III is the most severe non-lethal form of this disease. Patients have triangular facies, blue or grey sclerae, dentinogenesis imperfecta, vertebral compression and scoliosis. About half of affected individuals exhibit "popcorn" formation at femoral growth plates (Obafemi et al. 2008).

OI type IV is moderately severe and has a broad phenotypic range that overlaps with OI type I and III. Patients have long bone fractures, that for the most allow ambulation. Other features such as the colour of the sclerae, hearing loss and dentinogenesis imperfecta are variable (Marini, Forlino et al. 2007).

During collagen synthesis, procollagen molecules undergo an extracellular maturation process, in which N- and C- propeptides are removed by specific proteases. Mutations of the major C-protease enzyme BMP1/mTLD cause a severe form of OI (OI type XIII). Patients with homozygous substitution in BMP1 signal peptide have high bone mineral density, similarly to the one observed in collagen substrate defects (Lindahl et al. 2011), while the homozygous substitution (Phe249Leu) has osteoporotic outcome, probably due to a residual BMP1 activity (Martínez-Glez et al. 2012).

Defects in collagen modification (group B)

This group includes five autosomal recessive forms of OI. Three forms are caused by defects in the collagen 3-hydroxylation complex (OI type VII, VIII and IX); one is due to mutations in the gene

encoding for the trimeric endoplasmic reticulum-membrane cation channel TRIC-B and the last is caused by mutation in *SPARC* (OI type XVII).

The collagen 3-hydroxylation complex, that will be more extensively described in the chapter IV, is composed by Prolyl-3-hydroxylase 1 (P3H1), cartilage associated protein (CRTAP) and peptidyl-prolyl-*cis-trans* isomerase B (PPIB or cyclophilin B, CyPB) (Figure 3). These proteins assemble in a 1:1:1 complex within ER where it hydroxylates in position C-3 specific proline residues in the unfolded collagen α chains (Marini, Cabral et al. 2007). The best substrate is Pro986 residue of α1(I), α1(II) and α2(V) collagen chains. The complex has also a chaperone function.
P3H1 is the active enzyme of the complex (Vranka et al. 2004), whereas CRTAP is the helper protein without a catalytic domain (Morello et al. 1999). Finally, CyPB is the *cis-trans* isomerase that allows the proline residue to reach the *trans* conformation, necessary for the protein folding (Morello et al. 2006).
Null or missense mutations causing loss-of-function of *CRTAP* are responsible for OI type VII (Morello et al. 2006; Barnes et al. 2006), whereas loss-of-function of P3H1 causes OI type VIII (Cabral et al. 2012). Both OI forms show a severe to lethal phenotype and biochemically are characterized by overmodification of full collagen helical region (Eyre et al. 2011). Since the complex is also expressed in cartilage, patients have osteochondrodystrophy with neonatal fractures and broad undertubulated long bones, white sclerae, rhizomelia (shortening of the proximal segment of the limbs), growth deficiency and low bone mineral density (Marini, Cabral et al. 2007). Missense mutations in CyPB are responsible for OI type IX, biochemically and phenotypically different from P3H1 and CRTAP deficiency. Patients show moderate or lethal phenotype without rhizomelia, although they share white sclerae and undertubulated long bones with P3H1 and CRTAP patients (Barnes et al. 2010).

OI type XIV is caused by defects in *TMEM38B* which encodes TRIC-B, a trimeric ER-membrane cation channel synchronised with the inositol trisphosphate gated channel involved in calcium release (Zhou et al. 2014). Calcium is important to regulate the activity of several ER proteins involved in collagen metabolism. Alterations in ER Ca^{2+} homeostasis can alter the expression and activities of multiple collagen interacting proteins and dysregulate the process of collagen biosynthesis, leading to abnormal collagen modification (Cabral et al. 2016) (Figure 3). Mutations in *TMEM38B* are often

exon deletions or nonsense mutations, which cause mainly premature stop codon in the protein. Patients are characterized by moderately severe OI with generalized osteopenia, multiple long bone fractures, bowing deformities and blue sclerae (Cabral et al. 2016; Webb et al. 2017).

SPARC encodes for the secreted acid, cysteine-rich protein, known simply as osteonectin. It is the glycoprotein responsible for maintaining cell shape through the binding to collagen type I and other extracellular proteins (Bradshaw 2009). Missense mutations in *SPARC* have been associated to recessive Osteogenesis Imperfecta type XVII. The residues substituted by the mutations seem to form physiologically an intra-molecular salt bridge in SPARC and are essential for the binding of SPARC to collagen type I. The resulting collagen shows a delay in its migration, suggesting over-modification of the protein during triple helical formation. Trabecular bone is hyper-mineralized showing that homozygous mutations in SPARC can give rise to severe bone fragility in humans (Mendoza-Londono et al. 2015).

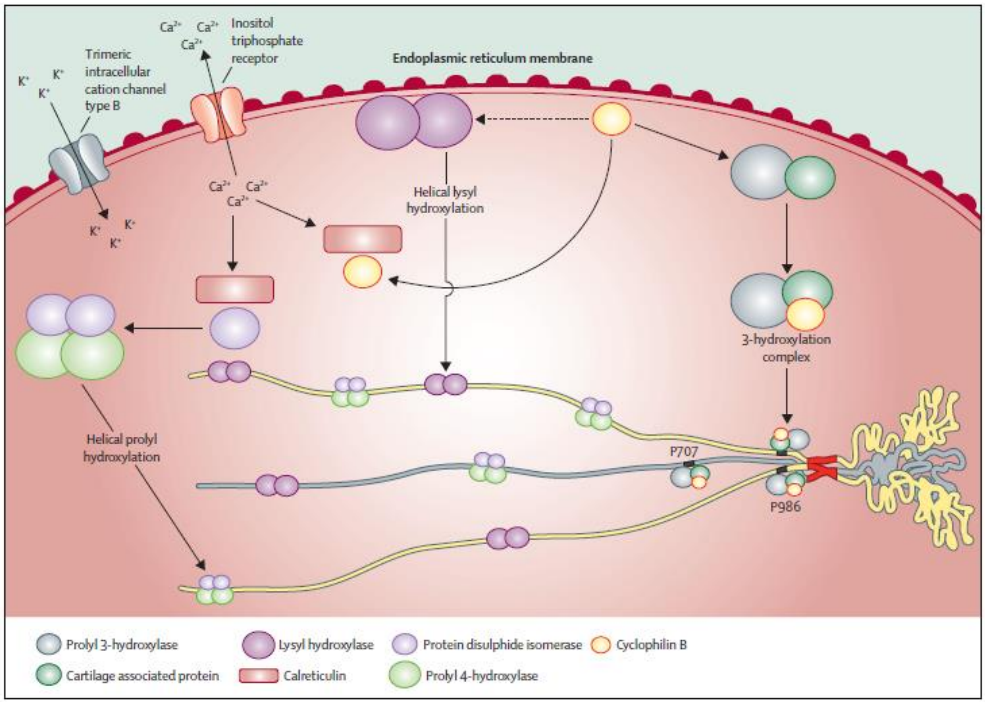

Figure 3. **Proteins involved in type I procollagen post-translational modification and folding in the endoplasmic reticulum**. Prolyl 3-hydroxylase, cartilage associated protein, and cyclophilin B form a trimeric complex necessary for the hydroxylation of the α1(I) Pro986 and α2(I) Pro707 residues. Cyclophilin B also affects the activity of lysyl hydroxylase 1, which hydroxylates lysine residues in the helical region of type I procollagen. The regulation of calcium ion flux from the endoplasmic reticulum to the cytosol and viceversa, regulated by TRIC-B channel is relevant for procollagen post-translational modification, likely due to the

calcium role in modulating calreticulin interaction with cyclophilin B and with protein disulphide isomerase. Protein disulphide isomerase complexes with prolyl 4-hydroxylase to hydroxylate the 4-carbon position of proline residues located in the Y-position of the repetitive collagenic triplet, Gly-X-Y (from Forlino and Marini 2016).

Defects in collagen folding and cross-linking (group C)

This group includes recessive OI forms due to absence or dysfunction of the collagen chaperones HSP47 (OI type X) and FKBP65 (OI type XI). Also, the recently identified X-linked mutations in *MBTPS2* belongs to this group.

HSP47 is an ER resident collagen-specific chaperone encoded by *SERPINH1*. The role of HSP47 is to specifically stabilized the folded procollagen in the ER and transfer it to the Golgi (Koide et al. 2006). Defects in HSP47 cause OI type X. Missense mutations in *SERPINH1* were first described in 2010 (Christiansen et al. 2010). In 2016 a novel null mutation (c.338_357delins22) was found, that is predicted to generate a frameshift resulting in a premature termination codon and in a more severe outcome (Marshall et al. 2016).

In patients having these mutations the synthesis of mature type I collagen trimers was detected. On the other hand, even if most of the procollagen was normally secreted, a fraction was translocated from the ER compartment to vesicles. Thus, HSP47 was confirmed to have a dual function, first to assist with procollagen assembly in the ER and subsequently to assist in trafficking of trimeric molecules to the Golgi (Marshall et al. 2016).

Defects in *FKBP10*, encoding the ER-resident immunophilin FKBP65, cause three distinct recessive syndromes. FKBP65 deficiency causes OI type XI, ranging from progressive deforming, with long bones fractures, platyspondyly and scoliosis, to moderate with short stature and ambulation potential (Alanay et al. 2010). Mutations in *FKBP10* cause also Bruck syndrome 1, a peculiar disorder characterized by severe OI and congenital contractures of large joints, short stature and scoliosis (Schwarze et al. 2013). In the third case mutations in *FKBP10* cause Kuskokwim syndrome, a congenital contracture disorder with minimal skeletal fractures occurring uniquely in Yup'ik Eskimos in Alaska. Residual FKBP65 is sufficient in these patients to avoid bone dysplasia (Barnes et al. 2013).

In bone, hydroxylation of telopeptide lysines is necessary to form cross-links between collagen molecules in order to provide stability and tensile strength to fibrils (Eyre and Weis 2013). The lysyl hydroxylase 2 (LH2), encoded by *PLOD2*, is the enzyme able to hydroxylate collagen telopeptide lysines. An interaction between *FKBP10* and *PLOD2* seems to exist; in fact, patients with Bruck syndrome 1 with either *FKBP10* or *PLOD2* mutations have reduced hydroxylysine-derived cross links in bone collagen. Moreover, collagen telopeptide lysine hydroxylation in cells with mutation in *FKBP10* is strongly reduced. These findings confirm the interaction between FKBP65 and LH2 (Duran et al. 2017) (Figure 4).

Recently, Bachinger et al demonstrated an interaction between HSP47 and FKBP65 and their involvement during collagen biosynthesis in the ER. The authors demonstrated that when the two proteins associate, HSP47 enhances the PPIase activity of FKBP65 increasing the accessibility to collagen (Ishikawa et al. 2017) (Figure 4).

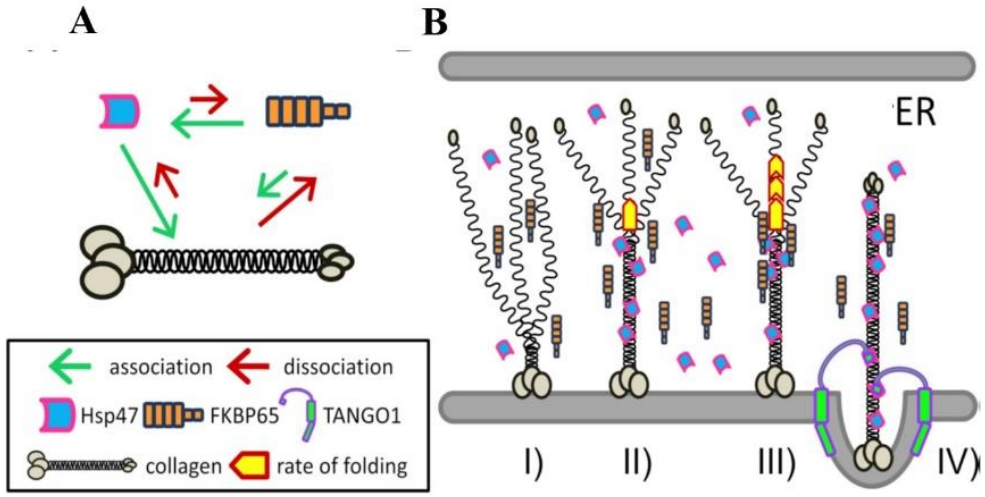

Figure 4. Schematic diagram of the interactions between collagen, Hsp47 and FKBP65 and a proposed model of collagen folding in the ER. (A) Illustration of the interactions between three proteins; collagen, Hsp47 and FKBP65. The length of the arrows indicates the strength of the association (green) and dissociation (red) between molecules. (**B)** Graphical representation of the combined effects of HSP47 and FKBP65 on collagen folding. **I)** triple helix formation is initiated from the C-terminal end, **II)** HSP47 binds to the newly formed triple helix, **III)** FKBP65 is recruited to HSP47 at the triple helix propagation site and accelerates the rate of folding and **IV)** FKBP65 is replaced by the SH3 domain of TANGO1 at the ER exit site for the loading of collagen into a special COPII vesicle (from Ishikawa et al. 2017)

An X-linked form of OI, caused by recessive mutation in *MBTPS2*, was recently identified (Lindert et al. 2016). *MBTPS2* encodes S2P, an integral membrane protein involved in the regulated intramembrane proteolysis (RIP) pathway and in cholesterol metabolism (Rawson 2004). Affected subjects from two independent pedigrees showed substitutions in S2P localized in highly conserved intramembrane residues at the C- terminal functional region (Lindert et al. 2016). The *MBTPS2* mutations did not destabilized S2P protein, but its ability to process the RIP substrates, interfering with their downstream pathways, like the control of cholesterol homeostasis, unfolded protein response and bone formation. The OI phenotype in presence of *MBTPS2* defects is a moderate to severe form of the disease that is still without any classification number because of the recent identification. The clinical features are fractures of ribs, femora and tibiae soon after birth, rhizomelia of upper and lower extremities, blue sclerae and *pectus carinatum*. In patients, collagen secretion in the matrix is reduced as well as the hydroxylation of helical lysine residue 87, which is critical for collagen crosslinking in bone (Lindert et al. 2016). Before the identification of these *MBTPS2* defects, missense mutations in the same gene have been associated with dermatological conditions ichthyosis follicularis, atrichia, and photophobia (IFAP/BRESHECK) (Khandpur et al. 2005). However, affected individuals in OI pedigrees did not have any symptoms associated with these conditions, even into adulthood.

Defects in bone mineralization (group D)

This group includes mutations in *IFITM5* (OI type V) and in *SERPINF1* (OI type VI) responsible for recessive OI forms characterized by compromised ossification and mineralisation.

OI type V is caused by mutation in the interferon-induced transmembrane protein 5, *IFITM5* (Semler et al. 2012). IFITM5, also known as BRIL is a member of the IFITM family and it is predominantly localised to the osteoblast plasma membrane (Kasaai et al. 2013). The majority of patients has the heterozygous point mutation in the 5'-UTR (c.-14C→T) which generates a new start codon, adding five residues (MALEP) to the N-terminal of the protein (Figure 5). Patients have moderately severe bone dysplasia with a combination of distinctive features such as radial head dislocation, ossification of the forearm interosseous membrane and subphyseal metaphyseal radiodense band (Semler et al. 2012).

Homozygous or compound heterozygous null mutations in *SERPINF1* cause OI type VI. *SERPINF1* encodes the Pigment Epithelium Derived Factor (PEDF), a potent anti-angiogenic factor expressed in a variety of cells, including chondrocytes, osteoblasts and mesenchymal stem cells (Becerra 2013; Quan et al. 2005). In bone, PEDF maintains bone homoeostasis and regulates osteoid mineralisation. Patients have no fractures in the first year, even though long bone fractures followed by vertebral compression and reduced bone mineral density appear during life. Bone histology reveals an increase amount of un-mineralised osteoid and a so called fish-scale lamellar pattern under polarised light (Glorieux et al. 2002). It is known that PEDF leads to osteoblast development by favouring the expression of osteogenic genes and mineral deposition, inhibiting osteoclast maturation. Thus, absence of the protein increases osteoclast number and bone resorption (Akiyama et al. 2010) (Figure 5).

A heterozygous *IFITM5* mutation that connects OI types V and VI has been reported (Farber et al. 2014). The Ser40Leu substitution interferes with modification of the nearby BRIL palmitoylation sites (Tsukamoto et al. 2013). This mutation causes severe progressive deforming osteogenesis imperfecta and bone histology typical for OI type VI and without any clinical or radiographic findings of type V (Forlino and Marini 2016).

Defects in osteoblast development with collagen insufficiency (group E)

This last group includes mutations in *WNT1*, *CREB3L1* and *SP7*, (OI type XV, XVI and XII respectively). Defects in these genes are expected to cause reduction in type I collagen expression, resulting in osteopenia combined with other manifestations of impaired osteoblast differentiation (Forlino and Marini 2016).

WNT1 belongs to a family of secreted glycoproteins able to bind LRP5/6 and Frizzled receptors and to start a complex intracellular signalling pathway involved in osteoblast differentiation and activity (Baron and Kneissel 2013) (Figure 5). Heterozygous mutations are associated to an early onset osteoporosis, whereas homozygous non-sense, missense, frameshift or splicing mutations occur in patients with severe OI characterized by short stature, frequent fractures and vertebral compression (Liu et al. 2016).

OI type XVI is caused by mutations in *CREB3L1,* which encodes the endoplasmic reticulum-stress transducer old astrocyte specifically induced substance (OASIS). The role of OASIS is to activate, once in the nucleus, *COL1A1* promoter (Murakami et al. 2009) (Figure 5).
The relation between *CREB3L1* mutations and OI has been proven by Keller et al (Keller et al. 2017). Expression of *CREB3L1* has been described in a few cell types, including osteoblasts. OASIS is an ER transmembrane protein with the N-terminal end in the cytoplasm, which contains a basic leucine zipper domain and an overlapping nuclear localization signal. Upon detection of ER stress, proteolytic cleavage releases the N-terminal fragment. This fragment is transported to the nucleus, where it functions as a transcription factor (Kondo et al. 2005).
From exome sequence analysis of members of a consanguineous family of Lebanese descent a trinucleotide deletion in cyclic AMP responsive element binding protein 3–like 1 (*CREB3L1*) that corresponds to an in-frame single amino acid deletion in OASIS was identified. The variant disrupts DNA-binding site preventing OASIS from transducing its targets due to either failure of the active N-terminal fragment to reach the nucleus or to interference with DNA-binding to gene-regulatory elements. This mutation results in a mild OI phenotype in heterozygotes and a lethal phenotype in homozygotes. Previously, homozygosity for whole-gene deletion of *CREB3L1* was shown to result in lethal OI in a Turkish family (Symoens 2013).

Finally homozygous mutation in *SP7,* encoding OSTERIX, leads to the severe recessive OI type XVII (Lapunzina et al. 2010). OSTERIX is a transcription factor required for osteoblast differentiation and bone formation during embryonic development, specifically expressed in osteoblast lineage cells and, at lower levels, in pre-hypertrophic chondrocytes (Zhou et al. 2010) (Figure 5). The mutation causes the truncation of a fifth of the protein, but further molecular and biochemical data need to be collected, in order to better understand the correlation between *SP7* defects and OI.

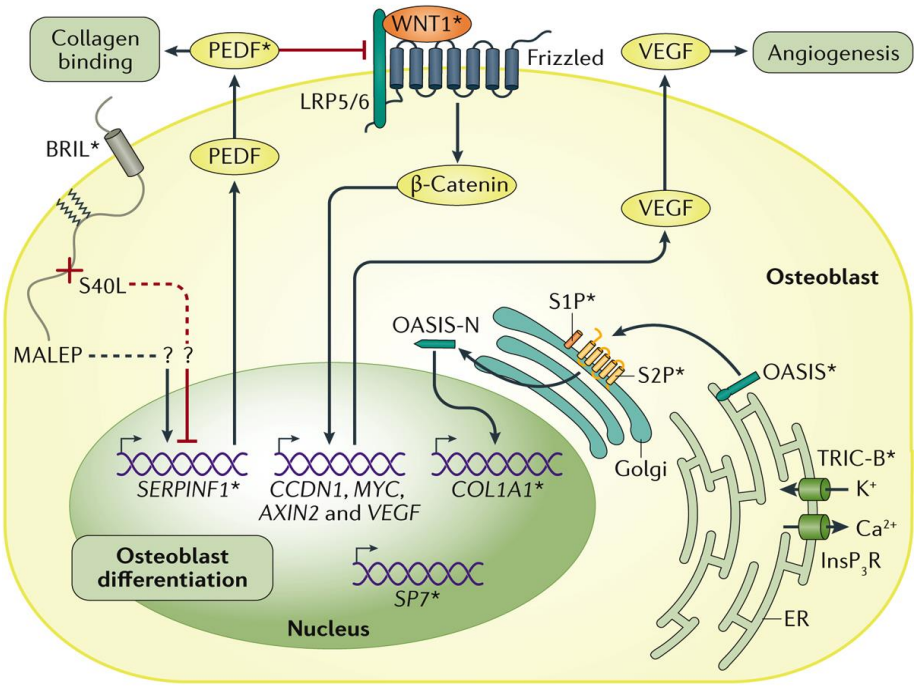

Figure 5. Defects in bone formation and mineralization in osteogenesis imperfecta. WNT1 is a secreted ligand that stimulates the transcription of genes involved in osteoblast differentiation by interacting with LRP5/6 and Frizzled on osteoblast precursor cells. Endopeptidase S2P is a protease in the Golgi membrane that is involved in regulating intramembrane proteolysis of transcription factors, such as OASIS, which is transported from the ER membrane to the Golgi for processing in presence of ER stress. Upon cleavage, OASIS moves to the nucleus, where it regulates the expression of genes involved in osteoblast differentiation. PEDF, encoded by *SERPINF1*, is an important collagen-binding protein regulating bone homoeostasis and osteoid mineralization and it has also strong anti-angiogenic functions by an unknown mechanism. The question marks refer to the presence of other factors in this pathway, which are not yet clear. The plus sign refers to increased transcription of the *SERPINF1* gene. S40L refers to the *IFITM5* mutation Ser40Leu. *IFITM5* encodes for BRIL, member of IFITM family, localized on osteoblast plasma membrane.
Dashed lines indicate unknown pathways. InsP3R, inositol-1,4,5-triphosphate receptor; OASIS-N, N-terminal of OASIS; MALEP, methionine, alanine, leucine, glutamate and proline pentapeptide; VEGF, vascular endothelial growth factor. *Mutations in the genes encoding these proteins are associated with osteogenesis imperfecta (from Marini et al. 2017).

Table 1. OI classification. (modified from Forlino and Marini 2016) DI = Dentinogenesis Imperfecta; HBM= High Bone Mass.

Inheritance	Gene	OMIM number	Sillence type	Protein	Typical features
Defects in collagen synthesis, structure, or processing (group A)					
AD	*COL1A1*	166200	I	Collagen type I, α 1	Rare to very severe bone deformity; normal sclerae, grey to dark blue; absent to common hearing loss and DI
		166210	II		
		259420	III		
		166220	IV		
AD	*COL1A2*	166200	I	Collagen type I, α 2	Rare to very severe bone deformity; normal sclerae, grey to dark blue; absent to common hearing loss and DI
		166210	II		
		259420	III		
		166220	IV		
AR	*BMP1*	614856	XIII	Bone morphogenetic protein 1	Mild to severe bone deformity; normal sclerae; umbilical hernia and HBM
Defects in collagen modification (group B)					
AR	*CRTAP*	610682	VII	Cartilage-associated protein	Severe rhizomelia; normal grey sclerae
AR	*LEPRE1*	610915	VIII	Leucine proline-enriched proteoglycan 1/prolyl 3-hydroxylase 1	Severe rhizomelia; normal grey sclerae
AR	*PPIB*	259440	IX	Peptidylprolyl isomerase B/cyclophilin B	Severe bone deformity; grey sclerae
AR	*TMEM38B*	615066	XIV	Transmembrane protein 38 B	Severe bone deformity; normal to blue sclerae
AR	*SPARC*	182120	XVII	Secreted acid cysteine-rich protease/osteonectin	White sclerae; occurrence of bone fractures after the first year; mild joint hyperlaxity
Defects in collagen folding and cross-linking (group C)					
AR	*SERPINH1*	613848	X	Serpin peptidase inhibitor, clade H, member 1/heat shock protein 47	Severe bone deformity; blue sclerae; presence of DI; skin blisters and bullae at birth; inguinal hernia
AR	*FKBP10*	610968	XI	FK506 binding protein 10	Mild to severe bone deformity; normal grey sclerae; variable congenital contractures
AR	*PLOD2*	609220	-	Procollagen- lysine, 2-oxoglutarate 5-dioxygenase 2	Moderate to severe bone deformity; progressive joint contractures
XR	*MBTPS2*	308205	-	Site-2 metalloprotease	Prenatal fractures of ribs and long bones; moderate short stature; blue sclerae; *pectus carinatum*; bowing of lower extremity long bone; generalized osteopenia
Defects in bone mineralization (group D)					
AD	*IFITM5*	610967	V	Interferon- induced transmembrane protein 5	Variable bone deformity; normal to blue sclerae; infrequent hearing loss; ossification of the interosseous membrane; radial head dislocation
AR	*SERPINF1*	613982	VI	Pigment epithelium- derived factor	Moderate to severe bone deformity; normal sclerae; unmineralised osteoid; fish scale appearance of lamellar bone pattern
Defects in osteoblast development with collagen insufficiency (group E)					
AR	*SP7*	613849	XII	Transcription factor 7/osterix	Severe bone deformity; normal sclerae; delayed tooth eruption; midface hypoplasia
AR	*WNT1*	615220	XV	Wingless-type MMTV integration site family, member 1	Severe bone deformity; white sclerae; possible neurological defects
AR	*CREB3L1*	616229	XVI	cAMP responsive element binding protein 3 like 1	Severe bone deformity

Zebrafish

Zebrafish (*Danio rerio*) was described for the first time by the scottish physician Francis Hamilton in 1822 (Hamilton 1822). Zebrafish is a member of the order Cypriniformes, a large group of freshwater fish coming from Bihar, in Northeastern India, but is also present in the South and West of peninsular India and beyond India, as far North as Pakistan and Nepal, as well as East into Bangladesh and possibly Myanmar (Parichy 2015). Members of the Otophysi, zebrafish are characterized by the presence of the Weberian apparatus, composed by perylimphatic and endolymphatic spaces of the inner ear, which are connected to a modified swim bladder through a series of modified anterior vertebral elements, called Weberian ossicles (Mayden et al 2007). In addition, zebrafish locomotion is characterized by the so called burst-and-coast swimming style, in which fish move forward (burst) in a single motion and glide (coast) to a slow speed, or stop from which they burst forward again (Kalueff et al., 2013).

As early as the 1930s the zebrafish became crucial in the research field as classical developmental and embryological model (Figure 6). At that time the combination of the transparency of embryos and larvae, useful for the *in vivo* visualization of cell-biological events, and the easy embryos manipulation were considered the main advantages of this organism. Through the 1980s the development of zebrafish genetic techniques, such as cloning (Streisinger et al. 1981), mutagenesis (Chakrabarti et al.1983), transgenesis (Stuart et al. 1988) and mapping approaches (Streisinger et al. 1986) allowed to support the use of zebrafish to apply invertebrate-style forward genetics to questions of vertebrate development. In 1990s the identification of thousands of zebrafish mutants through genetic screens made this organism a mainstream model in developmental biology and, recently, a model for several human diseases (Lieschke and Currie 2010).

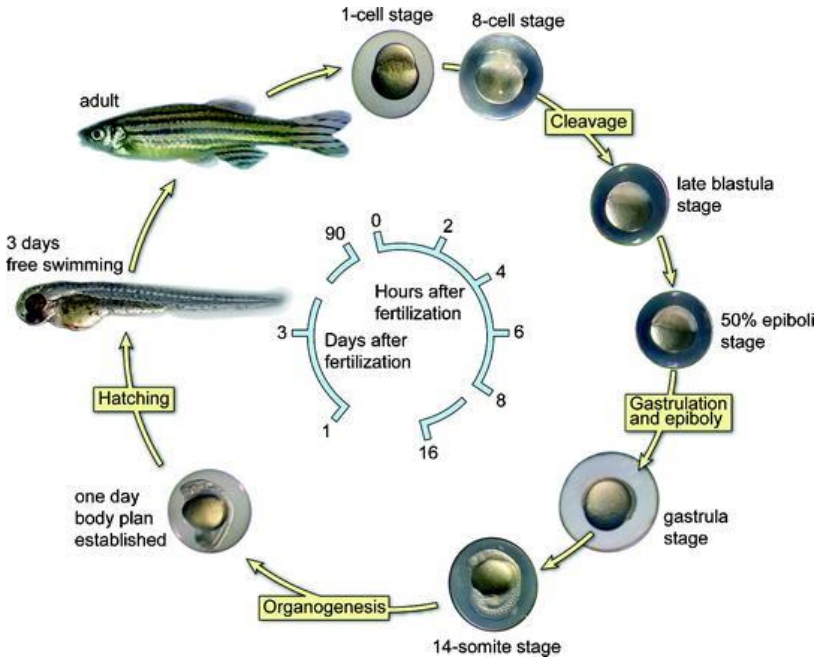

Figure 6. Schematic representation of the embryonic developmental stages of zebrafish. The cycle starts at the top with a fertilized single egg. The embryos develop quickly to a 14-somite stage within 16 h. After 24 h, the complete body plan of the embryo has been established meaning that all organs are present. Two days after fertilization, the embryos hatch and become free swimming. Zebrafish are adult and fertile at 3 months of age (Van't Padje et al. 2010).

Forward-genetics approaches are largely used to create mutants. Males fish are exposed to the mutagen ethylnitrosurea (ENU), which typically induces point mutations. After the exposure to ENU males are crossed with females wild-type and the germ line fish are identified. Once obtained the F1 population of fish the phenotype can be evaluated (Knapik 2000). In this way mutants are generated by random mutagenesis and selected on the basis of a common phenotype (Figure 7). Zebrafish forward-genetic screens are facilitated by the transparency of embryos. This is an important advantage in respect to the use of mice, in which aspects of organogenesis and disease pathology cannot be examined without surgery or post-mortem examination. Thanks to forward genetics screens several zebrafish mutants have been generated with mutations in genes orthologous to those causing human congenital diseases (Lieschke and Currie 2010). However, three major disadvantages limited the use of these random mutagenesis. First, the positional cloning of the causal mutations can be costly and laborious. Second, random mutagenesis usually generates heterozygous mutants and

recessive inherited phenotypes will need further screenings techniques. Finally, it is unlikely to be able to inactivate every gene in the genome with the random mutagenesis, which limits the depth and integrity of the genetic screens (Gaj et al. 2011).

Gene editing became appealing in the last years thanks to reverse genetics approaches. Genes of interest can be manipulated to generate models for specific diseases, allowing then to study the phenotypic consequences (Figure 7). Zebrafish imposed itself as tool for reverse genetics. At the beginning one of the most rapid and economical technique for performing reverse genetic analysis was the approach employing morpholino-modifying anti-sense oligonucleotide (MOs), which provided transient gene knock down by binding to RNA and inhibiting protein synthesis (Nasevicius 2000). Anyway, recent study demonstrated that approximately 80% of morphant phenotypes were not recapitulated in actual genetic mutants (Howe et al. 2013). Several are the causes of this disparity; for instance the short acting period (2-4 days) because of MOs degradation and dilution and the uncertain off-target effect induced by increased dose of MOs, such as non-specific p53 activation (Robu et al. 2007). In the last ten years the use of MOs is being replaced with other mutagenesis techniques able to generate knock out and knock-in models. The DNA editing techniques mainly used are the zinc finger nucleases (ZNFs), transcription activator-like effector nucleases (TALENs) and the clustered regularly interspaced short palindromic repeat (CRISPR) (Gaj 2013). They facilitated the wide application of genome editing thanks to high site specificity, flexible design, and easy operation. Compared to ZFNs and TALENs, the easy programmability of the DNA binding domains (sgRNAs) is the most advantageous feature of CRISPR/Cas system, making it the most amenable approach to high-throughput mutagenesis projects (Liu et al. 2017).

At certain sites, the efficiency of the CRISPR/Cas9 system can reach up to 98%, and the rates of mutagenesis at potential off-target sites are low (1–3%) (Hruscha et al. 2013). However, a broader range of DNA sequence modifications is highly desirable such as locus-specific SNP introduction or gene insertion (Stankiewicz 2010). Homology direct repair-mediated genome editing has been successfully employed in zebrafish after co-injection of a donor plasmid or a ssDNA (Li et al. 2015). However, this remains a low-efficiency process especially when integrating a relatively long DNA fragment in targeted site (Auer et al. 2014) In this context, genome-specific knock-in techniques in zebrafish are still under improvement (Li et al. 2015).

The advantages of zebrafish, as a genetically editable vertebrate model system, are reflected by their large brood size and the easy husbandry. Hundreds of eggs could be fertilized externally, which are subjected to direct observations and manipulations under a microscope. Within the first five days, the optically clear fish embryos develop rapidly with no artificial feeding required, and this is the most accessible time window to study the effects of certain genetic perturbations without being confounded by environmental factors (Lieschke and Currie 2010).

Another appealing approach, that proves once again the importance of zebrafish in the research field, is the transgenesis technique. The simple injection of constructs into fertilized eggs can result in 50-80% efficiency of germline transgenesis without the need to target the female pronucleus, as in mice. This advantage, together with the transparency of embryos, results in an expanding panel of transgenic zebrafish expressing fluorescent proteins in various cell types and organs (Udvadia and Linney 2003).

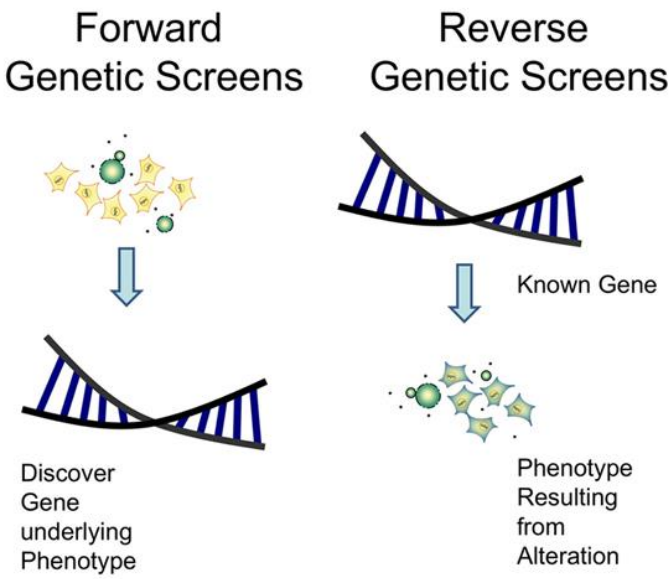

Figure 7. Forward and reverse genetic approaches. (from https://igtrcn.org/aphid-genetics/)

Zebrafish and collagen type I

In mammal collagen type I is widely distributed in different organs, such as skin, bone and muscle, and it is composed by two α1 chains and one α2 chain (Gelse et al. 2003). In zebrafish, collagen type I α chains are encoded by three genes, *col1a1a*, *col1a1b* and *col1a2*, coding for the collagen type I α1, α3 and α2 chains respectively. Nevertheless, neither information about their expression during development, nor biochemical data about the molecular composition were available before our research described in Chapter I. The similarity between α1(I) and α3(I), described from both amino acid sequence and peptide analysis by different chromatography techniques, suggests that these proteins are translated from two genes originated from the duplication of the ancestor α1(I) coding gene (Matukas V.J. 1969).

At present, α3(I) has been described only in bonyfish collagen and in some fish it has an organ-specific existence (Kimura et al. 1988). For instance, the skin of chum salmon *Oncorhynchus keta* and Japanese char *Salvelinus pluvius* contains exclusively α1(I) α2(I) α3(I) heterotrimers, whereas their muscles contain $[\alpha1(I)]_2$ α2(I) (Saito et al. 2001).

Zebrafish and bone

Zebrafish has recently become a valid model to better investigate the regulation of bone formation linked to skeletal diseases (Table 2). All the advantages reported above, such as the simplicity to generate mutants and the easy manipulation required, allow to directly observe physiological or pathological bone development under dissecting microscope. Alternative screening approaches include RNA or antibody staining to detect changes in patterns of gene expression (Currie et al. 1999), staining with specific dyes (Schilling et al. 1996), or even the use of X-Rays to search for mutants with abnormal bone structures (Fisher and Halpern 1999).

Tetrapods' bones can develop both in presence of transient cartilage template, which is subsequently ossified in a process called endochondral ossification and in the absence of a cartilage template (intramembranous ossification). These differences in embryonic origins are reflected in differences in the expression of osteoblast markers and activities of signalling molecules during osteoblastogenesis (Abzhanov et al. 2007).

The tetrapods' ossification processes are conserved in zebrafish. The *intramembranous* ossification includes bones that develop directly within a connective tissue membrane and are homologous with

similarly formed bones in primitive vertebrates (dermal bones), while bones that ossify around (*perichondral*) or within (*endochondral*) a cartilage model are termed "cartilage bones" (Cubbage et al. 1996). The cells involved in bone formation are osteoblasts, also in teleosts. In general, similarly to tetrapods, zebrafish osteoblast differentiation can be broken down into three overlapping stages based upon gene expression: early differentiation, with the expression of *runx2a* and/or *runx2b*, intermediate differentiation, with the expression of *osx* (*osterix*) and a mature state of differentiation distinguished by the expression of the bone matrix proteins *colIa2* (*collagen type I alpha 2*, Fisher et al. 2003) and *osn* (*osteonectin/sparc*) (Li et al. 2009). These findings suggest that the transcriptional hierarchy found in mammals is conserved during zebrafish osteoblastogenesis. This is true thanks to the significant degrees of homology between genes involved in mammalian bone metabolism with regard to their amino acid sequence and gene expression during embryogenesis in zebrafish and higher vertebrates (Renn et al. 2006) .

Teleosts' osteoblasts display various morphologies, depending on the secretory activity and their position on bone (Huysseune 2000). Structurally, bone tissue in teleost fish develops first as woven bone and then parallel-fibered and lamellar bone develops in more mature individuals (Renn et al. 2006). The zebrafish bone contains osteocytes, which probably have the role to govern bone remodelling in response to mechanical load (Burger et al. 2003). Moreover, osteoclasts activity is conserved and essential for bone resorption in zebrafish (Burger et al. 2003).

As in mammals, in fact, in zebrafish bone remodelling is required for several reasons, such as to guarantee the mineral homeostasis, for fins regeneration or to replace one skeletal tissue to another (for example cartilage in bone) (Witten and Huysseune 2009). These similarities at the cellular level support the suggestion that important regulatory mechanisms such as, for instance, signalling transduction pathways implicated in bone homeostasis are conserved between fish and tetrapods.

Despite these similarities, mineral metabolism in teleost presents some peculiar features in respect to mammals. In mammals, calcium is released from skeleton through bone resorption by osteoclasts or by osteocytic osteolysis and it is deposited into the skeletal tissues. Teleost have several alternative sources of calcium, and resorption of the endoskeleton is used only as last resort. (Witten and Huysseune 2009). Freshwater teleosts can obtain calcium by gills epithelium through ATP-driven active calcium transport, even at low environmental calcium levels (Guerreiro et al. 2002). In addition, in case of mineral deficiency teleost can resorb their scales. Bone resorption in teleost is

mainly caused by phosphorous requirement, which comes mainly from the diet, rather than calcium deficiency (Roy et al. 2002; Lall and Lewis-McCrea 2007, Roy and Lall 2003).

Vertebral column development

Zebrafish vertebral column is composed by vertebrae and intervertebral discs and develops in a segmented manner from the head to the tail (Due et al. 2001). The development of the vertebral column starts with the formation of the perichordal centrum, a mineralized ring-shaped structure surrounding the notochord, which allows the foundation for later segmented vertebrae formation.
The segmentation of the vertebral column becomes evident at 15 days post fertilization and large vacuolated notochord-like cells are clearly visible in the intervertebral discs of zebrafish larvae. Starting from one month post fertilization the intervertebral discs are occupied by two large vacuoles connected to the notochordal canal at the center of vertebral bodies and are composed by two tissues called the nucleus pulposus and the annulus fibrosus. In contrast to intervertebral discs, the vertebral body is occupied for the most part by calcified bone and, inside the vertebral body, there is a notochordal canal located at the center of the vertebra, which is likely the remaining of the original notochord (Due et al. 2001).

Table 2. Example of zebrafish models of human bone and skeletal disorders (modified from Gavaia et al.2014).

Human bone/skeletal disorders	Fish model systems	Affected gene(s)	Ref.
Osteogenesis imperfecta (OI)	*chihuahua (chi)* *microwaved (med)* *frilly fins (frf)*	*col1a1* *bmp1*	(Fisher et al. 2003; Asharani et al. 2012)
Mucopolidosis II (ML-II)	*gnptab*	*gnptab*	(Flanagan-Steet et al. 2009)
Craniosynostosis	*dolphin (dol) stocksteif (sst)*	*cyp26bI*	(Laue et al. 2011)
Idiopathic scoliosis	*curveback*	Not determined	(Gorman KF et al. 2007)
Holoprosencephaly (HPE)	*sonic-you (syu)*	*shh*	(Schauerte et al. 1998)
Campomelic dysplasia	*jellyfish (jef)*	*sox9a*	(Yan et al. 2002)
Arterial calcification of infancy (ectopic mineralisation)	*dragonfin*	*enppI*	(Huitema et al. 2012)
DiGeorge syndrome (DGS)	*van-gogh (vgo)*	*tbxI*	(Piotrowski et al. 2003)
Cranio-lenticulo-sutural dysplasia (CLSD)	*crusher (cru)*	*sec23a*	(Lang et al. 2006)
Osteopahty related to mineral homeostasis	*no bone (nob)*	*entpd5*	(Huitema et al. 2012)
Osteopahty related to abnormal ECM deposition	*feelgood (fel)* *man o'war (mow)* *bulldog (bul)*	*crebl312* *uxsI* *sec24d*	(Melville et al. 2011; Eames et al. 2010; Sarmah et al. 2010)
Osteopahty related to delayed ossification	*calcification slow (bcs)*	Not determined	(Xi Y et al. 2013)
Hyperossification	*rapunzel (rpx)*	*rpz*	(Green et al. 2009)
Raine syndrome	*fam2b*	*fam20b*	(Eames et al. 2011)
Enhlers-Danlos symdrome (EDS)	*b4galt7*	*b4galt7*	(Nissen et al. 2006)

Zebrafish OI mutants

Among all the models for human bone diseases listed in Table 2, four show an osteogenesis imperfecta phenotype and have been proposed as OI zebrafish models.

The zebrafish *Chihuahua (chi/+)* is carrying in heterozygosis a missense mutation responsible for the Gly574Asp (p.Gly736Asp) substitution in the triple helical domain of the α1 chain of collagen type I. *Chi/+* mutants are characterized by skeletal deformity and extreme bone fragility, resembling human OI type III (Fisher et al. 2003). A deep phenotypic investigation of this model was the first part of my research project (Gioia et al. 2017).

The zebrafish mutant *frilly fins (frf $^{-/-}$)* resembles the rare recessive osteogenesis imperfecta type XIII (van Eeden et al. 1996). *frf $^{-/-}$* carries a missense mutation in the Bmp1a protease domain. Homozygous mutants show a severe delayed ossification of the vertebrae, and when mineralisation occurs the vertebrae are misshapen or fused (Mackay et al. 2013). Their phenotype is characterized by ruffled larval fin, shortened body axis and malformed craniofacial structures and fin shape (Asharani et al. 2012).

Microwaved (med $^{-/-}$) mutants have mutation in *col1a1a* and display a similar phenotype to *frf* with delayed ossification and undulation in the larval fin.
Med $^{-/-}$ mutants carry a homozygous G>A transition predicted to substitute a highly conserved glutamic acid with a lysine at position 888 (p.Glu888Lys). They displayed traits similar to those seen in individuals with classical OI even if the transmission is recessive, such as reduced bone density, that was observed in fish both in vertebral bodies and in the distal fin rays.(Asharani et al. 2012)

Recently, a zebrafish model of Bruck syndrome was generated. It is characterized by severe musculoskeletal malformations with evidence of bone fragility. It carries a loss-of-function mutation in *plod2*, which encodes the lysyl hydroxylase 2 (Lh2). Mutants show reduced telopeptide lysyl hydroxylation with aberrant cross-linking of bone type I collagen, severe skeletal and muscular malformations and structural defects in the larvae notochord sheath (Gistelinck et al. 2016). It is known that skeletal anomalies and bone fragility, which characterized Bruck syndrome (BS) patients, clinically overlap with osteogenesis imperfecta phenotype (Forlino et al. 2011). This aspect allows us to consider *plod2* another valid OI zebrafish model (Figure 8).

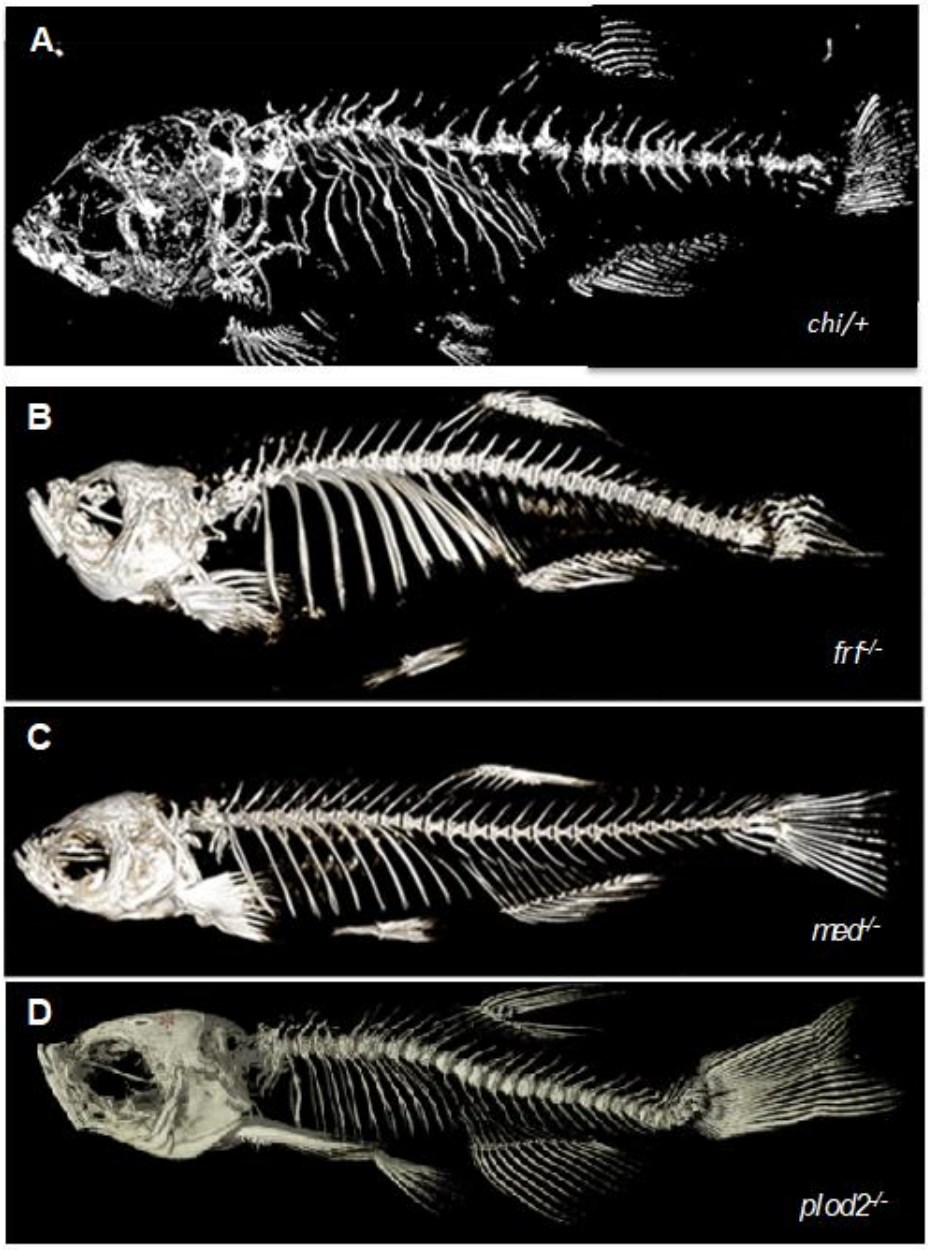

Figure 8. Zebrafish mutants of bone dysplasia. Osteogenesis imperfecta models: **A)** Dominant *chihuahua (chi/+)* mutant, **B)** Recessive *frilly fin (frf$^{-/-}$)* mutant, **C)** Recessive *microwaved (med$^{-/-}$)* mutant; Bruck syndrome model: **D)** Recessive *plod2 (plod2$^{-/-}$)* mutant.

Aims

Osteogenesis imperfecta (OI) is a bone disease characterized by bone fragility, frequent fractures in absence of trauma and growth deficiency. The more common dominant forms are caused by mutations in collagen type I genes, *COL1A1* and *COL1A2*, while the rarest and more recently identified autosomal recessive forms are due to deficiency in proteins involved in procollagen type I synthesis, post translational modifications, processing, folding and secretion. Mutations affecting bone forming cells differentiation and activity have also been reported.

Traditionally the OI outcome was considered a consequence of the altered extracellular matrix due either to matrix insufficiency or to the presence of mutant collagen, impairing both collagen-collagen and collagen-non-collagenic protein interactions and affecting cell-cell and cell-matrix interactions and tissue mineralization. More recently, the impaired osteoblasts homeostasis due to mutant collagen retention in the endoplasmic reticulum has been demonstrated to play a role in OI outcome both in dominant as well as in most of the recessive forms.

In the era of "precision medicine" a detailed knowledge of the specific molecular basis of each form of the disorder will advance clinical diagnosis and potentially stimulate targeted therapeutic approaches (Chen et al. 2018).

Nowadays, no definitive cure is available for OI and to develop novel drug therapies the small teleost zebrafish (*Danio rerio*) is a particularly appealing model (Fleming et al. 2005)**.**

Its small size, high proliferative rate, embryo transparency and small amount of drug required make zebrafish the model of choice for drug screening studies, when a valid disease model is available.

My research activity was focused on the characterization of the zebrafish type I collagen, whose chains composition was still unknown, but this information was necessary to use zebrafish as a model for collagen related disorders (Chapter I). Then, I contributed to the characterization of the zebrafish *Chihuahua*, carrying a G574D substitution in the triple helical domain of the α1 chain of type I collagen, validating it as a model for classical dominant OI (Chapter II and III). I used this model to test a novel treatment for OI using chemical chaperones targeting the cellular stress caused by mutant collagen retention (Chapter II). Finally, I generated new zebrafish models for the recessive OI forms type VII, VIII and XIV with the goal to have new tools for both a better understanding of the pathophysiology of the disease and for drug screening approaches (Chapter IV).

Chapter I.

Zebrafish Collagen Type I: Molecular and Biochemical Characterization of the Major Structural Protein in Bone and Skin.

The main protein directly or indirectly involved in OI is collagen type I, the major protein component of the extracellular matrix of bone and skin. In order to use zebrafish as a good model to study skeletal diseases and in particular OI, a deep investigation of the teleost collagen type I structure was missing. The main purpose of the first project of my PhD thesis was to perform a deep molecular and biochemical characterization of zebrafish collagen type I. We demonstrated that, both in zebrafish embryos and adult tissues, three α chains contribute to the formation of the collagen type I triple helix, although the exact stoichiometry and post-translational modifications need to be further defined.

In detailed the spatio temporal expression of the three genes *col1a1a, col1a1b* and *col1a2* encoding for the α1(I), α3(I) and α2(I) chains was evaluated by means of microarray, qPCR and *in situ* hybridization.

SDS-PAGE of collagen extracted from zebrafish embryos and from adult zebrafish skin, bone and scales, followed by mass spectrometry analysis, were performed in order to demonstrate the presence of all three chains and to clarify their stoichiometry. Mass spectrometry data on α chain bands cut from SDS-PAGE showed a statistically significant higher α3(I)/α1(I) ratio in external (skin and scales) versus internal (bone) tissues pointing out to a tissue-specific collagen composition. In contrast to the mass spectrometry data, the amino acid analysis of collagen type I extracted from zebrafish bone, skin and scales revealed an equal ratio for α1(I), α2(I) and α3(I) in all examined tissues.

Chapter II.

The chaperone activity of 4PBA ameliorates the skeletal phenotype of Chihuahua, a zebrafish model for dominant osteogenesis imperfecta.

The aim of this second part of my research project was to validate the zebrafish *Chihuahua* as a good model for classical dominant OI and use it as tool in drug screening studies. *Chihuahua* was created by ENU mutagenesis in the laboratory of Professor Shannon Fisher (Department of Pharmacology &

Experimental Therapeutics, Boston University School of Medicine, Boston, USA) and it carries the heterozygous G574D (p.G736D) substitution in the α1 chain of type I collagen. X-Ray analysis and specific skeletal staining showed in *Chihuahua* the presence of bone deformities, fragility and mineralization delay, typical features of human OI. Moreover, the peculiar OI collagen type I migration pattern characterized by delay and broadened of the α bands was observed in SDS-PAGE. Mutant collagen type I showed also a reduced thermal stability.

The presence of endoplasmic reticulum (ER) enlargement, likely due to mutant collagen retention in osteoblasts and fibroblasts of mutant fish, was demonstrated by electron and confocal microscopy analysis.

To target ER stress we used two already FDA approved chemical chaperones, 4 phenylbutyrate (4PBA) and Tauroursodeoxycholic Acid (TUDCA).

Only 4PBA was able to improve *Chihuahua* bone outcome both at larval as well as at adult age.

Chapter III.

Chihuahua zebrafish presents with severely impaired bone material quality as described in classical dominant human osteogenesis imperfecta.

A common OI patient's feature is the high bone fragility that arises from low bone mass and abnormalities in bone material properties, such as reduced toughness. Alterations of bone tissue characteristics are similar in most types of OI and the degree of mineralization of the bone matrix is almost universally increased, both in mild and in more severe forms of the disease. The zebrafish *Chihuahua* (*chi/+*), similarly to human severe OI type III, shows deformations and fractures in the ribs, altered mineralization patterns and a smaller body size. In collaboration with Prof Busse, University of Hamburg, the changes in bone morphology, structure and tissue composition of *Chihuahua* at multiple length scales were determined. Morphological changes were investigated with high-resolution micro-CT imaging, while vertebrae tissue composition was assessed with quantitative backscattered electron microscopy and Fourier-transform infrared spectroscopy. These techniques allowed to quantify calcium content, matrix porosity, as well as mineral crystallinity and collagen maturity in comparison to control fish. Specific phenotypes were identified at the skeletal level such as an accumulation of brittle fractures and deformities and heterogeneous mineralization patterns, whereas at tissue level an increased mineral density, reduced mineral and collagen maturity, and

increased matrix porosity were detected. These characteristics are clearly resembling the bone of human patients, confirming once again the validity of the zebrafish *Chihuahua* as a good model of the dominant form of OI.

Chapter IV.

Generation and characterization of recessive osteogenesis imperfecta type VII, VIII and XIV zebrafish models using CRISPR/Cas9 system.

Although about 85–90% of OI cases are caused by structural or quantitative mutations in the collagen genes *COL1A1* and *COL1A*2, since 2006 many other causative genes for OI have been detected mainly associated to recessive transmission. These findings made OI better defined as a collagen-related disease. Recessive forms of OI are mainly caused by defects in genes involved in collagen post translational modification, folding, collagen production and bone mineralization.

The major project of my PhD research activity was the generation of OI type VII, VIII and XIV zebrafish models caused by loss-of-function of cartilage associated protein (Crtap), prolyl 3 hydroxylase 1 (P3h1) and trimeric cation channel B (Tric-b), respectively.

To this aim the genome editing CRISPR/Cas9 system was employed.

OI type VII and VIII models have been deeply characterized both from a morphological and biochemical point of view and validated as good model of the disease. X-Ray, µCT and specific skeletal staining allowed to appreciate bone abnormalities and delay mineralization during mutant fish development. Overglycosylation of mutant collagen type I was also demonstrated by SDS-PAGE, reproducing a typical patients' collagen feature.

The generation of the OI type XIV zebrafish has been successfully obtained only more recently and the model characterization is still ongoing. The first heterozygous mutant line obtained carries a deletion that includes the KEV sequence, fundamental for the correct formation and function of the channel. Furthermore, three other heterozygous fish were identified, which carry mutations resulting in protein premature stop codon. The final aim of this study will be deeply characterize the three lines to elucidate OI pathophysiology as well as Tric-b activity *in vivo*.

All three selected OI forms in human and in mice are characterized by mutant collagen intracellular retention and potentially ER stress. Thus, these recessive models will be used to attempt the same pharmacological treatment based on chemical chaperones, successfully tested in the *Chihuahua*

model for dominant OI. The possibility to treat both dominant and recessive forms of OI, using the same rationale and the same drug, that is already on the market, paves the way for a plausible future therapy for patients.

Chapter I

Zebrafish collagen type I

Zebrafish, together with other teleosts such as medaka, platyfish, stickleback and killifish, are important as model species for studying human development, physiology, health, and disease (Schartl 2013). They are useful as laboratory research models, thanks to easy husbandry, high fertility, external fertilization, embryo transparency, tractable genetics and their amenability for high throughput drug screening. Moreover, although zebrafish proteins display less than 70% identity to their human orthologues, conservation in the functional domains, such as substrate binding regions, is considerably higher, approaching values of 100% similarity (Langheinrich 2003). Despite these advantages some evolutionary divergences between teleosts and tetrapods need to be taken into consideration.

A teleost genome duplication (TGD) occurred 320 mya (millions of years ago) in an ancestor of teleost lineage. After this evolutionary event 12-24% of genes were retained as two paralogs genes in teleosts compared to one gene in tetrapods. TGD paralogs could have undergone to changes in their function, such as the partitioning of ancestral gene activity among duplicates or the acquisition of new gene functions (Force et al. 1999; Postlethwait et al. 2004). These differences could make difficult to transfer the knowledge obtained in teleosts species to humans.

Nowadays, progress in sequencing techniques has enabled the relatively cheap and fast generation of genomic and transcriptomic sequence data from several fish species to better understand gene function evolution among vertebrates (Braasch et al. 2014) (Figure 1).

Chromosome numbers in teleost fish are remarkably conserved compared to mammals (Amores et al. 2014). Even within single order of mammals, chromosome numbers often change considerably; for example among Cervidae (deer) the haploid number varies between 3 and 40 and among Rodentia (rodents), the haploid number varies between 5 and 51. Among teleosts with a sequenced genome, zebrafish (Danio rerio) has 25 haploid chromosomes like most teleosts, platyfish (Xiphophorus maculatus) and medaka (Oryzias latipes) have 24, cod (Gadus morhua) 23, fugu pufferfish (Takifugu rubripes) 22, and both stickleback (Gasterosteus aculeatus) and green pufferfish (Tetraodon nigroviridis) have 21 (Figure 1) (Amores et al 2014)

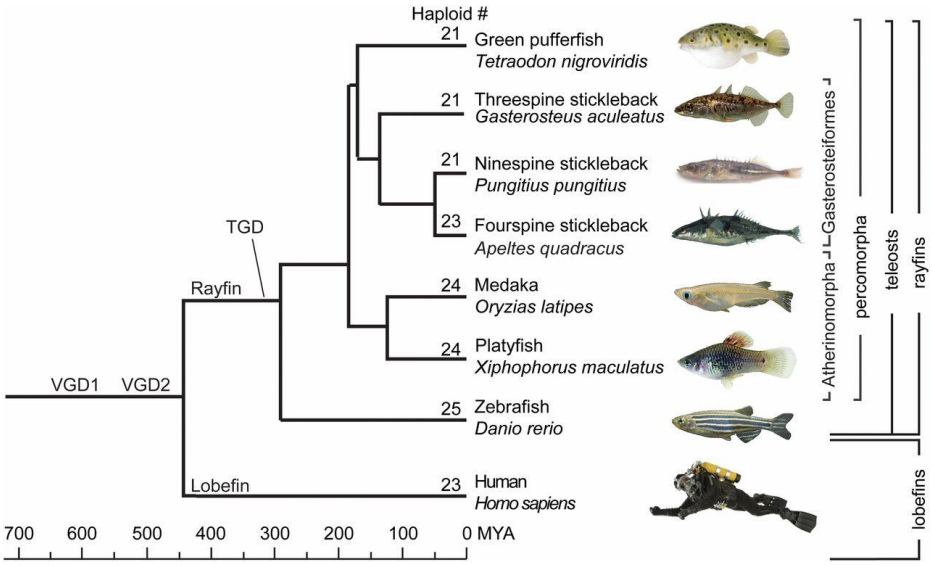

Figure 1. Phylogenetic relationship among lobe-fin (Sarcopterygii) and ray-fin (Actinopterygii) fish. The chromosome haploid number between Homo Sapiens and teleosts is similar. (Amores et al. 2014) TGD: Teleost genome duplication, VGD1: vertebrate genome duplication 1, VGD2: vertebrate genome duplication 2, MYA: millions of years ago.

The most abundant protein present in bone is collagen type I. In all tetrapods it is mainly composed of two identical α1 chains and one α2 chain encoded by *COL1A1* and *COL1A2*, respectively.

In teleosts, including zebrafish, the genome duplication gave rise to a third gene, namely *col1a1b*, coding for the collagen type I α3 chain. The similarity, described from both amino acid sequence and peptide analysis by different chromatography techniques, between α1(I) and α3(I) suggested that these proteins were translated from two genes originated from the duplication of the ancestor α1(I) coding gene (Matukas 1969).

At present, α3(I) is found only in bonyfish collagen and the organ-specific existence of α3(I) has been shown in many bonyfish (Kimura et al. 1988). In fact, collagen type I stoichiometry in some teleosts was demonstrated to be tissue dependent. For instance, the skins of chum salmon *Oncorhynchus keta* and Japanese char *Salvelinus pluvius* contain exclusively α1(I) α2(I) α3(I) heterotrimers, whereas their muscles contain $[\alpha1(I)]_2$ α2(I) (Saito et al. 2001).

In zebrafish the existence of three gene, *col1a1a*, *col1a1b* and *col1a2* coding for α1(I), α3(I) and α2(I) was reported (Morvan-Dubois et al. 2003), but neither information about their expression during development, nor biochemical data about the molecular composition were available.

Thus, part of my research thesis attempted to fill this gap and the results were published in the following paper.

We demonstrated the co-regulation of α1(I), α3(I) and α2(I) during embryonic and larval period and their expression in adults. Analysis of collagen type I extracted from adult bone, skin and scales revealed equal amounts of α1(I), α3(I) and α2(I) chains. However, a tissue-specific stoichiometry and/or post-translational modification status for collagen type I was not excluded and will need further study.

Personal contributions to Chapter I

- *In silico* analysis. I performed the *in silico* analysis using Genomicus and Clustal W2.
- Collagen extraction. I contributed to collagen type I extraction from embryos and adult zebrafish bone, skin and scales. I contributed to perform the collagen amino acid analysis and the SDS-PAGE

SCIENTIFIC REPORTS

OPEN

Zebrafish Collagen Type I: Molecular and Biochemical Characterization of the Major Structural Protein in Bone and Skin

Received: 07 October 2015
Accepted: 26 January 2016
Published: 15 February 2016

C. Gistelinck[1,*], R. Gioia[2,*], A. Gagliardi[3], F. Tonelli[2], L. Marchese[2], L. Bianchi[3], C. Landi[3], L. Bini[3], A. Huysseune[4], P. E. Witten[4], A. Staes[5,6], K. Gevaert[5,6], N. De Rocker[1], B. Menten[1], F. Malfait[1], S. Leikin[7], S. Carra[8], R. Tenni[2], A. Rossi[2], A. De Paepe[1], P. Coucke[1], A. Willaert[1,†] & A. Forlino[2,†]

Over the last years the zebrafish imposed itself as a powerful model to study skeletal diseases, but a limit to its use is the poor characterization of collagen type I, the most abundant protein in bone and skin. In tetrapods collagen type I is a trimer mainly composed of two α1 chains and one α2 chain, encoded by *COL1A1* and *COL1A2* genes, respectively. In contrast, in zebrafish three type I collagen genes exist, *col1a1a*, *col1a1b* and *col1a2* coding for α1(I), α3(I) and α2(I) chains. During embryonic and larval development the three collagen type I genes showed a similar spatio-temporal expression pattern, indicating their co-regulation and interdependence at these stages. In both embryonic and adult tissues, the presence of the three α(I) chains was demonstrated, although in embryos α1(I) was present in two distinct glycosylated states, suggesting a developmental-specific collagen composition. Even though in adult bone, skin and scales equal amounts of α1(I), α3(I) and α2(I) chains are present, the presented data suggest a tissue-specific stoichiometry and/or post-translational modification status for collagen type I. In conclusion, this data will be useful to properly interpret results and insights gained from zebrafish models of skeletal diseases.

In the last years, the small fresh water teleost *Danio rerio* (zebrafish) imposed itself as a good model for the study of heritable skeletal diseases[1]. Several zebrafish mutants that accurately model human skeletal diseases have been reported, such as *frilly fins*, *microwaved* and *chihuahua*, all reproducing the brittle bone disease osteogenesis imperfecta[2,3]. Furthermore, the molecular basis and the key regulators of skeletogenesis were demonstrated to be highly conserved between zebrafish and mammals[4,5]. The embryo transparency together with the availability of many zebrafish lines expressing fluorescent proteins under the control of skeletal specific promoters facilitated the investigation of early skeletal development[6], whereas the generation of mutant lines for specific cartilage and bone proteins favoured the understanding of late skeletogenesis events[7,8]. Furthermore, the TALEN and CRISPR/Cas-based methods for genome editing developed in the last years allow the rapid generation of new zebrafish skeletal mutants[9]. Of relevance, since zebrafish are aquatic animals, the weight-bearing demand on the skeleton is reduced, therefore many bone mutant lines survive far longer than mouse models allowing characterization from embryonic to adult stages. Finally, due to their ability to produce large clutches of transparent embryos and their small size, high-throughput drug screening is also easier and economically advantageous using zebrafish instead of murine models and this is particularly appealing for the identification of osteogenic and osteotoxic molecules[10].

[1]Center for Medical Genetics Ghent, Ghent University, Ghent, Belgium. [2]Department of Molecular Medicine, Biochemistry Unit, University of Pavia, Pavia, Italy. [3]Functional Proteomics Lab., Department of Life Sciences, University of Siena, Siena, Italy. [4]Biology Department, Ghent University, Ghent, Belgium. [5]Department of Medical Protein Research, VIB, Ghent, Belgium. [6]Department of Biochemistry, Ghent University, Ghent, Belgium. [7]Eunice Kennedy Shriver National Institute of Child Health and Human Development, National Institutes of Health, Bethesda, MD, USA. [8]Department of Biosciences, University of Milano, Milan, Italy. *These authors contributed equally to this work. †These authors jointly supervised this work. Correspondence and requests for materials should be addressed to A.F. (email: aforlino@unipv.it)

The most abundant protein present in bone is collagen type I, but its features in zebrafish are still puzzling the research field. More insights into the stoichiometry and localization of collagen type I during zebrafish development and in adult tissues are necessary to properly interpret findings gained from zebrafish models for skeletal diseases.

Type I collagen is a member of the fibrillar collagen family, since it is characterized by a distinctive uninterrupted "collagenous" domain, a right handed triple helix formed by three left handed α chains supercoiled around a central axis[11]. In the endoplasmic reticulum, type I collagen is synthesized as a pro-collagen molecule characterized by the presence of N- and C-propeptides flanking the triple helical region via two short telopeptides (N- and C- telopeptide). In particular, the C-propeptide contains a variable sequence of 15 residues, known as the chain recognition region, necessary for chain identification, association and stoichiometry[12]. In the C-propeptide there is also a series of conserved cysteine residues involved in the formation of intra- and inter-chain disulphide bonds necessary for the correct conformation of the propeptide itself and for the covalent stabilization of the newly forming triple helix molecule[13]. Following secretion, specific peptidases are responsible for the removal of the N- and C-propeptides, allowing the mature triple helix to self-assemble into fibrils. Fibrils are stabilized by cross-links occurring between specific lysine and hydroxylysine residues located in the telopeptides (9^N and 16^C in α1 and 5^N in α2) and at both the extremities of the triple helical domain (at positions 87 and 930 in α1 and 87 and 933 in α2)[14]. These residues are involved in the formation of both inter- and intra-molecular covalent bonds. Structural or quantitative defects in type I collagen cause osteogenesis imperfecta (OI), also known as brittle bone disease, an inherited skeletal disorder that is mainly characterized by increased bone fragility, fracture risk and reduced bone strength[15]. Several studies have also demonstrated the association between variants identified in the genes encoding for collagen type I and bone density and risk of fractures in patients with senile osteoporosis[16].

In all tetrapods type I collagen is mainly composed of two identical α1 chains and one α2 chain, encoded by *COL1A1* and *COL1A2* genes, respectively. However, homotrimeric type I collagen, consisting of three α1 chains, was described as a minor component of human skin[17], present in chick embryos[18] and associated with the extracellular matrix produced by cancer cells[19]. In many teleosts, including zebrafish, the presence of a distinct gene coding for a third α(I) chain, named α3, has been reported[20]. Based on amino acid sequence and on peptide analysis, the described third chain of type I collagen was shown to be phylogenetically more similar to the α1(I) than to the α2(I) chain. The similarity between α1(I) and α3(I) suggested that the genes for both proteins probably originated from the duplication of an ancestor α(I) coding gene during the whole genome duplication event that occurred ~320 mya at the basis of teleost evolution[21]. The first description of the presence at protein level of the α3(I) chain in fishes dates back to 1965[22], when it was identified in the collagen type I extracted from the Atlantic cod (*Gadus morhua*) skin. Several years later Kimura and colleagues classified teleosts in three groups based on the α3 properties of acid soluble collagen type I[23]. A first teleost group, including ayu, flying fish and saury, missed this chain; a second group, including salmon and rainbow trout, was characterized by the presence of an α3 chain co-eluting with α2 by chromatographic separation and co-migrating with α1 by electrophoresis; finally, in a third group including most of the teleosts, α3 was co-migrating with α1 both by chromatography and by electrophoresis[24]. In all the analysed fishes the suggested stoichiometry for the three α(I) chains was 1:1:1. Interestingly, in acid soluble collagen type I obtained from carp and tilapia skin, α3 was present in very low amount, suggesting the presence of two different type I collagen heterotrimers, $(\alpha1)_2\alpha2$ and $\alpha1\alpha2\alpha3$[24]. The first complete primary structure of a teleost type I collagen was identified in 2001 in rainbow trout, and a 1:1:1 stoichiometry for the three chains was demonstrated in skin, whereas muscle type I collagen was mainly constituted by α1 and α2 with a stoichiometry of $(\alpha1)_2\alpha2$[25].

In zebrafish the existence of three genes, *col1a1a*, *col1a1b* and *col1a2* coding for collagen type I α1, α3 and α2 chains was reported[20], but to date neither information about their expression during development nor biochemical data about the molecular composition are available. In this work, we report for the first time an extensive molecular and biochemical analysis of zebrafish collagen type I. A similar spatio-temporal expression pattern for *col1a1a, col1a1b* and *col1a2* was demonstrated starting from the oocyte stage until adult age. The existence of the α3 chain was demonstrated at the protein level both in zebrafish embryos and in adult skin, scales and bone. In embryos α1(I) was present in two distinct post-translationally glycosylated states, suggesting a developmental or tissue specific type I collagen composition in zebrafish. In adult tissues no significant differences were observed in type I collagen in terms of electrophoretic migration, amino acid composition and denaturation temperature and the prevalence of a 1:1:1 ratio for α1(I), α2(I) and α3(I) was suggested.

Results

Similarity and differences between zebrafish and mammal type I procollagen. A synteny analysis of the genes surrounding the zebrafish collagen type I genes *col1a1a, col1a1b* and *col1a2* was first undertaken. The analysis of the chromosomal regions surrounding the zebrafish *col1a1a* and *col1a1b*, as well as the mouse and human *COL1A1* genes, revealed a shared synteny, supporting the presence of a common ancestral chromosomal origin (Fig. 1a). However, the number of the syntenic genes flanking human/mouse *COL1A1* and zebrafish *col1a1a* and *col1a1b* is limited and also their location and arrangement are different. (Fig. 1a, Supplementary Table S1).

A strong synteny was identified between the genomic regions surrounding the zebrafish *col1a2* and human/murine *COL1A2* locus (Fig. 1b, Supplementary Table S2).

To evaluate the conservation of the type I collagen alpha chains we considered the whole chain sequence (proα1(I), proα2(I) and proα3(I)) as well as their different procollagen domains, namely the N-propeptide, N-telopeptide, triple helix, C-telopeptide and C-propeptide. Amino acid (AA) sequence alignments revealed that zebrafish proα1(I) and proα3(I) chains share 78% of AA identity and the same theoretical molecular weight (137 kDa) and isoelectric point (5.4) (Table 1). Moreover, zebrafish proα1(I) shows 77% and 76% conserved AA with human and murine proα1(I) chains respectively, while proα3(I) has 75% identity with both of them. Since

Figure 1. Synteny maps comparing the genes flanking type I collagen loci among human (*H. sapiens*), mouse (*M. musculus*) and zebrafish (*D. rerio*) chromosomes. The maps were obtained using the genome browser Genomicus. The human genes were used as roots. The position of the genes (Mb) relative to the investigated locus is based on Ensemble database and shown on top of the chromosome line. The exact chromosomal position of all the conserved genes is reported in the Supplementary Tables S1 and S2. The direction of the arrows indicates the gene orientation in respect to the reference gene. (**a**) Synteny map for *COL1A1* locus. Eleven genes flanking human and murine *COL1A1* are present in the zebrafish genome flanking both *col1a1a* and *col1a1b* loci (asterisk). (**b**) Synteny map revealed 27 conserved genes flanking human *COL1A2* that have orthologs in zebrafish chromosome 19 surrounding *col1a2*.

zebrafish type I procollagen domains have not yet been described in literature, their boundaries were inferred from the alignment with the human and murine proα chains. The percentage of identity between zebrafish and human/mouse is high for all the analysed domains of the three chains (Table 1).

As expected, due to the obligatory presence of glycine every third amino acid, a high sequence identity could be found for the triple helical domain (80% for α1 and 75% for α3 with both human and murine α1 chains). A BLASTP analysis comparing the second and third amino acid of the collagenous triplets Gly-X-Y was performed. The identity was over 60% for the α1 and α3 chains and over 50% for the α2 chain (Table 1). These results suggest a relatively high level of conservation for the collagen-non collagenous protein binding domains, that are known to be essential for collagen type I synthesis, secretion and function. As expected, based on their relevance for collagen α chain recognition and folding, the highest identity is found in the C-propeptide domain (85% and 83% for proα1 compared to human and murine proα1 chains respectively, and 78% and 76% for proα3 in respect to human and murine proα1). Interestingly, in proα3 this latter domain, crucial for chain association in the trimer, lacks one of the 4 conserved cysteine residues involved in inter-chain bonds (Cys63 of the proα1(I) C-propeptide), whereas no difference was found in number and position of the cysteines involved in intra-chain disulfide bonds (Fig. 2a,b). Also, the chain recognition region is more divergent in proα3 than in proα1 when compared to mammalian proα1 (Fig. 2a, Table 1).

In the extracellular environment, type I collagen self-assembles into fibrils stabilized by inter- and intra-molecule covalent cross-links involving specific Lys/Hyl residues in the α1 and α2 chains[26]. All the Lys/Hyl residues involved in human/mouse collagen type I cross-links are conserved in zebrafish with the exception of the α2(I) Lys/Hyl 933 that is substituted by an arginine. However, a Lys/Hyl is present at position 930 in the zebrafish α2(I) collagen sequence (Fig. 2c).

An important feature in determining the stability of the triple helix is the number of GG + GGG and GPP amino acid repeats. Low number of GG + GGG and high number of GPP repeats generally increase the stability of the triple helix[27]. In zebrafish α3(I) the number of GG + GGG repeats is about two-fold higher than in zebrafish α1(I), and both chains contain more of these repeats with respect to human and murine α1(I) (Supplementary Table S3). Interestingly, the number of GPP repeats is slightly higher in zebrafish α1(I) than in zebrafish α3(I) and significantly lower in zebrafish α1(I) and α3(I) when compared to human and mouse α1(I). Similarly, in zebrafish α2(I) the number of GG + GGG repeats is higher than in human and mice α2(I), but there is no significant difference in the GPP contents.

D. rerio α1(I) NP_954684.1		Identity %		
		D. rerio α3(I) NP_958886.1	*H. sapiens* α1(I) NP_000079.2	*M. musculus* α1(I) NP_031768.2
total protein	aa 1–1447	78	77	76
N-propeptide	aa 23–146	79	53	45
N-telopeptide	aa 147–162	58	70	63
triple helical region	aa 163–1176	78	80	80
triple helical region (no Gly)	aa 163–1176	67	68	69
C-telopeptide	aa 1177–1201	78	58	52
C-propeptide	aa 1202–1447	82	85	83
recognition sequence	aa 1322–1344	78	87	87
D. rerio α3(I) NP_958886.1		*D. rerio* α1(I) NP_954684.1	*H. sapiens* α1(I) NP_000079.2	*M. musculus* α1(I) NP_031768.2
total protein	aa 1–1449	78	75	75
N-propeptide	aa 23–150	79	58	44
N-telopeptide	aa 151–165	58	47	67
triple helical region	aa 166–1177	78	75	75
triple helical region (no Gly)	aa 166–1177	67	62	63
C-telopeptide	aa 1178–1204	78	59	59
C-propeptide	aa 1205–1449	82	78	76
recognition sequence	aa 1324–1346	78	74	74
D. rerio α2(I) NP_892013.2			*H. sapiens* α2(I) NP_000080.2	*M. musculus* α2(I) NP_031769.2
total protein	aa 1–1352		71	68
N-propeptide	aa 23–68		70	66
N-telopeptide	aa 69–80		86	54
triple helical region	aa 81–1094		69	68
triple helical region (no Gly)	aa 81–1094		54	52
C-telopeptide	aa 1095–1109		65	57
C-propeptide	aa 1110–1352		79	75
recognition sequence	aa 1227–1249		65	70

Table 1. Identity analysis of type I collagen α chains between zebrafish (*D. rerio*) and human (*H. sapiens*) and mouse (*M. musculus*), respectively, following sequence alignment.

Spatiotemporal co-expression of zebrafish collagen type I genes in early development. In order to evaluate how the three collagen type I genes are transcribed during early zebrafish development, we assessed their relative expression at different time points during embryonic and larval development (8 hpf up to 12 dpf) by means of microarray and RT-qPCR analysis. The expression profiles of all three type I collagen genes were highly similar, with a peak in relative expression between 3 and 4 dpf (Fig. 3a,b), corresponding with the onset of bone formation in zebrafish embryos[28]. The expression of all three type I collagen genes was shown to be present, although at very low level, during the first hours post fertilization (Supplementary Fig. 1).

To further explore the spatio-temporal expression of the *col1a1a, col1a1b* and *col1a2* genes during embryonic development, whole mount *in situ* hybridization (WISH) was carried out at 24, 48, 72 and 96 hpf (Fig. 4a). At every time point, expression of all three genes could be detected in the epidermis. Interestingly, only *col1a1a* was shown to be expressed in the median fin fold and in the apical ectodermal ridge of the pectoral fin at 48, 72 and 96 hpf (Fig. 4a,b). Because several elements of the craniofacial skeleton appear at 96 hpf, hybridized embryos at this time point were processed for semi-thin sectioning to evaluate and compare tissue-specific expression in internal structures (Fig. 4c and Table 2). All three type I collagen genes are expressed in mesenchymal cells that have entered final differentiation. Thus, all three collagen I genes are expressed in the osteoblasts surrounding the first bones that ossify in the larva: i.e. parasphenoid, opercular bone and cleithrum[28,29]. Fibroblasts of tendons and ligaments are particularly strongly labelled, as are the myosepta, connective tissue that separates the consecutive myomeres (Fig. 4c). These signals are consistent with the involvement of these cells in the production of a collagen-rich extracellular matrix. Likewise, the somewhat stronger signal in the mesenchyme surrounding the ceratobranchial 5 compared to the other ceratobranchials, can be explained by the more precocious perichondral ossification of these elements as tooth-bearing pharyngeal jaws[30].

Collagen type I in zebrafish embryos. Collagen type I was extracted by means of pepsin digestion and salt precipitation from 48 hpf embryos in order to evaluate its chain composition. Electrophoretic separation of collagen type I showed three monomeric α bands (Fig. 5a). Mass spectrometry analysis of these bands revealed that the upper one represented α1(I) chain co-migrating with α1(II), the middle band contained a mixture of α1(I) and α3(I) peptides and the lower band represented the α2(I) chain (Supplementary Table S4). The

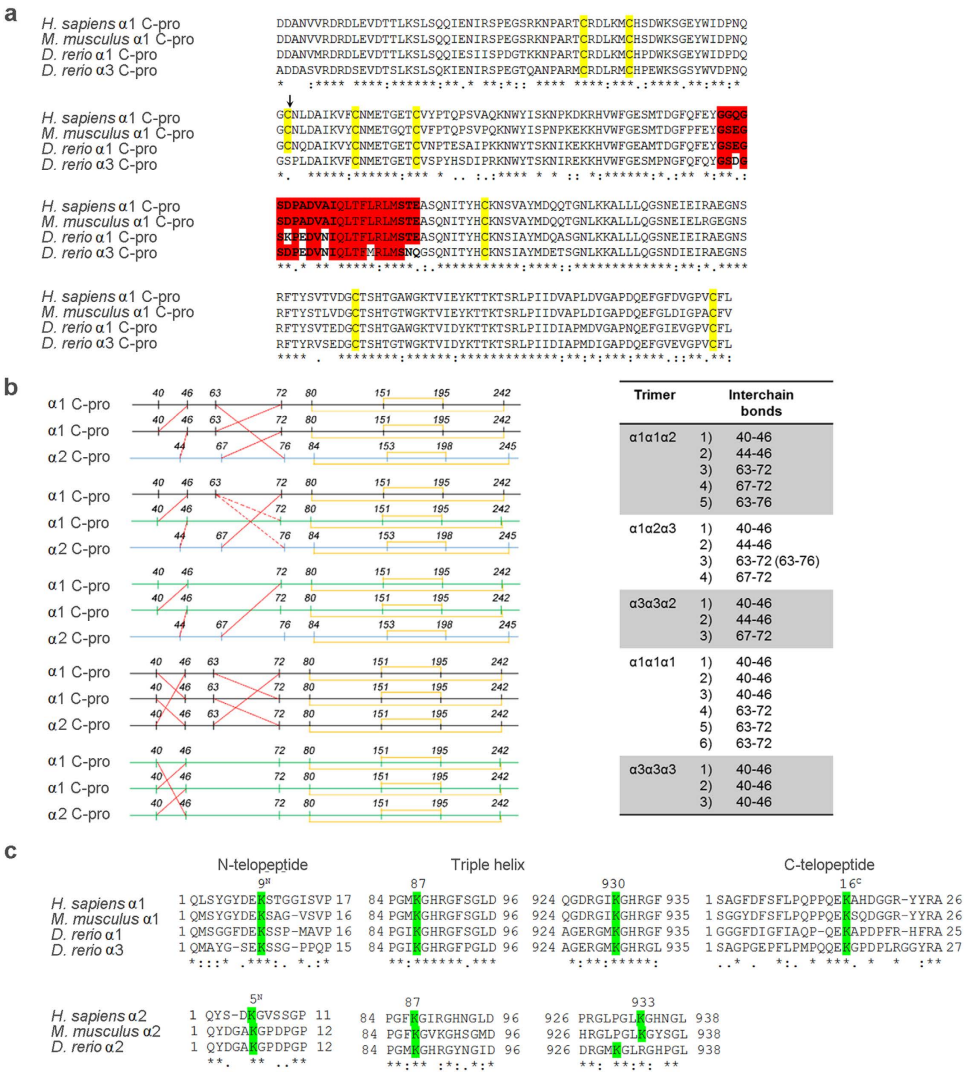

Figure 2. Comparison of conserved protein regions and amino acids with crucial function in type I procollagen chain assembly and extracellular collagen fibril formation. (**a**) Alignment of the α1 and α3 C-propeptide sequence in *D. rerio* with the α1 C-propeptide of human (*H. sapiens*) and mouse (*M. musculus*). In the recognition sequence (highlighted in red), responsible for the α chain assembly in a trimeric molecule, the α3 chain has 6 different AA when compared to human/mouse α1 whereas for α1 only 3 AA are different. The cysteine residues responsible for inter- and intra-chain disulfide bonds (yellow) are all conserved in zebrafish α1 but Cys63 (arrow), involved in inter-chain bonds, is missing in α3 and substituted with a Ser. (**b**) Representative pattern of the inter- and intra-chain disulfide bonds (in red and yellow respectively) in all the possible trimer compositions. (**c**) Lys/Hyl residues known to be involved in type I collagen cross-link stabilization are highlighted in green. The human/mouse Lys/Hyl α2(I) 933 is substituted in zebrafish α2 by an arginine, but a Lys/Hyl is present in position 930.

identification of α3(I) peptides demonstrated for the first time the translation of the *col1a1b* gene in zebrafish. The migration of the α1(I) chain in two distinct bands suggested the existence of two different levels of glycosylation for this chain, which could be attributed either to the presence of trimers with different stoichiometry and/or to a tissue specific glycosylation due to the tissue heterogeneity of the sample.

Collagen type I stoichiometry in adult zebrafish tissues. SDS-PAGE of both completely (pepsin soluble, PSC) and uncompletely (acid soluble, ACS) cross-linked type I collagen extracted from internal (bone) and external (skin and scales) zebrafish tissues showed the canonical pattern reported for tetrapods, characterized by the presence of γ trimers, β dimers and two monomeric α bands[31]. As expected, acid soluble collagen migrated slightly slower than pepsin extracted collagen, due to the presence of N- and C-telopeptides (Fig. 5b). No obvious difference in size or relative quantity was detected among the bands of the three analysed tissues in both collagen fractions (Supplementary Table S5). Mass spectrometry of the α bands revealed in the upper band the co-migration of α1(I) and α3(I) and in the lower band the presence of α2(I) (Supplementary Table S6). The co-migration of α1(I) and α3(I) indicated their highly similar experimental molecular weight and glycosylation

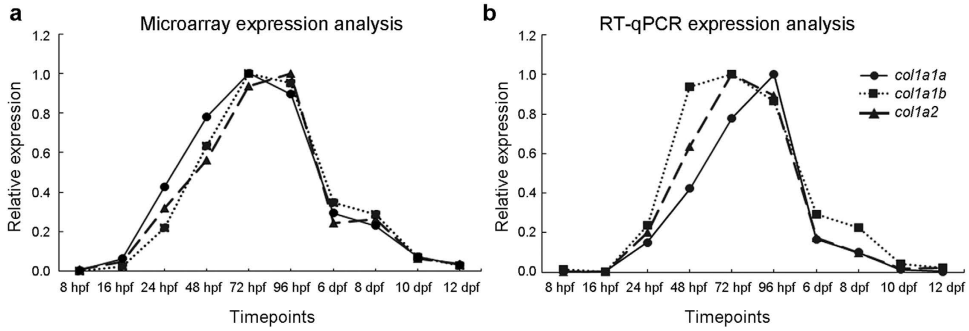

Figure 3. Expression of collagen type I genes in early zebrafish development. Relative expression values were normalized to maximum expression values for each gene and depicted in the y-axis. Both microarray (**a**) and RT-qPCR (**b**) analysis show similar expression patterns for *col1a1a*, *col1a1b* and *col1a2* with an expression peak for all three genes at 72–96 hpf.

level. The densitometric ratio between the upper and lower α bands was around 2 for all three tissues, both in reducing and in non-reducing conditions (Supplementary Table S5), indicating there is generally twice as much α1(I) + α3(I) than α2(I). In the attempt to separate α1(I) from α3(I) chains based on their isoelectric point, 2D PAGE was performed. All the spots corresponding to γ trimers, β dimers and α monomers, resolved from each tissue, were analyzed by mass spectrometry (Fig. 5c). The identification of α1(I) and α3(I) chains from the same spot suggests similar pI values that prevent a proper resolution of these chains (Supplementary Table S7). Next, selected reaction monitoring (SRM) mass spectrometry was used to determine the abundance of α1(I) and α3(I) chains in gel-excised alpha bands from bone, skin and scales collagen extracts. A known concentration of synthetic peptide unique for α1(I) and α3(I) respectively was spiked-in, followed by comparison of the relative intensities of the endogenous and the synthetic spiked-in peptide. A pairwise comparison using the Wilcoxon rank sum test shows that the ratio α3(I)/α1(I) is equal between skin and scales (p-value = 0.059 > 0.05). The ratio in bone however is statistically different when compared to skin or scales (p-value = $2.2e^{-10} < 0.05$), suggesting different amounts or molecular modifications of α1(I) and α3(I) in external (skin and scales) versus internal (bone) zebrafish tissues (Fig. 5d). Spectral counting of the unique peptides for α1(I) and α3(I), as measured in an LC-MS/MS run, revealed relative ratios of α3(I)/α1(I) among the three different tissues that were similar to the ones obtained by SRM mass spectrometry.

To estimate collagen type I chain stoichiometry in collagen extracts from bone, skin and scales, amino acid analysis was conducted. Based on the detected amount of Tyr residues (n = 2), that are theoretically absent in both α1(I) and α3(I) chains, a significant presence of α1(I) or α3(I) homotrimers could be excluded in all three tissues (Supplementary Table S8). The presence of a single α2 chain in the collagen type I trimers from the various tissues was assumed based on the fact that in tetrapods a single α2 chain is generally present in type I collagen molecules and based on the detected densitometric ratios between upper and lower α(I) bands in SDS-PAGE (Supplementary Table S5). This leaves us with three possible ratios for the three α chains (α1:α2:α3 in a 2:1:0 or 1:1:1 or 0:1:2 ratio). To discriminate among these possibilities, we considered the amino acids isoleucine and leucine since, based on theoretical amino acid composition, their ratio is over two-fold different between α1(I) (Ile/Leu = 0.92) and α3(I) (Ile/Leu = 0.36) chains. Based on the experimental ratio determined for these amino acids in the type I collagen from the three tissues (skin: 0.57 ± 0.05, bone: 0.54 ± 0.07 and scales: 0.55 ± 0.10), a 1:1:1 ratio for the three α chains in all tissues is inferred (Table 3). However, assuming that different trimers can be synthesized in various amounts, the existence of α1α2α3 alone or the presence of equal amounts of $\alpha 1_2\alpha 2$ and $\alpha 3_2\alpha 2$ or a combination of the three trimers cannot be excluded.

Collagen type I purified from skin, bone and scales has similar thermal stability. A single denaturation peak with an apparent melting temperature T_m ~ 35 °C (±0.5 °C) was observed for zebrafish collagen type I in differential scanning calorimetry thermograms in 2 mM HCl, pH 2.7 at 0.25 °C/min heating rate (Fig. 5e). We observed no significant differences between acid soluble and pepsin treated collagens (data not shown) or between skin and bone collagens (Fig. 5e). The apparent T_m of scales collagen was ~0.4 °C lower, but within possible ~0.5 °C sample-to-sample variation (despite better than 0.1 °C reproducibility of the DSC instrument, sample-to-sample variations in DSC buffer and post-translational modification of collagen might affect T_m by up to ~0.5 °C). The apparent T_m at pH 7.4 (corrected by −1.7 °C to account for the stabilizing effect of phosphate-glycerol buffer compared to physiological saline[32]) was close to that at pH 2.7, also consistent with our previous observations for type I collagen from other species. The absence of any distinct peak at higher T_m in our samples further supports the absence of a detectable amount of homotrimers in zebrafish type I collagen. Higher T_m of α1(I) homotrimers compared to $(\alpha 1)_2\alpha 2$ heterotrimers is expected to produce a pronounced second peak, e.g. observed in homotrimer/heterotrimer mixtures of mouse type I collagen[33].

Discussion

In this study, we performed a deep molecular and biochemical characterization of type I collagen in zebrafish. As collagen type I is the major structural protein in bone and skin, these data are of fundamental importance, not only to gain insights in the composition of the extracellular matrix of these tissues, but also to properly interpret

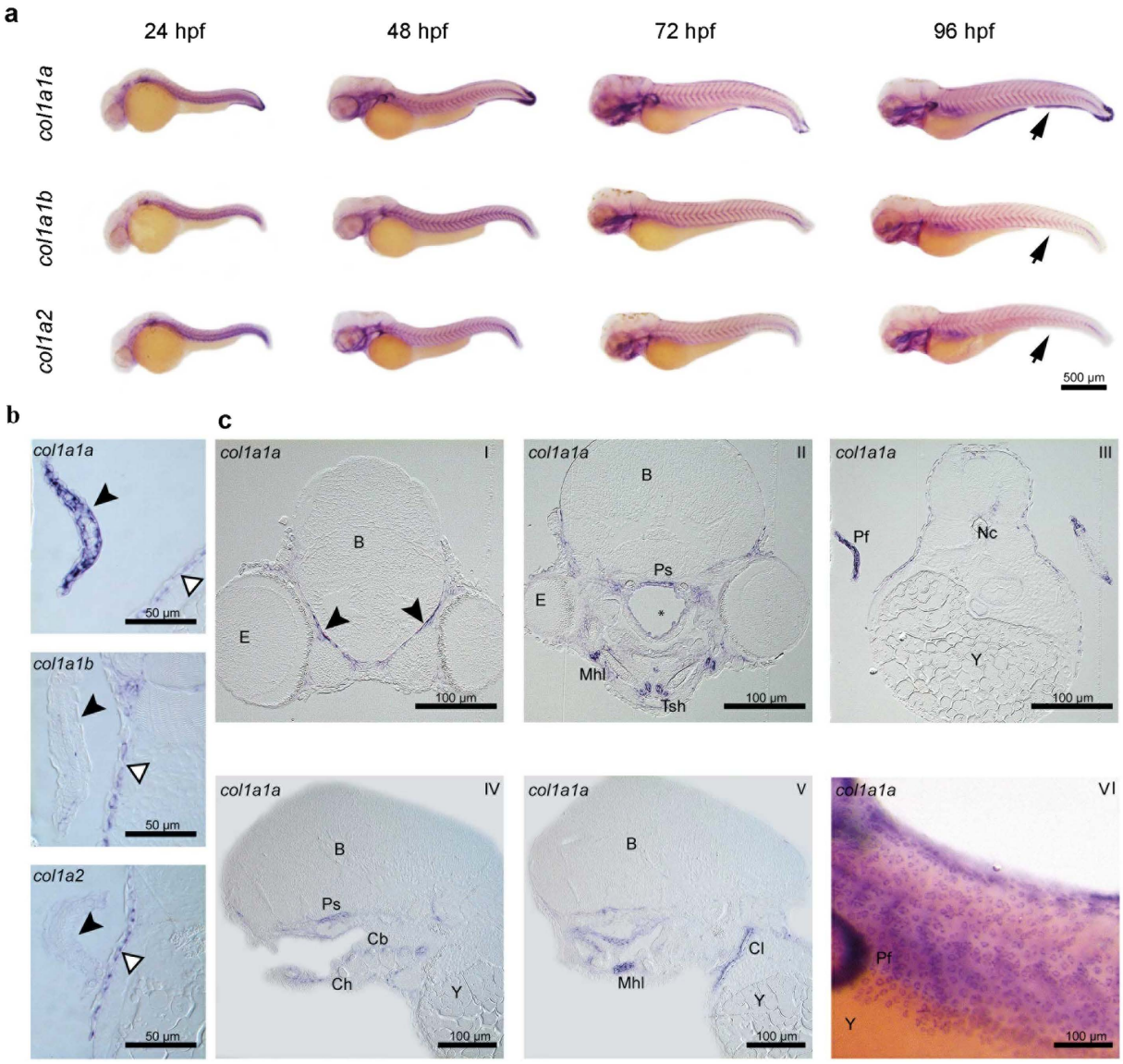

Figure 4. Whole mount *in situ* hybridization (WISH) for type I collagen genes in zebrafish embryos. (**a**) WISH for *col1a1a, col1a1b* and *col1a2* at different time points (24, 48, 72 and 96 hpf) of zebrafish development. Expression patterns are similar for all three type I collagen genes. However, expression of *col1a1a,* but not of *col1a1b* nor *col1a2,* was clearly noted in the fin fold (indicated by the arrowhead) and in the pectoral fins at 96 hpf. (**b**) Expression of *col1a1a*, *col1a1b* and *col1a2* at 96 hpf in the pectoral fin (black arrowheads). Only for *col1a1a* a clear signal could be detected. Note that basal epidermal cells are similarly labeled for all three collagen type I genes (open arrowheads). (**c**) Cross (CI-CIII) and sagittal (CIV-CV) sections of 96 hpf WISH specimens, showing details of expression of *col1a1a* in various cell or tissue types: meninges (CI, arrowheads), osteoblasts surrounding the parasphenoid bone (Ps, CII, CIV) and the cleithrum (Cl, CV), fibroblasts of the mandibulo-hyoid ligament (Mhl, CII, CV) and of the tendon of the sternohyoideus muscle (Tsh, CII) and distal epidermal/subepidermal layers of the pectoral fins (CIII). Mesenchymal cells around ceratobranchials 1–4 display a weak, and around ceratobranchial 5 a somewhat stronger signal (Cb 1–5, CIV). CVI shows the expression of *col1a1a* in the basal cells of the epidermis. Further abbreviations: B, brain; Ch, ceratohyal; E, eye; Nc, notochord; Pf, pectoral fin; Y, yolk. Cavity marked by * on CII is an artefact.

results obtained from zebrafish models of heritable skin and bone diseases. Collagen type I mutations are responsible for various human diseases such as osteogenesis imperfecta[34], Caffey disease (CAFFD)[35], Ehlers-Danlos syndrome 1 (EDS1) and 7A (EDS7A)[36]. For some of these diseases zebrafish models already exist and TALEN and CRISPR/Cas genome editing now allows easy and efficient generation of novel mutants that could be used both to clarify pathophysiology and to test novel pharmacological approaches.

Type I collagen in tetrapods is mainly present as a heterotrimer constituted by two α1 and one α2 chains encoded by *COL1A1* and *COL1A2* genes respectively. Also in zebrafish, type I collagen is a trimer, but its α chain composition is puzzling since three types of α chains were identified, namely α1, α2 and α3, encoded by *col1a1a,*

	col1a1a	*col1a1b*	*col1a2*
Epithelia			
epidermis	++	++	++
pectoral fin	+++	–	–
fin fold	+++	–	–
Connective tissues/fibroblasts			
connective tissue around brain	+ to ++	++	+
mesenchyme below Meckel's cartilage	++	++	+
mandibulo-hyoideal ligament	+++	++	++
tendon of muscle sternohyoideus	+++	++	+ to ++
muscle attachment to endoskeletal disk	+	+	+
myosepta	+	++	+
Bones/osteoblasts			
parasphenoid	++	++	+
opercular	+++	++	++
cleithrum	++ to +++	++	+ to ++
ceratobranchials 1–4	+	+	+
ceratobranchial 5	++	++	+

Table 2. Assessment of tissue specific mRNA expression for *col1a1a*, *col1a1b* and *col1a2* at 96 hpf using whole mount *in situ* hybridization followed by sectioning of the samples. The intensity of the detected signal is indicated as: not present (−), weak (+), average (++) or strong (+++).

col1a2 and *col1a1b* genes, respectively[20]. Our data demonstrated a co-regulation and interdependence of the three collagen type I genes during embryonic and larval zebrafish development. Expression analysis revealed peaking relative expression at 3–4 dpf of all three genes, coinciding with the formation of the first bony structures in the head of the zebrafish embryo, and thus emphasizing their relevance for bone formation during early development. Whole mount *in situ* hybridization (WISH) in zebrafish embryos and subsequent semi-thin sectioning showed overlapping expression patterns for all three genes, suggesting a strong co-expression and possibly co-regulation of type I collagen genes.

Expression of zebrafish collagen type I genes was mainly observed in the ectoderm, along developing bony elements, and in ligaments and tendons. This shows that the collagen type I genes are expressed in the same tissues as in humans, including bone and skin. Notably, several epithelial tissues expressed type I collagen genes. Expression of all three collagen genes produced a typical 'leopard' pattern in the skin. Sections revealed that transcripts were located in basal cells of the epidermis. Le Guellec *et al.* previously reported *col1a2* expression in the basal epidermis of zebrafish but did not consider the two other collagen genes[37]. Likely, all three type I collagen genes are involved in the production of the primary dermal stroma. Expression of *col1a1a*, but not of *col1a1b* nor *col1a2*, is also seen in the fin fold and in the distal margin of the pectoral fin. This signal is likely related to the formation of actinotrichia, non-calcified flexible rods that constitute the first fin skeleton formed during development. Durán *et al.* reported the expression of *col1a1a*, along with another type of collagen, *col2a1b*, and their contribution to actinotrichia formation[38]. Given the absence of *col1a1b* and *col1a2* expression, our findings also support the presence of α1(I) homotrimers in actinotrichia. Given that the signal at 96 hpf is clearly observed on both sides of the basement membrane, we propose that both epidermal and subepidermal cells synthesize *col1a1a* for integration in the actinotrichia, in support of the findings of Durán *et al.*[38].

The expression, although at very low level, of all three collagen genes in zebrafish oocytes, indicates a role of maternal collagen type I transcripts in the earliest stages of development. In general, this study underlines the essential role for collagen type I during zebrafish embryogenesis, similarly as was already shown in other vertebrates; for instance lack of *Col1a1* expression in the homozygous *Col1a1*^{Mov13} mice is not compatible with life[39].

In order to confirm that the annotated collagen type I genes in zebrafish are indeed the orthologues of the human/mouse collagen type I genes, we performed synteny analysis. Alignment of the genomic regions surrounding the zebrafish *col1a1a* and *col1a1b* genes with the regions flanking the human/murine *COL1A1* locus revealed a shared synteny, confirming the idea that the annotated collagen type I genes in zebrafish are indeed the orthologues of the human/mouse collagen type I genes and supporting the hypothesis that they all originate from a common ancestral gene, present in the last common ancestor of zebrafish and mammals. The same is valid for the zebrafish *col1a2* and the human *COL1A2* gene. On the other hand, the finding that only for a limited number of genes, flanking human and murine *COL1A1*, orthologues are present in the zebrafish genome flanking both *col1a1a* and *col1a1b* loci, shows a structural divergence of the chromosomal segments surrounding human and zebrafish type I collagen genes. Moreover, the different location and arrangement of the syntenic genes flanking *col1a1a* and *col1a1b* respectively suggested a divergent evolution of the corresponding chromosomal regions. Whether these differential chromosomal contexts also reflect specific divergent functions or expression patterns of the human versus zebrafish genes or the zebrafish *col1a1a* versus *col1a1b* genes can be suggested, but should be further investigated.

The high conservation of the sequence necessary for α chain recognition as well as of the C propeptide cysteine residues necessary for covalent inter-chain stabilization indicates that likely also in zebrafish, as in tetrapodes, the

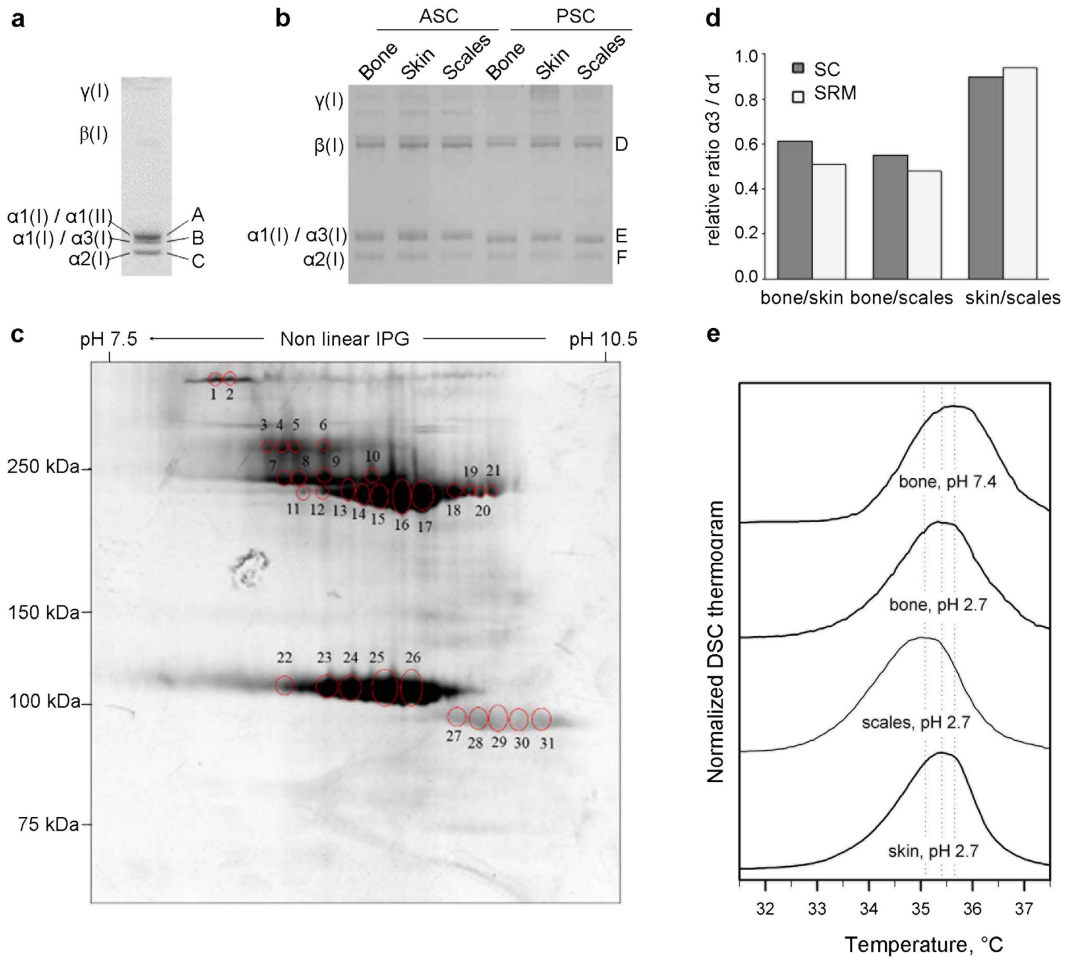

Figure 5. Analysis of type I collagen extracted from 48 hpf embryos and adult bone, skin and scales. (**a**) 1D SDS PAGE of pepsin extracted (PSC) type I collagen from 48 hpf embryos. The identification of the bands A, B and C was performed by mass spectrometry as detailed in Supplementary Table S4. The densitometric ratio between α1(I)-α1(II)/α2(I) was 1.70 ± 0.03, whereas the ratio α1(I)-α3(I)/α2(I) was 1.15 ± 0.09. (**b**) 1D SDS PAGE of acid soluble (ASC) and PSC from adult bone, skin and scales. The identity of the bands D, E and F was determined by mass spectrometry as detailed in Supplementary Table S6. (**c**) Representative 2D SDS PAGE of PSC from scales. Similar results were obtained for skin and bone. The identification of the spots 1 to 31 was performed by mass spectrometry as detailed in Supplementary Table S7. γ: collagen type I gamma trimers; β: collagen type I beta dimers. (**d**) Relative ratio α3(I)/α1(I) between bone, skin and scales as measured by selected reaction monitoring (SRM) and spectral counting (sc). In SRM, for each tissue three biological and two technical repeat measurements were analyzed. Spectral counts were measured in the same samples for one biological replicate. Skin and scales show high similarity (SRM multi Wilcoxon test p-value > 0.05) whereas bone is clearly distinguished (SRM multi Wilcoxon test p-value < 0.05) from these other tissues in their α3(I)/α1(I) ratio. The coefficient of variance calculated across all replicates, both technical and biological, per tissue type shows a good reproducibility in the measurement of α3(I)/α1(I) ratio (cv = 24%); (**e**) DSC thermograms of type I collagen purified from bone, skin and scales of adult zebrafish. DSC was performed in 0.2 M sodium phosphate, 0.5 M glycerol (pH 7.4) at 0.25 °C/minute heating rate (representative bone thermogram is shown, similar results were obtained from the other two tissues) and in 2 mM HCl, pH 2.7 at 0.25 °C/minute heating rate (the thermogram for the three tissues is represented).

α1:α2:α3	Ile/Leu (Theoretic Values)
2:1:0	0.770
1:1:1	0.584
0:1:2	0.398
	Ile/Leu (Experimental Values)
Skin	0.565 ± 0.050
Bone	0.535 ± 0.065
Scales	0.553 ± 0.097

Table 3. Theoretic and experimental Ile/Leu values.

assembly of type I collagen trimer starts with C-propeptide association through a series of non-covalent interactions, that are then stabilized by the formation of inter-molecular disulphide bonds[40,41]. The lack of zebrafish α3 chain Cys63, that is known to participate in inter chain bounds, may have implication for chain stoichiometry. Further, the lysine residues known to be relevant for cross linking formation in type I collagen were identified in zebrafish, their conserved presence further support their relevance through evolution.

Interestingly, SDS PAGE of collagen extracted from zebrafish embryos followed by mass spectrometry analysis showed the presence of two α1(I) populations with a distinct molecular weight, one co-migrating with α1(II) and the other with α3(I). Since we obtained the embryonic collagen from whole body lysates it is likely that the variability in molecular weight of α1(I) is due to a difference in glycosylation level between different embryonic tissues, suggesting a developmental specific collagen composition. Possibly a fraction of collagen type I could be indeed constituted by α1(I) homotrimers coming from actinotrichia and maybe also lepidotrichia forming cells, characterized by overglycosylation of the α1(I) chains that migrate slower in SDS-PAGE. Indeed, only *col1a1a* and not *col1a1b* nor *col1a2* expression was detected in the fin folds by *in situ* hybridization. Due to the co-migration of α1(I) either with α1(II) or α3(I) chains it was impossible to determine exact ratios between these chains and hence make assumptions about the stoichiometry of chain association of embryonic collagen type I.

To gain insights into the composition of collagen type I in specific adult zebrafish tissues we analyzed collagen from skin, scales and bone by means of SDS-PAGE. We demonstrated an identical electrophoretic pattern for collagen type I obtained from all these tissues in 1D gels electrophoresis: a band containing co-migrating α1(I) and α3(I) and another band with lower molecular weight representing α2(I), with a stoichiometry of 2:1 between the two bands. 2D gel electrophoresis did not allow further separation of α1(I) and α3(I) spots. SRM and spectral counting mass spectrometry data shows a statistically significant higher α3(I)/α1(I) ratio in external (skin and scales) versus internal (bone) tissues pointing out to a tissue-specific collagen composition. Interestingly, similar findings have been previously reported in the Salmoniformes, a different order of Actinopterygii; in the skin of rainbow trout all three α(I) chains were detected, whereas in muscle, an internal tissue, only α1(I) and α2(I) were found to be present[25]. In contrast to the mass spectrometry data, our amino acid analysis of collagen type I extracted from zebrafish bone, skin and scales revealed an equal ratio for α1(I), α2(I) and α3(I) in all examined tissues. This apparent discrepancy between mass spectrometry and AA analysis could be explained considering the different nature of the analyzed samples in the different assays. Acid hydrolysis for amino acid analysis was performed on whole pepsin extracted collagen fraction that includes monomeric α chains as well as β dimers and γ trimers, whereas mass spectrometry data were obtained from electrophoretically separated monomeric α bands. It is known that collagen cross-links in soft tissue and bone are different as the lysyl hydroxylation level differs and a higher amount of immature cross-links is present in mineralized tissue[42]. Furthermore, at the supramolecular level, differences in organization and diameter of type I collagen fibrils have been reported between zebrafish bone, skin and scales[37,43,44].Thus our data can indeed reflect such differences and pave the way for further investigation. Alternatively, we cannot exclude that differences in trypsin cleavage or site specific hydroxylation may influence the mass spectrometry data obtained, since it is known that collagen is not an easy target for proteolysis and that hydroxylation/glycosylation of bone and soft tissue collagen differ in tetrapods.

For the first time we were able to determine the temperature stability of zebrafish collagen type I that was characterized by apparent T_m ~35 °C in all three analyzed tissues. Human collagen type I is characterized by a T_m of 41.4 °C in skin and 43.3 °C in bone, due to the higher level of posttranslational modification in the latter[42]. In warm-blooded animals, increased post-translational modification and T_m of collagen from inner organs and tissues is likely related to higher physiological temperature of the latter[45]. Consistently, no such difference was present in cold-blooded zebrafish, which has no significant temperature gradient across the body. The lower T_m of zebrafish collagen type I compared to warm-blooded animals is consistent with generally observed correlation of collagen thermal stability with normal body temperature in different species[46]. It could be attributed to a higher number of GG + GGG motifs and a lower number of GPP triplets in zebrafish α(I) chains.

In conclusion, we provided a deep molecular and biochemical characterization of zebrafish collagen type I, the most abundant extracellular matrix protein in bone and skin. We demonstrated that, both in zebrafish embryos and adult tissues, three instead of two types of alpha chains contribute to the formation of the collagen type I triple helix, although the exact stoichiometry and post-translational modifications need to be further defined. These data will further pave the way to the use of zebrafish as a model for skin and skeletal diseases linked to abnormal type I collagen synthesis.

Material and Methods

Animals. Wild-type AB zebrafish were housed in ZebTEC semi-closed recirculation housing systems (Techniplast, Italy) and kept at a constant temperature (27–28 °C), pH (7.5) and conductivity (500 μS) on a 14/10 light/dark cycle. Embryos were collected by natural spawning and staged according to Kimmel[47].

Ethic Statement. All experiments were performed in accordance with the approved guidelines, in agreement with EU Directive 2010/63/EU for animals. The experimental protocols were approved by the Italian Ministry of Health (Approval Animal Protocol N. 1/2013) and by Ghent University Committee (Permit Number: ECD 15/22).

***In silico* analysis.** Synteny maps of the chromosomic regions surrounding type I collagen genes were constructed using human genes as reference by combining PhyloView and AlignView from Genomicus 81.01 (http://www.genomicus.biologie.ens.fr/genomicus-81.01/cgi-bin/search.pl)[48] with Ensembl Comparative Genomics data. Zebrafish type I collagen domains were determined by alignment with *H. sapiens* and *M. musculus* sequences using ClustalW2[49] and based on the annotation available from the osteogenesis imperfecta and

Ehlers-Danlos syndrome variant database (www.le.ac.uk/genetics/collagen/)[50]. Percentage of identity was estimated using protein BLAST at NCBI.

Collagen Extraction. Collagen was purified by a modification of the methods described in[51]. Briefly, bone, scales and skin obtained from adult fishes were delipidated in 0.1 N NaOH at 4 °C for 6 h, bone and scales were decalcified in 0.5 M EDTA, pH 7.4 at 4 °C for 48 h. Whole 2 days post-fertilization (dpf) embryos were manually dechorionated and homogenized in a Potter chamber in Phosphate Buffered Saline (PBS, Sigma Aldrich), pH 7.5 containing protease inhibitors (1.52 mg/mL EDTA, 1.57 mg/mL benzamidine, 0.25 mg/mL N-ethylmaleimide and 1 mM phenylmethanesulfonylfluoride). The acid-soluble collagen (ASC) was extracted by tissue incubation with 0.5 M acetic acid, while the pepsin-soluble fraction (PSC) was obtained digesting the remaining tissue with 0.1 mg/mL pepsin in 0.5 M acetic acid. Quantification was performed by measuring the 4-hydroxyproline amount[52].

Collagen Analysis by 1D-SDS-PAGE. Collagen (0.5 μg) was separated by 6% SDS-PAGE in the presence of 0.5 M urea. Gels were fixed in 45% methanol and 10% acetic acid, stained with 0.08 M picric acid, 0.04% Coomassie Brilliant Blue R250 (Sigma Aldrich) and destained in water. Versadoc3000 (BIO-RAD) and QuantityOne software (BIO-RAD) were used for gels digitalization and band densitometry.

Collagen analysis by 2D-PAGE. 2D-PAGE was performed using the Immobiline-polyacrylamide system as described in[53]. Isoelectric focusing (IEF) was carried out on preformed non-linear wide-range immobilized pH gradients (pH 6–11; 18 cm long IPG strips; GE Healthcare) and performed using the Ettan™ IPGphor™ III system (GE Healthcare). IPG strips were rehydrated with 350 μl of 8 M urea, 4% CHAPS, 1% dithioerythritol (DTE) and 2% carrier ampholytes pH 6–11. PSC collagen was loaded (40 μg diluted in 8 M urea, 4% CHAPS, 1% DTE and bromophenol blue) by anodic cup loading in the Ettan™ IPGphor Cup Loading Manifold Polymeric Tray (GE Healthcare). IEF was achieved according to the following voltage steps at 16 °C: 200 V for 7 h, from 200 V to 3500 V in 2 h, 3500 V for 2 h, from 3500 V to 5000 V in 2 h, 5000 V for 3 h, from 5000 V to 8000 V in 1 h, 8000 V for 3 h, from 8000 V to 10000 V in 1 h, 10000 V until a total of 100,000 Vh was reached. The second dimension was carried out at 10 °C on 9–16% polyacrylamide linear gradient gels. Gels were stained according to a silver staining protocol compatible with MS[54] and digitalized using an Image Scanner III (GE Healthcare). Computer-aided 2-D image analysis was carried out using ImageMaster 2-D Platinum 7.0 software (GE Healthcare).

MALDI TOF Mass Spectrometry Analysis. Protein identification was carried out by peptide mass fingerprinting[55,56] on an Ultraflex III MALDI-TOF/TOF mass spectrometer (Bruker Daltonics, Billerica, MA) as detailed in Supplementary Methods.

Selected Reaction Monitoring (SRM) analysis. Gel pieces containing α1(I) and α2(I) were excised, washed with acetonitrile 50%, dried and re-hydrated in 10 μl of a 0.02 μg/μl sequencing-grade modified trypsin stock solution (Promega Corporation, Madison, WI, USA). Excess trypsin solution was removed and fragments submerged in 50 mM ammonium bicarbonate. Trypsin digestion proceeded overnight at 37 °C and was stopped with trifluoroacetic acid (TFA). The peptide mixture was completely dried, re-dissolved in 20 μl of 0.1% TFA in acetonitrile 2% (HPLC solvent A) and analyzed as detailed in Supplementary Methods. Out of the identified peptides that were proteotypic for α1(I) and α3(I), 4 peptides were selected for selective reaction monitoring (SRM) analysis for each protein. The 8 resulting peptides were synthesized to contain stable heavy isotopes using standard solid-phase Fmoc chemistry on a SyroI peptide synthesizer (Biotage, Uppsala, Sweden). Amino acids were coupled in a 4-fold molar excess using 1-hydroxybenzotriazole/hexafluorophosphate activation. Synthetic peptides were cleaved from the resin during 4 h using TFA (Biosolve, Valkenswaard, The Netherlands) containing 2.5% ethanedithiol and 2.5% water. Peptides were then further purified by RP-HPLC.

SRM analysis was performed on an Ultimate 3000 RSLC nano HPLC system (Thermo Fisher Scientific) coupled to a TSQ Vantage mass spectrometer (Thermo Fisher Scientific) as described in the supplementary material and methods section. Peptide amounts present in the samples were calculated using the light/heavy ratios. Each sample was analyzed in triplicate.

A high variance of this ratio between the four peptides representing the same protein was detected, which is most likely due to the variability of the (proline) hydroxylation status between the endogenous (light) peptides. This issue was tackled by using the peptide with the highest detected amount for each protein (Supplementary Table S9), assuming this peptide is either close to complete hydroxylation or close to complete non-hydroxylation and hence assuming there is less variation in the degree of hydroxylation. Ratios of α1(I) and α3(I) were calculated using these peptides. For both biological and technical replicate analysis together, the median value was calculated of the ratio α3(I)/α1(I) for each tissue type. Next the Huber scale was calculated to get an idea of the variation on the replicates. The spectral count of the unique peptides for α1(I) and α3(I) was measured (in the same samples for one biological replicate) in an LC-MS/MS run.

Differential Scanning Calorimetry (DSC). Collagens were further purified by several rounds of precipitation in 0.7 M NaCl, 0.5 M acetic acid, re-suspended and extensively dialyzed in 2 mM HCl or in 0.2 M Na-phosphate, 0.5 M glycerol, pH 7.4. Collagen denaturation thermograms were measured at 0.25 °C/min heating rate in a Nano III differential scanning calorimeter (Calorimetry Sciences Corporation, USA).

Chemical characterization of collagen type I α chains. Collagen samples (27 μg) were hydrolysed in 6 M HCl at 110 °C under nitrogen and hydrolysates were derivatized with orthophthalaldelyde (OPA) and 9-fluorenyl-methyl-chloroformate (FMOC).

OPA and FMOC derivatives were analyzed by Jasco X-LC Amino Acid Analyzer with a fluorescence detector (excitation/emission at 342/456 nm for OPA-amino acids and excitation/emission at 272/312 nm for FMOC-amino acids) and by AminoQuant II amino acid analyzer (HP1090) with a diode array detector (338 nm for OPA and 262 nm for FMOC-amino acids). All results are means of three independent analyses performed on the two instruments.

qPCR. RNA was extracted from 20 embryos for each age (0, 1, 2, 4, 4.7, 5.3, 8, 11, 13, 16, 18, 24, 48, 72, 120 hpf and 6, 8, 10, 12 dpf) using the miRNeasy mini kit (Qiagen, Germany) in combination with on-column DNase I treatment (Qiagen, Germany) according to the manufacturer's guidelines. RNA quality index (RQI) was measured using an Experion automated electrophoresis system (software version 3.2, Bio-Rad). cDNA was synthesized from 1 μg RNA in a 20 μl reaction with the iScript kit (Bio-Rad, USA). qPCR reactions were performed and reported according to MIQE guidelines[57]. Normalization was carried out using zebrafish Expressed Repetitive Elements (ERE) (*hatn10*, *loopern4*)[58]. Expression data were analysed using qbase + software version 2.5 (Biogazelle, http://www.qbaseplus.com). We normalized the expression values to maximum expression values for each gene.

Primers for *col1a1a, col1a1b* and *col1a2* were designed using primerXL software (http://primerxl.org/). Sequences will be available upon request.

Microarray gene expression analysis. Expression analysis was performed using custom designed 60 K Zebrafish Gene Expression Arrays (AMADID 041801; Agilent Technologies) according to the manufacturer's instructions with 100 ng RNA as input. Normalization of these data was performed using the VSN package in R.

***In situ* hybridization.** Whole-mount *in situ* hybridization was carried out as previously described[59]. Dioxygenin uridine-5′-triphosphate (DIG) labeled RNA probes targeting *col1a1a*, *col1a1b* and *col1a2* genes were used. Further details are specified in the supplemental material and methods section. Embryos (24, 48, 72 and 96 hpf) were observed with a Leica M165 FC Fluorescent Stereo Microscope (Leica Microsystems, GmbH, Wetzlar, Germany). Four specimens for each gene were embedded in epon and cross sectioned (4 μm). Photomicrographs were acquired with a Zeiss Axioimager Z1 equipped with DIC optics and an Axiocam MRc camera[60].

Statistical Analysis. Statistical analysis was performed using SigmaStat 11.0. All values were expressed as mean ± standard deviation.

References

1. Apschner, A., Schulte-Merker, S. & Witten, P. E. Not all bones are created equal-using zebrafish and other teleost species in osteogenesis research. *Method Cell Biol* **105,** 239–255 (2011).
2. Mackay, E. W., Apschner, A. & Schulte-Merker, S. Vitamin K reduces hypermineralisation in zebrafish models of PXE and GACI. *Development* **142,** 1095–1101 (2015).
3. Fisher, S., Jagadeeswaran, P. & Halpern, M. E. Radiographic analysis of zebrafish skeletal defects. *Dev Biol* **264,** 64–76 (2003).
4. Li, N., Felber, K., Elks, P., Croucher, P. & Roehl, H. H. Tracking gene expression during zebrafish osteoblast differentiation. *Dev Dynam* **238,** 459–466 (2009).
5. Witten, P. E. & Huysseune, A. A comparative view on mechanisms and functions of skeletal remodelling in teleost fish, with special emphasis on osteoclasts and their function. *Biol Rev Cam Philos* **84,** 315–346 (2009).
6. Hammond, C. L. & Moro, E. Using transgenic reporters to visualize bone and cartilage signaling during development *in vivo*. *Front Endocrinol* **3,** 91 (2012).
7. Andreeva, V. *et al.* Identification of adult mineralized tissue zebrafish mutants. *Genesis* **49,** 360–366 (2011).
8. Xi, Y., Chen, D., Sun, L., Li, Y. & Li, L. Characterization of zebrafish mutants with defects in bone calcification during development. *Biochem Bioph Res Co* **440,** 132–136 (2013).
9. Hwang, W. Y. *et al.* Efficient genome editing in zebrafish using a CRISPR-Cas system. *Nat Biotechnol* **31,** 227–229 (2013).
10. Laize´ V, e. a. Fish: a suitable system to model human bone disorders and discover drugs with osteogenic or osteotoxic activities. *Drug Discov Today Dis Models* **13,** 29–37 (2014).
11. Brodsky, B. & Persikov, A. V. Molecular structure of the collagen triple helix. *Adv Protein Chem* **70,** 301–339 (2005).
12. Lees, J. F., Tasab, M. & Bulleid, N. J. Identification of the molecular recognition sequence which determines the type-specific assembly of procollagen. *EMBO J* **16,** 908–916 (1997).
13. Hulmes, D. J. Building collagen molecules, fibrils, and suprafibrillar structures. *J Struct Biol* **137,** 2–10 (2002).
14. Yamauchi, M. & Sricholpech, M. Lysine post-translational modifications of collagen. *Essays Biochem* **52,** 113–133 (2012).
15. Marini, J. C. *et al.* Consortium for osteogenesis imperfecta mutations in the helical domain of type I collagen: regions rich in lethal mutations align with collagen binding sites for integrins and proteoglycans. *Hum Mutat* **28,** 209–221 (2007).
16. Gonzalez-Bofill, N. *et al.* Effects of COLIA1 polymorphisms and haplotypes on perimenopausal bone mass, postmenopausal bone loss and fracture risk. *Osteoporosis Int* **22,** 1145–1156 (2011).
17. Uitto, J. Collagen polymorphism: isolation and partial characterization of alpha 1(I)-trimer molecules in normal human skin. *Arch Biochem Biophys* **192,** 371–379 (1979).
18. Jimenez, S. A., Bashey, R. I., Benditt, M. & Yankowski, R. Identification of collagen alpha1(I) trimer in embryonic chick tendons and calvaria. *Biochem Bioph Res Co* **78,** 1354–1361 (1977).
19. Rupard, J. H., Dimari, S. J., Damjanov, I. & Haralson, M. A. Synthesis of type I homotrimer collagen molecules by cultured human lung adenocarcinoma cells. *American J Pathol* **133,** 316–326 (1988).
20. Morvan-Dubois, G., Le Guellec, D., Garrone, R., Zylberberg, L. & Bonnaud, L. Phylogenetic analysis of vertebrate fibrillar collagen locates the position of zebrafish alpha3(I) and suggests an evolutionary link between collagen alpha chains and hox clusters. *J Mol Evol* **57,** 501–514 (2003).
21. Christoffels, A. *et al.* Fugu genome analysis provides evidence for a whole-genome duplication early during the evolution of ray-finned fishes. *Mol Biol Evol* **21,** 1146–1151 (2004).
22. Piez, K. A. Characterization of a collagen from codfish skin containing three chromatographically different alpha chains. *Biochemistry-US* **4,** 2590–2596 (1965).
23. Kimura, S. Wide Distribution of the Skin Type-I Collagen Alpha-3 Chain in Bony Fish. *Comp Biochem Phys B* **102,** 255–260 (1992).
24. Kimura, S., Ohno, Y., Miyauchi, Y. & Uchida, N. Fish skin type I collagen: wide distribution of an alpha 3 subunit in teleosts. *Compar Biochem Phys B* **88,** 27–34 (1987).

25. Saito, M., Takenouchi, Y., Kunisaki, N. & Kimura, S. Complete primary structure of rainbow trout type I collagen consisting of alpha1(I)alpha2(I)alpha3(I) heterotrimers. *Eur J Biochem* **268,** 2817–2827 (2001).
26. Hulmes, D. J. S. In *Col*lagen *S*tructure *and Mechanics* (ed P. Fratzl) Ch. 2, 15–47 (2008).
27. Persikov, A. V., Ramshaw, J. A. & Brodsky, B. Prediction of collagen stability from amino acid sequence. *J Biol Chem* **280,** 19343–19349 (2005).
28. Cubbage, C. C. a. M., P. M. Development of the cranium and paired fins in the zebrafish Danio rerio (Ostariophysi, Cyprinidae). *J Morphol* **229,** 121–160 (1996).
29. Mabee, P. M., Olmstead, K. L. & Cubbage, C. C. An experimental study of intraspecific variation, developmental timing, and heterochrony in fishes. *Evolution; international journal of organic evolution* **54,** 2091–2106 (2000).
30. Huysseune, A., Van der heyden, C. & Sire, J. Y. Early development of the zebrafish (Danio rerio) pharyngeal dentition (Teleostei, Cyprinidae). *Anat Embryol* **198,** 289–305 (1998).
31. Miller, E. J. & Rhodes, R. K. Preparation and characterization of the different types of collagen. *Method Enzymol* **82** Pt A, 33–64 (1982).
32. Leikina, E., Mertts, M. V., Kuznetsova, N. & Leikin, S. Type I collagen is thermally unstable at body temperature. *P Natl Aca Sci USA* **99,** 1314–1318 ((2002).
33. Kuznetsova, N. V., McBride, D. J. & Leikin, S. Changes in thermal stability and microunfolding pattern of collagen helix resulting from the loss of alpha2 (I) chain in osteogenesis imperfecta murine. *J Mol Biol* **331,** 191–200 (2003).
34. Forlino, A., Cabral, W. A., Barnes, A. M. & Marini, J. C. New perspectives on osteogenesis imperfecta. *Nat Rev Endocrinol* **7,** 540–557 (2011).
35. Nistala, H., Makitie, O. & Juppner, H. Caffey disease: new perspectives on old questions. *Bone* **60,** 246–251 (2014).
36. Malfait, F. & De Paepe, A. The Ehlers-Danlos syndrome. *Adv Exp Med Biol* **802,** 129–143 (2014).
37. Le Guellec, D., Morvan-Dubois, G. & Sire, J. Y. Skin development in bony fish with particular emphasis on collagen deposition in the dermis of the zebrafish (Danio rerio). *Int J Dev Biol* **48,** 217–231 (2004).
38. Duran, I., Mari-Beffa, M., Santamaria, J. A., Becerra, J. & Santos-Ruiz, L. Actinotrichia collagens and their role in fin formation. *Dev Biol* **354,** 160–172 (2011).
39. Schnieke, A., Harbers, K. & Jaenisch, R. Embryonic lethal mutation in mice induced by retrovirus insertion into the alpha1 (I) collagen gene. *Nature* **304,** 315–320 (1983).
40. Byers, P. H., Click, E. M., Harper, E. & Bornstein, P. Interchain disulfide bonds in procollagen are located in a large nontriple-helical COOH-terminal domain. *P Natl Aca Sci USA* **72,** 3009–3013 (1975).
41. Pace, J. M., Kuslich, C. D., Willing, M. C. & Byers, P. H. Disruption of one intra-chain disulphide bond in the carboxyl-terminal propeptide of the proalpha1(I) chain of type I procollagen permits slow assembly and secretion of overmodified, but stable procollagen trimers and results in mild osteogenesis imperfecta. *J Med Genet* **38,** 443–449 (2001).
42. Notbohm, H. *et al.* Comparative study on the thermostability of collagen I of skin and bone: influence of posttranslational hydroxylation of prolyl and lysyl residues. *J Protein Chem* **11,** 635–643 (1992).
43. Zylberberg, L. & Nicolas, G. Ultrastructure of scales in a teleost (Carassius auratus L.) after use of rapid freeze-fixation and freeze-substitution. *Cell Tissue Res* **223,** 349–367 (1982).
44. Metz, J. R., de Vrieze, E., Lock, E.-J., Schulten, I. E. & Flik, G. Elasmoid scales of fishes as model in biomedical bone research. *J Appl Ichthyol* **28,** 382–387 (2012).
45. Makareeva, E. *et al.* Carcinomas contain a matrix metalloproteinase-resistant isoform of type I collagen exerting selective support to invasion. *Cancer Res* **70,** 4366–4374 (2010).
46. Privalov, P. L. Stability of proteins. Proteins which do not present a single cooperative system. *Adv Protein Chem* **35,** 1–104 (1982).
47. Kimmel, C. B., Ballard, W. W., Kimmel, S. R., Ullmann, B. & Schilling, T. F. Stages of embryonic development of the zebrafish. *Dev Dynam* **203,** 253–310 (1995).
48. Louis, A., Nguyen, N. T., Muffato, M. & Roest Crollius, H. Genomicus update 2015: KaryoView and MatrixView provide a genome-wide perspective to multispecies comparative genomics. *Nucleic Acids Res* **43,** D682–689 (2015).
49. McWilliam, H. *et al.* Analysis Tool Web Services from the EMBL-EBI. *Nucleic Acids Res* **41,** W597–600 (2013).
50. Dalgleish, R. The Human Collagen Mutation Database 1998. *Nucleic Acids Res* **26,** 253–255 (1998).
51. Forlino, A., Kuznetsova, N. V., Marini, J. C. & Leikin, S. Selective retention and degradation of molecules with a single mutant alpha1(I) chain in the Brtl IV mouse model of OI. *Matrix Biol* **26,** 604–614 (2007).
52. Tenni, R. *et al.* Self-aggregation of fibrillar collagens I and II involves lysine side chains. *Micron* **37,** 640–647 (2006).
53. Gorg, A. *et al.* The current state of two-dimensional electrophoresis with immobilized pH gradients. *Electrophoresis* **21,** 1037–1053 (2000).
54. Sinha, P., Poland, J., Schnolzer, M. & Rabilloud, T. A new silver staining apparatus and procedure for matrix-assisted laser desorption/ionization-time of flight analysis of proteins after two-dimensional electrophoresis. *Proteomics* **1,** 835–840 (2001).
55. Hellman, U., Wernstedt, C., Gonez, J. & Heldin, C. H. Improvement of an "In-Gel" digestion procedure for the micropreparation of internal protein fragments for amino acid sequencing. *Anal Biochem* **224,** 451–455 (1995).
56. Soskic, V., Gorlach, M., Poznanovic, S., Boehmer, F. D. & Godovac-Zimmermann, J. Functional proteomics analysis of signal transduction pathways of the platelet-derived growth factor beta receptor. *Biochemistry-US* **38,** 1757–1764 (1999).
57. Bustin, S. A. *et al.* The MIQE guidelines: minimum information for publication of quantitative real-time PCR experiments. *Clin Chem* **55,** 611–622 (2009).
58. Vanhauwaert, S. *et al.* Expressed repeat elements improve RT-qPCR normalization across a wide range of zebrafish gene expression studies. *PloS one* **9,** e109091 (2014).
59. Thisse, C. & Thisse, B. High-resolution *in situ* hybridization to whole-mount zebrafish embryos. *Nat Protoc* **3,** 59–69 (2008).
60. Verstraeten, B., Sanders, E. & Huysseune, A. Whole mount immunohistochemistry and *in situ* hybridization of larval and adult zebrafish dental tissues. *Methods Mol Biol* **887,** 179–191 (2012).

Acknowledgements

We thank Prof. Franco Cotelli, Department of Biosciences, University of Milano, Milan, Italy for data discussion, Dr Velia Penza, Department of Molecular Medicine, Biochemistry Unit, University of Pavia, Italy for initial collagen preparation from embryos and adult zebrafish, Dr Patrizia Arcidiaco, Centro Grandi Strumenti, University of Pavia, Italy for support with amino acid analysis and the animal facility "Centro di servizio per la gestione unificata delle attività di stabulazione e di radiobiologia" of the University of Pavia. We thank the Consorzio Interuniversitario Biotecnologie (CIB) who provided one year fellowship for RG. This work was supported by Fondazione Cariplo [grant n. 2013-0612] to AF, Telethon [grant n. GGP13098] to AF, the European Community, FP7, "Sybil" project [grant n. 602300] to AR and AF, the Ghent University Methusalem grant BOF08/01M01108 to ADP and by funding from the Belgian Science Policy Office Interuniversity Attraction Poles (BELSPO-IAP) program through the project IAP P7/43-BeMGI.

Author Contributions

Conceived and designed the project: A.W., P.C., F.M., A.D.P., B.M. and A.F.; designed experiments: A.W., R.G., C.G., A.S., K.G., A.H., N.D.R., L.Bianchi, L.Bini and A.F.; performed experiments: C.G., A.S., A.H., N.D.R., R.G., F.T., A.G., C.L., L.M., R.T., S.L. and S.C.; analyzed data: C.G., A.H., E.W., A.W., A.S., K.G., R.G., F.T., A.R., R.T., L.Bianchi, L.Bini, S.L., S.C. and A.F.; wrote manuscript: C.G., A.W., A.H., R.G. and A.F.; critical review of the manuscript: all authors.

Additional Information

Supplementary information accompanies this paper at http://www.nature.com/srep

Competing financial interests: The authors declare no competing financial interests.

How to cite this article: Gistelinck, C. *et al.* Zebrafish Collagen Type I: Molecular and Biochemical Characterization of the Major Structural Protein in Bone and Skin. *Sci. Rep.* **6**, 21540; doi: 10.1038/srep21540 (2016).

Chapter II

The chemical chaperone 4 phenylbutyric acid ameliorated OI phenotype in the osteogenesis imperfecta zebrafish model Chihuahua

Osteogenesis imperfecta treatment approaches

OI patients in general are managed by a multidisciplinary team and the therapy consists of pharmacological, orthopaedic and dental treatment, physical medicine, treatment for hearing loss and prevention of complications (Monti et al. 2010). The first goal of treatment for adults with OI involves preserving bone density, often through vitamin D and calcium supplementation, with regular monitoring of hearing and dentition and maintenance of muscle strength through physical therapy (Bishop 2014).

The current drug therapy is mainly based on oral and intravenous bisphosphonates prescription (Van Dijk et al. 2011). Bisphosphonates are antiresorptive compounds deposited on the surface of bone through the interaction with hydroxyapatite crystals and they are taken by precursors or mature osteoclasts through endocytosis, inducing cell death (Papapoulos 2008). This therapy aims to increase the bone volume by decreasing the rate of bone resorption and turnover. In fact, despite the bone would still contain defective collagen, the treatment will improved bone properties, such as bone microarchitecture, bone mass, long bone bowing deformity, and restore vertebral size and shape (Monti et al. 2010). However, some animal and human studies have raised doubts concerning the long-term safety of bisphosphonates because of the possibility of a reduction of bone quality and mineralization heterogeneity, that lead to an increase in bone brittleness (Nicolaou et al. 2012). Bisphosphonates treatment on the mouse model Brtl/+ between 2 and 8 weeks of age resulted in extremely large gains in femoral metaphyseal bone mass, but had a little amelioration on cortical bone mass and strength, which required a full 12 weeks of treatment to show a modest effect. Furthermore, alendronate appeared to increase brittleness in Brtl/+ (Uveges et al. 2009). Similar results were obtained also in the osteogenesis imperfecta mouse model *oim* (Misof et al. 2005). This observation of a reduced or absent effect of bisphosphonates on OI cortical bone mass is also reflected in clinical data where in pediatric OI a beneficial effect on vertebral trabecular bone, but an equivocal effect on long bone strength was observed (Sakkers et al. 2004; Ward et al. 2011).

Denosumab is an FDA-approved fully humanized antibody targeting RANKL, the receptor activator of NF-kB ligand, which acts as stimulator of osteoclast formation and it is secreted by osteoblasts and osteocytes. The inhibition of RANKL blocks osteoblast-mediated-osteoclast differentiation. Studies performed on *oim/oim* model showed a significantly increase of bone density in femurs after

denosumab treatment, together with periosteal and endosteal diameters and bone stiffness (Bargman et al. 2011). Recently, a case study on three osteoporotic women affected by OI type I treated with Denosumab showed increased bone mineral density (BMD), improvement in bone formation and bone resorption markers and reduced incidence on bone fractures (Uehara et al. 2017). In children with OI type VI two years treatment with Denosumab gave promising results. After treatment a suppression of bone resorption was observed together with the increase of areal BMD. Moreover fracture rate was decreased in all four patients and mobility scores showed a slight increase (Hoyer-kuhn et al. 2014).

Different alternative treatments are also considered for OI, like the use of recombinant growth hormone (rGH) thanks to its stimulatory effect on the synthesis of collagen and on bone growth. Patients responding to rGH have increased bone mineral density and improved bone histology (Mayne 1989) Responders to recombinant human growth hormone have higher baseline collagen type I C-propeptide, a marker for increase matrix production (Hussar 2003). However, no effect has been reported on fracture risk (Boudko and Bachinger 2012). Interestingly, in patients with quantitative defects in collagen, the co-administration of rGH and bisphosphonates provided better results than each treatment alone (Doro et al. 2010). Finally, the rGH administration is associated with reduced side effects compared to bisphosphonate or anti-RANKL antibody treatment (Marini et al. 2003).

Other drugs with anabolic effect on bone are under investigation. There are two antibodies, one against the Transforming growth factor β (TGF-β), an osteoblast-produced regulator of bone remodelling, and one against sclerostin, a negative osteocyte-produced regulator of bone formation acting on the Wnt pathway, known to stimulate osteoblast activity.

TGF-β is produced by osteoblasts (Yang et al. 2013), secreted predominantly in inactive, latent forms (Dallas et al. 1994) and deposited into the bone matrix (Hering et al. 2001), from where it can be released and activated during bone resorption by osteoclasts (Oreffo et al. 1989). TGF-β acts as a central coordinator of bone remodelling by coupling the activity of bone-resorbing osteoclasts and bone-forming osteoblasts (Tang et al. 2009).

Alteration in TGF-β signalling was described in murine models for dominant and recessive OI (Grafe et al. 2014; Bianchi et al. 2015). The mouse model of dominant OI carrying the G610C mutation in the *Col1a2* gene (*Col1a2*$^{tm1.1Mcbr}$) displayed a higher expression of TGF-β target genes, indicating

upregulation of TGF-β pathway. This variation led to altered trabecular bone parameters, including reduced bone volume, trabecular number and thickness. Similarly, *Crtap*$^{-/-}$ mice, model for OI type VII, showed excessive TGF-β signalling in the skeletal structures resulting in low bone mass. In both cases, rescue experiments with a TGF-β neutralising antibody restored bone mass and improved whole-bone strength (Grafe et al. 2014). Indeed, also the dominant OI murine model Brtl/+ is characterized by distinctive cytoskeletal alterations that disturb TGF-β signalling, further pointing to this pathway as a good target for OI therapy (Bianchi et al. 2015).

Sclerostin is a potent inhibitor of bone formation which is secreted primarily by osteocytes (Poole et al. 2018). It functions by inhibiting canonical Wnt signaling through its binding to the Wnt signaling co-receptors Frizzle and LRP5/6, present on cells of the osteoblast lineage. Neutralizing antibodies have been developed to reduce sclerostin activity, preventing sclerostin inhibition of bone formation. Sinder et al. demonstrated that sclerostin antibody (Scl-Ab) increased bone formation leading to improve bone mass and strength in the growing Brtl/+ mouse (Sinder et al. 2013). Moreover, they showed a potent effect of Scl-Ab on cortical bone mass and long bone strength, contrasting the existing bisphosphonates data reported in both animal models and clinical studies (Uveges et al. 2009). Thus, Scl-Ab may provide a novel anabolic therapeutic option for pediatric OI by reducing long-bone susceptibility to fracture.

Teriparatide (TPD), a recombinant form of parathyroid hormone (hPTH), is a bone anabolic therapy, FDA approved for the treatment of osteoporosis. TPD increases bone remodelling, formation, and density; improves bone microstructure and reduces fracture risk (Neer et al. 2001). Clinical trials for OI treatment indicated that TPD therapy significantly increases bone density and ameliorates bone strength in adults with a mild form of OI. On the other hand, the observed benefits were reduced in patients with more severe forms (OI type III/IV) (Orwoll et al. 2014).

Being OI a genetic disorder, it was thought that gene therapy (antisense oligonucleotides, ribozymes, small interfering RNA (siRNA) and short hairpin RNA (shRNA)) directed towards replacement or silencing of the mutant allele could represent the future of medical treatment for the dominant forms of this disease in order to correct directly the causative defect (Besio and Forlino 2015). But, the main problems are related to the lack of specificity against the mutant transcript, the limited stability of the

antisense molecules and the lack of a bone specific delivery system. Thus, antisense suppression therapy is currently limited to *in vitro* studies (Monti et al. 2010).

Finally, the combination of gene and cell therapy may represent a new strategy for future OI treatment. Bone marrow or mesenchymal stem cells (MSCs) transplantation with donor healthy cells or with endogenous cells in which the mutation has been *in vitro* corrected can replace cells harbouring the causative variant with functional MSCs that differentiate into normal bone cells (Guillot et al. 2017; Le Blanc et al. 2005; Naomi et al. 2015). The low rate of cell engraftment in bone still represents one of the main limitations in the development of gene and cell-based strategies.

Despite the various therapeutic approaches, no definitive cure is available for OI and the patients are demanding the development of novel treatments both to cure the disease and/or to ameliorate their life quality.

Chemical chaperones: a novel therapeutic approach for OI?

Collagen type I characterized by abnormal structure is a common feature in many OI forms and the consequent cellular stress, caused by its partial retention in the endoplasmic reticulum (ER), has been recently identified as a potential novel target to treat the disease (Forlino et al. 2007).

Chemical chaperones are small molecules that mimic function of endogenous chaperones and recently they have imposed themselves as a good class of drugs able to prevent the intracellular mislocalization and the aggregation of proteins associated with human diseases (Perlmutter 2002).
4-Phenylbutyric acid (4-PBA) is a low molecular weight terminal aromatic substituted fatty acid approved for clinical use as an ammonia scavenger in children with urea cycle disorders and known to act as chaperone (Brusilow and Maestri 1996). 4-PBA penetrates the blood–brain barrier and exhibits significant neuroprotective effects in mouse models of neurodegenerative diseases, such as Alzheimer's disease (AD) (Ricobaraza et al. 2009). In addition, 4-PBA seems promising for the treatment of familial hypercholesterolemia by allowing mutant low-density lipoprotein receptors trapped in the ER to reach the cell surface (Tveten et al. 2007).
4-PBA showed also protective effects against ER stress- induced neuronal cell death, even if the mechanism behind is still unclear (Mimori, et al. 2012).

Another chemical chaperone already FDA approved for the treatment of cholestatic liver diseases is the bile acid tauroursodeoxycholate (TUDCA). TUDCA acts as cytoprotective of hepatocytes and restores glucose homeostasis by reducing ER stress, playing a key role in pathogenesis of obesity, insulin resistance, and diabetes (Ozcan et al. 2006; Xie et al. 2002).

As part of my PhD research I demonstrated the goodness of 4-PBA to ameliorate the bone outcome of the zebrafish *Chihuahua*, in short and long term treatment, after its deep molecular, skeletal and biochemical validation as OI model. The results are reported in the attached recently published paper.

Personal contribution to Chapter II

- Morphometric evaluation. I contributed to the measurement of both embryos and adult fish before and after treatment.
- Skeletal staining. I contributed to perform Alcian Blue and Alizarin Red staining.
- Growth curve determination.
- X-Rays
- Collagen type I analysis. I contributed to collagen type I extraction from bone, skin and scales.
- TEM analysis. I contributed to sample preparation for Transmission Electron Microscopy analysis on adult WT and mutant caudal fins.
- Picro Sirius Red staining. I performed the Picro Sirius Red staining of adult WT and Chihuahua tails.
- Whole Mount immunostaining.
- Confocal analysis. I contributed to sample preparation for Confocal microscopy analysis on WT and mutant embryos.
- Drug toxicity test and drug treatment
- Western Blot.
- qPCR.

OXFORD

Human Molecular Genetics, 2017, Vol. 26, No. 15 2897–2911

doi: 10.1093/hmg/ddx171
Advance Access Publication Date: 5 May 2017
Original Article

ORIGINAL ARTICLE

The chaperone activity of 4PBA ameliorates the skeletal phenotype of *Chihuahua*, a zebrafish model for dominant osteogenesis imperfecta

Roberta Gioia[1,†], Francesca Tonelli[1,†], Ilaria Ceppi[1], Marco Biggiogera[2], Sergey Leikin[3], Shannon Fisher[4], Elena Tenedini[5], Timur A. Yorgan[6], Thorsten Schinke[6], Kun Tian[7], Jean-Marc Schwartz[7], Fabiana Forte[8], Raimund Wagener[8], Simona Villani[9], Antonio Rossi[1] and Antonella Forlino[1,*]

[1]Department of Molecular Medicine, Biochemistry Unit, University of Pavia, Pavia, Italy, [2]Department of Biology and Biotechnology, University of Pavia, Pavia, Italy, [3]Section on Physical Biochemistry, Eunice Kennedy Shriver NICHD, NIH, Bethesda, MD, USA, [4]Department of Pharmacology & Experimental Therapeutics, Boston University School of Medicine, Boston, MA, USA, [5]Center for Genome Research, Department of Medical and Surgical Sciences, University of Modena and Reggio Emilia, Modena, Italy, [6]Institute of Osteology and Biomechanic, Center for Experimental Medicine, University of Hamburg, Hamburg, Germany, [7]Faculty of Biology, Medicine and Health, University of Manchester, Manchester, UK, [8]Medical Faculty, Center for Biochemistry, Center for Molecular Medicine, University of Cologne, Cologne, Germany and [9]Department of Public Health and Experimental and Forensic Medicine, Unit of Biostatistics and Clinical Epidemiology, University of Pavia, Pavia, Italy

*To whom correspondence should be addressed at: Department of Molecular Medicine, Biochemistry Unit, University of Pavia, Via Taramelli 3/B, 27100 Pavia, Italy. Tel: +39 0382 987235; Fax: +39-0382-423108; Email: aforlino@unipv.it

Abstract

Classical osteogenesis imperfecta (OI) is a bone disease caused by type I collagen mutations and characterized by bone fragility, frequent fractures in absence of trauma and growth deficiency. No definitive cure is available for OI and to develop novel drug therapies, taking advantage of a repositioning strategy, the small teleost zebrafish (*Danio rerio*) is a particularly appealing model. Its small size, high proliferative rate, embryo transparency and small amount of drug required make zebrafish the model of choice for drug screening studies, when a valid disease model is available. We performed a deep characterization of the zebrafish mutant *Chihuahua*, that carries a G574D (p.G736D) substitution in the α1 chain of type I collagen. We successfully validated it as a model for classical OI. Growth of mutants was delayed compared with WT. X-ray, μCT, alizarin red/alcian blue and calcein staining revealed severe skeletal deformity, presence of fractures and delayed mineralization. Type I collagen extracted from different tissues showed abnormal electrophoretic migration and low melting temperature. The presence of endoplasmic reticulum (ER) enlargement due to mutant collagen retention in osteoblasts and

[†]These authors contributed equally to this work.

Received: February 17, 2017. **Revised:** April 28, 2017. **Accepted:** May 2, 2017

fibroblasts of mutant fish was shown by electron and confocal microscopy. Two chemical chaperones, 4PBA and TUDCA, were used to ameliorate the cellular stress and indeed 4PBA ameliorated bone mineralization in larvae and skeletal deformities in adult, mainly acting on reducing ER cisternae size and favoring collagen secretion. In conclusion, our data demonstrated that ER stress is a novel target to ameliorate OI phenotype; chemical chaperones such as 4PBA may be, alone or in combination, a new class of molecules to be further investigated for OI treatment.

Introduction

Osteogenesis imperfecta (OI, OMIM # 166200, 166210, 259420, 166220) is a heritable skeletal disease mainly caused by dominant mutations in *COL1A1* or *COL1A2* genes coding for the α1 and α2 chain of type I collagen, the most abundant component of the bone organic matrix (1). Additional dominant and recessive OI forms due to mutations in other genes have been described, all affecting the synthesis, secretion, processing or matrix incorporation of type I collagen or the osteoblasts differentiation and activity, and all sharing the abnormal skeletal phenotype (2). Bone fragility, skeletal deformity and growth delay were traditionally exclusively attributed to the presence of an altered extracellular matrix. More recently, a role of abnormal osteoblasts homeostasis due to the mutant collagen retention and affecting cell differentiation and activity has been hypothesized as a relevant player in modulating OI pathophysiology, opening new opportunities for the treatment of the disease (3,4).

A different ability to cope with intracellular stress modulates the phenotypic outcome of the Brtl mouse, a well characterized model for classical OI (3,5). Brtl carries in heterozygosis a typical glycine substitution (G349C) in the α1(I) chain and, in presence of the same causative mutation, shows either a lethal or a moderately severe phenotype (6). In lethal mice an up-regulation of molecules involved in apoptosis and protein degradation was detected, whereas in mice with a moderately severe outcome the up-regulation of chaperones was described (3,5). More recently, we showed a different cytoskeletal assembly in lethal Brtl cells; our data demonstrated that compromised cytoskeletal organization impaired both cell signaling and cellular trafficking specifically in mutant lethal mice, altering bone properties (7). These results suggested that a disturbed intracellular homeostasis in bone cells could modulate OI outcome. Indeed, osteoblast malfunctioning was reported to negatively affect bone properties also in a different murine model for dominant OI, the Amish mouse (*Col1a2*$^{tm1Mcbr/J}$) carrying a G610C substitution in the α2(I) chain (8,9).

Based on these observations, the targeting of osteoblast malfunction, favoring either mutant collagen refolding and secretion or its selective intracellular degradation, seems particularly attractive to ameliorate OI outcome. No definitive therapy is so far available for OI and the correction of the genetic defect by gene/cell therapy approaches, although particularly appealing, will require long time and efforts. In the meantime, the search for novel drugs able to improve the quality of life represents a strong patients' demand. Furthermore, since cellular stress has been found not only in classical dominant OI, but also in several novel recessive OI forms due to mutations in protein affecting collagen post-translational modifications, it may represent a common and valuable target for multiple OI types. The availability of various molecules already approved by Food and Drug Administration (FDA) for other purposes and usable in a repositioning approach will facilitate the transition from the bench to the bedsite, allowing to skip pharmacokinetics tests and phase I safety trials (10).

Among the others, 4 phenylbutyrate (4PBA) and tauroursodeoxycholic acid (TUDCA) are two well-known molecules approved for urea cycle disorders and cholestasis respectively, and known to have other functions (11–13). 4PBA is mainly an ammonia scavenger, but it has also chaperone activity, since it interacts with hydrophobic domains of misfolded proteins favoring their folding (13). 4PBA also works as mild histone deacetylase inhibitor, promoting gene transcription (14).

TUDCA, the taurine conjugate form of ursodeoxycholic acid (UDCA), is a soluble bile acid and its main effect as chemical chaperone is based on improving protein folding capacity by activation of the unfolded protein response (UPR) sensor activating transcription factor 6 and by assisting the trafficking of mutant proteins. Furthermore, it inhibits the phosphorylation of eIF2a, a target of the UPR sensor protein kinase RNA-like endoplasmic reticulum (ER) kinase, responsible for inhibition of protein translation and apoptosis activation (15).

The *in vivo* evaluation of pharmacological treatments represents the most powerful and desirable approach in drug screening studies, since it allows consideration not only of the cell specific effects of the compound, but also its absorption, organ distribution, metabolism, excretion and toxicity in the whole organism. Of course, the availability of a valid model able to provide large dataset of results in short time and at low cost is a fundamental prerequisite. Murine models do not seem to satisfy such features due to the considerable effort required for their generation and validation, housing space and cost, amount of drugs necessary for the studies and number of animals to be sacrificed. Recently the small teleost *Danio rerio* stood up as a better choice for drug screening trials (16). *Danio rerio*, known as zebrafish, has been used extensively for genetic studies of vertebrate development due to its high fecundity, externally fertilization and embryo transparency. These characteristics, together with the high-quality genome sequence available (17,18), the generation of transgenic lines with fluorescent proteins expressed under cell/tissue specific promoters (19), the possibility to easily knock down genes by morpholino (20) and to generate mutant lines with the CRISPR/Cas 9 editing system (21), strongly expanded zebrafish use for the investigation of human diseases. Indeed, large-scale mutagenesis studies revealed that zebrafish reproduces many of the diseases described in tetrapods, including those affecting the skeletal system (22). Despite the evolutionary distance between humans and teleosts, zebrafish shares 82% of disease associated targets and a large number of drug metabolism pathways (17,23). In particular, considering the skeletal system, the gene expression profile associated with bone development is highly conserved between tetrapods and zebrafish. Moreover, the types of ossification, membranous and endochondral, as well as the presence of all the bone cell types are common to zebrafish and humans (24,25). Indeed multiple skeletal disorders have been recapitulated in zebrafish, including both dominant and recessive OI forms (22,26–29) and screening for anabolic bone compounds was previously successfully accomplished (30).

The use of zebrafish as a cheap and convenient tool for drug screening studies is further supported by the ability to administer most drugs in a small volume of water without need for invasive

procedures and to house zebrafish, at least in the larval stage, in multi-well plates suited for high-throughput analysis and automated screening (11,30).

A zebrafish model for the classical form of OI, named *Chihuahua* (*Chi*/+), was discovered as a result of a large N-ethyl-N-nitrosourea (ENU)-mutagenesis screening and identified by an X-ray-based screening aimed at recognizing abnormal skeletal patterning. *Chi*/+ carries in heterozygosis a typical glycine substitution (G574D, p.G736D) in the triple helical domain of the α1 chain of type I collagen, the most common cause of classical OI and revealed the bone outcome of severe human OI (22).

In the present study we performed the first deep investigation of *Chi*/+ fish from larval to adult stage validating it as a model for classical OI from a biochemical, morphological and cellular point of view. We confirmed the intracellular retention of mutant collagen causing ER enlargement in zebrafish and succeeded in ameliorating the outcome of OI by administration of 4PBA targeting osteoblasts malfunction.

Results

In order to use the zebrafish *Chihuahua* mutant for drug screening studies to discover novel OI therapies, a deep phenotypic characterization of larval and adult mutant fish was performed. Since OI is mainly associated with short stature, extreme bone fragility and skeletal deformity, these parameters were first investigated.

Adult *Chi*/+ fish are shorter and show deformed and fragile bones compared with WT

The growth of heterozygous *Chi*/+ and WT zebrafish was followed from 2 to 40 weeks post-fertilization (wpf) by measuring the standard length (SL) (Fig. 1A). Although *Chi*/+ fish were shorter than WT from 3 wpf, the difference was significant only starting from 18 wpf (*Chi*/+: 12.55 ± 2.45 mm, $n = 15$; WT: 15.34 ± 4.08 mm, $n = 12$; $P = 0.04$) and by 40 wpf the mutants were ∼70% the size of the controls ($P = 0.006$) (Fig. 1B). The gross *Chi*/+ outcome showed an abnormal body and head shape, thus morphometric measurements were performed. The height at anterior of anal fin (HAA), the distance from the snout to the most posterior point of operculum (SOL) and the ventral to dorsal head height (HE) were evaluated (Fig. 1A). At 18 wpf HAA was similar in *Chi*/+ and WT (2.82 ± 0.85 mm, $n = 15$ and 3.05 ± 0.95 mm, $n = 12$, respectively; $P = 0.51$), but the significant lower SL/HAA ratio (*Chi*/+: 4.60 ± 0.58 and WT: 5.13 ± 0.43; $P = 0.01$) confirmed a more stocky body shape in mutants with respect the WT. The SOL/HE ratio was also significantly smaller in mutant fish (*Chi*/+: 1.23 ± 0.05 and WT: 1.33 ± 0.09; $P = 0.001$) supporting a more flattened head. By 19 wpf the SOL was shorter in *Chi*/+ compared with WT (3.35 ± 0.61 mm and 3.92 ± 0.69 mm: $P = 0.032$).

The abnormal shape of the caudal fin, already described in (22), gave rise to a lower ratio between the longest and shortest tail axes in *Chi*/+ compared with control fish (Fig. 1C). The difference was detectable, although not significant, at 1 month post-fertilization (mpf; *Chi*/+: 1.50 ± 0.05, $n = 4$; WT: 1.52 ± 0.11, $n = 10$; $P = 0.66$), but significance was reached at 2 mpf (*Chi*/+: 1.64 ± 0.14, $n = 26$; WT: 1.85 ± 0.09, $n = 27$; $P < 0.001$).

Rib fractures and vertebral fusions were detected in adult *Chi*/+ fish by X-ray and confirmed by alcian blue/alizarin red staining (Fig. 1D and E). The skeletal specific staining allowed also a more detailed analysis of bone deformities. Vertebrae were clearly misshapen, with altered and highly irregular post-zygapophysis and prezygapophysis protrusions (Fig. 1E, ii). Ribs appeared twisted and misshapen, with numerous calli indicating the healing of spontaneously occurring fractures (Fig. 1E, i). Fin structure was seriously compromised as already reported by Duran *et al.* (31), in particular the pelvic fins appeared atrophic and twisted (Fig. 1E, iii and iv).

Also, the slope of the neural spine was altered in mutant fish. The mean of the neural spine slope of the 10 precaudal vertebrae (measured as described in Materials and Methods; Fig. 1E, ii) was steeper in *Chi*/+ compared with WT fish starting from 1 mpf (55.66° ± 6.52° and 49.69° ± 5.23°, respectively; $P < 0.001$; $n = 4$ in each group) and a significant difference was confirmed at 2 mpf (*Chi*/+: 57.57° ± 6.64°, $n = 5$; WT: 54.83° ± 5.34°, $n = 4$; $P = 0.04$).

A strong reduction of bone mineral density in mutant compared with WT fish ($n = 5$ for each genotype and time point) was demonstrated by μCT images performed at 3 mpf (Fig. 1F) and 10 mpf (data not shown).

In general, most of the analyzed parameters revealed a worsening of the mutant phenotype with age.

Similar size but delay in mineralization characterized *Chi*/+ larvae compared with WT

Starting from 5 days post-fertilization (dpf), the presence of a pronounced fin fold bending already described by Fisher *et al.* (22) distinguished *Chi*/+ from WT. The angle of the fin fold bending, measured as described in Materials and Methods (Fig. 2A), was significantly different between *Chi*/+ and WT (137.77° ± 13.91°, $n = 204$ and 177.12° ± 2.90°, $n = 217$, respectively; $P < 0.001$).

Vital calcein labelling of 5 dpf fish revealed a delayed vertebral ossification. The notochord ossification began with the third and fourth vertebral centra and spread as expected in the two directions both in control ($n = 78$) and in *Chi*/+ ($n = 96$) fish (Fig. 2B). Interestingly, while all WT larvae showed almost complete ossification of the third, fourth and fifth centra (c3, c4, c5), about 50% of the *Chi*/+ larvae showed no ossification of these bones (Fig. 2C).

Alcian blue and alizarin red staining of 11 dpf larvae confirmed a significant mineralization delay in *Chi*/+ cranial bones compared with WT ($n = 50$ and 65, respectively) (Fig. 2D). The mineralization of 5th ceratobranchial (5CB), cleithrum (CL) and notochord (NC) was considered as example of endochondral, membranous and perichordal bone ossification, respectively. Three classes of mineralization were identified, namely beginning/no mineralization, incomplete and complete, based on the level of alizarin red staining. A significant reduction of bone mineralization was detected in mutant fish compared with WT for 5CB ($P = 0.003$) and cleithrum ($P = 0.007$), the bones with mineralization type conserved in tetrapods. No difference was instead present for notochord ($P = 0.802$) (Fig. 2E; Supplementary Material, Table S1).

Type I collagen is overmodified in *Chi*/+ zebrafish

Acid soluble and pepsin digested type I collagen extracted from skin, scales and bone of adult *Chi*/+ showed broader and slightly slower bands of the α chains with respect to control fish in SDS-PAGE, indicating the presence of collagen overmodification, a typical OI feature (Fig. 3A).

We recently demonstrated that the normal type I collagen melting temperature (T_m) in zebrafish is ∼35 °C (32) Fig. S1, but the T_m of *Chi*/+ skin and bone type I collagen determined by

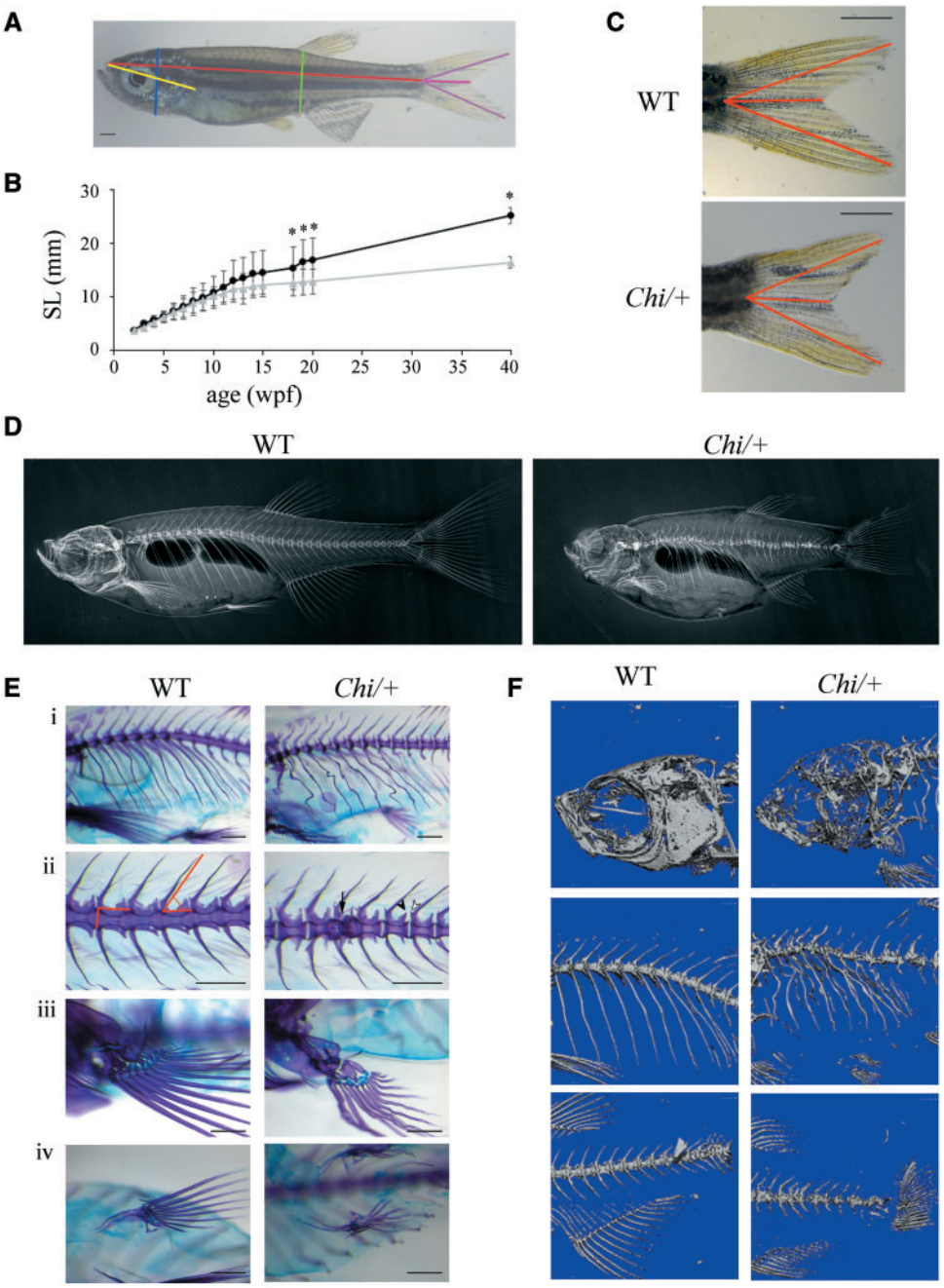

Figure 1. Morphological characterization of adult (*Chi/+*) zebrafish. **(A)** Morphometric parameters measured in adult fish. Standard length (SL) in red, height at anterior of anal fin (HAA) in green, height at eye (HE) in blue, snout-operculum length (SOL) in yellow, major axes of the caudal fin in purple, minor axis of the caudal fin in pink. **(B)** The growth curve shows that mutant fish ($n = 15$, grey triangles) are significantly smaller than WT ($n = 12$, black squares) from the 18th week post-fertilization (wpf). SL: standard length. $^*P < 0.05$. **(C)** Representative image of WT and *Chi/+* caudal fin. The caudal fin of mutant fish has less pronounced lobes than the WT fin. The distances measured as described in Materials and Methods are highlighted in red. Scale bar: 1 mm. **(D)** WT and *Chi/+* X-rays show severe alterations in the skeleton of mutant fish. **(E)** Skeleton magnifications of 3 months old WT and *Chi/+* fish stained with alcian blue and alizarin red. Major and minor axes of the vertebral body and the slope of the neural spine are indicated (ii). Deformed ribs with bone calli (**i**), fused vertebrae (**ii**, arrow), misshapen prezygapophysis and post-zygapophysis (**ii**, white and black arrowheads), deformed pectoral (**iii**) and pelvic fins (**iv**) are evident in mutant fish. Scale bar: 500 μm. **(F)** μCT of 3 months old WT and *Chi/+* fish reveals the severe under mineralization of mutant animals.

differential scanning calorimetry (DSC) showed a broad thermogram. The deconvolution of the curve resulted in three peaks, corresponding to a T_m of ~35, ~33 and ~30 °C (Fig. 3B; Supplementary Material). Type I collagen melting temperature lower than normal is caused by abnormal protein structure and, based on these data, two populations of collagen molecules containing mutant chains seemed to be present in *Chi/+* together with normal collagen. Interestingly, from the peak integration, the mutant collagen molecules corresponded to ~ 33% of total collagen in bone (Fig. 3B) and ~20–25% in skin (data not shown). This implies that limited amount of mutant collagen was incorporated in *Chi/+* tissues.

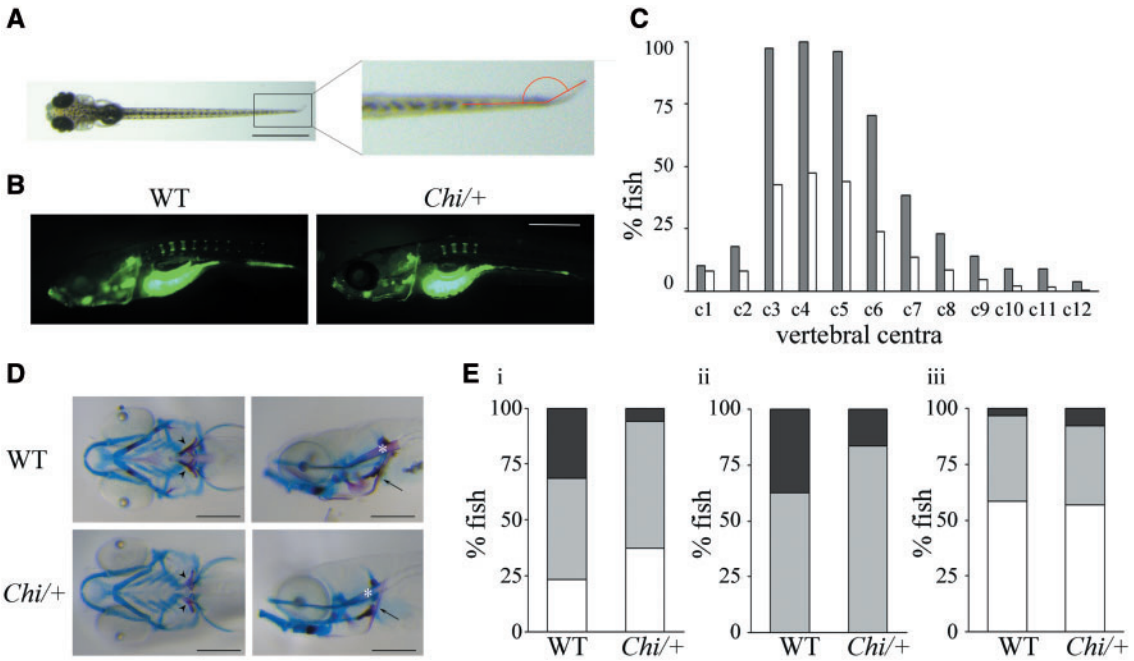

Figure 2. Skeletal evaluation of *Chi/+* larvae. **(A)** Fin fold angle is represented in red in 11 dpf fish. Scale bar: 1 mm. **(B)** Representative images of 5 dpf larvae WT and *Chi/+* stained with calcein. The delay in vertebral centra ossification is evident. Scale bar: 250 μm. **(C)** Percentage of 11 dpf fish presenting calcein positive (mineralized) vertebrae. c: vertebral centrum. Grey: WT; white: *Chi/+*. **(D)** Alcian blue and alizarin red staining of WT and *Chi/+* 11 dpf larvae in ventral and lateral orientation. 5th ceratobranchyal (5CB, arrowhead), cleithrum (CL, arrow) and notochord (NC, asterisk) are indicated. Scale bar: 200 μm. Delayed mineralization, represented by reduced alizarin red staining, is evident in the mutant larvae. **(E)** Percentage of 11 dpf WT and *Chi/+* larvae presenting distinctive levels of mineralization in the 5CB **(i)**, the CL **(ii)** and the NC **(iii)**. White indicates beginning/no mineralization, grey indicates incomplete mineralization and black indicates complete mineralization.

Enlarged ER in *Chi/+* fish

One of the typical features in OI patients and murine model type I collagen producing cells is the intracellular retention of the mutant protein associated with an enlargement of the ER cisternae and with cellular stress.

The easiest bone tissue to investigate in adult fish is represented by fin rays lepidotrichia, where it is relatively simple to identify in histological sections osteoblast lining cells of the hemi-rays. By transmission electron microscopy (TEM) we detected a general enlargement of the ER cisternae in adult *Chi/+* osteoblasts, absent in WT samples ($n = 5$ for each group) (Fig. 3C).

The presence of enlarged ER cisternae in mutant fish was also detected at embryo stage by injecting zebrafish embryos with the mRNA coding for a yellow fluorescent protein (YFP) targeting the ER. The percentage of embryos with strong intracellular fluorescent signal, supporting the presence of enlarged ER cisternae, was clearly higher in *Chi/+* (66.7%, $n = 9$) compared with WT (16.7%, $n = 12$) fish (Fig. 3D).

Increased Hsp47 expression in *Chi/+* compared with control larvae

Hsp47 is a fibrillar collagen specific chaperone known to assist procollagen assembly in the ER and its trafficking into the Golgi (33,34). As specific antibodies for zebrafish Hsp47 were not available, a rabbit was immunized with recombinant zebrafish Hsp47b lacking the ER retention signal. After affinity purification, the polyclonal antibodies specifically detected zebrafish Hsp47b (Supplementary Methods). Whole mount immunostaining using Hsp47b antibody on 5 dpf *Chi/+* ($n = 38$) and WT ($n = 36$) larvae showed a stronger signal in mutant compared with WT fish. A higher expression of Hsp47 in tail fin fold, skin and intersomitic space was evident in *Chi/+* compared with WT (Fig. 3E; Supplementary Material, Table S2).

4PBA ameliorates bone mineralization defect in *Chi/+* larvae

The enlarged ER detected in mutant *Chi/+* cells and the Hsp47 up-regulation prompted us to use the *Chi/+* model to target *in vivo* cellular stress as possible novel OI therapy. The administration of two different FDA approved molecules, 4PBA and TUDCA, known to act also as chemical chaperones was attempted. To determine the highest non-toxic dosage, toxicity tests at increasing concentrations were performed first. Doses of 0.05 mM for 4PBA and of 0.5 mM for TUDCA were chosen since they corresponded to the highest drug concentrations associated to normal phenotype at the end of the toxicity test (data not shown).

The period of treatment was selected based on the knowledge that at 11 dpf the organogenesis is completed and mineralization can be easily detected; furthermore, zebrafish can be kept in 96-well/plate limiting the drug requirement.

At the end of the treatment the fin fold bending and the mineralization level of 5CB, CL and NC in treated and untreated *Chi/+* and WT zebrafish were evaluated.

4PBA significantly increased the fin fold angle in *Chi/+* (treated: $145.99° \pm 13.58°$, $n = 192$; placebo: $137.77° \pm 13.92°$, $n = 204$; $P < 0.001$) (Fig. 4A). On the contrary, no significant effect was evident after TUDCA treatment (treated: $134.37° \pm 22.16°$, $n = 130$; placebo: $130.54° \pm 20.01°$, $n = 118$; $P = 0.16$), although after drug administration the caudal fin fold was slightly straightened (Fig. 4E).

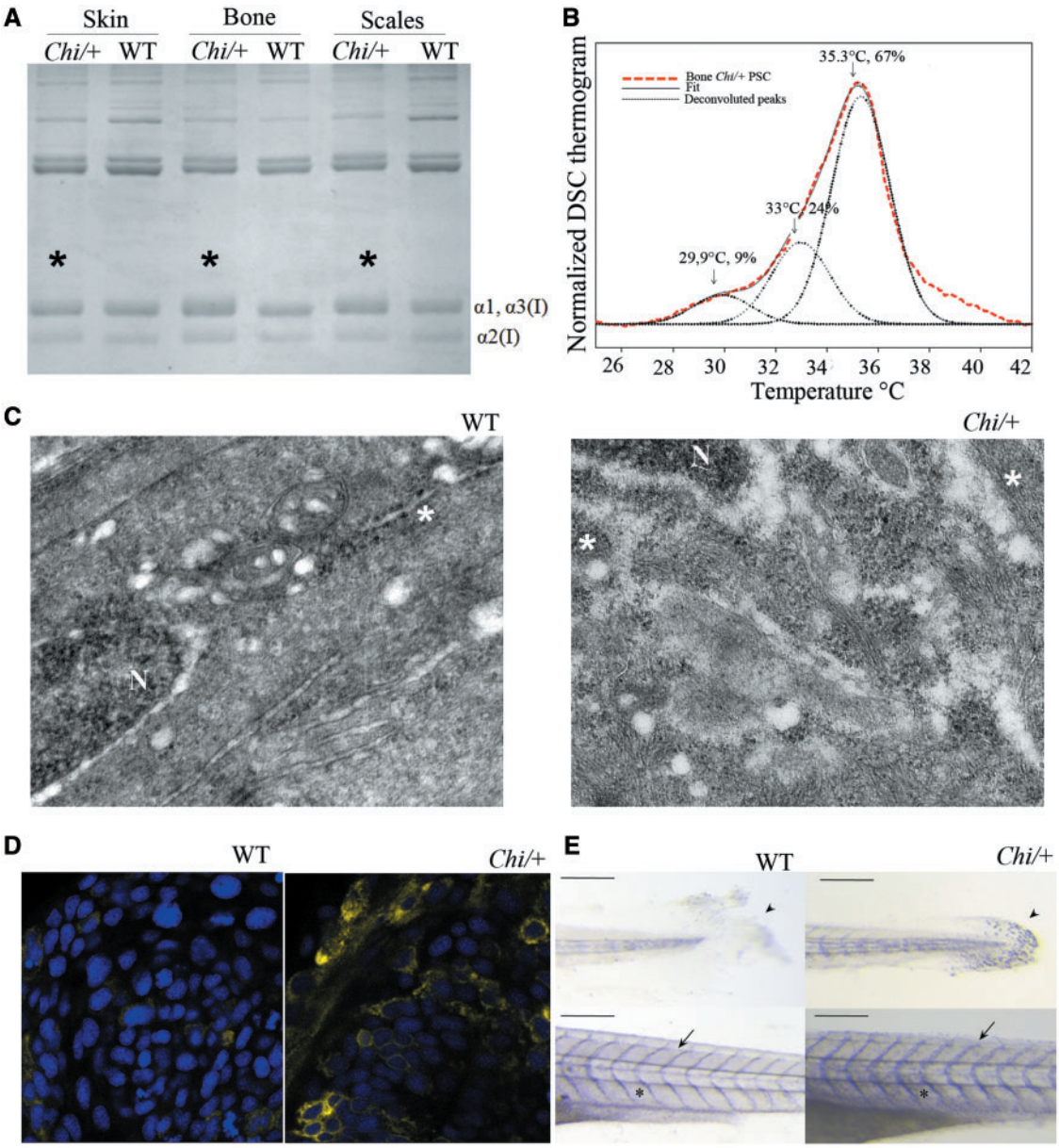

Figure 3. Biochemical and cellular evaluation of *Chi/+* collagen type I. **(A)** SDS-PAGE of collagen type I extracted from skin, bone and scales of WT and *Chi/+* adult fish. Mutant collagen is characterized by broader α bands (asterisks), indicating collagen type I overmodification. **(B)** Representative DSC thermogram of collagen extracted from bone of *Chi/+* adult fish. The presence of three melting temperature (T_m) peaks is evident from the deconvolution analysis of the thermogram. Similar result was obtained for collagen extracted from skin and scales (data not shown). **(C)** Transmission electron microscopy image of the caudal fin of WT and *Chi/+* adult fish. The enlargement of endoplasmic reticulum (ER) cisternae is evident in mutant fish. N: nucleus; *: rough endoplasmic reticulum (ER). Magnification 12000X. **(D)** Confocal microscopy images of 24 hpf embryos WT and *Chi/+* injected with mRNA expressing yellow fluorescent protein in the ER. A stronger signal in the mutant sample is demonstrated. Magnification 40X, zoom 4X. **(E)** Whole mount immunohistochemistry of 5 dpf WT and *Chi/+* embryos using Hsp47b antibody. A stronger signal is evident in tail, skin and intersomitic space in mutant larvae. Arrow: intersomitic space, arrowhead: tail; asterisk: skin. Scale bar: 200 μm.

Regardless the difference between the genotypes, 4PBA administration had a borderline significant effect on 5CB mineralization ($P = 0.07$), determining an overall 10% increment of the number of mineralized fish with respect the placebo group (Fig. 4B; Supplementary Material, Table S3). The effect of the treatment on 5CB mineralization was also explored within genotypes. 4PBA increased the complete mineralization in both WT and *Chi/+* with respect untreated fish, but the statistical relevance was not achieved (Supplementary Material, Table S4).

Similarly 4PBA significantly improved the mineralization of the NC ($P = 0.001$) (Fig. 4D; Supplementary Material, Table S3). This amelioration was evident in both genotypes, but the significance was detected only in WT ($P = 0.002$) (Supplementary Material, Table S4).

No 4PBA effect was detected on CL mineralization classes ($P = 0.424$) (Fig. 4C; Supplementary Material, Tables S3 and S4).

Mineralization analysis of treated and untreated mutant and WT fish did not reveal any significant difference following the TUDCA administration (Fig. 4F–H).

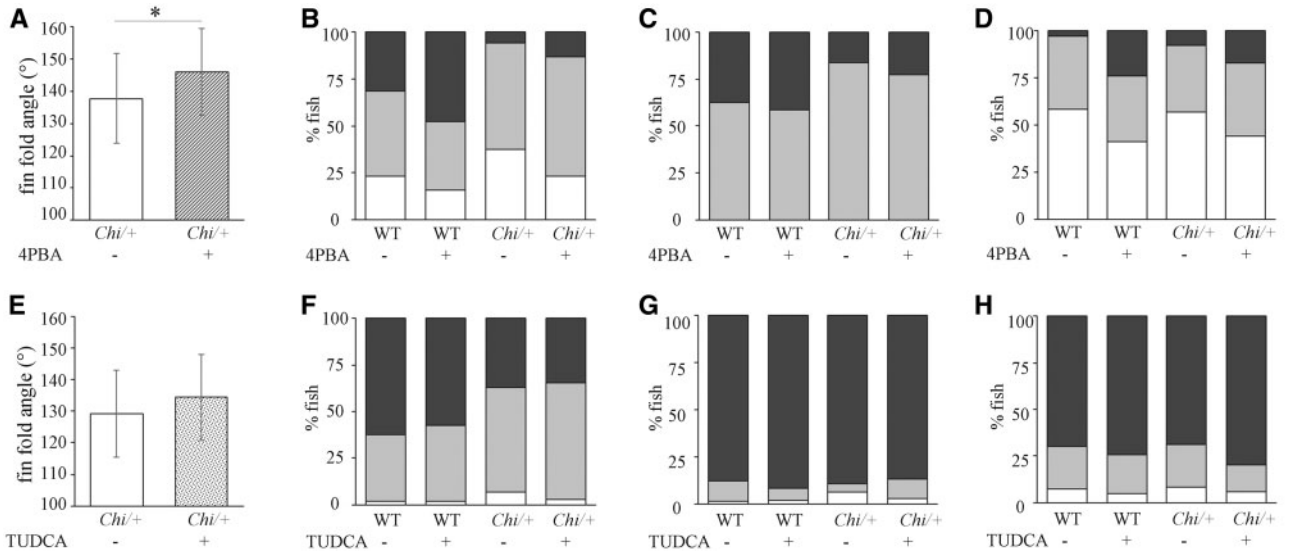

Figure 4. Effect of 4PBA and TUDCA treatment on *Chi/+* larvae. The caudal fin fold angle of 11 dpf *Chi/+* larvae increased after treatment with both 4PBA **(A)** and TUDCA **(E)**, but only 4PBA determined a significant straightening. $^{*}P < 0.001$. The administration of 4PBA increased the mineralization level of the 5CB **(B)**, CL **(C)** and NC **(D)** in mutant larvae. The treatment with TUDCA was ineffective in increasing the mineralization of all evaluated bones (CB, **F**; CL, **G** and NC, **H**) both in WT and in *Chi/+* larvae. In **(B)**–**(D)** and **(F)**–**(H)**, white boxes indicate beginning/no mineralization, grey boxes incomplete mineralization and black boxes complete mineralization.

Long-term 4PBA administration ameliorates skeletal phenotype in adult *Chi/+*

Based on the promising data obtained from the short term 4PBA administration to *Chi/+* larvae, mutant and WT fish were treated from 1 dpf to 3.5 mpf (WT: placebo $n = 18$, treated $n = 22$; *Chi/+*: placebo $n = 24$, treated $n = 21$). SL, tail shape and neural spine slope were evaluated at the end of the treatment.

The SL for both mutant and WT placebo was shorter than expected based on the growth curve values, in fact their size was compatible with 11 wpf animals. This was likely due to growing the zebrafish in bench tanks, the reduced water volume, the less controlled temperature and the limited food administration necessary to limit the water replacement. As expected a significant difference was not detected in the placebo groups (*Chi/+*: 10.40 ± 1.70 mm; WT: 11.37 ± 3.09 mm; $P = 0.40$), but 4PBA administration increased the *Chi/+* length to WT values (11.36 ± 2.11 mm and 11.55 ± 2.75 mm, respectively; $P = 0.77$).

The treatment normalized the mutant tail shape. The ratio between the longest and shortest tail axes (measured as reported in Materials and Methods and described in Fig. 1A) was significantly different in WT versus placebo mutant fish (1.77 ± 0.14 and 1.55 ± 0.10, respectively; $P < 0.001$), but it was increased in *Chi/+* after 4PBA treatment (*Chi/+*: 1.73 ± 0.25; $P = 0.08$), approaching the WT value (Fig. 5A).

The 4PBA also improved the morphology of the mutant skeleton. The slope of the neural spine in the precaudal vertebrae following drug administration was significantly reduced with respect untreated mutant fish ($50.69° \pm 7.86°$ and $53.06° \pm 8.19°$, respectively; $P = 0.002$), reaching the WT untreated value ($49.78° \pm 6.10°$) (Fig. 5B). The comparison performed on the single vertebral centra revealed that the most significant reduction of the slope was detected on the more caudal vertebrae analyzed (Supplementary Material, Table S5).

Mean vertebrae length and area were also increased significantly in *Chi/+* treated compared with the placebo group (length: 0.26 ± 0.06 mm and 0.22 ± 0.04 mm; $P = 0.04$; area: 0.045 ± 0.02 mm^2 and 0.034 ± 0.02 mm^2; $P = 0.047$).

4PBA treatment reduced ER cisternae size and increased the amount of extracellular collagen

In order to understand the mechanism of 4PBA in ameliorating the skeletal phenotype of *Chi/+* fish, TEM of 11 dpf 4PBA treated embryos was performed to investigate the ER cisternae size. Electron microscopy images revealed the presence of normal ER cisternae in treated *Chi/+*, although they were still coexisting with cisternae of enlarged size (Fig. 5C).

Whole mount immunostaining of 5 dpf treated and placebo *Chi/+* fish using Hsp47b antibody did not show any reduction in the expression of this type I collagen specific chaperone, that remains up regulated in mutant fish after treatment (Supplementary Material, Table S2).

Interestingly, more type I collagen was detected in mutant fish following 4PBA treatment, supporting an amelioration of its secretion. No such effect was detected following TUDCA administration. Taking advantage of the regenerative property of zebrafish tail, about half of adult *Chi/+* fish tail was cut and the secreted and newly deposited collagen was evaluated in absence or presence of 4PBA ($n = 3$ and 4, respectively) or TUDCA ($n = 4$ in each group) after 7 days. The higher percentage of fluorescent green signal in the regrown tails of 4PBA treated *Chi/+* zebrafish under polarized light after staining with picro sirius red clearly demonstrated an increased amount of collagen in the secreted matrix (Fig. 5D; Supplementary Material, Table S6). This increase was undetectable upon TUDCA administration (Supplementary Material, Table S7).

4PBA did not affect early and late osteoblast-specific genes expression

To evaluate if the inhibitory effect of 4PBA on class I and II histone deacetylases was affecting the transcription of bone forming cells specific genes, the expression of an early (*sp7*) and two late (*col1a1a* and *bglap*) osteoblast genes was evaluated by qPCR after 7 days of treatment in WT and *Chi/+* larvae. No difference

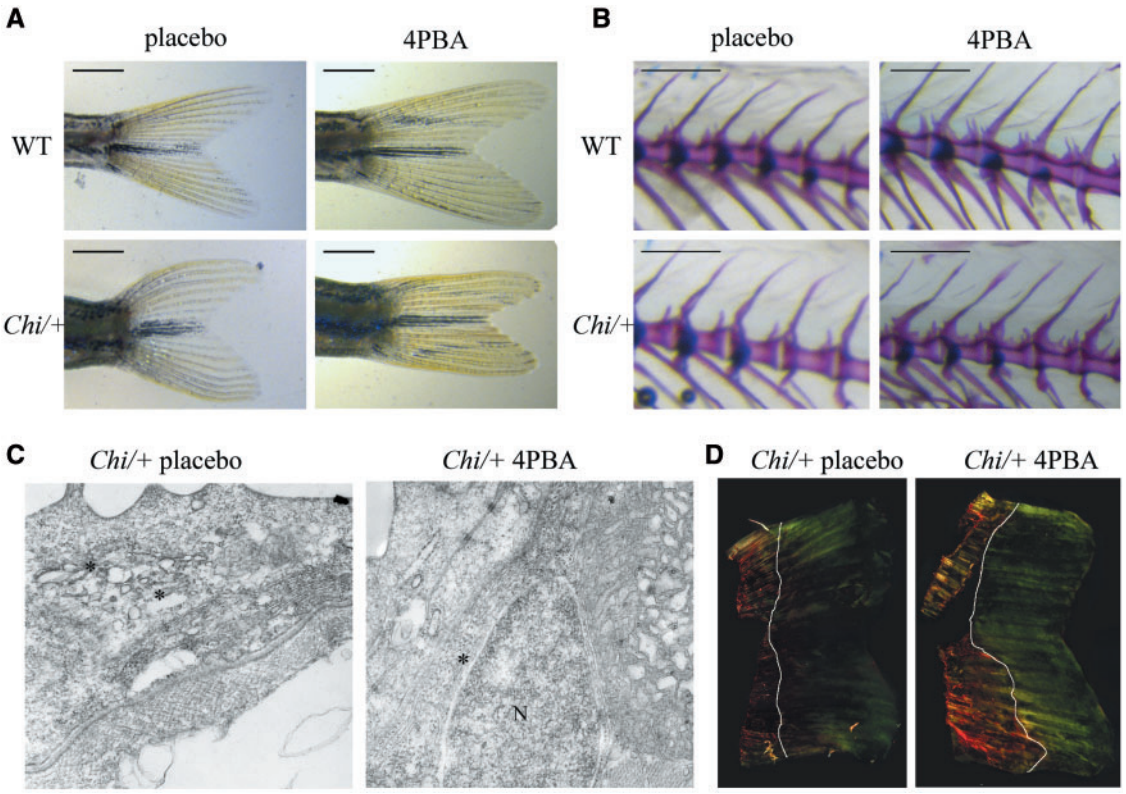

Figure 5. 4PBA treatment ameliorated the tail shape **(A)** and normalized the neural spine slope **(B)** of *Chi/+* fish after 14 weeks of treatment. Scale bar: 1 mm in **(A)** and 500 μm in **(B)**. **(C)** Transmission electron microscopy of 11 dpf *Chi/+* larvae showed a general reduction of the ER cisternae size after 4PBA treatment. Magnification 12000X. **(D)** Representative images of picro sirius red staining *Chi/+* zebrafish regrown tail after 7 days from tail clipping in absence or presence of 4PBA. A strongest signal in the sample obtained from 4PBA treated fish confirmed a higher amount of collagen in the matrix following 4PBA treatment. White lines indicate the portion of tail regrown in 7 days. Magnification 10X.

was detected for all of the three genes (Supplementary Material, Fig. S2A–C).

Western blot analysis using an antibody against acetylated-H3 did not reveal any significant difference in its expression following 0.05 mM 4PBA treatment in tissue lysates from larvae and adult fish (Supplementary Material, Fig. S2D and E), indicating that the inhibitory effect of 4PBA on histone deacetylases was not significant at the used concentration.

Discussion

With the ultimate aim to develop and validate a high throughput drug screening tool to find novel cure for the untreatable brittle bone disease OI, our study accomplished three major findings. First, the mutant zebrafish *Chihuahua* (*Chi/+*) was validated as model for classical OI by deep biochemical, morphometric and cellular characterization. Second, the power and advantages of this model for drug screening both in larvae and in adult were highlighted by defining easily traceable output. Finally, by a candidate approach 4PBA was identified to have potential to treat OI most likely based on its chaperone activity.

Chihuahua mirrored morphological, biochemical and cellular OI outcome

Short stature is a main hallmark for OI patients and small size is a common feature in OI murine models (2,6,8,35,36). The growth curve analysis performed from 2 to 40 wpf confirmed in *Chi/+* a growth delay together with a more stocky body and head shape compared with WT.

The two main biochemical properties of OI mutant type I collagen are excessive post-translational modification and reduced thermal stability due to altered structure (37,38). A slower and broader electrophoretic migration of α bands in type I collagen extracted from different *Chi/+* tissues supported the presence of overhydroxylated and overglycosylated protein also in this model. Furthermore, the T_m of type I collagen in mutant *Chi/+* was reduced. The DSC thermogram showed, together with the expected peak at ∼35 °C corresponding to the fraction of collagen molecules containing only normal α chains (32), two lower T_m peaks at ∼33 and ∼30 °C suggesting the presence of at least two different populations of collagen molecules with mutant ($\alpha1^{G574D}$) chains. In zebrafish, type I collagen may contain not only α1 and α2 chains, but also a third chain, namely α3, which is encoded by the *col1a1b* gene and absent in tetrapods (32,39). We recently proposed the presence of an equimolar amount of the three α chains in zebrafish type I collagen, leaving open the possibility of the existence of α1α3α2 alone or the presence of equal amounts of α1α1α2 and α3α3α2 or a combination of the three trimers (32).

Since only a single DSC peak with T_m ∼35 °C was observed in wild-type fish (Supplementary Material, Fig. S1), the additional DSC peaks of *Chi/+* bone collagen with T_m ∼33 °C and T_m ∼30 °C (Fig. 3B) likely represent the molecules with one and two $\alpha1^{G574D}$ chains, respectively (38). Based on our previous findings on zebrafish type I stoichiometry (32) the presence of $\alpha1^{G574D}\alpha1^{G574D}\alpha2$ trimers suggests that zebrafish collagen contains either all three

possible trimers or just α1α1α2 and α3α3α2, but not α1α3α2 alone. The observation of ∼33% mutant molecules in bone (Fig. 3B) and <25% mutant molecules in skin (data not shown), which are values lower than expected based on the proposed stoichiometry (Supplementary Material, Table S8), indicated either a low matrix incorporation for the mutant collagen or its partial intracellular retention.

Indeed enlargement of ER in *Chi*/+ mutant fish was demonstrated in fibroblasts by confocal microscopy and in osteoblasts by electron microscopy. Intracellular retention of mutant collagen has been widely demonstrated both *in vitro* and *in vivo* in OI patients and in murine models (35,40). The size of the ER correlates with the unfolded protein load and ER expansion is expected in presence of excessive misfolded proteins and it is normally associated to cellular stress.

Finally, whole mount immunohistochemistry on 5 dpf WT and mutant zebrafish revealed a strong Hsp47 signal in *Chi*/+ in the skin, in the space among somites and in the tail fin. An increased Hsp47 expression either at transcript or protein level, as well as an increased intracellular colocalization with mutant type I collagen, were reported in cells from OI patients and murine models (9,41). Hsp47 is an ER chaperone known to play a role in collagen synthesis by stabilizing the procollagen molecules. Hsp47 also facilitates type I collagen transfer from the ER to the Golgi compartment (33,34). An increased expression of Hsp47 in cells expressing structurally abnormal type I collagen may either represent an attempt to favor its proper synthesis and secretion and/or the impossibility for the mutant collagen to move properly throughout the secretory pathway.

Chihuahua: a zebrafish reproducing bone OI phenotype

μCT, X-ray and skeletal-specific staining confirmed the bone deformity and multiple rib fractures seen in adults *Chi*/+ zebrafish as originally reported (22), but also provided novel insight validating *Chi*/+ as good model for human OI. Furthermore, several vertebral compressions were identified both in abdominal and in caudal regions. Vertebral compressions associated with vertebral fractures are described in human OI and are mainly consequences of poor quality of bones that are unable to sustain the mechanical loading. Interestingly, none of the OI murine models reproduced the vertebral phenotype, mainly because rodents, as quadrupeds, have a structure of spine and center of gravity quite different from humans. Zebrafish instead bear cranial-to caudal spinal loads that are originated by swimming forward through water coupled with caudal propulsion and that are quite comparable to the gravitational load to which humans are subjected. Overall, the similar biomechanical forces along the spine seem to make fish more susceptible to vertebral damage (42) and thus a better model for mimicking human spine defects.

Vertebrae distortion was also detected in mutant fish, as demonstrated by a steeper slope of the neural spines compared with WT. The presence of mutant collagen in *Chi*/+ could be responsible for the deformity, since neural and haemal appendices are intramembranous bones and the lack of cartilage anlage underlines a relevant role for type I collagen in shape and mineralization of these structures (43).

Duran *et al*. described the presence of abnormal actinotrichia and lepidotrichia shape and length during fin development and regeneration in *Chi*/+ zebrafish (44). Actinotrichia are the first fin skeletal structures formed during development and they represent a support and a scaffold for the migration of mesenchymal stem cells responsible for the generation of the fin fold connective tissue (45,46). They consist of collagen fibrils mainly composed of a specific type of collagen II and of homotrimeric collagen I. The presence of abnormal actinotrichia in *Chi*/+ zebrafish underlined the importance of structurally correct collagen molecules for proper fin formation.

The significant reduction of the ratio between long- and short-tail axes in *Chi*/+ adults allowed us to quantify this abnormality originally reported by Fisher (22).

A significantly less acute angle of the *Chi*/+ larvae fin fold compared with WT was detected. It is interesting to notice that up to 3 dpf *col1a1a*, encoding for the α1 chain of type I collagen, is the only type I collagen coding gene that is expressed in the fin fold (31). Therefore, the change in the angle may either be the consequence of the presence of mutant protein and/or its reduced amount due to possible intracellular retention as discussed in following sections.

Of note, although no size difference could be detected at larval stage in mutant *Chi*/+ compared with WT, as previously reported, a delay of mineralization was detected at the level of 5th ceratobranchial, cleithrum and notochord tip, examples of endochondral, membranous and perichordal bones. Delayed mineralization is another common feature in OI, reported for several OI murine models (47) and is known to affect both membranous and endochondral bones (48).

4PBA administration ameliorated the bone phenotype in *Chi*/+ larvae and adults acting mainly as chemical chaperone

A definitive cure for OI will require the correction of the genetic defect, and although gene therapy approaches are under investigation, the bench to bed transition of such strategies is far in time (49–51). In the last years drug repositioning approach demonstrated to be an elective choice for disease treatment based on economic and timing reasons and it is definitely appealing for rare disorders (10). The identification of curative effect of molecules already approved by FDA will bypass at least some of the more expensive and time consuming phases for drugs development.

The availability of a validated zebrafish model for classical OI motivated our study on this direction.

Based on recent findings, the outcome of OI and of other skeletal disorders associated with misfolded structural proteins partially retained inside the cells is not only due to abnormal extracellular matrix, but also to altered cellular homeostasis. Thus, targeting cellular stress could represent a valid approach to ameliorate the disease phenotype (52–54).

For our study, we treated the OI zebrafish model *Chi*/+ with 4PBA and TUDCA, already approved by the FDA for urea cycle disorders and cholestasis respectively and known to have chaperone activity (11,12). Their administration was facilitated by the fact that they are water soluble molecules.

Only 4PBA significantly improved straightening of the fin fold in mutant larvae and rescued the mineralization delay in *Chi*/+ zebrafish. Although significant values were not always reached, a clear tendency to higher mineralization was detected in 5CB and NC of treated WT and mutant fish. Furthermore, a long-term treatment with 4PBA from 1 dpf to 3.5 mpf resulted in an amelioration of growth, vertebral shape and tail symmetry.

We first evaluated the effect of the drugs at larval stage taking advantage of the small amount of the required drug and the space for husbandry. For the evaluation of drug efficacy, the fin

fold bending characteristic of the *Chi/+* model, most likely associated to the presence of mutant type I collagen, was first determined. The small fin fold phenotype and/or abnormal tail shape is a common feature in various zebrafish models of skeletal diseases caused either by the absence or the presence of mutant structural proteins (44,55,56). The most abundant structural elements in the early fin fold and in the distal region of adult tail are actinotrichia, structures containing both collagen I and collagen II (31). Collagen IX is known to interact with collagen II and to have a role in vascular plexus formation in caudal fins. A mutation in *col9a1* is present in the *persistent plexus* (*prp*) zebrafish mutant. Interestingly, overexpression of *col9a1* in *prp* ameliorates the fin fold phenotype, supporting the idea that also increasing the amount of structurally abnormal protein in extracellular matrix may lead to an amelioration of the phenotype (56). This is reminiscent to what was observed in OI patients and murine models following bisphosphonate treatment, leading to reduced bone turnover and consequently to an increase of collagen I content in the bone matrix.

Type I collagen is the major organic component of bone and its amount is strictly linked to bone mineral density (57). Using TEM analysis in zebrafish larvae and a tail fin regeneration assay in adults we demonstrated that the amelioration of the bone phenotype in *Chi/+* after administration of 4PBA is caused by an increase of collagen secretion associated to a reduction of ER cisternae size due to the chaperone function of the drug. TEM showed a partial rescue of the ER cisternae enlargement, showing a prevalence of normal size cisternae in larvae grown in the presence of 4PBA and picro sirius red staining of the regenerated tail in 4PBA treated mutant fish revealed an increase in collagen amount.

The intracellular collagen folding requires specialized chaperones (i.e. PDI, FKBP65, HSP47) (58) and it seems unlikely that the small 4PBA molecule could mimic such a complex group of proteins. It may be possible that 4PBA interacts with hydrophobic unfolded regions of the triple helix and limits the intracellular aggregation of mutant collagen favoring its secretion and maybe limiting its degradation (59,60). However, we cannot exclude that 4PBA acts intracellularly on non-collagenous proteins whose folding and secretion may be compromised by the flooding of the ER.

Since 4PBA is also known to act as a mild inhibitor of histone deacetylase, such a role was further investigated.

The culture of osteoblasts in the presence of Na-butyrate was reported to increase histone acetylation, to stimulate cell proliferation, and to promote osteoblast maturation by favoring *Runx2* expression (61). The presence of Na-butyrate stimulated alkaline phosphatase activity in murine calvarial organ cultures (62).

To date little *in vivo* data exist that suggest a dose dependency of 4PBA for the inhibition of histone deacetylase and/or its chaperone function. Luo *et al*. demonstrated that intraperitoneal injection of 4PBA 20 mg/kg/day for 4 weeks was enough to attenuate ER stress in a murine model of myocardia hypertrophy, whereas a 100 mg/kg/day was necessary to inhibit histone deacetylases (63). On the other hand, a single injection of 10 mg/Kg was sufficient to protect mice from radiation preserving histone H4 acetylation (64).

Based on existing *in vitro* and *in vivo* data and considering that, at least for some drugs the micromolar doses in zebrafish are comparable to milligrams per kilograms in mice (65), the 4PBA concentration used in our study should not significantly inhibit histone deacetylase activity.

Indeed distinct difference in expression of acetylated histone 3 was not detected at protein level in 11 dpf 4PBA treated larvae as well as in tail extracts from adult treated zebrafish. Similarly, no difference in the transcription of bone markers was detected by qPCR.

The lack of effect following TUDCA administration is not unexpected. The two molecules are chemically different and they can act in different ways, as already reported (66,67). Furthermore, we cannot exclude a yet unknown contribution of 4PBA for bone homeostasis.

In conclusion, we reported a comprehensive investigation of the *Chi/+* zebrafish OI model validating it as a powerful tool for study OI pathophysiology. We identified peculiar phenotypic outcomes that could be easily used as tools to validate the efficiency of molecules in high throughput drug screening tests. 4PBA was demonstrated to be a promising candidate for OI due to its chaperone activity.

Materials and Methods

Husbandry

Wild-type AB (WT) and heterozygous *Chihuahua* (*col1a1a*$^{dc124/+}$, *Chi/+*) zebrafish arise from natural spawning or from *in vitro* fertilization. The mutant *Chi/+*, provided by Professor Shannon Fisher (Dept of Pharmacology & Experimental Therapeutics, Boston University School of Medicine, USA), carries a G2207A mutation in *col1a1a*, causing a p.G736D (G574D) substitution in the α1 chain of type I collagen. Embryos were kept in Petri dishes in fish water ($NaHCO_3$ 1.2 mM, instant ocean 0.1 g/L, $CaSO_4$ 1.4 mM, methylene blue 0.00002% w/v) at 28 °C until 6 day post-fertilization (dpf), then housed in ZebTEC semi-closed recirculation housing systems (Tecniplast) and kept at a constant temperature (27–28 °C), pH (7.5) and conductivity (500 μS) on a 14/10 light/dark cycle. For the experiments stated below larvae and adult fish were anesthetized using a solution of tricaine (3-amino benzoic acidethylester, Sigma Aldrich) 0.0016% w/v, in fish water and sacrificed by tricaine overdose (0.03% w/v). All experiments were performed in accordance with the approved guidelines, in agreement with EU Directive 2010/63/EU for animals. The experimental protocol was approved by the Italian Ministry of Health (Approval Animal Protocol No. 1/2013).

Genotyping

Depending on the experiment type, DNA was extracted from single embryos, pool of embryos or caudal fin biopsies from adult zebrafish. Tissues were lysed in Tris–HCl 100 mM, pH 8.5, EDTA 5 mM, SDS 0.2% w/v, NaCl 200 mM and proteinase K (Sigma Aldrich) 2.5 mg/ml, for at least 3 h at 55 °C. DNA was precipitated with isopropanol and dissolved in Tris–HCl 20 mM, EDTA 1 mM, pH 8.0. The *Chi/+* genotype was evaluated by PCR amplification of *col1a1a* (NC_007114.6) followed by restriction enzyme digestion. The following primers were used: sense 5'-TCTTAAGGGT GACAGAGTGAGTATGAC-3' (23101253–23101279) and reverse 5'-CAACTTCAAGATGTTTCATCACTTAGTATG-3' (23101543–2310 1514). Since the mutation creates a novel BtsCI restriction site, the amplicon was digested with this enzyme (New England Biolabs) and the products separated on 2% agarose gel. A single 290 bp band revealed the presence of the WT allele, while the mutant allele generated 141 and 149 bp fragments.

Morphometric evaluation

Zebrafish were anesthetized with tricaine and images were acquired with a Leica M165 FC microscope (Leica) connected to a

Leica DFC425 C digital camera (Leica). Measurements were performed using the Leica LAS v4.5 software (Leica).

The fin fold angle was measured on dorsal images of 11 dpf zebrafish as the angle between the notochord axis and the line connecting the posterior tip of the notochord and the terminal end of the fin (Fig. 1A).

Using lateral images of embryos and adult fish the following parameters were measured: SL, defined as the distance from the snout to the caudal peduncle or, in pre-flexion larvae that do not have a caudal peduncle, to the posterior tip of the notochord; HAA, defined as the distance from ventral to dorsal, measured immediately anteriorly to the anal fin and perpendicularly to the axis defined by SL; Snout-Operculum Length (SOL), defined as the distance from snout to the most posterior point of operculum; height at eye (HE), defined as the distance from ventral to dorsal, measured immediately posteriorly to the eye and perpendicularly to the axis defined by SL (68) (Fig. 1A). The symmetry of the tail was evaluated as the ratio between the mean of the two major axes (defined as the distance between the central part of the caudal peduncle and the tip of each caudal lobe) and the minor axis (the distance between the central part of the caudal peduncle and the conjunction point of the two caudal lobes) of the tail (Fig. 1A and C).

The shape and the size of vertebrae were evaluated on images of adult fish stained with alcian blue and alizarin red acquired on lateral orientation. For the dimension, the major and the minor axis of each vertebra were defined respectively as the mean of the length measured dorsally and ventrally and as the mean of the height measured anteriorly and posteriorly to the vertebral centrum (Fig. 1E, ii). The slope of the neural spine is measured as the angle between the major axis and the line connecting the edge of the spine with the most anterodorsal region of the centrum (Fig. 1E, ii). The first 10 vertebrae articulated with the ribs were considered.

Growth curve determination

WT and *Chi*/+ zebrafish were collected from *in vitro* fertilization and genotyped at 6 dpf based on the caudal fin fold curvature. Lateral images of each fish were acquired every week from 11 until 137 dpf and at 280 dpf. SL was measured as described above.

X-ray

X-rays of adult 3.5 months old fish were acquired with a Faxitron Mx-20 (Faxitron), using 25 kV for 10 s. The Kodak DirectView Elite CR System and k-Pacs software (Kodak) were used.

μCT

WT and *Chi*/+ zebrafish at 3 ($n = 5$ and 6, respectively) and 10 mpf ($n = 5$ for both genotype) were sacrificed, fixed overnight at 4 °C in paraformaldehyde (PFA) 4% (w/v) and stored in ethanol 75% v/v. For μCT fish were placed in a radiotranslucent sample-holder, foam pads were applied to prevent shifting during the scan process and the specimens were scanned with a μCT 40 desktop cone-beam μCT (Scanco Medical) using a voxel size of 10 μm with 1000 projections per slice at a tube energy of 55 kV with an intensity of 145 μA. Reconstructed slices were segmented using the script 'UCT_EVALUATIONV6' of the Scanco MicroCT software suite with the following parameters: sigma = 0.8; support = 1; lower = 165–185; upper = 1000; unit = 6. The lower threshold was varied between 165 and 185 to provide the optimal signal/noise ratio for each sample. Three-dimensional reconstructions were imaged using the program μCT Ray V3.8 of the Scanco MicroCT software suite.

Skeletal staining

Cartilage and bone were stained with alcian blue and alizarin red using a protocol modified from Walker *et al.* (69). Both larval and adult WT and *Chi*/+ zebrafish were sacrificed and fixed overnight in PFA 4% w/v in PBS (Sigma Aldrich) with $CaCl_2$ 0.9 mM and $MgCl_2$ 0.49 mM, pH 7.4 at 4 °C. Scales and internal organs were manually removed from adults, and fat was eliminated by an overnight bath in acetone. Embryos and adult fish were stained overnight at room temperature (RT) with a solution of alcian blue 8GX (Sigma Aldrich) 0.02% w/v, ethanol 70% v/v, $MgCl_2$ 80 mM and then rehydrated in a series of ethanol (80, 50, 25%), in Tris–HCl 100 mM, pH 7.5, $MgCl_2$ 10 mM, 5 min each. Bleaching to eliminate the pigmentation was performed with H_2O_2 3% v/v, KOH 0.5% w/v at RT and followed by two washes in glycerol 25% v/v, KOH 0.1% w/v. Soft tissues were digested with 1 mg/ml (for larvae) or 10 mg/ml (for adult fish) trypsin dissolved in a 30% v/v, solution of saturated $B_4Na_2O_7$ for a time depending on fish size. After the staining in alizarin red S (Sigma Aldrich) 0.01% w/v, glycerol 25% v/v, Tris–HCl 100 mM, pH 7.5 overnight at RT, fish were washed in increasing glycerol/KOH 0.1% series (50%, 80%) and finally stored at 4 °C in glycerol 100%, KOH 0.1%. Images were acquired using a Leica M165 FC microscope connected to a Leica DFC425 C digital camera. The mineralization of the 5th ceratobranchial, the notochord and the cleithrum was evaluated. Three operators blinded to the genotype of the fish qualitatively described the level of ossification of these bones for each embryo as beginning/no ossification, intermediate ossification or complete ossification independently.

Calcein ($C_{30}H_{26}N_2O_{13}$, Sigma Aldrich) was used as vital dye to stain calcified bones. WT and *Chi*/+ 5 dpf zebrafish were transferred to a physiologic solution (NaCl 0.9% w/v, pH 7.5) containing calcein 0.2% w/v for 20 min, washed with fish water until water was clean and kept in clear water overnight. The day after animals were anesthetized with tricaine and mounted in methylcellulose (Sigma Aldrich) 3% w/v. Fish images were acquired as previously described using a GFP filter. Three operators blinded to the genotype of the fish evaluated the ossification of the centra independently.

Type I collagen analysis

Bones (vertebrae, ribs and head bones), scales and skin were dissected from adult mutant and WT fish following sacrifice. The tissues were defatted for 6 h in NaOH 0.1 N at 4 °C. The scales and bones were decalcified for 48 h in EDTA 0.5 M pH 7.4 at 4 °C. The acid-soluble type I collagen (ASC) was obtained by protein extraction in acetic acid 0.5 M at 4 °C for 48 h. The ASC was then precipitated by NaCl 0.9 M in acetic acid 0.5 M. The pepsin-soluble fraction (PSC) was obtained by further digestion of the pellet obtained from the acetic acid extraction with pepsin 0.1 mg/ml in acetic acid 0.5 M at 4 °C for 48 h. The PSC was precipitated by NaCl 0.9 M in acetic acid 0.5 M overnight at 4 °C. Both ACS and PSC fractions were quantified by measuring the 4-hydroxyproline amount after acid hydrolysis. The purified collagen was analyzed on 6% polyacrylamide gel electrophoresis (SDS-PAGE) in the presence of urea 0.5 M. The gels were

stained overnight with picric acid 0.08 M, Coomassie Brilliant Blue R250 (Sigma Aldrich) 0.04% w/v destained in tap water and acquired with Versadoc3000 (BIO-RAD).

Differential scanning calorimetry

DSC thermograms of collagen solutions in HCl 2 mM, pH 2.7 were recorded in an N-DSC III differential scanning calorimeter (Calorimetry Sciences Corporation) at 0.25 °C/min heating rate.

Transmission electron microscopy

Following anesthesia in 0.0016% tricaine the caudal fin biopsies were obtained from adult WT and *Chi*/+ fish and rapidly transferred in Karnowsky fixative (sodium cacodylate 0.1 M, pH 7.8, glutaraldehyde 1.5% v/v, paraformaldehyde 4% w/v) overnight at 4 °C. Samples were then decalcified in EDTA 14% w/v pH 7.1 at 4 °C, for 24 h for *Chi*/+ and 48 h for WT. *Chi*/+11 dpf embryos treated with placebo or 4PBA were sacrificed with 0.03% tricaine and fixed with Karnowsky fixative overnight at 4 °C. The samples were then post-fixed in OsO_4 2% w/v in H_2O for 2 h at RT, rinsed in distilled water and dehydrated in ethanol. The specimens were infiltrated with LR White acrylic resin overnight at 4 °C and polymerized in gelatin capsules at 60 °C for 24 h. Thin sections (60–70 nm thick) were cut on a Reichert OM-U3 ultramicrotome with a diamond blade and collected on 300-mesh nickel grids. The grids were finally stained with saturated acqueous uranyl acetate followed by lead citrate and observed with a Zeiss EM900 electron microscope, operated at 80 kV with an objective aperture of 30 μm.

Confocal analysis of embryos

The ER-YFP vector (by courtesy of Yung-Yao Lin of the Wellcome Trust Sanger Institute, Hinxton, Cambridge, UK) which encodes a fluorescent fusion protein carrying calreticulin ER targeting and lysine–aspartate–glutamate–leucine retrieval sequences was used to analyze ER morphology (70). The mRNA was *in vitro* transcribed from the linearized construct using the mMACHINE mMESSAGE kit (Ambion) according to the supplier's instructions. The RNA integrity was verified on denaturing 1% agarose gel and the RNA clean-up and concentration was performed using the RNeasy MiniElute Cleanup kit (QIAGEN). The ER-YFP RNA was microinjected into embryos at the stage of 2–4 cells, using 300 pg of RNA and dextran conjugated with Alexa 647 (Molecular Probes) 0.05% w/v as tracer in a total volume of 4 nL for each injection. Microinjection was carried out using an InjectMan micromanipulator (Eppendorf) assembled on a Leica M165 FC stereomicroscope. At 24 hpf, the chorion was manually removed and the embryos fixed in PFA 4% w/v overnight at 4 °C. The samples were permeabilized with PBS containing Triton X-100 (BDH Chemicals) 0.1% v/v, in ice for 10 min, and stained with 4',6-diamidino-2-phenylindole (DAPI, Sigma Aldrich) 100 ng/ml for 30 min. The embryos were cut in half: the tail was mounted on a cover slip in 30 μL of 1% low melting agarose at 60 °C to be analyzed at confocal microscopy (TCS SP2-Leica), while the head was used for genotyping. The fluorescence intensity was qualitatively evaluated by three independent operators blinded to the fish genotype. The results were expressed as percentage of fish with brighter signal.

Picro sirius red collagen staining

The caudal fin of adult *Chi*/+ zebrafish was cut and either treated with 4PBA ($n = 4$), or TUDCA ($n = 4$) or with placebo ($n = 3$ for 4PBA experiment, $n = 4$ for TUDCA experiment) for 7 days. Then, the regrown caudal fins were cut again and fixed overnight in PFA 4% w/v in PBS. Tails were stained 1 h in Sirius Red 0.1% w/v (Direct Red 80, Sigma Aldrich) in saturated aqueous solution of picric acid (Sigma Aldrich). After the staining tails were washed in acetic acid 0.5% v/v, and directly dehydrated three times in absolute ethanol. Samples were clarified with xylene and mounted with DPX (Sigma Aldrich). Slides were observed under polarized light with the LEICA DM2500 microscope (Leica) and acquired using the LEICA ICC50 W digital camera (Leica). The analysis of the total and the green area were performed using Leica LAS4.5 software.

Whole mount immunostaining

4PBA treated (WT $n = 26$, *Chi*/+ $n = 24$) and untreated (WT $n = 36$, *Chi*/+ $n = 38$) zebrafish embryos were collected at 5 dpf, fixed overnight in PFA 4% w/v in PBS., washed in PBS and permeabilized overnight in methanol at −20 °C. Samples were hydrated with ethanol (100, 80, 70, 50, 0%) in PBS and digested with proteinase K 0.1% w/v in PBS at 25 °C for 15 min and hyaluronidase 2% w/v in PBS at 25 °C for 20 min. Embryos were fixed in PFA 4% for 30 min and PFA was eliminated by incubating samples with NH_4Cl 50 mM in PBS, for 1 h at RT. To block endogenous peroxidase activity embryos were incubated with bovine serum albumin (BSA, Sigma Aldrich) 0.5% w/v and H_2O_2 0.5% v/v, for 30 min at RT. After a 5 min wash with PBS, Tween-20 0.05% v/v (Sigma Aldrich) (PBS-T), blocking solution (BSA 5% w/v in PBS-T) was added for 2 h at RT. Hsp47b affinity purified antibody (1:1000 in 5% BSA/PBS-T) and anti-rabbit secondary antibody (1:200 in 1% BSA/PBS-T) were used. DAB substrate (Thermo Scientific) was finally added until appearance of the staining. Fish were incubated in increasing glycerol series (50%, 80%) and finally stored at 4 °C in glycerol 100%. Images were acquired using a Leica M165 FC microscope connected to a Leica DFC425 C digital camera. Three operators blinded to the genotype and the treatment of the fish evaluated presence or absence of the signal independently.

Drug toxicity test

Toxicity tests were performed to determine the relevant drug dosage. WT embryos (10 per group) were manually dechorionated at 24 hpf and treated from 1 to 7 dpf with different concentrations of the drug dissolved in fish water (0.05, 0.1, 0.5, 1, 5 and 10 mM for 4PBA (Sigma Aldrich), and 0.05, 0.1, 0.2, 0.5 and 1 mM for TUDCA (Sigma Aldrich) or with placebo in 96-well plates, using 200 μl per fish. Half of the volume was replaced with fresh solution every day. The number of surviving and the number of misshaped zebrafish were evaluated at the end of the treatment, in order to define the highest concentration without visible side effects.

Drug treatment

WT and *Chi*/+ embryos were obtained by *in vitro* fertilization, manually dechorionated at 24 hpf, and grown in 96-well plates (1 fish per well). 200 μl/embryo water per embryo with or without 4PBA 0.05 mM or TUDCA 0.5 mM were added starting from 1 dpf to 11 dpf. Half of the volume was replaced with fresh

solution every day. At 11 dpf fish were anesthetized with tricaine and lateral images were acquired using a Leica M165 FC microscope connected to a Leica DFC425 C digital camera. The caudal fin fold angle was evaluated, as described above, and used for genotyping. The fish collection mode varied based on the different experiments as detailed below.

For the long-term treatment, 4PBA was dissolved in water as described above for embryo treatment, and then larvae were transferred into tanks filled with 200 ml system water. Half of the volume was replaced every day with fresh solution, and fish were fed as described. The animals were sacrificed at 3.5 months. Digital images and X-ray were acquired. Then the fish were fixed in 4% PFA w/v in PBS for alcian blue and alizarin red staining. Morphometric analysis and mineralization level of 5th ceratobranchyal, cleithrum and notochord were performed as described above.

Western blot

4PBA treated or untreated mutant and WT 11 dpf embryos (4 for each genotype and treatment) were pooled and proteins were extracted using 20 μl of RIPA buffer (Tris–HCl 10 mM, pH 7.6, EDTA 5 mM, pH 8.0, NaCl 140 mM, NP40 0.5% v/v) added with protease inhibitors (EDTA 1.52 mg/ml, benzamidine 1.57 mg/ml, N-etilmaleimide 0.25 mg/ml, phenylmethylosulfonylfluoride 1 mM). 3.5 mpf WT and *Chi*/+ 4PBA treated and untreated fish caudal tails were cut, lysed in 100 μl/tail RIPA buffer containing protease inhibitor and sonicated 5 times for 10 s. Samples were centrifuged at 17 000*g* for 30 min, at 4 °C to remove cellular debris.

Proteins from two embryos or one tail were dissolved in Laemmli buffer with dithiothreitol 100 mM, denaturated for 10 min at 90 °C, separated in SDS-PAGE on a 15% polyacrylamide gel and transferred to a PVDF (GE Healthcare) membrane. Membrane was blocked with BSA 5% w/v in PBS with Tween-20 0.05% v/v (Sigma Aldrich) (T-TBS) and incubated with primary polyclonal Acetyl-Histone H3 (Lys9) antibody (Thermo scientific, J.942.2) diluted 1:1000 in BSA 5% w/v in T-TBS or with primary polyclonal actin antibody (1–19) (Santa Cruz Biotechnology, sc-1616) diluted 1:1000 in 2% w/v BSA in TBS-T overnight at 4 °C. Donkey anti-rabbit IgG-HRP antibody (Santa Cruz Biotechnology, sc-2077) or donkey anti-goat IgG-HRP antibody (Santa Cruz Biotechnology, sc-2020) were used as secondary antibodies both diluted 1:10 000 in BSA 2% w/v in TBS-T, 1 h at RT. ECL Prime Western Blotting Detection Reagent (GE Healthcare) was used for signal detection, membranes were acquired with Image Quant LAS4000 (GE Healthcare) and analysed using Image Quant TL (GE Healthcare) software.

qPCR

4PBA treated or untreated mutant and WT 11 dpf embryos were pooled ($n = 20$ for each group, 3 groups for each genotype and treatment) and RNA was extracted with Qiazol (Qiagen) following manufacturer's instructions. RNA quantity was determined with NanoDrop spectrophotometer and RNA quality by agarose gel electrophoresis. cDNA was synthesized from 1 μg of RNA using the High Capacity cDNA Transcription kit (Applied Biosystems) according to the manufacturer's protocol in a final volume of 20 μL.

qPCR was performed in 25 μL with SYBR Select Master Mix (Applied Biosystems) using the Mx3000P thermocycler (Stratagene) and the MxPro software (Stratagene). The following primers were used: for *col1a1a* (NM_199214.1) 5'-GAGT GATGGGTGCTATTGG-3' (1748–1766) and 5'-GGAATCCTCTG TCACCTCTA-3' (1996–1977); for *bglap* (NM_001083857.3) 5'-TG ACGTGGCCTCTATCATCA-3' (163–182) and 5'-TTTATAGGCGG CGATGATTC-3' (316–297); for *sp7* (NM_212863.2) 5'-GCTCCAA TCTTCACAGCACA-3' (944–963) and 5'-GCTGTGGACAGGTTTCTT CC-3' (1166–1147); for *actb1* (NM_131031.1) 5'-GAAGGAGATCACC TCTCTTGCTC-3' (995–1017) and 5'-GTTCTGTTTAGAAGCACTTC CTGTG-3' (1188–1164). The annealing temperature was 58 °C for *bglap* and *sp7* amplification and 60 °C for *col1a1a*. ΔΔCt method was used to compare gene expression in the different samples.

Statistical analysis

All values are expressed as mean ± standard deviation. The WT and *Chi*/+ comparisons were performed applying unpaired parametric or non-parametric *t* test. Mineralization was evaluated by three independent blinded operators and defined in specific classes (beginning/no mineralization, incomplete mineralization, complete mineralization). Categorical variables were summarized by percentage. Differences in mineralization between treatments and genotypes were evaluated with Chi-squared test. For statistic significance, P value <0.05 was considered. All the analyses were performed using STATA 12®.

Supplementary Material

Supplementary Material is available at *HMG* online.

Acknowledgements

We thank Dr Patrizia Vaghi, Centro Grandi Strumenti, University of Pavia, Italy, for technical assistance with confocal microscopy and the animal facility 'Centro di servizio per la gestione unificata delle attività di stabulazione e di radiobiologia' of the University of Pavia.

Conflict of Interest statement. None declared.

Funding

The work was supported by Fondazione Cariplo (grant No. 2013-0612), Telethon (grant No. GGP13098) and the European Community, FP7, 'Sybil' project (grant No. 602300). Funding to pay the Open Access publication charges for this article was provided by Fondazione Telethon.

References

1. Forlino, A., Cabral, W.A., Barnes, A.M. and Marini, J.C. (2011) New perspectives on osteogenesis imperfecta. *Nat. Rev. Endocrinol.*, **7**, 540–557.
2. Forlino, A. and Marini, J.C. (2016) Osteogenesis imperfecta. *Lancet*, **387**, 1657–1671.
3. Forlino, A., Tani, C., Rossi, A., Lupi, A., Campari, E., Gualeni, B., Bianchi, L., Armini, A., Cetta, G., Bini, L. *et al.* (2007) Differential expression of both extracellular and intracellular proteins is involved in the lethal or nonlethal phenotypic variation of BrtlIV, a murine model for osteogenesis imperfecta. *Proteomics*, **7**, 1877–1891.
4. Mertz, E.L., Makareeva, E., Mirigian, L.S., Koon, K.Y., Perosky, J.E., Kozloff, K.M. and Leikin, S. (2016) Makings of a brittle bone: unexpected lessons from a low protein diet study of a mouse OI model. *Matrix. Biol.*, **52–54**, 29–42.
5. Bianchi, L., Gagliardi, A., Gioia, R., Besio, R., Tani, C., Landi, C., Cipriano, M., Gimigliano, A., Rossi, A., Marini, J.C. *et al.*

(2012) Differential response to intracellular stress in the skin from osteogenesis imperfecta Brtl mice with lethal and non lethal phenotype: a proteomic approach. *J. Proteomics*, **75**, 4717–4733.
6. Forlino, A., Porter, F.D., Lee, E.J., Westphal, H. and Marini, J.C. (1999) Use of the Cre/lox recombination system to develop a non-lethal knock-in murine model for osteogenesis imperfecta with an alpha1(I) G349C substitution. Variability in phenotype in BrtlIV mice. *J. Biol. Chem.*, **274**, 37923–37931.
7. Bianchi, L., Gagliardi, A., Maruelli, S., Besio, R., Landi, C., Gioia, R., Kozloff, K.M., Khoury, B.M., Coucke, P.J., Symoens, S. *et al.* (2015) Altered cytoskeletal organization characterized lethal but not surviving Brtl+/- mice: insight on phenotypic variability in osteogenesis imperfecta. *Hum. Mol. Genet.*, **24**, 6118–6133.
8. Daley, E., Streeten, E.A., Sorkin, J.D., Kuznetsova, N., Shapses, S.A., Carleton, S.M., Shuldiner, A.R., Marini, J.C., Phillips, C.L., Goldstein, S.A. *et al.* (2010) Variable bone fragility associated with an Amish COL1A2 variant and a knock-in mouse model. *J. Bone Miner. Res.*, **25**, 247–261.
9. Mirigian, L.S., Makareeva, E., Mertz, E.L., Omari, S., Roberts-Pilgrim, A.M., Oestreich, A.K., Phillips, C.L. and Leikin, S. (2016) Osteoblast malfunction caused by cell stress response to procollagen misfolding in alpha2(I)-G610C mouse model of osteogenesis imperfecta. *J. Bone Miner. Res.*, **31**, 1608–1616.
10. Nosengo, N. (2016) Can you teach old drugs new tricks? *Nature*, **534**, 314–316.
11. Matoori, S. and Leroux, J.C. (2015) Recent advances in the treatment of hyperammonemia. *Adv. Drug. Deliv. Rev.*, **90**, 55–68.
12. Wagner, M. and Trauner, M. (2016) Recent advances in understanding and managing cholestasis. [version 1; referees 2 approved] *F1000Res*, **5**, 705.
13. Iannitti, T. and Palmieri, B. (2011) Clinical and experimental applications of sodium phenylbutyrate. *Drugs R D*, **11**, 227–249.
14. Fass, D.M., Shah, R., Ghosh, B., Hennig, K., Norton, S., Zhao, W.N., Reis, S.A., Klein, P.S., Mazitschek, R., Maglathlin, R.L. *et al.* (2010) Effect of inhibiting histone deacetylase with short-chain carboxylic acids and their hydroxamic acid analogs on vertebrate development and neuronal chromatin. *ACS Med. Chem. Lett.*, **2**, 39–42.
15. Vang, S., Longley, K., Steer, C.J. and Low, W.C. (2014) The unexpected uses of urso- and tauroursodeoxycholic acid in the treatment of non-liver diseases. *Glob. Adv. Health Med.*, **3**, 58–69.
16. MacRae, C.A. and Peterson, R.T. (2015) Zebrafish as tools for drug discovery. *Nat. Rev. Drug Discov.*, **14**, 721–731.
17. Howe, K., Clark, M.D., Torroja, C.F., Torrance, J., Berthelot, C., Muffato, M., Collins, J.E., Humphray, S., McLaren, K., Matthews, L. *et al.* (2013) The zebrafish reference genome sequence and its relationship to the human genome. *Nature*, **496**, 498–503.
18. Flicek, P., Amode, M.R., Barrell, D., Beal, K., Billis, K., Brent, S., Carvalho-Silva, D., Clapham, P., Coates, G., Fitzgerald, S. *et al.* (2014) Ensembl 2014. *Nucleic Acids Res.*, **42**, D749–D755.
19. Moro, E., Vettori, A., Porazzi, P., Schiavone, M., Rampazzo, E., Casari, A., Ek, O., Facchinello, N., Astone, M., Zancan, I. *et al.* (2013) Generation and application of signaling pathway reporter lines in zebrafish. *Mol. Genet. Genomics*, **288**, 231–242.
20. Blum, M., De Robertis, E.M., Wallingford, J.B. and Niehrs, C. (2015) Morpholinos: antisense and Sensibility. *Dev. Cell*, **35**, 145–149.
21. Gonzales, A.P. and Yeh, J.R. (2014) Cas9-based genome editing in zebrafish. *Methods Enzymol.*, **546**, 377–413.
22. Fisher, S., Jagadeeswaran, P. and Halpern, M.E. (2003) Radiographic analysis of zebrafish skeletal defects. *Dev. Biol.*, **264**, 64–76.
23. Braasch, I., Gehrke, A.R., Smith, J.J., Kawasaki, K., Manousaki, T., Pasquier, J., Amores, A., Desvignes, T., Batzel, P., Catchen, J. *et al.* (2016) The spotted gar genome illuminates vertebrate evolution and facilitates human-teleost comparisons. *Nat. Genet.*, **48**, 427–437.
24. Li, N., Felber, K., Elks, P., Croucher, P. and Roehl, H.H. (2009) Tracking gene expression during zebrafish osteoblast differentiation. *Dev. Dyn.*, **238**, 459–466.
25. Weigele, J. and Franz-Odendaal, T.A. (2016) Functional bone histology of zebrafish reveals two types of endochondral ossification, different types of osteoblast clusters and a new bone type. *J. Anat.*, **229**, 92–103.
26. Garbes, L., Kim, K., Riess, A., Hoyer-Kuhn, H., Beleggia, F., Bevot, A., Kim, M.J., Huh, Y.H., Kweon, H.S., Savarirayan, R. *et al.* (2015) Mutations in SEC24D, encoding a component of the COPII machinery, cause a syndromic form of osteogenesis imperfecta. *Am. J. Hum. Genet.*, **96**, 432–439.
27. Kamoun-Goldrat, A.S. and Le Merrer, M.F. (2007) Animal models of osteogenesis imperfecta and related syndromes. *J. Bone Miner. Metab.*, **25**, 211–218.
28. Gistelinck, C., Eckhard Witten, P., Huysseune, A., Symoens, S., Malfait, F., Larionova, D., Simoens, P., Dierick, M., Van Hoorebeke, L., D., Paepe, A. *et al.* (2016) Loss of type I collagen telopeptide lysyl hydroxylation causes musculoskeletal abnormalities in a Zebrafish model of Bruck syndrome. *J. Bone Miner. Res.*, **31**, 1930.
29. Cho, S.Y., Asharani, P.V., Kim, O.H., Iida, A., Miyake, N., Matsumoto, N., Nishimura, G., Ki, C.S., Hong, G., Kim, S.J. *et al.* (2015) Identification and in vivo functional characterization of novel compound heterozygous BMP1 variants in osteogenesis imperfecta. *Hum. Mutat.*, **36**, 191–195.
30. Fleming, A., Sato, M. and Goldsmith, P. (2005) High-throughput in vivo screening for bone anabolic compounds with zebrafish. *J. Biomol. Screen*, **10**, 823–831.
31. Duran, I., Mari-Beffa, M., Santamaria, J.A., Becerra, J. and Santos-Ruiz, L. (2011) Actinotrichia collagens and their role in fin formation. *Dev. Biol.*, **354**, 160–172.
32. Gistelinck, C., Gioia, R., Gagliardi, A., Tonelli, F., Marchese, L., Bianchi, L., Landi, C., Bini, L., Huysseune, A., Witten, P.E. *et al.* (2016) Zebrafish collagen type I: molecular and biochemical characterization of the major structural protein in bone and skin. *Sci. Rep.*, **6**, 21540.
33. Ito, S. and Nagata, K. (2017) Biology of Hsp47 (Serpin H1), a collagen-specific molecular chaperone. *Semin. Cell. Dev. Biol*, **62**, 142–151.
34. Ishikawa, Y., Ito, S., Nagata, K., Sakai, L.Y. and Bachinger, H.P. (2016) Intracellular mechanisms of molecular recognition and sorting for transport of large extracellular matrix molecules. *Proc. Natl. Acad. Sci. U.S.A.*, **113**, E6036–E6044.
35. Lisse, T.S., Thiele, F., Fuchs, H., Hans, W., Przemeck, G.K., Abe, K., Rathkolb, B., Quintanilla-Martinez, L., Hoelzlwimmer, G., Helfrich, M. *et al.* (2008) ER stress-mediated apoptosis in a new mouse model of osteogenesis imperfecta. *PLoS Genet.*, **4**, e7.
36. Chen, F., Guo, R., Itoh, S., Moreno, L., Rosenthal, E., Zappitelli, T., Zirngibl, R.A., Flenniken, A., Cole, W., Grynpas, M. *et al.* (2014) First mouse model for combined osteogenesis imperfecta and Ehlers-Danlos syndrome. *J. Bone Miner. Res.*, **29**, 1412–1423.
37. Marlowe, A., Pepin, M.G. and Byers, P.H. (2002) Testing for osteogenesis imperfecta in cases of suspected non-accidental injury. *J. Med. Genet.*, **39**, 382–386.

38. Makareeva, E., Mertz, E.L., Kuznetsova, N.V., Sutter, M.B., DeRidder, A.M., Cabral, W.A., Barnes, A.M., McBride, D.J., Marini, J.C. and Leikin, S. (2008) Structural heterogeneity of type I collagen triple helix and its role in osteogenesis imperfecta. *J. Biol. Chem.*, **283**, 4787–4798.
39. Morvan-Dubois, G., Le Guellec, D., Garrone, R., Zylberberg, L. and Bonnaud, L. (2003) Phylogenetic analysis of vertebrate fibrillar collagen locates the position of zebrafish alpha3(I) and suggests an evolutionary link between collagen alpha chains and hox clusters. *J. Mol. Evol.*, **57**, 501–514.
40. Forlino, A., Kuznetsova, N.V., Marini, J.C. and Leikin, S. (2007) Selective retention and degradation of molecules with a single mutant alpha1(I) chain in the Brtl IV mouse model of OI. *Matrix Biol.*, **26**, 604–614.
41. Gioia, R., Panaroni, C., Besio, R., Palladini, G., Merlini, G., Giansanti, V., Scovassi, I.A., Villani, S., Villa, I., Villa, A. *et al.* (2012) Impaired osteoblastogenesis in a murine model of dominant osteogenesis imperfecta: a new target for osteogenesis imperfecta pharmacological therapy. *Stem Cells*, **30**, 1465–1476.
42. Gorman, K.F. and Breden, F. (2007) Teleosts as models for human vertebral stability and deformity. *Comp. Biochem. Physiol. C Toxicol. Pharmacol.*, **145**, 28–38.
43. Fleming, A., Keynes, R. and Tannahill, D. (2004) A central role for the notochord in vertebral patterning. *Development*, **131**, 873–880.
44. Duran, I., Csukasi, F., Taylor, S.P., Krakow, D., Becerra, J., Bombarely, A. and Mari-Beffa, M. (2015) Collagen duplicate genes of bone and cartilage participate during regeneration of zebrafish fin skeleton. *Gene Expr. Patterns*, **19**, 60–69.
45. Wood, A. (1982) Early pectoral fin development and morphogenesis of the apical ectodermal ridge in the killifish, Aphyosemion scheeli. *Anat. Rec.*, **204**, 349–356.
46. Wood, A. and Thorogood, P. (1984) An analysis of in vivo cell migration during teleost fin morphogenesis. *J. Cell. Sci.*, **66**, 205–222.
47. Kozloff, K.M., Carden, A., Bergwitz, C., Forlino, A., Uveges, T.E., Morris, M.D., Marini, J.C. and Goldstein, S.A. (2004) Brittle IV mouse model for osteogenesis imperfecta IV demonstrates postpubertal adaptations to improve whole bone strength. *J. Bone Miner. Res.*, **19**, 614–622.
48. Shapiro, J.R., Byers, P.H., Glorieux, F.H. and Sponseller, P.D. (2013) *Osteogenesis Imperfecta. A Translational Approach to Brittle Bone Disease*. Elsevier, The Netherlands.
49. Besio, R. and Forlino, A. (2015) New frontiers for dominant osteogenesis imperfecta treatment: gene/cellular therapy approaches. *Adv Regenerative Biol.*, **2**, 27964.
50. Rousseau, J., Gioia, R., Layrolle, P., Lieubeau, B., Heymann, D., Rossi, A., Marini, J.C., Trichet, V. and Forlino, A. (2014) Allele-specific Col1a1 silencing reduces mutant collagen in fibroblasts from Brtl mouse, a model for classical osteogenesis imperfecta. *Eur. J. Hum. Genet.*, **22**, 667–674.
51. Lindahl, K., Kindmark, A., Laxman, N., Astrom, E., Rubin, C.J. and Ljunggren, O. (2013) Allele dependent silencing of collagen type I using small interfering RNAs targeting 3'UTR Indels - a novel therapeutic approach in osteogenesis imperfecta. *Int. J. Med. Sci.*, **10**, 1333–1343.
52. Boot-Handford, R.P. and Briggs, M.D. (2010) The unfolded protein response and its relevance to connective tissue diseases. *Cell. Tissue Res.*, **339**, 197–211.
53. Makareeva, E., Aviles, N.A. and Leikin, S. (2011) Chaperoning osteogenesis: new protein-folding disease paradigms. *Trends Cell. Biol.*, **21**, 168–176.
54. Briggs, M.D., Bell, P.A., Wright, M.J. and Pirog, K.A. (2015) New therapeutic targets in rare genetic skeletal diseases. *Expert. Opin. Orphan. Drugs*, **3**, 1137–1154.
55. Gray, R.S., Wilm, T.P., Smith, J., Bagnat, M., Dale, R.M., Topczewski, J., Johnson, S.L. and Solnica-Krezel, L. (2014) Loss of col8a1a function during zebrafish embryogenesis results in congenital vertebral malformations. *Dev. Biol.*, **386**, 72–85.
56. Huang, C.C., Wang, T.C., Lin, B.H., Wang, Y.W., Johnson, S.L. and Yu, J. (2009) Collagen IX is required for the integrity of collagen II fibrils and the regulation of vascular plexus formation in zebrafish caudal fins. *Dev. Biol.*, **332**, 360–370.
57. Shen, B., Mu, J.X. and Pei, F.X. (2007) Relationship among bone mineral density, collagen composition, and biomechanical properties of callus in the healing of osteoporotic fracture. *Chin. J. Traumatol.*, **10**, 360–365.
58. Ishikawa, Y. and Bachinger, H.P. (2013) A molecular ensemble in the rER for procollagen maturation. *Biochim. Biophys. Acta*, **1833**, 2479–2491.
59. Ishida, Y. and Nagata, K. (2009) Autophagy eliminates a specific species of misfolded procollagen and plays a protective role in cell survival against ER stress. *Autophagy*, **5**, 1217–1219.
60. Ishida, Y., Yamamoto, A., Kitamura, A., Lamande, S.R., Yoshimori, T., Bateman, J.F., Kubota, H. and Nagata, K. (2009) Autophagic elimination of misfolded procollagen aggregates in the endoplasmic reticulum as a means of cell protection. *Mol. Biol. Cell*, **20**, 2744–2754.
61. Lee, H.W., Suh, J.H., Kim, A.Y., Lee, Y.S., Park, S.Y. and Kim, J.B. (2006) Histone deacetylase 1-mediated histone modification regulates osteoblast differentiation. *Mol. Endocrinol.*, **20**, 2432–2443.
62. Schroeder, T.M. and Westendorf, J.J. (2005) Histone deacetylase inhibitors promote osteoblast maturation. *J. Bone Miner. Res.*, **20**, 2254–2263.
63. Luo, T., Chen, B. and Wang, X. (2015) 4-PBA prevents pressure overload-induced myocardial hypertrophy and interstitial fibrosis by attenuating endoplasmic reticulum stress. *Chem. Biol. Interact.*, **242**, 99–106.
64. Coulon, S.M., Miller, A.C., Reed, J.M. and Martin, C.K. (2012) Reliability of a common solution-based taste perception test: implications for validity and a briefer test. *Eat Behav.*, **13**, 42–45.
65. Trendowski, M., Wong, V., Wellington, K., Hatfield, S. and Fondy, T.P. (2014) Tolerated doses in zebrafish of cytochalasins and jasplakinolide for comparison with tolerated doses in mice in the evaluation of pre-clinical activity of microfilament-directed agents in tumor model systems in vivo. *In Vivo*, **28**, 1021–1031.
66. de Almeida, S.F., Picarote, G., Fleming, J.V., Carmo-Fonseca, M., Azevedo, J.E. and de Sousa, M. (2007) Chemical chaperones reduce endoplasmic reticulum stress and prevent mutant HFE aggregate formation. *J. Biol. Chem.*, **282**, 27905–27912.
67. Cortez, L. and Sim, V. (2014) The therapeutic potential of chemical chaperones in protein folding diseases. *Prion*, **8**,
68. Parichy, D.M., Elizondo, M.R., Mills, M.G., Gordon, T.N. and Engeszer, R.E. (2009) Normal table of postembryonic zebrafish development: staging by externally visible anatomy of the living fish. *Dev. Dyn.*, **238**, 2975–3015.
69. Walker, M.B. and Kimmel, C.B. (2007) A two-color acid-free cartilage and bone stain for zebrafish larvae. *Biotech. Histochem.*, **82**, 23–28.
70. Lin, Y.Y., White, R.J., Torelli, S., Cirak, S., Muntoni, F. and Stemple, D.L. (2011) Zebrafish Fukutin family proteins link the unfolded protein response with dystroglycanopathies. *Hum. Mol. Genet.*, **20**, 1763–1775.

Chapter III

Characterization of bone properties and material composition of the zebrafish Chihuahua

Bone in OI patients

Alterations of bone tissue properties such as high bone fragility, that arises from low bone mass, and abnormalities in bone material properties, such as reduced toughness, are similar in most types of osteogenesis imperfecta. Moreover, the degree of mineralization of the bone matrix is almost universally increased (Boyde et al.1999) both in mild and in more severe OI cases (Rauch et al. 2008). The mechanisms behind the increased mineralization in OI patients are still unclear. Interestingly, both in children with OI and in *oim* mouse model the thickness of bone mineral particles is the same or smaller than in controls (Vanleene et al. 2012; Fratzl-Zelman et al. 2014). The combination of increased matrix mineral content and similar particle size implies that mineral particles are more packed in the extracellular matrix. Moreover, as the extracellular matrix contains mostly collagen, the total space left for water between collagen molecules and mineral particles is decreased in osteogenesis imperfecta (Paschalis et al. 2016), making the bone stiffer. Probably the decreased amount of low mineralized bone areas indicates a more rapid incorporation of mineral in the bone matrix (Weber et al. 2006).

OI bone is also characterized by reduced nanoporosity compared to normal tissue. This defect is due to the presence of less water in OI bone (Paschalis et al. 2016). Water is important to generate tensile forces, which are necessary to guarantee the mechanical properties of collagen-based materials, such as bone (Masic et al. 2015). For this reason the reduced nanoporosity observed in OI tissue can contribute to the characteristic bone fragility (Paschalis et al. 2016).

To proof that the zebrafish *Chihuahua* is a valid model of classical OI also at the bone property level, I contributed to the investigation of its bone by micro-CT (μCT), raman spectroscopy and quantitative backscattered electron microscopy. These analyses were conducted in collaboration with Björn Busse at the Department of Osteology and Biomechanics, University Medical Center Hamburg-Eppendorf. The resulting manuscript has been recently submitted to Journal of Bone and Mineral Research.

Personal contributions to Chapter III

- Collection of WT and Chihuahua zebrafish for the analysis.

The manuscript was submitted to JBMR (Journal of Bone and Mineral Research) and it is now under major revision.

- In order to satisfy the reviewers, I optimized the quantitation of bone formation rate in larvae, and the new data had been added to the revised version of the manuscript.

Severely impaired bone material quality in *Chihuahua* zebrafish resembles classical dominant human osteogenesis imperfecta

Imke A.K. Fiedler, M.Sc.[1], Felix N. Schmidt, M.Sc.[1], Christine Plumeyer, B.Sc.[1], Petar Milovanovic, M.D., Ph.D.[1], Roberta Gioia, Ph.D.[2], Francesca Tonelli, M.Sc.[2], Antonella Forlino, Ph.D.[2], Björn Busse, Ph.D.[1*]

[1]Department of Osteology and Biomechanics, University Medical Center Hamburg-Eppendorf

[2]Department of Molecular Medicine, Biochemistry Unit, University of Pavia

***Corresponding Author**

Björn Busse, Ph.D.

Department of Osteology and Biomechanics, University Medical Center Hamburg-Eppendorf

Lottestr. 55A, 22529 Hamburg, Germany

Phone: +49-40-7410-56687, Email: b.busse@uke.uni-hamburg.de

Disclosure

The authors have nothing to disclose.

Abstract

Excessive skeletal deformations and brittle fractures in the vast majority of patients suffering from osteogenesis imperfecta (OI) are a result of substantially reduced bone quality. Since the mechanical competence of bone is dependent on the tissue characteristics at small length scales, it is of crucial importance to assess how osteogenesis imperfecta manifests at the micro- and nanoscale of bone. In this context, the *Chihuahua* (*Chi/+*) zebrafish, carrying a heterozygous glycine substitution in the α1 chain of collagen type I, has recently been proposed as suitable animal model of dominant OI. Similar to human severe OI type III, *Chi/+* show skeletal deformities, altered mineralization patterns and a smaller body size. Using a multimodal approach targeting bone quality parameters, this study aims at quantifying the changes in bone morphology, structure and tissue composition of *Chi/+* at multiple length scales. Morphological changes were assessed with high-resolution micro-CT imaging and showed that the vertebrae in *Chi/+* had a significantly smaller size, thinner cortical shell and distorted shape. Tissue composition in vertebrae was investigated with quantitative backscattered electron microscopy and Fourier-transform infrared spectroscopy, showing higher mean calcium content, greater matrix porosity, as well as lower mineral crystallinity and collagen maturity in comparison to controls. This study provides comprehensive quantitative data on bone quality indices in *Chi/+* and thus further validates this mutant as an important model reflecting osseous characteristics associated with human classical dominant osteogenesis imperfecta, both at the whole bone level and the tissue level.

Keywords: Bone histomorphometry, Genetic animal models, Bone matrix, Osteogenesis imperfecta

Introduction

Osteogenesis imperfecta (OI) is a genetic disorder of bone and connective tissues which affects approximately 1 in 10,000 births and has multiple implications on skeletal growth and bone mineralization [1]. The mechanical integrity of the diseased bone is often drastically impaired, leading to an increased bone fragility [2,3]. As a consequence, patients suffer from excessive skeletal deformations and multiple brittle fractures [3–5]. The compromised fracture resistance in the vast majority of OI patients is due to a dominant mutation of the genes responsible for synthesis of collagen I, *i.e*. the organic framework of bone [6–8]. This results in a diminished structure of the organic matrix accompanied by delayed mineralization and thus retardation in skeletal growth and maturation.

The severity of the disease can vary largely and depends on the type of OI[9]. Among the dominant mutations affecting the collagen I genes, the mildest and most common form of OI is type I with spontaneous fractures occurring after a child started walking, minor deformities, an almost normal stature, and mild bone fragility. The most severe and lethal form is type II with fractures occurring *in utero* and death before birth. Intermediate forms are type III with severe phenotypes including fractures, scoliosis, major deformities and a very small stature, and type IV with moderate phenotypes including fractures and a small stature [10].

Since these types of OI often evidently manifest at the skeletal and whole bone level in terms of low bone mass and the presence of fractures or deformities, initial diagnostic approaches commonly employ X-ray absorptiometry and radiography [1,7,11]. Based on bone biopsies from patients, OI has further been characterized at the tissue level, *i.e.* at the micro-and nanoscale of bone, where the ultrastructural alterations have been observed to correlate well with the clinical severity of OI [12]. For tissue of OI type I to IV there have been reports on impaired mechanical behavior at sub-micron scale [13,14], the presence of irregularly hyper-mineralized regions [14] and changes in the structure of the nanoscopic bone components, *i.e.* collagen fibrils and hydroxyapatite crystals [14]. Since the material properties of bone at small length scales, *i.e.* bone tissue quality, determines the mechanical competence of bone at the whole bone and skeletal level, it is of crucial importance to assess in which way the bone tissue quality is compromised by OI [13]. Yet, current treatment options are mainly aiming at increasing bone strength through increasing overall bone mass [15–17]. Conventional measures including musculoskeletal exercise are therefore often combined with pharmacological approaches widely based on antiresorptive bisphosphonate therapy [8,15]. However, given the particularly wide age range of patients in addition to the large

clinical variability and the genetic diversity of OI, the success of such therapies often remains inconclusive [18,19].

Thus, for better understanding the impact of the disease on all skeletal length scales, and to accelerate the search for enhanced treatment options of the brittle bone disease, a large number of animal models have been established and characterized [20,21]. Besides well studied mammalian models including mice [22–25] and dogs [26], novel small-sized animal models are emerging. The zebrafish *(Danio rerio)* has become a valued animal model in the field of biomedical research due to its short generation time, genetic similarity to humans, small size, and low husbandry costs [27]. In the context of OI and similar genetic bone disorders, few zebrafish mutations have so far been generated and characterized with regard to the skeletal phenotype [21,28,29]. Fisher *et al.* have first described the dominant G574D mutation in the *Chihuahua* (*Chi/+*) zebrafish, which affects the *col1a1a* gene encoding for the α1 chain of collagen I and therefore shares genetic similarities to severe dominant human OI. Carrying a glycine substitution in the α1(I), these zebrafish suffer from defects and retardation in bone growth and maturation [30]. Recently, this mutant has been characterized more deeply by Gioia *et al* [31], where static and dynamic bone formation markers have confirmed severe skeletal deformities and delayed mineralization, confirming the suitability of *Chi/+* mutants as promising model for classical dominant OI.

To expand the validity of *Chi/+* as model for human OI, further data on the material properties influencing the fracture behavior of bone is needed. Using a multimodal array of techniques focusing on the macro- to nanoscale of zebrafish bone, the study aims to provide quantitative data on the alterations in bone morphology, structure and composition in *Chi/+* zebrafish from the skeletal to the tissue level.

Materials & Methods

Chihuahua (*Chi/+*, *col1a1a*$^{dc124/+}$) and wild-type AB (WT) zebrafish were bred in-house at the animal facility "Centro di servizio per la gestione unificata delle attività di stabulazione e di radiobiologia" of the University of Pavia. The mutant *Chi/+* carries a G2207A mutation in *col1a1a*, causing a heterozygous G574D substitution in the α1 chain of type I collagen [30]. Husbandry, breeding and housing conditions of the zebrafish are described in detail in Gioja *et al.* [31]. All animals have been sacrificed at 10 months and kept frozen at -80° C (n=12/group).

Micro-Computed Tomography (Micro-CT)

Skeletal morphology and bone microstructures were assessed using micro-CT at a resolution of 5 µm (Skyscan 1272, Bruker, Kontich, Belgium). Six fish per group were fixed in 3.5 % formalin for 24 h and placed in a moist chamber during scanning. Whole body scans were acquired at 55 kV and 166 µA without an X-ray filter. Ring artifact and beam hardening correction was kept constant for all samples during reconstruction with NRecon (Bruker, Kontich, Belgium). After applying a fixed threshold for all samples, 3D evaluation was conducted using CTAn (Bruker, Kontich, Belgium). Quantification of changes in bone morphology of *Chi/+* and WT was performed on the first and second precaudal vertebrae of each fish. Hereby, neural and hemal arches were excluded from the analysis. Determined parameters were bone volume (BV, mm^3), defined as the vertebral body without the inner space; vertebral body height (VBH, µm); vertebral thickness (V.Th, µm); and eccentricity (Ecc, 0-1).

Fourier-Transform Infrared (FTIR) Spectroscopy

The molecular composition, maturity of the mineral- and collagen phase as well as matrix porosity was evaluated by FTIR spectroscopy. Six zebrafish per group were fixed in 3.5 % formalin for 24 hours, subsequently underwent step-wise dehydration in increasing concentrations of ethanol, and were embedded in poly methyl methacrylate (PMMA). Sample blocks were polished coplanar for tissue composition analysis, whereby the precaudal vertebral end plates cut in lateral plane were selected as region of interest. *Chi/+* and WT vertebrae were scanned using FTIR spectroscopy (Spotlight 400 attached to Frontier 400, PerkinElmer, Waltham, MA, USA) in Attenuated Total Reflectance (ATR) mode. Maps with dimensions of 65 µm × 130 µm were acquired at a spatial resolution (*i.e.* pixel size) of 1.56 µm with eight scans per pixel and a wavenumber range from 4000 – 570 cm^{-1}. Post-processing and spectral analysis was performed using a custom-written Matlab script (R2016b, MathWorks, Natick, MA, USA) and included the subtraction of the PMMA signal, smoothing of the absorbance signal and linear baseline removal. Peaks of interest were identified based on the second derivative of the original spectra. The phosphate peak was located between 1154 and 900 cm^{-1}, the carbonate peak was centered at 870 cm^{-1}, and the amide I peak envelope was located between 1710 and 1600 cm^{-1}. Bone tissue parameters were determined by dividing respective peak areas, including the mineral-to-matrix ratio (*i.e.* area of phosphate/amide I), carbonate-to-phosphate ratio (*i.e.* area of carbonate/phosphate), crystallinity (*i.e.* area of phosphate sub peaks 1028/1018 cm^{-1}), and collagen maturity (*i.e.* amide I sub peaks 1660/1690 cm^{-1}. Matrix porosity was determined by relating the

PMMA peak located at 1725 $cm^{-1}$to the amide I peak. Using Raman spectroscopy with a spatial resolution of < 1 µm, this approach has recently been used to determine the parameter nano-porosity[32]. Due to the lower resolution of 1.56 µm used in this present study, the parameter also includes porous structures above the nanometer scale. Hence, the parameter is hereinafter referred to as matrix porosity.

Quantitative Backscattered Electron Imaging (qBEI)

For analyzing the bone mineral density distribution (BMDD) in precaudal vertebrae of *Chi/+* and WT zebrafish, electron imaging was performed on identical samples and in identical regions of interest as previously analyzed by FTIR spectroscopy. Prior to imaging, samples were carbon-coated. Six specimens per group were investigated using a scanning electron microscope (LEO 435 VP; LEO Electron Microscopy Ltd., Cambridge, UK) operated at 20 kV and 680 pA using a constant working distance of 20 mm (BSE Detector, Type 202; K.E. Developments Ltd., Cambridge, UK). BMDD was determined on grey value images according to previously described protocols [33–35]. Calibration of the system was performed using a carbon-aluminum standard, facilitating the quantification of bone mineral as calcium weight percentage. Determined parameters were the mean calcium content (CaMean, wt%), the heterogeneity of the bone mineral distribution (CaWidth, wt%), the amount of low mineralized bone (CaLow, %), and the amount of highly mineralized bone (CaHigh, %).

Statistical Analysis

Statistical analysis was performed using SPSS (Version 24, IBM, Armonk, NY, USA). Normal distribution and homogeneity of variance was tested using Shapiro-Wilk tests and Levene's test, respectively. Group comparisons were carried out using independent t-tests at a significance level of α=0.05. Results are presented as mean±one-fold standard deviation.

Results

Bone quality analyses performed on *Chi/+* and their age-matched WT controls gained distinct bone phenotypes of the mutation at several length scales. At the skeletal level, predominant manifestations included a shorter body length and abnormal mineralization patterns. At the whole bone level, precaudal vertebrae of *Chi/+* showed substantially altered morphology. At the tissue level, vertebrae of *Chi/+* presented a high degree of mineralization, low mineral crystallinity and low matrix maturity in addition to elevated matrix porosity.

Skeletal morphology and whole bone structure

Micro-CT 3D reconstructions of *Chi/+* and WT zebrafish revealed substantial differences between the groups regarding their macroscopic skeletal morphology and mineralization (Fig. 1 A, B). *Chi/+* zebrafish had significantly reduced body length compared to WT with 17.1±2.8 mm vs. 27.5±1.8 mm (p=0.001). Along with accumulated fractures and deformations in the anal, dorsal and caudal fin bones, in the ribs, and in the neural and hemal arches of the vertebrae, the skeletal apparatus of *Chi/+* zebrafish presented heterogeneous mineralization as indicated by differences in X-ray absorption. At the whole bone level, particularly along the spine of *Chi/+* zebrafish, regions of high mineralization were observed directly adjacent to regions of lower mineralization, *i.e.* highly mineralized and fused vertebrae in precaudal and caudal regions were located next to low mineralized spinal regions in-between.

The quantification of bone morphological differences in the precaudal vertebrae gained significantly smaller vertebral bodies in *Chi/+* compared to WT zebrafish with a significantly lower vertebral body height compared to WT with 288±44 µm vs. 488±52 µm, p<0.001 (Fig. 1 C), as well as significantly lower vertebral thickness with 13.5±1.0 µm vs. 17.2±0.8 µm, p<0.001 (Fig. 1 D). Notably, precaudal vertebral bodies of *Chi/+* presented a mineralized core (Fig. 1 B, right), which was excluded from the morphometric evaluation. While the eccentricity (*i.e.* roundness) of vertebral bodies was similar between both groups (Fig. 1 E), *Chi/+* zebrafish presented a significantly reduced BV of 0.004±0.001 mm^3 vs 0.008±0.001 mm^3 in WT controls, p<0.001 (Fig. 1 F).

Tissue composition, maturity and porosity

Bone tissue composition analysis of *Chi/+* and WT zebrafish vertebrae by FTIR spectroscopy gained substantial differences in the majority of mineral- and collagen-related parameters (see Fig. 2 A-E). The carbonate-to-phosphate ratio was significantly higher in *Chi/+* compared to WT with 0.092±0.002 vs. 0.089±0.002, p<0.01 (Fig. 2 A), while the parameter crystallinity, a measure for crystal maturity and size, was significantly lower in *Chi/+* zebrafish compared to WT controls with 11.5±1.6 vs. 20.1±6.3, p=0.005 (Fig. 2 B). The mineral-to-matrix ratio was insignificantly elevated in *Chi/+* (Fig. 2 C). In addition, the collagen maturity ratio was significantly lower in *Chi/+* compared to WT with 10.1±5.8 vs. 24.2±5.7, p=0.003 (Fig. 2 D). With regard to the matrix porosity of vertebral tissue, *Chi/+* presented significantly higher values than WT with 0.184±0.085 vs. 0.090±0.022, p = 0.025 (Fig. 2 E).

Bone mineral density distribution

BMDD acquired with quantitative backscattered electron microscopy showed clear differences in the mineralization pattern between *Chi/+* and WT controls (Fig. 3 A-E). As depicted in Fig. 3 B, the distribution of calcium was shifted towards higher concentrations in *Chi/+*. The mean calcium weight percentage of both groups was slightly below 30 wt%, whereby CaMean of *Chi/+* was significantly higher compared to WT with 27.8±0.8 wt% vs. 26.7±0.9 wt%, p=0.039 (Fig. 3 C). At tissue level, the heterogeneity of mineralization measured by CaWidth was similar between the groups as depicted in Fig. 3 D, and so was the percentage of low calcium concentrations CaLow. High calcium concentrations CaHigh in *Chi/+* were twofold compared to WT with 25.1±12.9% vs. 13.5±6.4 %, p=0.075 (Fig. 3 E).

Discussion

Applying an array of bone quality analyses including micro-CT, qBEI and FTIR spectroscopy this study revealed and quantified changes in the morphology, structure and molecular composition of bone from the osteogenesis imperfecta zebrafish model *Chihuahua* carrying a heterozygous glycine substitution in the α1 chain of type I collagen. Alterations in bone phenotype induced by the mutation manifested at all investigated skeletal length scales, *i.e.* from skeletal to whole bone to tissue level.

3D histomorphometry performed on whole skeleton of *Chi/+* and WT zebrafish validated the presence of skeletal deformities and the occurrence of fractures described in recent radiographic and histological investigations performed on this *Chi/+* zebrafish model [31]. Similar to cases of human OI, these abnormalities are present in both the axial and the appendicular skeleton [5]. Focusing on the vertebral bodies at whole bone scale, results of this study showed substantially decreased bone volume and cortical shell of the vertebrae, which goes well in line with clinical observations on human osteogenesis imperfecta cases type I-IV [3,36,37]. Interestingly, the eccentricity of the vertebral bodies, *i.e.* their roundness, was not affected by the mutation, indicating that the lateral locomotion patterns of *Chi/+* zebrafish did not lead to permanent malformations at whole bone level along the spine. Yet, *Chi/+* zebrafish presented distinct vertebral features visible in the first precaudal and mid-caudal vertebrae, which enclosed an atypical mineralized core. The mineral-to-matrix ratio distribution in whole precaudal vertebrae (Fig. 2 A, inserts) indicates a high ratio of phosphate to amide I inside this mineralized core (bright pixels) when compared to cortical vertebral regions (darker pixels). This indicates either a high

degree of mineralization or a low degree of collagen content within this region. qBEI images of the identical region in the precaudal vertebrae (Fig. 3 A, inserts) showed highly heterogeneous mineral distribution in the core and low calcium content compared to cortical regions (low gray values). Combining these results, mineralized tissue in the core of *Chi/+* vertebrae seems to be a heterogeneous, low mineralized tissue with low presence of collagen.

In cases of human OI, the accumulation of multiple vertebral fractures has been identified to cause progressive spinal deformity [38], thus it is likely that the observed deformations along the spinal column of the *Chi/+* zebrafish could also be linked to a history of fractures. In a clinical setting, substantial macroscopic anomalies including fractures and deformities often allow the identification of OI based on radiographic indications [1]. However, this approach is not sufficiently conclusive to also serve as basis for reliable fracture risk assessment, since the mechanical competence of healthy and pathological bone is determined by the material properties at tissue level [13]. In this context, mouse models of OI have considerably aided in correlating the mechanical properties of OI-affected bone with ultra-structural defects at tissue level, and thus in better understanding the origins of OI-related bone fragility [24,39–42].

In this study on zebrafish carrying the α1-G574D mutation, the tissue composition analysis revealed that both the organic collagen matrix and the inorganic mineral crystal phase were significantly affected in *Chi/+* vertebral bone. While at skeletal level OI-affected bones present with reduced bone mineral density and bone mass [6], the mineralization pattern of OI can be highly heterogeneous throughout the skeleton. To that effect, an increased degree of mineralization at tissue level has been reported for murine OI models [24,39,42] and human OI [43–45]. Analogous, the mineral density distribution in the bone tissue of the *Chi/+* zebrafish was shifted towards higher calcium concentrations compared to WT zebrafish. Hence, *Chi/+* zebrafish present with elevated mean calcium concentrations, while in contrast, the mineral crystallinity of the hydroxyapatite particles was significantly decreased. The parameter crystallinity as assessed with vibrational spectroscopy has been correlated with the maturity, size and purity of the hydroxyapatite crystals in bone, and thus indicates smaller, less stoichiometric crystals in *Chi/+* zebrafish. Moreover, *Chi/+* zebrafish showed a high carbonate-to-phosphate ratio, supporting high carbonate substitution in the crystal lattice composition and thus lower crystal maturity.

These findings in zebrafish are well in line with previous observations made in murine OI models [46], and in human tissue of OI type I-IV, suggesting that affected tissue comprises an increased mineral-to-matrix ratio and tissue mineral density (TMD) with smaller but more

abundant crystals [13,43]. In addition to a smaller size of crystals, the orientation of crystals in an OI-mouse model have been shown to more random than in healthy cases [47]. While this observation is most probably linked to a more random orientation of collagen fibrils, it suggests an additional parameter of interest to investigate in the bone tissue of *Chi/+* mutants.

In addition to altered mineral properties, the molecular structure of the collagen matrix differed significantly in *Chi/+* zebrafish as evidenced by vibrational spectroscopy. While it should be noted, that the collagen-related sub peak positions and ratios employed in the spectral analysis have not yet been correlated to the collagen I molecule of zebrafish bone using biochemical analyses (*e.g.* with high performance liquid chromatography), we found that the established ratio for collagen maturity (1660/1690 cm^{-1}) [48] yielded a significant difference towards lower collagen maturity in *Chi/+*. In combination with reduced crystallinity, these parameters may relate to an increased remodeling rate, which has been described in cases of human OI [37,43,49]. The amount of low calcium values determined with quantitative backscattered electron microscopy has been correlated to the amount of bone which undergoes primary mineralization [43]. As this value was not altered in *Chi/+* zebrafish, it stands to reason that the turnover kinetics in this zebrafish model are similar to human OI cases, featuring increased resorption rates at normal bone formation rates [43].

Besides compositional changes of the collagen and mineral phase, the tissue of *Chi/+* mutants further showed a higher matrix porosity, indicating substantial alterations in the microscopic structure. Hereby, the parameter matrix porosity was determined as the ratio of PMMA to amide I, as previously derived with Raman spectroscopy [32]. During the tissue preparation process, the latter infiltrates into nano- and microscopic spaces that are void of mineral and collagen, *e.g.* within the crystal lattice or within the inter- and intra-fibrillar space. Based on Raman spectroscopic analyses using this parameter with sub-microscopic resolution on biopsies from children suffering from OI compared to healthy controls, it was recently suggested, that smaller but more abundant and densely packed crystals in OI cases are leading to a decrease in nanoporosity [32]. However, this decrease has been found in immature tissue, *i.e.* in mineralization fronts of recently remodeled tissue (1-3 days), but not in more mature tissue. Based on observations made in classical dominant OI cases [50], bone tissue of *Chi/+* zebrafish likely features more randomly organized collagen fibrils with more inter-fibrillar cavities, offering an explanation for the herein detected elevated matrix porosity above the micron scale. Such micro-structural changes coupled with an altered chemical composition of the collagen and mineral components compromise

the mechanical properties of the tissue, consequently leading to an increased bone fragility characteristic for classical dominant OI.

This study provides quantitative data on the bone morphology, structure and tissue composition of zebrafish carrying a dominant collagen mutation. Multimodal and multiscale bone characterization revealed a drastic impairment of bone quality in the skeleton of *Chi/+* zebrafish. Specific phenotypes at the skeletal level include a shorter skeletal size, accumulation of bone deformities and heterogeneous mineralization patterns, and at tissue level an increased mineral density, reduced mineral and matrix maturity, and increased matrix porosity. Detected at all investigated length scales, these characteristics are clearly resembling to human OI. Analogous to human OI cases, where the mechanical properties of bone are impaired, the observed deformities in *Chi/+* mutants are a consequence of altered bone quality at tissue level. The *Chihuahua* zebrafish can therefore be expected to provide an exceeding animal model for human OI. Further investigations of this model will be of great value for improving current treatment strategies of OI, particularly in the form of novel drug screening tests and drug administration as well as in the form of conventional therapies including musculoskeletal exercise.

Acknowledgements

The authors thank Dr. Shannon Fisher (Department of Pharmacology & Experimental Therapeutics, Boston University School of Medicine, USA) for providing the mutation of *Chihuahua* zebrafish and Dr. Katharina Jähn (Department for Osteology and Biomechanics, University Medical Center Hamburg-Eppendorf) for her assistance. The research leading to these results received funding from PIER (Partnership for Innovation, Education and Research) under grant no. PIF-2014-28 and DFG (Deutsche Forschungsgemeinschaft/ German Research Foundation) under grant no. BU 2562/2-1/3-1 to BB; from Fondazione Cariplo (grant No. 2013-0612) and Telethon (grant No. GGP13098) to AF; and from the Joachim Herz Stiftung in cooperation with PIER to FNS.

Authors' contributions: IAKF, PM, AF and BB designed the study; RG, FT and AF generated the fish for this study; IAKF, PM, FNS and CP prepared the specimens for experimental analyses; IAKF, FNS, CP, and PM acquired and analyzed the data; IAKF performed the statistical analysis; IAKF, FNS, PM, RG, FT, AF and BB interpreted the data. IAKF and BB wrote the manuscript. All authors approved the final version of the manuscript.

References

1. Marini JC, Forlino A, Bächinger HP, et al. Osteogenesis imperfecta. Nature reviews. Disease primers. 2017;3:17052.
2. Martin E, Shapiro JR. Osteogenesis imperfecta: Epidemiology and pathophysiology. Current Osteoporosis Reports. 2007;5(3):91–7.
3. Glorieux FH. Osteogenesis imperfecta. Best practice & research. Clinical rheumatology. 2008;22(1):85–100.
4. Rauch F, Glorieux FH. Osteogenesis imperfecta. The Lancet. 2004;363(9418):1377–85.
5. Renaud A, Aucourt J, Weill J, et al. Radiographic features of osteogenesis imperfecta. Insights into Imaging. 2013;4(4):417–29.
6. Alharbi SA. A Systematic Overview of Osteogenesis Imperfecta. Mol Biol. 2015;05(01).
7. Biggin A, Munns CF. Osteogenesis Imperfecta: Diagnosis and Treatment. Current Osteoporosis Reports. 2014;12(3):279–88.
8. Forlino A, Marini JC. Osteogenesis imperfecta. The Lancet. 2016;387(10028):1657–71.
9. Marini JC, Forlino A, Cabral WA, et al. Consortium for osteogenesis imperfecta mutations in the helical domain of type I collagen: regions rich in lethal mutations align with collagen binding sites for integrins and proteoglycans. Human mutation. 2007;28(3):209–21.
10. Sillence DO, Senn A, Danks DM. Genetic heterogeneity in osteogenesis imperfecta. Journal of Medical Genetics. 1979;16(2):101–16.
11. Le Zionts, Nash JP, Rude R, Ross T, Stott NS. Bone mineral density in children with mild osteogenesis imperfecta. Bone & Joint Journal. 1995;77-B(1):143–7. Available from: http://bjj.boneandjoint.org.uk/content/jbjsbr/77-B/1/143.full.pdf.
12. Sarathchandra P, Pope FM, Kayser MV, Ali SY. A light and electron microscopic study of osteogenesis imperfecta bone samples, with reference to collagen chemistry and clinical phenotype. J. Pathol. 2000;192(3):385–95.
13. Imbert L, Aurégan J-C, Pernelle K, Hoc T. Mechanical and mineral properties of osteogenesis imperfecta human bones at the tissue level. Bone. 2014;65:18–24.
14. Gu C, Katti DR, Katti KS. On-site SEM and nanomechanical properties of human OI bone. Bioinspired, Biomimetic and Nanobiomaterials. 2016;5(3):106–20.
15. Thomas IH, DiMeglio LA. Advances in the Classification and Treatment of Osteogenesis Imperfecta. Current Osteoporosis Reports. 2016;14(1):1–9.

16. Seikaly MG, Kopanati S, Salhab N, et al. Impact of Alendronate on Quality of Life in Children With Osteogenesis Imperfecta. Journal of Pediatric Orthopaedics. 2005;25(6):786–91.
17. Besio R, Forlino A. New frontiers for dominant osteogenesis imperfecta treatment: Gene/cellular therapy approaches. Advances in Regenerative Biology. 2015;2(1):27964.
18. Vasanwala RF, Sanghrajka A, Bishop NJ, Högler W. Recurrent Proximal Femur Fractures in a Teenager With Osteogenesis Imperfecta on Continuous Bisphosphonate Therapy: Are We Overtreating? Journal of Bone and Mineral Research. 2016;31(7):1449–54.
19. Marom R, Lee Y-C, Grafe I, Lee B. Pharmacological and biological therapeutic strategies for osteogenesis imperfecta. American journal of medical genetics. Part C, Seminars in medical genetics. 2016;172(4):367–83.
20. Kamoun-Goldrat AS, Le Merrer MF. Animal models of osteogenesis imperfecta and related syndromes. Journal of bone and mineral metabolism. 2007;25(4):211–8.
21. Enderli TA, Burtch SR, Templet JN, Carriero A. Animal models of osteogenesis imperfecta: applications in clinical research. ORR. 2016;8:41–55. Available from: https://www.dovepress.com/getfile.php?fileID=32674.
22. Chipman SD, Sweet HO, McBride DJ, et al. Defective pro alpha 2(I) collagen synthesis in a recessive mutation in mice: A model of human osteogenesis imperfecta. Proceedings of the National Academy of Sciences. 1993;90(5):1701–5.
23. Forlino A, Porter FD, Lee EJ, Westphal H, Marini JC. Use of the Cre/lox recombination system to develop a non-lethal knock-in murine model for osteogenesis imperfecta with an alpha1(I) G349C substitution. Variability in phenotype in BrtlIV mice. The Journal of biological chemistry. 1999;274(53):37923–31.
24. Daley E, Streeten EA, Sorkin JD, et al. Variable bone fragility associated with an Amish COL1A2 variant and a knock-in mouse model. Journal of Bone and Mineral Research. 2010;25(2):247–61.
25. Lisse TS, Thiele F, Fuchs H, et al. ER stress-mediated apoptosis in a new mouse model of osteogenesis imperfecta. PLoS genetics. 2008;4(2):e7.
26. Campbell BG, Wootton JA, Macleod JN, Minor RR. Canine COL1A2 mutation resulting in C-terminal truncation of pro-alpha2(I) and severe osteogenesis imperfecta. Journal of Bone and Mineral Research. 2001;16(6):1147–53.
27. Mackay EW, Apschner A, Schulte-Merker S. A bone to pick with zebrafish. BoneKEy reports. 2013;2:445.

28. Gistelinck C, Witten PE, Huysseune A, et al. Loss of Type I Collagen Telopeptide Lysyl Hydroxylation Causes Musculoskeletal Abnormalities in a Zebrafish Model of Bruck Syndrome. Journal of Bone and Mineral Research. 2016;31(11):1930–42.
29. Asharani PV, Keupp K, Semler O, et al. Attenuated BMP1 function compromises osteogenesis, leading to bone fragility in humans and zebrafish. American journal of human genetics. 2012;90(4):661–74.
30. Fisher S, Jagadeeswaran P, Halpern ME. Radiographic analysis of zebrafish skeletal defects. Developmental Biology. 2003;264(1):64–76.
31. Gioia R, Tonelli F, Ceppi I, et al. The chaperone activity of 4PBA ameliorates the skeletal phenotype of Chihuahua, a zebrafish model for dominant osteogenesis imperfecta. Human molecular genetics. 2017.
32. Paschalis EP, Gamsjaeger S, Fratzl-Zelman N, et al. Evidence for a Role for Nanoporosity and Pyridinoline Content in Human Mild Osteogenesis Imperfecta. Journal of Bone and Mineral Research. 2016;31(5):1050–9.
33. Milovanovic P, Zimmermann EA, Riedel C, et al. Multi-level characterization of human femoral cortices and their underlying osteocyte network reveal trends in quality of young, aged, osteoporotic and antiresorptive-treated bone. Biomaterials. 2015;45:46–55.
34. Roschger P, Fratzl P, Eschberger J, Klaushofer K. Validation of quantitative backscattered electron imaging for the measurement of mineral density distribution in human bone biopsies. Bone. 1998;23(4):319–26.
35. Roschger P, Paschalis EP, Fratzl P, Klaushofer K. Bone mineralization density distribution in health and disease. Bone. 2008;42(3):456–66.
36. Jones SJ, Glorieux FH, Travers R, Boyde A. The microscopic structure of bone in normal children and patients with osteogenesis imperfecta: a survey using backscattered electron imaging. Calcified tissue international. 1999;64(1):8–17.
37. Rauch F, Travers R, Parfitt AM, Glorieux FH. Static and dynamic bone histomorphometry in children with osteogenesis imperfecta. Bone. 2000;26(6):581–9.
38. Diacinti D, Pisani D, D'Avanzo M, et al. Reliability of vertebral fractures assessment (VFA) in children with osteogenesis imperfecta. Calcified tissue international. 2015;96(4):307–12.
39. Vanleene M, Porter A, Guillot P-V, Boyde A, Oyen M, Shefelbine S. Ultra-structural defects cause low bone matrix stiffness despite high mineralization in osteogenesis imperfecta mice. Bone. 2012;50(6):1317–23.

40. Carriero A, Doube M, Vogt M, et al. Altered lacunar and vascular porosity in osteogenesis imperfecta mouse bone as revealed by synchrotron tomography contributes to bone fragility. Bone. 2014;61:116–24.
41. Carriero A, Zimmermann EA, Paluszny A, et al. How tough is brittle bone? Investigating osteogenesis imperfecta in mouse bone. Journal of Bone and Mineral Research. 2014;29(6):1392–401.
42. Kozloff KM, Carden A, Bergwitz C, et al. Brittle IV mouse model for osteogenesis imperfecta IV demonstrates postpubertal adaptations to improve whole bone strength. Journal of Bone and Mineral Research. 2004;19(4):614–22.
43. Roschger P, Fratzl-Zelman N, Misof BM, Glorieux FH, Klaushofer K, Rauch F. Evidence that abnormal high bone mineralization in growing children with osteogenesis imperfecta is not associated with specific collagen mutations. Calcified tissue international. 2008;82(4):263–70.
44. Rauch F. Material matters: a mechanostat-based perspective on bone development in osteogenesis imperfecta and hypophosphatemic rickets. Journal of musculoskeletal & neuronal interactions. 2006;6(2):142–6.
45. Boyde A, Travers R, Glorieux FH, Jones SJ. The Mineralization Density of Iliac Crest Bone from Children with Osteogenesis Imperfecta. Calcified tissue international. 1999;64(3):185–90.
46. Grabner B, Landis WJ, Roschger P, et al. Age- and genotype-dependence of bone material properties in the osteogenesis imperfecta murine model (oim). Bone. 2001;29(5):453–7.
47. Fratzl P, Paris O, Klaushofer K, Landis WJ. Bone mineralization in an osteogenesis imperfecta mouse model studied by small-angle x-ray scattering. The Journal of clinical investigation. 1996;97(2):396–402.
48. Farlay D, Duclos M-E, Gineyts E, et al. The Ratio 1660/1690 cm−1 Measured by Infrared Microspectroscopy Is Not Specific of Enzymatic Collagen Cross-Links in Bone Tissue. PLOS ONE. 2011;6(12):e28736. Available from: http://journals.plos.org/plosone/article/file?id=10.1371/journal.pone.0028736&type=printable.
49. Baron R, Gertner JM, Lang R, Vignery A. Increased bone turnover with decreased bone formation by osteoblasts in children with osteogenesis imperfecta tarda. Pediatric research. 1983;17(3):204–7.

50. Bishop N. Bone Material Properties in Osteogenesis Imperfecta. Journal of Bone and Mineral Research. 2016;31(4):699–708.

Figure legends

Figure 1

Skeletal morphology and structure of *Chihuahua* and WT zebrafish vertebrae based on micro-CT. **A)** Representative whole body scan of an adult wild type zebrafish (left) and an isolated precaudal vertebral body with typical double-cone geometry (center). Histomorphometric parameters are indicated in the longitudinal section of the vertebral body (right). **B)** Representative whole body scan of a *Chi/+* mutant (left) indicates heterogeneous mineralization in the skull and along the spine, deformities of ribs and fins possibly related to fractures, and fused or collapsed vertebrae. Vertebral bodies of *Chi/+* mutants showed abnormal geometry (center) and accumulation of mineralized tissue in its core (right). Histomorphometric analysis of precaudal vertebrae yielded **C)** a significantly smaller vertebral body height in *Chi/+*, **D)** significantly reduced vertebral thickness, **E)** similar eccentricity, and **F)** reduced bone volume. Based on skeletal features and whole bone characteristics, the *Chihuahua* zebrafish clearly resembles human severe osteogenesis imperfecta type III.

Figure 2

Molecular composition and structure assessed in precaudal vertebrae of WT and *Chi/+* using FTIR spectroscopy **A)** The carbonate-to-phosphate ratio, a measure for carbonate substitution in the crystal lattice, was significantly higher in *Chi/+*. **B)** Crystallinity, a measure for mineral crystal size, lattice purity and crystal age, was significantly lower in *Chi/+* mutants. **C)** The average mineral-to-matrix ratio was insignificantly higher in *Chi/+* than in WT. The inserts show representative spectral maps from whole vertebrae. Note the typical double-cone shape in WT in contrast to an altered structure in *Chi/+* including a mineralized core in *Chi/+*, which has a high mineral-to-matrix ratio (yellow pixels) in comparison to the cortical shell in both WT and *Chi/+* (red pixels). **D)** Collagen maturity was substantially reduced in *Chi/+* mutants. **E)** Matrix porosity was significantly elevated in *Chi/+* mutants compared to WT. Tissue composition analysis revealed clear implications of the mutation on the tissue quality in zebrafish which are characteristic for classical dominant osteogenesis imperfecta.

Figure 3

Bone mineral density distribution of WT and *Chi/+* zebrafish. **A)** The vertebral bodies yielded substantial differences in calcium concentration and distribution with brighter gray values in *Chi/+* than in WT. Inserts show representative qBEI images from whole precaudal vertebrae depicting a heterogeneously and lower mineralized core compared to the cortical shell (darker pixels) in *Chi/+* (arrow). Coupled with a high mineral-to-matrix ratio detected in the core tissue compared to the shell (Fig. 2 A), this tissue appears of lower degree of mineralization and lower collagen content compared to the cortical shell. **B)** The calcium concentration histogram was shifted towards higher concentrations in the *Chi/+* zebrafish. **C)** At tissue level, the mean calcium concentration was significantly elevated in *Chi/+* compared to WT. **D)** The heterogeneity of the calcium distribution was similar between the groups.

Figure 1

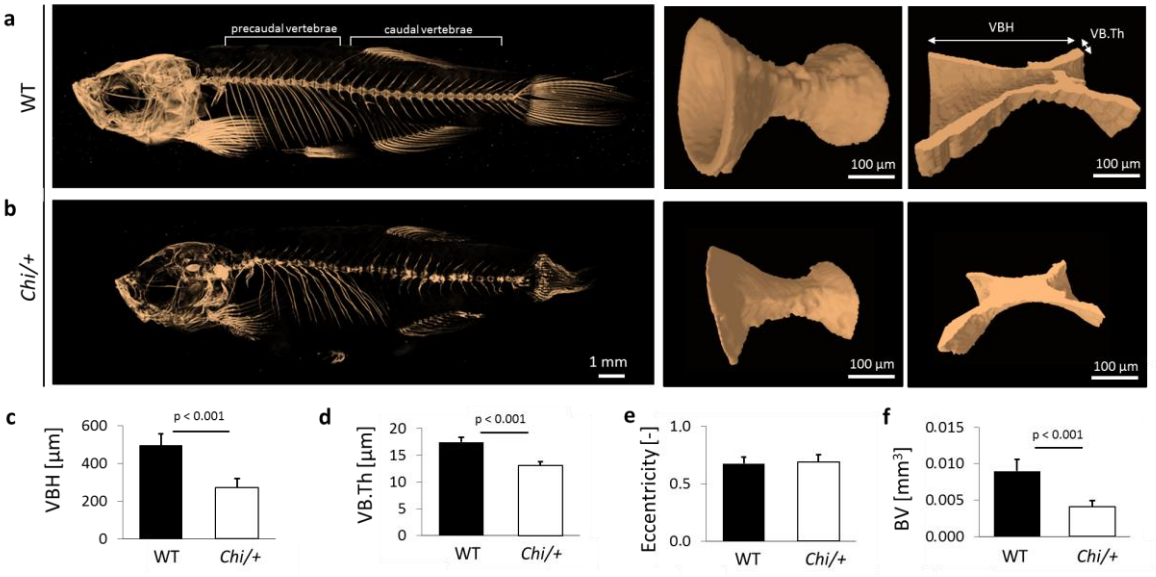
a
WT
precaudal vertebrae
caudal vertebrae
VBH
VB.Th
100 µm
100 µm
b
Chi/+
1 mm
100 µm
100 µm
c
VBH [µm]
p < 0.001
WT
Chi/+
d
VB.Th [µm]
p < 0.001
WT
Chi/+
e
Eccentricity [-]
WT
Chi/+
f
BV [mm³]
p < 0.001
WT
Chi/+

Figure 2

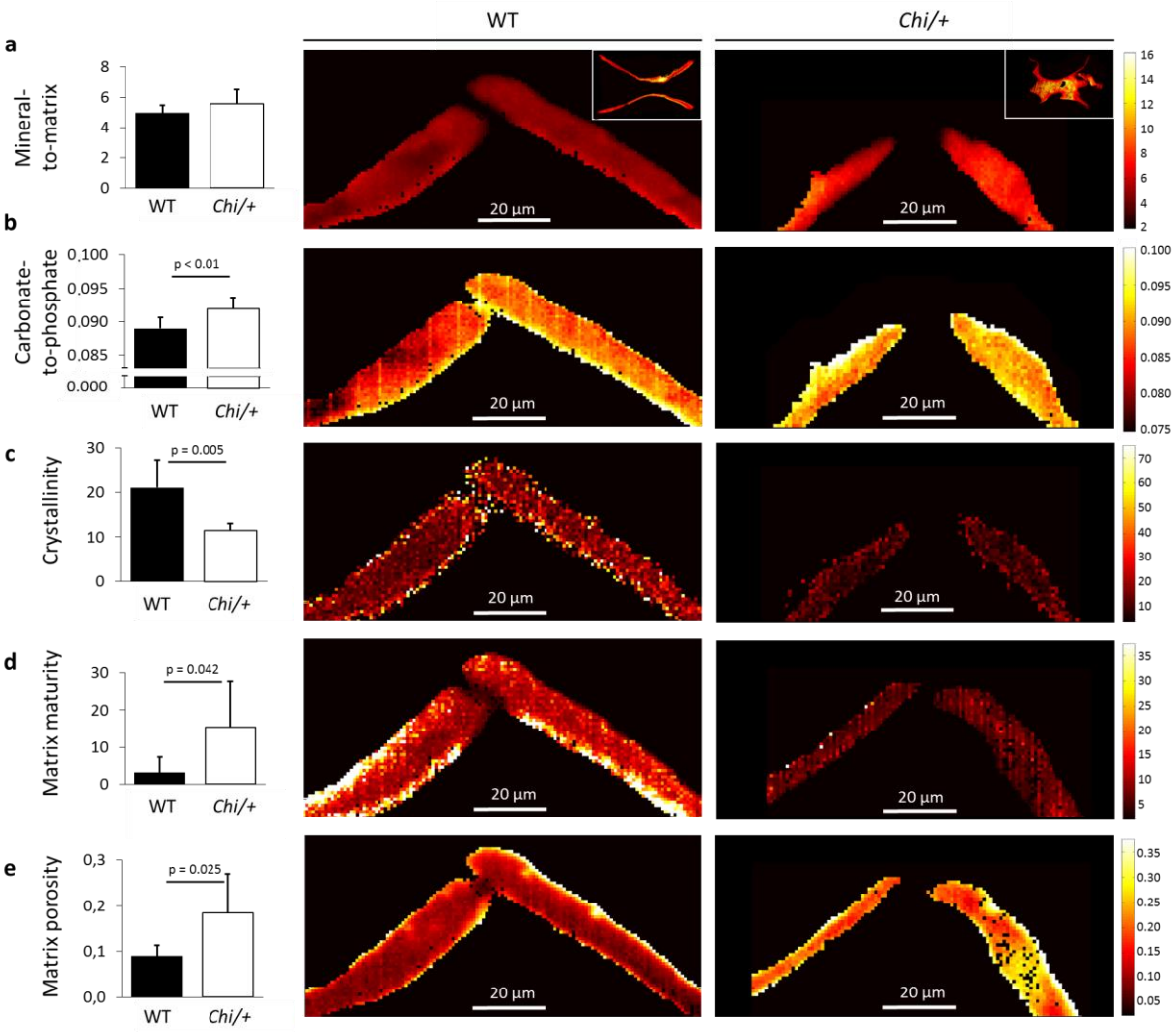

Figure 3

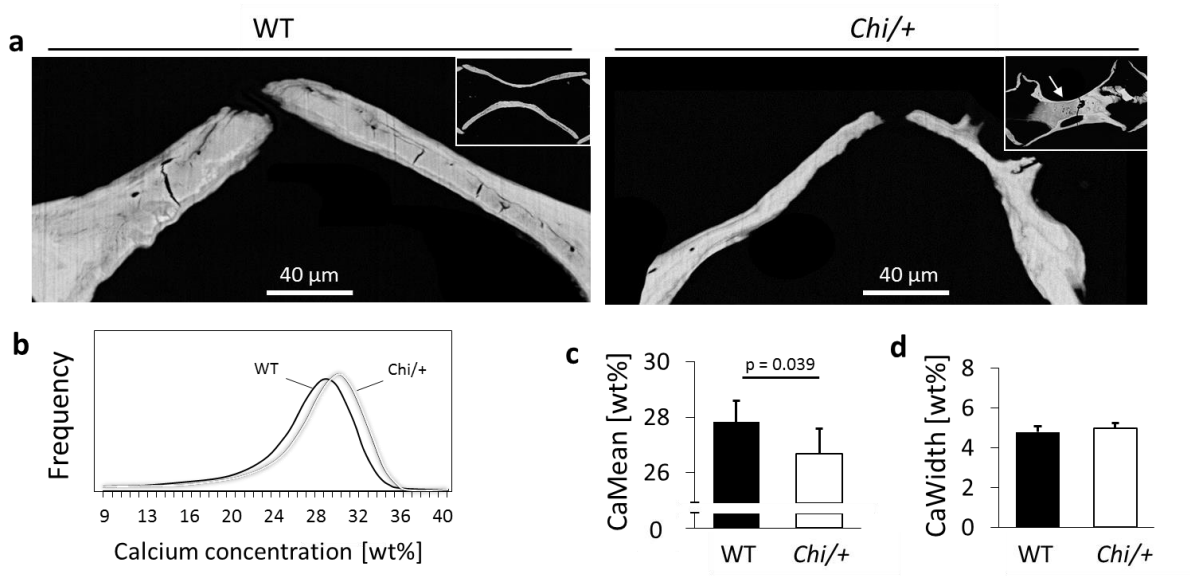

Chapter IV

Generation of new zebrafish models of recessive OI

Collagen prolyl 3-hydroxylation complex

Since I was interested in evaluating the effect of mutant collagen type I retention inside the cells I focused my attention on the recessive OI type VII and VIII, characterized by collagen type I overglycosylation and on OI type XIV, showing collagen type I underglycosylation.

Starting from 2006, clinical, biochemical, histomorphometric analysis, together with the generation of mouse models, led to the discovery of recessive deficiency of prolyl 3-hydroxylase 1 (P3H1), cartilage-associated protein (CRTAP) and cyclophilin B (CyPB), members of a trimeric complex, as main players in OI cases with positive collagen biochemistry and negative collagen sequencing (Marini, Cabral et al. 2007; Morello et al. 2006; Van Dijk et al. 2009).

P3H1 is a 83.4 kDa multifunctional protein of the 2-oxoglutarate dioxygenase family composed by 736 amino acids. It is encoded by *P3H1* (previously named *LEPRE1),* which is located on chromosome 1p34.1 in humans. P3H1 has been isolated for the first time from an ER-enriched extract from chick embryos. P3h1 null mice have a mild bone phenotype compared to human patients, although they display growth deficiency, rhizomelia, reduced bone mineral density, abnormal hypertrophic chondrocytes, and delayed secretion of over-modified collagen from cultured cells (Baldridge et al. 2008).

Following P3H1 purification from chick embryo ER extracts, two additional proteins, CRTAP and CyPB (peptidyl-prolyl *cis-trans* isomerase B/cyclophilin B), were co-purified. This event, together with the co-sedimentation of these three proteins in a 1:1:1 ratio on a sucrose gradient supported the existence of a novel intracellular collagen-modifying complex (Figure 1). P3H1 and CRTAP, together with CyPB, are involved in the 3-hydroxylation of proline residues in the sequence Pro-4Hyp-Gly. A single residue, proline 986, in each of the α1 chains of collagen types I and II is subjected to this post-translational modification. Furthermore, the complex hydroxylates proline 707 of α2(I) chain (Vranka et al. 2004).

In humans, *CRTAP* is located on chromosome 3p22.3 and encodes a 46.5 kDa protein with 401 amino acid residues, including a 26 amino acid signal peptide. CRTAP was isolated as a developmentally up regulated transcript in cultured chick chondrocytes (Castagnola et al. 1997). The functional role of CRTAP as a member of the 3-hydroxylation complex was confirmed by the demonstration that Pro986 was not 3-hydroxylated in either α1(I) or α1(II) collagen chains in the *Crtap*$^{-/-}$ mouse. Moreover, the null mice show post-translational over-modification of type I collagen, increased

collagen secretion and enlargement of collagen fibril diameter in skin and cartilage (Barnes et al. 2006).

The third member of the complex is CyPB, a peptidyl-prolyl isomerase of 23.7 kDa with 216 amino acid residues encoded by *PPIB* gene located on chromosome 15q22.31 and known to play a central role in the folding of procollagen in the ER. It is also secreted extracellularly, where it is crucial in inflammation, viral infection and cancer (Van Dijk et al. 2009). *In vitro* studies have shown that CyPB is not required for full prolyl 3-hydroxylation activity. P3H1 and CRTAP levels are one-third and two-thirds normal in the PPIB-null cells, indicating that CyPB enhances complex stability (Barnes et al. 2010). However, activity of the complex in the absence of CyPB is sufficient to normally 3-hydroxylate α1(I) Pro986 (Barnes et al. 2010). Moreover, the loss of *cis-trans* prolyl isomerization and the subsequent delayed collagen folding result, in the majority of cases, in collagen over-modification (Marini, Cabral et al. 2007). However, in one case with a moderate phenotype, the *PPIB* mutation affects the start codon and leads to undetectable CyPB levels and normally modified collagen (Barnes et al. 2010).

CRTAP and P3H1 are absent or reduced in cells containing null mutations in one of the two genes, indicating that they are mutually stabilized in the collagen prolyl 3-hydroxylation complex. Differently, CyPB levels are unaffected by mutations in either *CRTAP* or *P3H1* (Chang et al. 2009). Interestingly, amino acid analysis performed on *Ppib*$^{-/-}$ mice bone-collagen α chains reveals an increased global hydroxylation and glycosylation of lysyl residues. Moreover, mass spectrometric analysis shows site-specific alterations in lysine post-translational modification of bone collagen and it is known that the hydroxylation of helical lysine residues is catalysed by the lysyl hydroxylase 1 (LH1). Indeed, these results reveal that CyPB can contribute to LH1 folding, or stabilize its activity by binding to it (Cabral et al. 2014).

In humans, post-translational overmodification of collagen type I chains, synthesized by fibroblasts *in vitro*, is reported in presence of both homozygous or compound heterozygous mutations for *CRTAP* and *P3H1*, causing delayed electrophoretic mobility. Thus, collagen overmodification remains a common feature for both dominant and these recessive forms of OI, both in patients and animal models of the disease (Marini, Cabral et al. 2007).

Analysis of collagen from tissue and cultured fibroblasts from OI patients with mutations disrupting the expression of any protein of the complex reveals a lack or a decrease in 3-hydroxylation at proline residues α1(I) Pro986 and α2(I) Pro707 (Morello et al. 2006; Marini, Cabral et al. 2007; Pyott et al. 2011). Prolyl 3-hydroxylation is a well conserved post translational modification in many collagen types and, when defective, may be linked to a number of human diseases with musculoskeletal, ocular and renal pathologies (Hudson and Eyre 2014). Five decades ago the 3-hydroxyproline residue was identified in collagen through the amino acid analysis of collagen hydrolysates (Ogle et al. 1962). It is a rare amino acid with an occurrence of two residues per α chain in collagen type I and II, between three to six residues per α chain of collagen type V and XI and over ten residues per α chain of collagen type IV (Eyre et al. 2011; Dean et al. 1983; Risteli et al. 1980). Several novel molecular sites of 3Hyp in fibrillar collagens were identified using mass spectrometry, suggesting a local sequence substrate-specificity (Hudson et al. 2011). Moreover, a pronounced tissue specificity was also observed for several sites. For example, in collagen type II the Pro944 ranges in occupancy from 80% in vitreous humour to 20% in cartilage (Eyre et al. 2011).

The precise mechanisms by which mutations in *CRTAP* and *P3H1* result in OI remain undefined.
It is likely that the molecular pathogenesis is more complex than simply the lack of prolyl 3-hydroxylation in type I and perhaps other collagens (Barnes et al. 2010). *P3h1*$^{H662A/H662A}$ mice, carrying a knock-in mutation in the catalytic domain of P3h1 that inactivates the 3-hydroxylase activity of the enzyme without compromising the complex assembly, do not show any differences in collagen migration, in contrast to *P3h1*$^{-/-}$ mice. This data indicate that in absence of 3-Hyp no overmodification in collagen is detected and collagen is normally secreted (Homan et al. 2014). Indeed, Pro986 3-hydroxylation may be necessary for extracellular protein architecture rather than for helical folding (Homan et al. 2014).
Thus, it is possible that only the absence of CRTAP or P3H1 leads to slow collagen folding in the ER causing both overmodification of the helix and ER stress due to mutant collagen intracellular retention and partially secretion in the extracellular matrix, finally leading to the impairment of normal functions of connective tissue (Forlino and Marini 2016). However, further studies are needed.

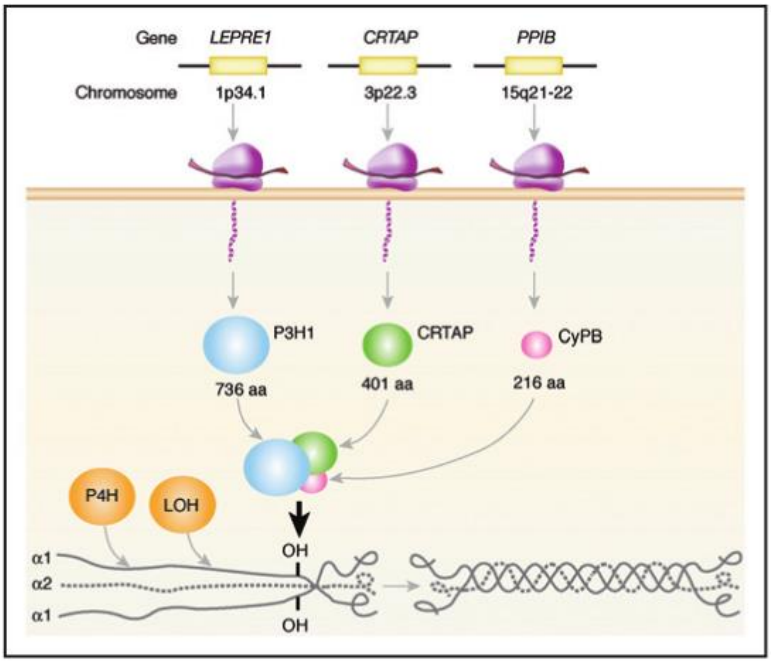

Figure 1. Collagen prolyl 3-hydroxylation complex from (Marini, Cabral et al. 2007).

Trimeric Intracellular Cation channel type B (TRIC-B)

Biosynthesis of collagen type I is a complex process involving several regulation events and it is a calcium-regulated process. Calcium binds collagen C-terminal globular domain and stabilizes interchain hydrogen and disulfide bonds required for procollagen trimerization and folding (Bourhis et al. 2012). Moreover, fluctuations of calcium concentrations mediate the activities of different chaperones, foldases and modifying enzymes in the ER important for collagen post translational modifications and folding. These events are mediated through calcium release by inositol triphosphate receptors (IP_3R) or ryanodine receptors (RyR) and calcium uptake by sarcoplasmic-ER Ca^{2+}-ATPase type 2b (SERCA2b) (Meldolesi and Pozzan 1998; Mekahli et al. 2011) (Figure 2). Thus, disruption of calcium homeostasis impairs several collagen interacting protein activities, altering the process of collagen biosynthesis.

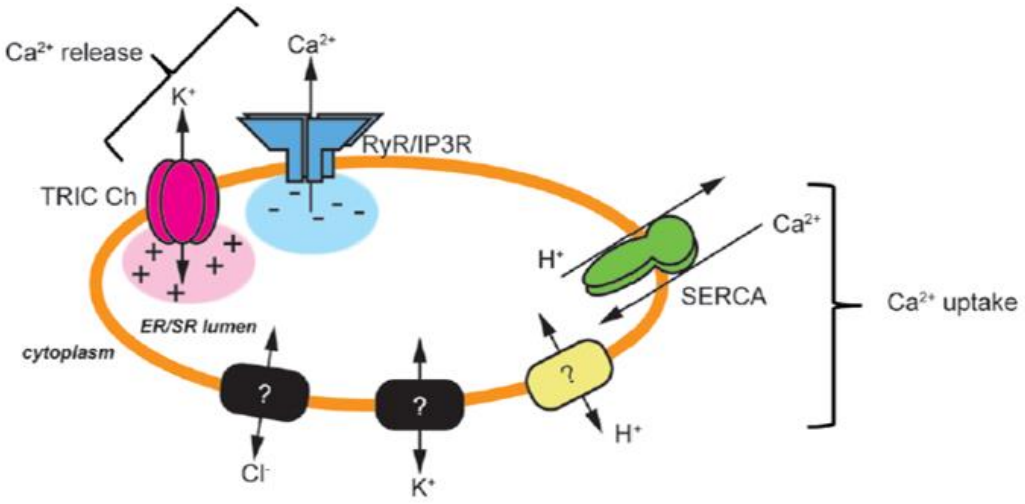

Figure 2. Schematic diagram of TRIC channels in intracellular Ca^{2+} stores. Physiological Ca^{2+} release mediated by ryanodine receptors (RyRs) and inositol triphosphate receptors (IP_3Rs) probably requires counter-ion movements to stabilize sarcoplasmic (SR)/endoplasmic reticulum (ER) potential. H^+, K^+ and Cl^- are other channels in the ER/SR. SERCA: sarcoplasmic-ER Ca^{2+}-ATPase (modified from Ichimura et al. 2016).

In 2007 Zhou et al discovered trimeric Intracellular Cation channels (TRIC) located at sarcoplasmic (SR)/endoplasmic reticulum of multiple cell types (Figure 3). TRIC-A is predominantly expressed in excitable tissues and, in particular, in SR of muscle cells. *Tric-a* knockout mice develop hypertension resulting from vascular hypertonicity, and the mutant vascular smooth muscle cells exhibit insufficient RyR-mediated Ca^{2+} release for inducing hyperpolarization (Venturi et al. 2012).

TRIC-B is an ubiquitous subtype expressed in the ER of all tissues (Yazawa et al. 2007). TRIC-B (ER membrane Intracellular Cation channel type B), encoded by *TMEM38B*, functions as homotrimeric monovalent cation channel, mainly dependent on voltage and permeable to monovalent cations (K^+) (Pitt et al. 2010). To better understand the properties of TRIC-B, Yang et al. solved in 2016 the crystal structures of *C. elegans* TRIC-B1 and TRIC-B2, both belonging to TRIC-B subtypes. They discovered an homotrimer in which each monomer forms a novel fold with seven transmembrane helices (M1-7) and four amphipathic α-helices lying on the cytoplasmic and luminal surfaces. Among the transmembrane helices, M4,5 and 6 resemble the inverted repeats of M1,2 and 3, while M7 is alone and fills the crevice between M4 and M6 (Yang et al. 2016) (Figure 3). The inositol 4,5-biphosphate head group of PIP2 intercalates between M5 and M6 directly attaching to the surface of pore lumen contributing to trimerization of TRIC-B1/B2 (Fig. 3A, B).

PIP2 is a lipid cofactor necessary for regulating the functions of ion channels on plasma membrane (Suh and Hille 2008). Anyway, the specific association of PIP2 with the SR/ER-localized TRIC channels demonstrates a prominent role of PIP2 in the intracellular ion channels too (Yang et al. 2016). Another component, needed to guarantee the correct function of the channel, is the KEV sequence. This motif is in the hydrophobic loop connecting transmembrane segments M1 and M2, it is conserved across animal species and contributes to forming the channel ion-conducting pore (Venturi et al. 2012; Yang et al. 2016).

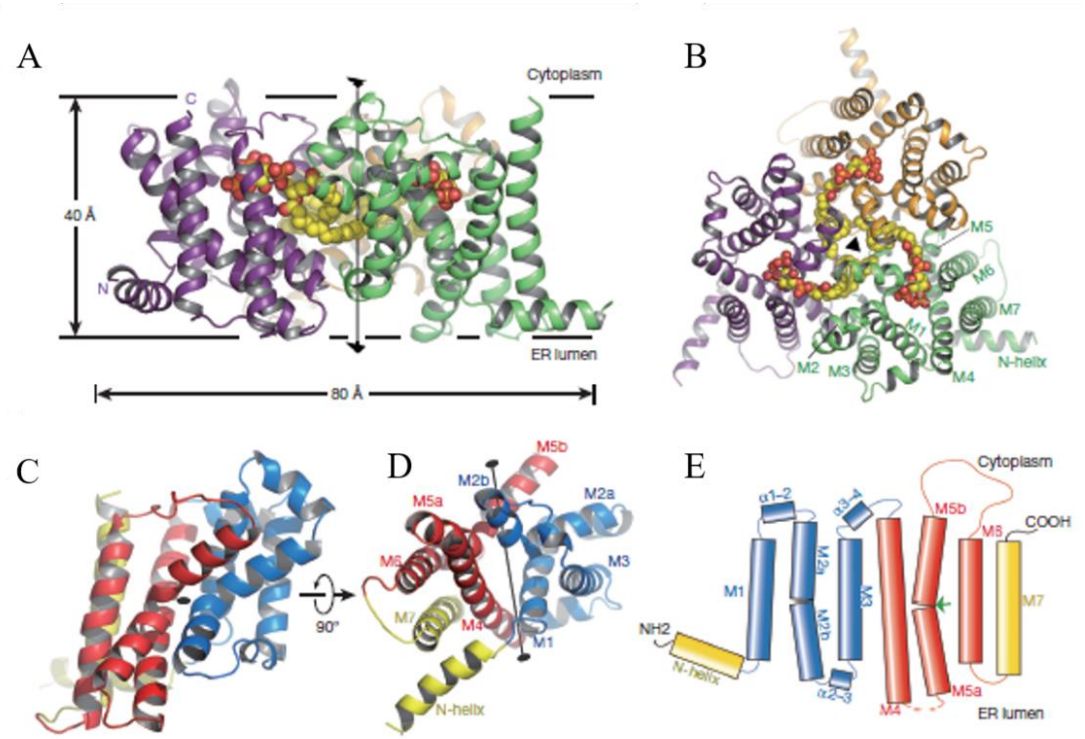

Figure 3. ***C. elegans*** **TRIC-B1 channel structure.** (**A**, **B**) The homotrimeric TRIC-B1 channel in complex with PIP2. The protein subunits are presented as ribbon models, while the PIP2 molecules are shown as yellow-and-red sphere models. (**C**, **D**) The structure of a TRIC-B1 monomer viewed along the membrane plane (**C**) and along the membrane normal from luminal side (**D**). (**E)** The topology of a *C. elegans* TRIC-B monomer. The colour codes are consistent with those in **C**. The green arrow indicates the location of a conserved 'GXG' motif at the M5 region susceptible to a mutation associated with osteogenesis imperfecta (from Yang et al. 2016).

Mutations in *TMEM38B* were recently connected to an osteogenesis imperfecta phenotype (OI type XIV) (Shaheen et al. 2012). They cause a moderately severe form of OI and patients are characterized by low bone volume associated with low bone turnover and relatively normal bone matrix mineralization, features that set this OI type apart from the high bone turnover and increased mineralization found in classical forms. The absence of TRIC-B channel causes an alteration of the ER Ca^{2+} homeostasis as demonstrated by the decrease of both cytoplasmic [Ca^{2+}] and IP_3R-mediated Ca^{2+}-flux in Ca^{2+}-free media obtained from proband primary fibroblasts and osteoblasts (Cabral et al. 2016). These findings validated the role for TRIC-B in maintaining intracellular Ca^{2+} levels (Yazawa et al. 2007).

Ca^{2+}/K^{+} flux abnormalities likely affect bone cell function, since intracellular calcium signalling is known to control osteoblast proliferation and differentiation, as well as osteoclast survival and resorptive activity, through regulation of gene transcription (Miyauchi et al. 1990).

As consequence, disruption of ER-Ca^{2+} flux kinetics in TMEM38B-null cells is associated with altered expression and activity of multiple collagen modifying enzymes and chaperones, resulting in abnormal post-translational modification and folding of type I collagen (Cabral et al. 2016).

Tric-b knockout mice die soon after birth due to respiratory failure. Alveolar epithelial cells from these mice exhibit insufficient production and secretion of surfactant lipids likely due to diminished IP_3R-mediated Ca^{2+} release (Yamazaki et al. 2009). On the contrary, Ca^{2+} release mechanism is mediated by RyRs in *Tric-a* KO mice, indicating that TRIC-A and TRIC-B channels may selectively support Ca^{2+} release through IP_3Rs and RyRs, respectively (Venturi et al. 2012).

It was interesting to notice that *Tric-b* knockout mice develop an osteogenesis imperfecta-like bone phenotype due to the fact that TRIC-B is essential for active osteoblast to produce large amount of collagen necessary for bone mineralization (Zhao et al. 2016). *Tric-b* KO mice are characterized by impaired bone mineralization associated to an insufficient collagen matrix and impaired collagen deposition by inhibiting collagen transport from the ER to the Golgi in osteoblasts. Moreover, the impairment of IP_3R mediated Ca^{2+} release from ER by osteoblasts results in Ca^{2+} overloading (Zhao et al. 2016).

Thus, the idea was to generate an OI type XIV zebrafish model, which has more chances to have a less severe phenotype and survive in respect to murine models, in order to deeper investigate the role of TRIC-B channel in the pathophysiology of the disease.

CRISPR/Cas system

The CRISPR (Clustered, Regularly Interspaced, Short, Palindromic Repeats)/Cas (CRISPR-associated) system is an adaptive immunity system found in bacteria and archaea, which provides prokaryotes with an effective defence against bacteriophages, plasmids and other mobile genetic elements (Koonin et al. 2013). This system consists of a *cas* gene cassette and a CRISPR chromosomal array composed of short and repetitive sequences, called repeats, which are preceded by an upstream leader sequence for the expression of the array and interrupted by short, unique spacer sequences derived from foreign DNA and therefore used as genetic memory (Figure 4). Repeats sequences are usually identical in terms of length and sequence. They can be palindromic, with a predicted stem-loop secondary structure, or not palindromic and so unstructured, leading to different mechanisms of CRISPR array processing during its expression (Richter et al. 2012). In contrast, the spacer sequences are mostly unique within a genome and they originate from extra-chromosomal sources such as plasmids, phages or transferable elements (Bolotin et al. 2005).
Such array was identified more than 25 years ago in *E. Coli*, but its function was not known until 2007, when Barrangou and colleagues showed that infection of *Streptococcus thermophilus* with lytic phages provided subsequent immunity to the phage. They understood that repeat sequences present in the bacterial genome worked in association with *cas* genes as acquired resistance against viruses (Barrangou et al. 2007).

It is now known that CRISPR/Cas mediated adaptive immunity occurs in three stages (Figure 4): acquisition of a short sequence from the invading DNA, called protospacer, and its insertion into the CRISPR array as a spacer. This step involves cleavage of the protospacer by Cas proteins and repeat duplication following recombination in the CRISPR array (step 1). Then, the long pre-crRNA is transcribed and undergoes processing to generate mature crRNAs, each composed of a repeat sequence and an invader-targeting spacer (step 2). After the recruitment of Cas proteins, each mature crRNA mediates the cleavage of foreign nucleic acid at sites complementary to the crRNA spacer sequence, which is known as interference (step 3) (Makarova et al. 2011).

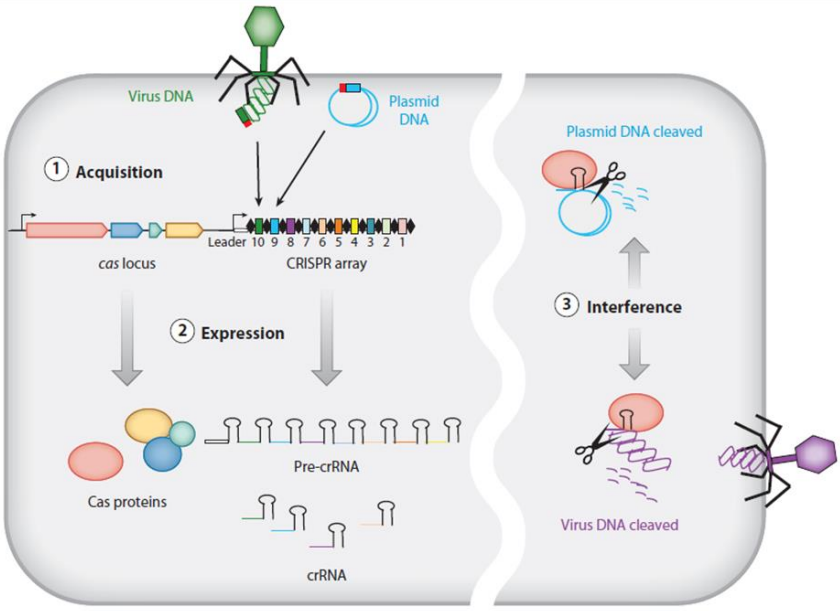

Figure 4. Function of the CRISPR/Cas system in prokaryotes from (Sampson and Weiss 2014).

The ability of CRISPR/Cas system to acquire foreign DNA and not DNA from their own chromosomes is due to a DNA sequence located adjacent to each protospacer in the foreign pathogen. It consists of a short sequence of 2-5 bp that can be different according to the CRISPR/Cas system and organism (Shah et al. 2013). These sequences, called protospacer adjacent motifs (PAMs), play a fundamental role in spacers' acquisition and generation of CRISPR array, and, subsequently, in the recognition of the complementary target DNA by the mature crRNA/Cas complex (Mojica et al. 2009).

In close proximity to the CRISPR array there are genes encoding the Cas proteins, which provide the enzymatic machinery required for the acquisition of new spacers from, and targeting, invading elements (Richter et al. 2012). Based on the diverse homology of Cas proteins, three CRISPR/Cas system types (I, II and III) can be identified, each one with a distinct molecular mechanism for interference. If the type I and III systems use a large complex of Cas proteins for crRNA-guided targeting, the type II system requires only the Cas9 protein for RNA-guided DNA recognition and cleavage. Cas1 and Cas2, responsible for spacer integration, are the two proteins that are present in all CRISPR-Cas system (Koonin et al. 2013).

In type I CRISPR/Cas systems and in most type III systems, the pre-crRNA processing is mediated

by a dedicated endoribonuclease, typically Cas6. However, in type I systems, Cas6 is a subunit of a multidomain complex called CASCADE (CRISPR-associated complex for antiviral defence); the crRNA remains associated with the complex that searches for a match in the target DNA and, once found, cleaves it (Brouns et al. 2003). In type III CRISPR/Cas systems the Cas6 does not bind to a repeat stem-loop, but to the first bases of the repeat and further crRNA maturation steps occur (Richter et al. 2012). Moreover in type III CRISPR/Cas system the Cas6 acts as independent protein and the CASCADE complex seems not involved in the processing of pre-crRNA (Wang et al. 2011).

Type II CRISPR/Cas system is encoded mainly in the genome of pathogenic and commensal bacteria that interact with eukaryotic hosts, like *Neisseria meningitidis*, *Legionella pneumophila* and *Listeria monocytogenes* (Makarova et al. 2011). For pre-crRNA cleavage and maturation, it requires the presence of a 1000-1600 amino acids long endonuclease, Cas9, as well as an accessory RNA, the *trans*-activating CRISPR RNA (tracrRNA), and a double-stranded RNA-specific RNase III. The dsRNA complex of crRNA and tracrRNA is associated with Cas9 and the spacer sequence within the crRNA can hybridize to complementary DNA sequences. Cas9 then mediates cleavage of the double-stranded targeted DNA flanked by a protospacer adjacent motif (PAM) (Sampson and Weiss 2014) with its HNH and RuvC-like nuclease domains, respectively (Jinek et al. 2012).

CRISPR/Cas9-mediated genome editing

In 2012 Jinek and colleagues showed that it was possible to engineer the tracrRNA and the crRNA as a single chimeric guide RNA (sgRNA or gRNA) that could direct Cas9 activity to specific DNA target *in vitro*. The gRNA retains two crucial features: a region of 20 nucleotides at the 5' end that determines the DNA target site and gives specificity, and the double-stranded loop structure at the 3' end that forms a complex with Cas9. These findings created a simple two-component system in which changes in the 20-nucleotide guide sequence of the sgRNA allow to programme Cas9 to target any DNA sequence of interest as long as it is adjacent to a PAM, usually NGG (Jinek et al. 2012).

At the target sites recognised by the tracrRNA:crRNA duplex and flanked by PAMs, the HNH nuclease domain of Cas9 cleaves the strand bound to crRNA, while the RuvC-like domain cuts the other DNA strand, forming double strand breaks (DSBs) at the specific sites. The cleavage leads to

the activation of two different repair mechanisms: the non-homologous end joining (NHEJ) and the homology-directed repair (HDR). When a homologous template is absent, NHEJ can connect the break sequences directly and induce random insertions or deletions (indels). If indels cause a frame shift in the reading frame, this can lead to the creation of premature stop codons; if insertions or deletions comprise three bases (or multiples of three bases), they may affect protein function. In the presence of a donor homologous template, the HDR pathway is activated and induces specific insertions, deletions or mutations (Peng et al. 2016) (Figure 5).

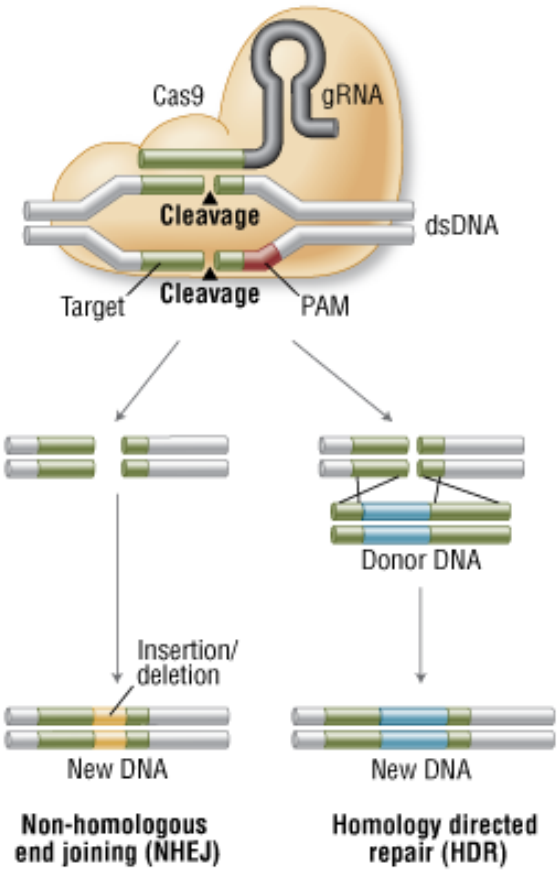

Figure 5. CRISPR/Cas9 for genome editing from (NEB: www.neb.com).

Several variables may affect CRISPR/Cas9 system, such as Cas9 activity, target site selection and sgRNA design, off-target effects and delivery methods. In order to deal with the large amount of sgRNAs that needs to be screened to guarantee the correct activity, specific features within and surrounding the target site sequence have been identified (Doench et al. 2014). In general, G-rich and A-depleted sgRNAs are more stable and more efficient. Considering the many criteria proposed, a growing number of computational tools now facilitates the design of sgRNAs (Doench et al. 2014).

The CRISPR/Cas9 system has been adapted as an efficient genome editing tool which allows to take step forward in biomedical research, thanks to the possibility to generate different animal models, but also in many other fields such as plant research focused on food security and genetically-modified crops (Ceasar et al. 2016). Undoubtedly, the CRISPR/Cas9 technology offers higher flexibility, simplicity and precision in gene targeting compared with the previously proposed technologies like zinc-finger nucleases (ZFNs) and TAL effector nucleases (TALENs). The low cost experiments needed for gRNA and Cas9 allowed many laboratories to adopt the CRISPR/Cas9 genome editing system. However, some practical issues, such as the delivery method, have to be further optimized to increase the application range of this technology (Gilles et al. 2014).

As already described in the first part of my thesis, zebrafish is considered nowadays a valid model to study different human diseases including skeletal dysplasias. The microinjection of gRNA and Cas9 mRNA in the transparent fertilized eggs is an easy and rapid technique. Thus, the combination of zebrafish and CRISPR/Cas9 system allows to generate models for human diseases without need of specific skills, in a short time and at low cost.
As major project of my PhD I generated three zebrafish models for recessive OI to better investigate the pathophysiology of the disease and as a tool for drug screening with the aim to identified novel pharmacological therapies.

Materials and methods

Zebrafish

Embryos were kept in petri dishes in fish water ($NaHCO_3$ 1.2 mM, instant ocean 0.1 g/L, $CaSO_4$ 1.4 mM, methylene blue 0.00002% w/v) at 28°C until 6 days post fertilization (dpf), then housed in ZebTEC semi-closed recirculation housing systems (Tecniplast) at 28°C, pH 7.5 and conductivity 500 μS on a 14/10 light/dark cycle. The Stand Alone is located in the centralized animal facility of the University of Pavia. Fish were fed three times a day alternating dry food and brine shrimps. For the experiments, larvae and adult fish were anesthetized using a solution of tricaine (3-amino benzoic acidethylester, Sigma Aldrich) 0.0016% w/v in fish water and sacrificed by tricaine overdose (0.03% w/v). Wild-type AB fish were provided by Professor Franco Cotelli (University of Milan) or obtained by European Zebrafish Research Center (Germany).

In silico analysis

Synteny analysis of *p3h1* (**ENSDARG00000071212**), *crtap* (**ENSDARG00000018010**) and *tmem38b* (**ENSDARG00000100549)** genes was performed using the genome browser Genomicus v88.01 (www.genomicus.biologie.ens.fr). Protein homology between zebrafish P3h1 (A0A0R4I9E8), Crtap (Q1L8P0) and Tmem38b (E7F2L4) and the human orthologues was analysed using UniProt Blast (http://www.uniprot.org/blast/).

Knock out generation

In silico gRNA selection

Target sequences for *p3h1* (5'-ggagaccgatttcaaggacctgg-3'), *crtap* (5'-ggagagcgtggagtttctggagg-3') and *tmem38b* (5'- ggttctcgtcacttccttcatgg - 3') were chosen using the free online software CHOPCHOP (https://chopchop.rc.fas.harvard.edu) (Montague et al. 2014).

Generation of gRNA and Cas9 mRNA

Each gRNA was synthesized by annealing two oligonucleotides, listed in the table below (Table 1). A BsmBI specific site overhanging was added at both 5' and 3' primer extremities.

Table 1: Oligonucleotides for the synthesis of the selected gRNAs to target *p3h1*, *crtap* and *tmem38b* genes; in red the BsmBI specific recognition sequence

Gene Of Interest	Oligonucleotides for annealing	
p3h1	5'-TAGGAGACCGATTTCAAGGACC-3'	5'-AAACGGTCCTTGAAATCGGTCT-3'
crtap	5'-TAGGAGAGCGTGGAGTTTCTGG-3'	5'-AAACCCAGAAACTCCACGCCT-3'
tmem38b	5'-TAGGTTCTCGTCACTTCCTTCA-3'	5'-AAACTGAAGGAAGTGACGAGAA-3'

The annealing programme used was 3 min at 95°C followed by 1 min at 25°C. gRNA fragments concentration was determined by absorbance at 260 nm. The double stranded fragments were cloned in pT7-gRNA vector (Addgene plasmid # 46759) (Jao et al. 2013) (Figure 6) previously linearized with BsmBI (New England BioLabs) 10 U/µL and purified with Nucleospin Gel and PCR Clean-up kit (Machinery-Nagel). Ligation was performed using T4 DNA ligase (Thermo Scientific) over night (o/n) at room temperature (RT). Transformation, using DH5α competent cells, was obtained through the following steps: 30 min in ice, followed by 90 sec at 42°C and 2 min in ice. Cells were grown in 900 µL of Luria Bertani Broth (LB) (final volume 1 mL) at 37°C for 1 h and then plated on agar plate containing 100 µg/mL ampicillin and let growing o/n. Colony PCR (10 min at 95°C, 3 min at 95°C, followed by 40 cycles of 1 min at 95°C, 1 min at 64°C and 1 min at 72°C, and a final 10 min of elongation at 72°C) with T7gRNA primer sense (5'-TACCGCACAGATGCGTAAGG-3') and one of the two annealing oligonucleotides as primer reverse was performed to verify the presence of the insert. The positive colonies were picked up and grown o/n in LB in presence of ampicillin 100 µg/mL. The plasmid DNA was then extracted using the EuroGOLD Plasmid Miniprep Kit I (Euroclone) and the presence of the correct insert was verified by sequencing (GATC Biotech AG). In order to obtain higher amount of the correct plasmid DNA, Qiagen Plasmid Maxi Kit (Qiagen) was used. gRNA was generated by linearization with BamHI (Promega) of the plasmid and

purification with Nucleospin Gel and PCR Clean-up Kit (Machinery-Nagel). *In vitro* transcription using MEGAshortscript T7 kit (Invitrogen) was performed, followed by DNA digestion with Turbo DNA-*free* Kit (Life Technologies). After *in vitro* transcription, the gRNA was purified using mirVana miRNA Isolation Kit (Invitrogen). The size and quality of resulting gRNA were confirmed by electrophoresis using a 10% (v/v) polyacrylamide-urea-SDS gel.

For Cas9 endonuclease pT3TS-nCas9n vector (Addgene plasmid # 46757) (Jao et al.2013) (Figure 6) was linearized by XbaI (New England BioLabs) digestion and purified using the Nucleospin Gel and PCR Clean-up Kit (Machinery-Nagel). DNA was transcribed using mMESSAGE mMACHINE T3 Kit (Invitrogen). DNA contaminant was removed through Turbo DNA-*free* Kit (Life Technologies), polyadenylation of RNA was performed with Poly(A) Tailing Kit (Ambion) and Cas9 transcript was purified using RNeasy Mini Kit (Qiagen). The obtained Cas9 mRNA was check by electrophoresis on 1% (w/v) formaldehyde agarose gel.

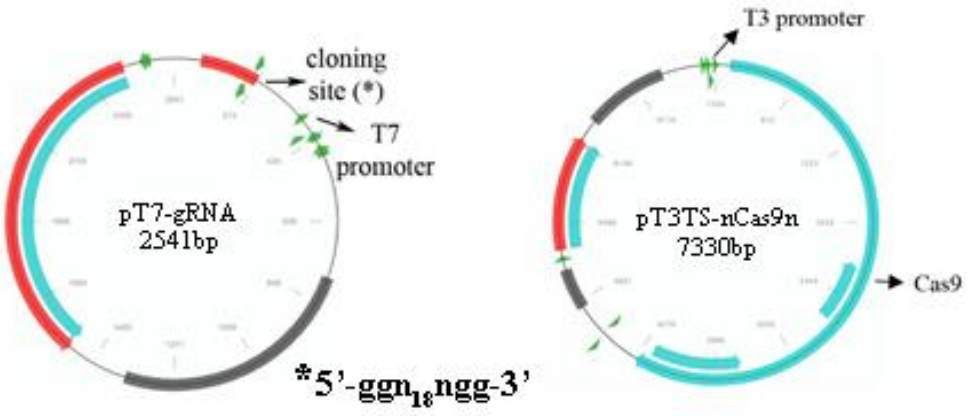

Figure 6. Addgene cloning vectors. (**A**) pT7-gRNA cloning vector (Addgene plasmid # 46759) (**B**) Cas9 expression plasmid (Addgene plasmid # 46757).

Microinjection

Microinjection was carried out using an InjectMan micromanipulator (Eppendorf) assembled on a Leica M165 FC stereomicroscope. The gRNA (12.5 ng/µL) and Cas9 mRNA (300 ng/µL) were mixed in Danieau solution (NaCl 58 mM, KCl 0.7 mM, $MgSO_4$ 0.4 mM, $Ca(NO_3)_2$ 0.6 mM, Hepes 5 mM, pH 7.6) together with a tracer dye 10x (dextran conjugated with tetramethylrhodamine, Molecular Probes) in a final volume of 5 µL and pre-heated at 60°C for 10 min. A microloader pipette with a thin tip (Eppendorf) was used to backload the mixture into borosilicate glass capillary (previously obtained with a micropipette puller), which was then secured to the micromanipulator. Embryos were lined on the edge of a slide inside a petri lid to facilitate the injection. Injection pressure and time were modulated to calibrate the injected volume, ranging from 2 to 4 nL per embryo.

The day after the injection, fish were screened, dead or deformed fish were eliminated and the others were checked under stereomicroscope using a fluorescent DSR filter. Fish showing a diffuse fluorescent signal were considered positively injected and let grow for further experiments.

DNA extraction

Depending of the type of experiments, DNA was extracted from single embryos, pool of embryos or caudal fins amputated from adult zebrafish. The specimen was digested in 100 µL of lysis buffer (Tris HCl 100 mM pH 8.5, EDTA 5 mM, SDS 0.2% (w/v), NaCl 200 mM) and 20 µL proteinase K (Sigma Aldrich) 15 mg/mL, for at least 3 h or o/n at 55°C. The sample was then centrifuged 10 min at 14000g at RT and DNA was precipitated using an equal volume of isopropanol. The sample was centrifuged again for 30 min at max speed at RT, the supernatant was discharged and the DNA pellet was washed gently with 400 µL of ethanol 70% (v/v). After ethanol removal, the pellet was air dried. The DNA was resuspended in 30 µL of Tris-EDTA buffer (Tris-HCl 20 mM, EDTA 1 mM, pH 8.0), incubating the samples at 55°C o/n. Concentration was determined by absorbance at 260 nm.

Genotyping

The genotype of the zebrafish models was evaluated by PCR amplification of *p3h1* (NC_007122.6), *crtap* (NC_007130.6) and *tmem38b* (NC_007132.7) using the following specific primers (Table 2):

Table 2. Primers designed for the amplification of the target genomic region.

Gene Of Interest (GOI)	Primers for PCR	
	Sense	**Reverse**
p3h1	5'-CTACACTAACATGTACATGTATGC-3' (4748 - 4771)	5'-ACAGTGTGTATATTCTGCATCCC-3' (5181 - 5203)
crtap	5'-CGTTACTCACTTTGAAGTAGGC-3' (23 - 44)	5'-CATTCCATTGCATCCGAATTGC-3' (460 - 481)
tmem38b	5'-TTACTGTCCGCTGGATGTGG-3' (11326-11345)	5'-GCAAATACAGCGACGCTCTG-3' (11448-11467)

1 µL of genomic DNA was added to the PCR mix, which included 1x Taq Polymerase buffer (GenScript), dNTPs 0.2 mM, Taq Polymerase 0.04 U/µL (GenScript) and primers 0.3 µM. The PCR cycle included 3 min of denaturation at 94°C, followed by 40 cycles of 30 sec at 94°C, 30 sec at the annealing temperature (60°C, 55°C and 56°C for *p3h1, crtap* and *tmem38b*, respectively), 1 min at 72°C and ended with 10 min of elongation at 72°C. The PCR product was checked by electrophoresis on a 1 % (w/v) agarose gel run at 100 V.

Mutants screening

T7 endonuclease I assay

Whole embryos or tail clips were used for the genomic DNA extraction as described before. DNA was amplified by PCR and 10 µL of the PCR amplicon were denatured and slowly renatured for facilitating heteroduplex formation. The annealing/reannealing procedure consisted of a 5 min denaturing step at 94°C, followed by cooling to 85°C, at −2°C per sec and further to 25°C, at −0.1°C per sec. The reannealed amplicon was then digested with 0.2 U/µL T7 endonuclease I in 1x Buffer 2 (New England BioLabs) at 37°C for 1 h. The sample was then separated on an 8% (v/v) polyacrylamide gel electrophoresis and acquired after ethidium bromide staining using the VersaDoc 3000 (BioRad).

Restriction enzymes digestion

Mutants screening was further confirmed by restriction enzymes digestion of the amplicon at 37°C for at least 3 h. The restriction enzymes used were Eco0109I (New England BioLabs) and BpmI (New England BioLabs) for *p3h1* and *crtap* mutants, respectively. The digestion was then analysed by 8%

(v/v) polyacrylamide gel electrophoresis and acquired by ethidium bromide staining using the VersaDoc 3000 (BioRad). For *tmem38b* the size difference of the WT (142 bp) and mutant alleles (118 bp) allowed their identification directly on the agarose gel of the PCR products.

Identification of mutation

The TOPO TA cloning Kit (Invitrogen) was used in order to isolate the single mutations obtained in F0 mosaics and F1 population of fish. PCR reaction was set up in 50 µL using 2 µL of genomic DNA as template. The cycle parameters were the ones used for genotyping and the last 10 min extension step at 72°C was essential to ensure that all PCR products were full length and 3' adenylated. PCR product was gel-purified using a Nucleospin Gel and PCR Clean-up Kit (Machinery-Nagel) and the TOPO cloning reaction was performed following the kit instructions. Briefly, the purified DNA was cloned into the pCR II-TOPO vector and the recombinant vector was used to transform competent *E. Coli* cells. Plasmid DNA was isolated from single colonies and sequenced by Sanger sequencing (GATC Biotech AG).

Morphometric analysis

Zebrafish were anesthetized with tricaine 0.03% (w/v) and images were acquired with a Leica M165 FC microscope (Leica) connected to a Leica DFC425 C digital camera (Leica). Measurements, as described in Parichy et al. 2009 were performed using the Leica LAS v4.5 software (Leica).
The following parameters were measured on larvae and adult fish (Table 3, Figure 7):

Table 3. Definitions of the parameters used for morphometric analysis of larval and adult fish. wpf: weeks post fertilization.

Parameter	Definition	Fish age (wpf)
Standard Length (**SL**)	Distance from the snout to the caudal peduncle; in pre-flexion larvae that do not have a caudal peduncle, to the posterior tip of the notochord	1, 2, 3, 4, 8, 24
Height at Anterior of Anal fin (**HAA**),	Distance from ventral to dorsal, measured immediately anteriorly to the anal fin and perpendicularly to the axis defined by SL	8, 24
Snout–Operculum Length (**SOL**)	Distance from snout to the most posterior point of operculum	8, 24
Height at Eye (**HE**)	Distance from ventral to dorsal, measured immediately posteriorly to the eye and perpendicularly to the axis defined by SL	8, 24

In addition, the level of insufflation of the swim bladder was evaluated by counting the number of lobes on lateral light images of larvae at 7, 14 and 21 days post fertilization (dpf).

Figure 7. Morphometric parameters measured in adult fish. Standard length (SL) in yellow, height at anterior of anal fin (HAA) in green, height at eye (HE) in blue, snout-operculum length (SOL) in red.

Alizarin Red skeletal staining

Skeletal characterization was performed using Alizarin Red, which stains mineralized bone. Fish were sacrificed by prolonged immersion in tricaine 0.03% (w/v). Embryos (at 7, 14, 21 and 28 dpf) were fixed overnight in paraformaldehyde (PFA) 4% (w/v) at 4°C, then washed in phosphate-buffered saline PBS/ 0.9 mM $CaCl_2$/ 0.49 mM $MgCl_2$, pH 7.4. The embryos were then bleached in H_2O_2 3% (v/v), KOH 0.5% (w/v) at RT to eliminate the pigmentation and then washed twice, 10 min each, in a solution of 25% glycerol/ 0.1% KOH to block bleaching reaction. Tissues were stained in 0.01% (w/v) Alizarin Red S (Sigma Aldrich)/ 25% glycerol/ 100 mM Tris, pH 7.5 for 1-2 h and then digested with trypsin (Sigma Aldrich) 1 mg/mL in 30% of saturated $B_4Na_2O_7$ solution for a time varying depending on the size of the embryo. A wash in saturated $B_4Na_2O_7$ solution was performed and then embryos were stained again in Alizarin Red S (Sigma Aldrich) 0.01% (w/v)/ 25% glycerol/ 100 mM Tris, pH 7.5 again for 1-2 h. Fish were washed in 50% glycerol/ 0.1% KOH for 10 min and then stored at 4°C in 100% glycerol/ 0.1% KOH.
Images of fish were acquired using a Leica M165 FC microscope connected to a Leica DFC425 C digital camera.

The mineralization of the notochord, the hyomandibular bone and the cerathoyal bone on 7 and 14 dpf larvae were qualitative evaluated by three operators blinded on the genotype. Ossification levels were classified as beginning, incomplete or complete ossification based on the alizarin red distribution along the bone. The level of mineralization of vertebral bodies was evaluated considering as mineralized the vertebrae with a continuous red staining from the dorsal to the ventral site.
Vertebral shape and size were evaluated on images of 28 dpf fish stained with alizarin red acquired on lateral orientation. For each vertebra, the mean of the length measured dorsally and ventrally and the mean of the height measured anteriorly and posteriorly to the vertebral centrum were determined. The first 10 vertebrae articulated with the ribs were considered.

X-Ray

X-Ray of 8, 16 and 24 weeks post fertilization fish were acquired by a Faxitron Mx-20 (Faxitron), using 25 kV for 10 seconds. The Kodak DirectView Elite CR System and k-Pacs software (Kodak) were used to acquire images.

µCT

40 weeks post fertilization fish were fixed in 3.5 % formalin for at least 24 h and placed in a moist chamber during µ-CT (Skyscan 1272, Bruker, Kontich, Belgium). Whole body scans were acquired at 55 kV and 166 µA with a 0.25 mm aluminum filter and at a resolution of 5 µm. Ring artifact and beam hardening correction was kept constant for all samples during reconstruction (NRecon, Bruker, Kontich, Belgium)

Steady state collagen analysis

Labelling of collagen with ^{3}H-proline was used to evaluate collagen overmodification. Caudal fins from adult fish were plated into 24 wells plate in Dulbecco's Modified Eagle Medium (D-MEM) containing 4 mM glutamine, 100 µg/ml penicillin, 0.1 mg/ml streptomycin, 1% fetal bovine serum (FBS). The labelling was performed for 24 h adding 30 µCi of ^{3}H-Pro/well.

The tail was washed with PBS supplemented with protease inhibitors (1.52 mg/mL EDTA, 1.57 mg/mL benzamidine, 0.25 mg/mL N-ethylmaleimide), and digested with 0.2 mg/ml pepsin in 0.5 M acetic acid o/n at 4°C in presence of 20 µg of bovine collagen as carrier. The sample was centrifuged at 13000 g for 20 min at 4°C and the surnatant was transferred in a new tube. The collagen was precipitated with 2 M NaCl, 0.5 M acetic acid for 30 min on ice, centrifuged at 13000 g for 20 min at 4°C and washed with ethanol 70% for 1 h on ice. The sample was centrifuged 13000 g for 20 min at 4°C, dried in vacuum and resuspended in 50 µL of 1x Laemmli buffer (62.5 mM Tris HCl, pH 6.8, 10% glycerol, 2% sodium dodecyl sulphate (SDS), 0.02% bromophenol blue).

The radioactivity (counts for minute, CPM) of the collagen samples was measured using a liquid scintillation analyser (TRI-CARB 2300 TR).

The same amount of ^{3}H-labeled collagens from each animal was denatured at 80°C for 10 min and separated on 6% polyacrylamide-urea-SDS gels. The gels were run at 80 V using the running buffer 19 mM Tris HCl, 0.1% (w/v) SDS and 192 mM glycine. Then gels were fixed 30 min in 30% methanol, 5% acetic acid and incubated 1 h in enhancer solution (EN^{3}HANCE PerkinElmen) with gentle agitation. After 30 min of washing in tap water the gels were dried for 2 h and placed in contact with a radiography film at -80°C. Films were developed and acquired by VersaDoc 3000 (BioRad).

RNA extraction

RNA was extracted from skin of adult wild type, *p3h1* knock out and from tails of adult wild type and *crtap* knock out mutants or from triplicate pools of 20 WT embryos at different stages of development to analyse *tmem38b* expression: namely, 2-4 cells, 16-32 cells, 64-128 cells, high, sphere, 30% epiboly, 50% epiboly, 80% epiboly, 5-10 somites, 15-20 somites, 24 hour post fertilization (hpf) ,48 hpf, 72 hpf and 96 hpf. The tissues were lysed in 500 µL of QIAzol Lysis Reagent (QIAGEN) and crumbled with scissors previously cleaned with NaOH 0.1 N, ethanol 96% and diethyl pyrocarbonate (DEPC) treated water. Embryos were lysed in 600 µL of QIAzol Lysis Reagent (QIAGEN) and RNA was extracted according to the supplier's instructions. Briefly 1:4 v/v chloroform was added to the lysate, left 10 min at RT and centrifuged at 12000 g at 4°C for 15 min to separate the aqueous phase from the organic components. Then the RNA was precipitated from the aqueous phase with a 1:1 v/v isopropanol followed by 10 min at RT and centrifugation at 12000 g at 4°C for 15 min. The pellet was washed with 400 µL ethanol 70%, centrifuged at 12000 g at 4°C for 15 min, air dried and resuspended in 30 µL of diethylpyrocarbonate (DEPC) treated water. DNase digestion was performed using the Turbo DNA Free Kit (Ambion) according with the manufacturer's instructions. RNA concentration was established by absorbance at 260 nm and RNA quality by agarose gel electrophoresis. Retrotranscription of 0.3 to 1 µg of RNA in a final volume of 20 µL was performed using the High Capacity cDNA Reverse Transcription kit (Applied Biosystems) according to the manufacturer's instruction.

Real time PCR (qPCR) analysis

p3h1 and *crtap* expression was evaluated in wild-type and mutant fish using the specific primers reported in Table 4.

Table 4. Primers used for amplification of *p3h1* and *crtap* target region by qPCR reaction. *dna15ta1*, *hatn10* and *loopern4* are the housekeeping genes used for normalization from Vanhauwaert et al. 2014.

Gene Of Interest (GOI)	Primers for qPCR	
	Sense	Reverse
p3h1	5'-ACATCACGGAAAGAGAGGTGG-3' (1112-1132)	5'-GTGTCTGGATCAACAAACGCT-3' (1203-1223)
β actin	5'- GAAGGAGATCACCTCTCTTGCTC -3' (995–1017)	5'- GTTCTGTTTAGAAGCACTTCCTGTG -3' (1188–1164)
crtap	5'-GAGCTGGCACTGAGAGACTT-3' (687-707)	5'-CCCGTCCATCGCAGATCATTA-3' (780-800)
dna15ta1	5'-TACTGTGCTCAAATTGCTTCA-3'	5'-AATGAGTACTGTGAACTTAATCCAT-3'
hatn10	5'-TGAAGACAGCAGAAGTCAATG-3'	5'-CAGTAAACATGTCAGGCTAAATAA-3'
loopern4	5'-TGAGCTGAAACTTTACAGACACAT-3'	5'-AGACTTTGGTGTCTCCAGAATG-3'

qPCR was performed in triplicate in a final volume of 25 µL using SYBR Select Master Mix (Applied Biosystem). qPCR cycle started with 10 min of denaturation at 95°C, followed by 40 cycles of 15 sec at 95°C, 30 seconds at the annealing temperature (68°C for *p3h1* and *β actin* and 60 °C for *crtap, dna15ta1*, *hatn10* and *loopern4*), 30 seconds at 72°C and terminated with a dissociation curve made of 1 min at 95°C, 30 seconds at 55°C and 30 seconds at 95°C. The relative expression of *p3h1* compared to the housekeeping *β actin* was obtained by ΔΔCt method. The relative expression of *crtap* compared to the average of three housekeeping *dna15ta1*, *hatn10* and *loopern4* was obtained by ΔΔCt method.

tmem 38b expression was evaluated for each sample in triplicate in a final volume of 25 µL using 0.125 µg of cDNA template, Taqman Universal PCR Master mix (Applied Biosystems) and commercial Taqman probes for *tmem38b* and *β- actin* (probe Dr03434781_m1 e Dr03432610_m1, Applied Biosystems). qPCR cycle started with 10 min of Taq activation at 95°C, followed by 40 cycles of 15 sec of denaturation at 95°C and 1 minute at 60°C.

The relative expressions of *tmem38b* compared to the housekeeping *β actin* were obtained by ΔΔCt method. The Mx3000P thermocycler (Stratagene) and the MxPro software (Stratagene) were used for both types of experiments.

In situ hybridization

The *tmem38b* DNA probe template was synthetized from the RT-PCR amplification of the of WT zebrafish mRNA using the following primer sense for exon 1 (5'-TCAATCTGAACGAGCTCGCATTT-3', 20-42 nt) and reverse for exon 10 (5'-AAGAAGCAGAAGCCAGCAAAAAG-3', 839-861 nt) of *tmem38b.* The amplicon was subcloned in the pGEM-T-Easy (Promega) vector and ligation was performed using T4 DNA ligase (Thermo Scientific) o/n at RT. Transformation, using DH5α competent cells, was obtained as described above. The colony PCR was then performed using the same primers used for the amplification of the region of interest. The positive colonies were picked and grown o/n in LB in presence of ampicillin 100 µg/mL. In order to obtain higher amount of the correct plasmid DNA, Qiagen Plasmid Maxi Kit (Qiagen) was used.

in situ hybridization requires a single strand RNA antisense probe able to bind *tmem38b* transcript sequence (ENSDART00000168983) and a sense probe, identical to *tmem38b* transcript sequence, as control.

In order to synthetize the RNA antisense probe, the plasmid was linearized by SacII (New England BioLabs) digestion, while for the sense RNA probe the plasmid was linearized by SpeI (Promega) digestion. Linearized plasmids were then purified using Nucleospin Gel and PCR Clean-up (Machinery-Nagel) kit and probes were *in vitro* transcribed with maxiscript SP6/T7 (Ambion) kit following the manufacturer's recommendations, using 1 µg of DNA as template. Transcription products were treated by DNAse digestion using Turbo DNA-*free* (Ambion) kit to eliminate the DNA template.

At least five embryos for age group (24, 48, 72, 96 and 120 hours post fertilization, hpf) were fixed in paraformaldehyde (PFA) 4% (w/v) o/n at 4°C, washed in PBS and dehydrated for 5 minutes per step in 75%/25%, 50%/50%, 25%/75% methanol/PBS and conserved in methanol 100% at -20°C. Samples were then rehydrated and washed in PBS-T (PBS + Tween 0.1%).

Tissues were digested with proteinase K 10 µg/mL at different times depending on the age of embryos: 10 minutes at 24 hpf and 30 minutes from 48 hpf. Once digested samples were fixed in PFA 4% (w/v) for 20 minutes and then washed in PBS-T. A blocking solution 50%/50% PBS-T/ hybridization buffer (formamide 50%, Fluka 47670), SSC 20X (NaCl 3 M, sodium citrate 0.3 M, pH 5), EDTA 5 mM pH 8, Tween-20 0.2%, CHAPS 0.5%) was added together with yeast RNA 50 µg/mL

(Yeast RNA Sigma R-6625) and heparin 100 µg/mL (Sigma H-7005) and samples were incubated at 64°C for at least 1 hour. A new hybridization buffer, added with specific antisense or sense probes (2 ng/µL), previously denatured at 90 °C for 10 minutes, was then prepared and embroys were incubated o/n at 64°.

Samples were then washed in hybridization buffer and SSC (Hyb/SSC 2x 75/25, Hyb/SSC 2x 50/50, Hyb/SSC 2x 25/75) at 64 °C and finally incubated in SSC 2x for 10 minutes and in SSC 0.2x for 30 minutes at 64°C.

Embryos were washed in piperazine-N,N'-bis (ethanesulfonic acid), 1,4-piperazinediethanesulfonic acid (PIPES,Sigma Aldrich) NaCl 0.5 M for 10 minutes and then treated with RNAse T1 200 U/mL and RNAseA 10µg/mL in PIPES NaCl 0.5 M for 10 minutes at 37°C and for 5 minutes at RT. Blocking with MAB ($C_4H_4O_4$ 0.15 M, NaCl 0.15 M ph 7.5) and 2% blocking Boheringer reagent (Roche 1096176) was performed for 1 hour at RT. Samples were incubated with anti-digoxigeninAP antibody (anti-DIG) (11093274901, Roche), 1:5000 in MAB blocking, o/n at 4°C.

After several washes in MAB, MABT (MAB + Tween-20 1%), Tris HCl 0.1 M pH 9.5 and Tween 0.1 %, NTMT (NaCl 0.1 M, Tris HCl pH 9.5 0.1 M, $MgCl_2$ 50 mM and Tween-20 1%) was added for 30 minutes. Samples were incubated in the dark with the solution NTMT, NBT (nitro blue tetrazolium) (Promega S380C) and BCIP (5-bromo-4-chloro-3-indolyl-phosphate) (Promega S381C), until the appearance of a violet signal.

Images of fish were acquired using a Leica M165 FC microscope connected to a Leica DFC425 C digital camera.

Statistical analysis

Statistical analysis was performed using Excel and SigmaPlot. All values were expressed as mean ± standard deviation (SD) or mean ± standard error of the mean (SEM), as indicated. Statistical comparisons were based on Student's T-test or Rank Sum Test. p value < 0.05 was considered significant.

Results

Despite the genome duplication event that took place during teleost phylogenetic differentiation (Postlethwait et al. 1998), one copy of *p3h1*, *crtap* and *tmem38b* genes is present in zebrafish. *p3h1* maps on chromosome 11 and it consists of 15 exons encoding for the 829 amino acids P3h1 protein. *crtap* gene is on chromosome 19, is composed by 7 exons and encodes for the 396 amino acids Crtap protein. *tmem38b* is on chromosome 21, composed by 11 exons and encodes for 289 amino acids Tmem38b protein.

First, using the genome browser Genomicus (v89.02), a synteny analysis to investigate the conservation of the chromosomal region surrounding *p3h1*, *crtap* and *tmem38b* among zebrafish and other vertebrates was performed. The analysis revealed a synteny block including *p3h1* locus, identified by the presence in all the analysed species of two conserved flanking genes (*Cldn19* and *C1Orf50/zge:112255*) (Figure 8 A). Similarly, six genes (*susd5*, *fbx12*, *clasp2*, *ubp1*, *pdcd6ip* and *arpp21*) were conserved around *crtap* locus in all analysed species, expect from the frog genome, demonstrating the presence of a synteny block (Figure 9 A). A synteny block was observed also for *Tmem38b*, identified by the presence in all the analysed species of two conserved flanking genes (*rad23B* and *klf4*) (Figure 10 A).

To evaluate the conservation of P3h1, Crtap and Tmem38b protein, a Blastp analysis was performed with UniProt (http://www.uniprot.org/blast/). Amino acid (AA) sequence alignments showed that zebrafish P3h1 (Figure 8 B) and Crtap (Figure 9 B) share 45% and 64% of AA identity with the human corresponding genes, respectively, while Tmem38b shares the 43% (Figure 10 B).

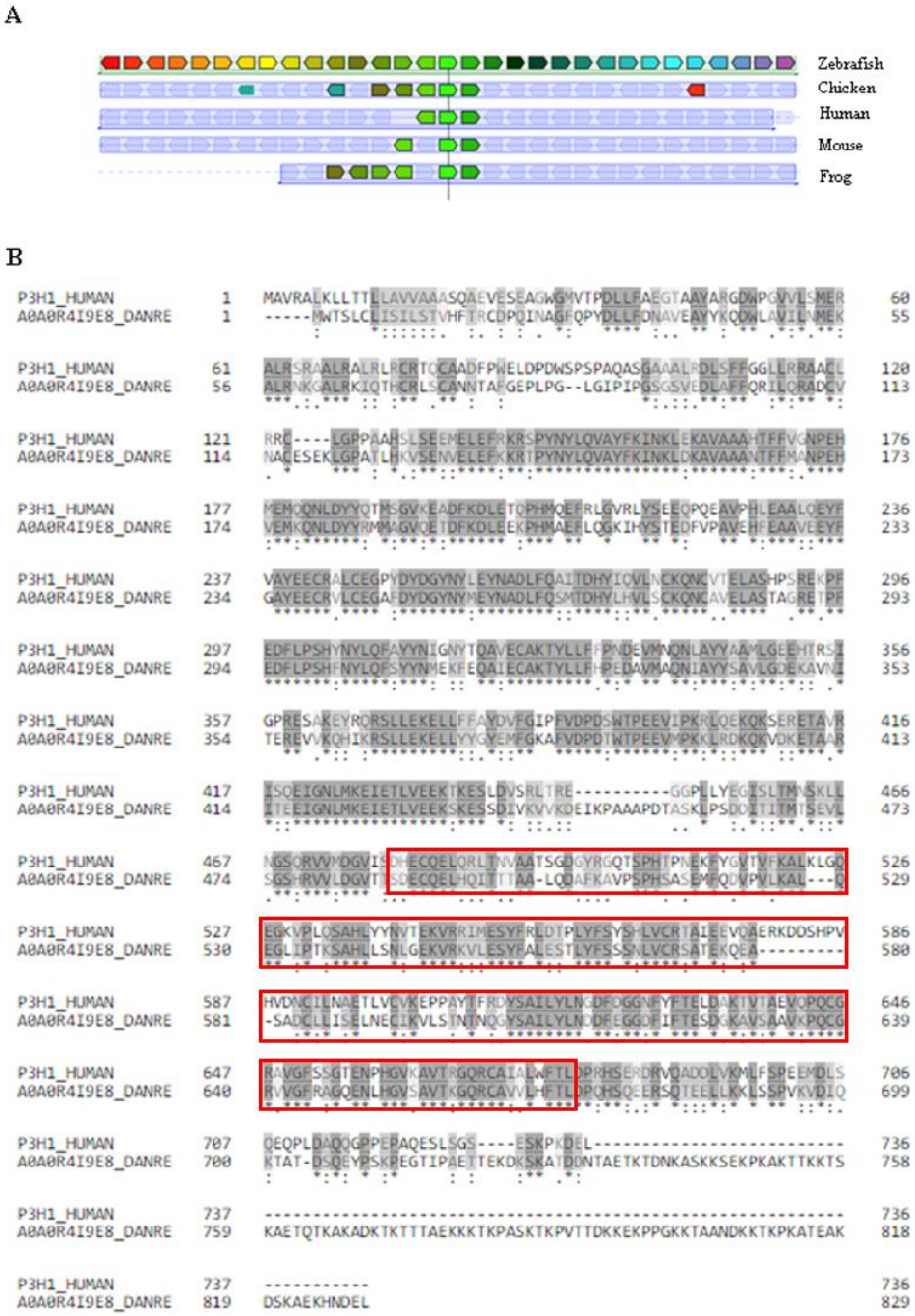

Figure 8. ***In silico*** **analysis of** ***p3h1*** **in zebrafish. (A)** Synteny map comparing the genes flanking *p3h1* locus among zebrafish (*D. rerio*), chicken (*G. gallus)*, human (*H. sapiens*), mouse (*M. musculus*) and frog (*X. tropicalis)* chromosomes. **(B)** Alignment of the *H. sapiens* and *D. rerio* P3h1. The light and dark grey colours indicate the similar and identical residues, respectively and the red boxes delimit the *p3h1* catalytic domain. Interestingly, 108/208 amino acids of the zebrafish catalytic domain are identical to the human sequence, raising the identity for this region to over 52%.

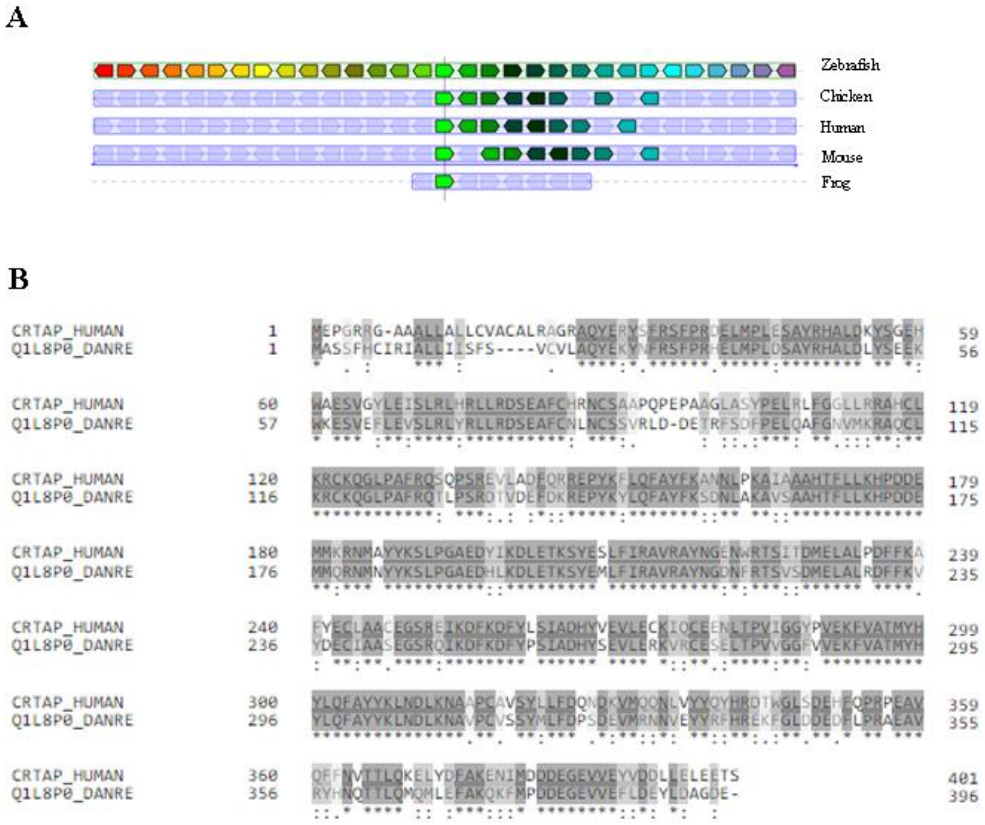

Figure 9. *In silico* analysis of *crtap* in zebrafish. (A) Synteny map comparing the genes flanking *crtap* locus among zebrafish (*D. rerio*), human (*H. sapiens*), mouse (*M.musculus*), chicken (*G. gallus)* and frog (*X. tropicalis)* chromosomes. **(B)** Alignment of the *H. sapiens* and *D. rerio* Crtap. The light and dark grey colours indicate the similar and identical residues, respectively.

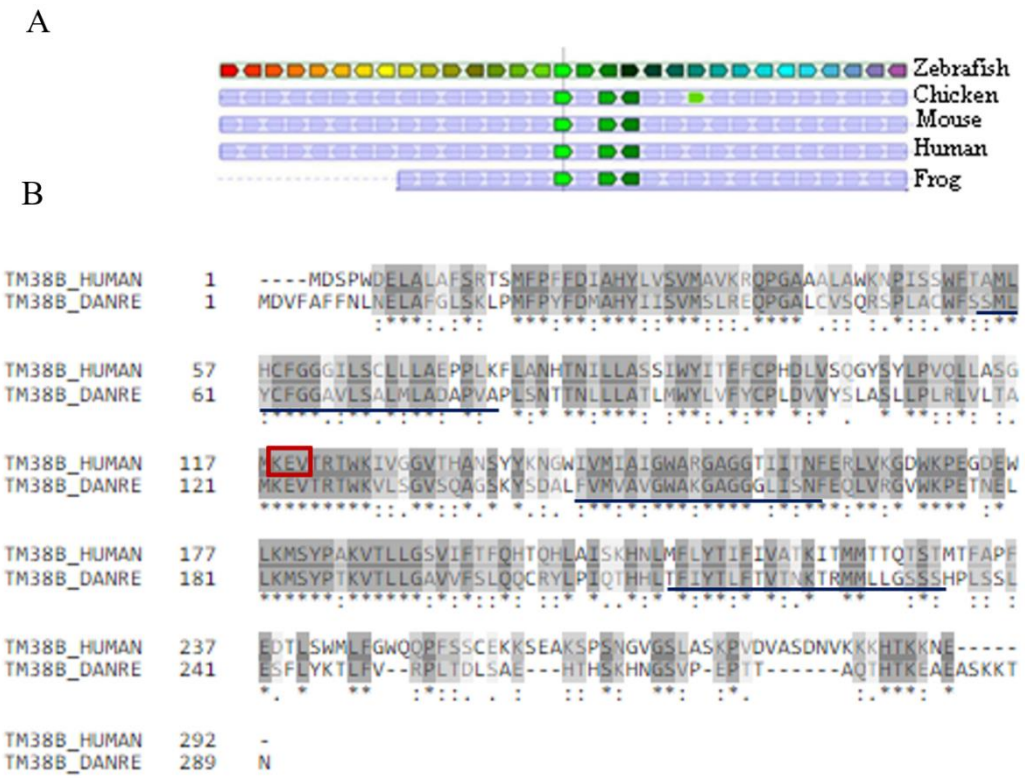

Figure 10. ***In silico*** **analysis of** ***tmem38b*** **in zebrafish. (A)** Synteny map comparing the genes flanking *tmem38b* locus among zebrafish (*D. rerio*), human (*H. sapiens*), mouse (*M.musculus*), chicken (*G. gallus)* and frog (*X. tropicalis)* chromosomes. **(B)** Alignment of the *H. sapiens* and *D. rerio* Tmem38b. The light and dark grey colours indicate the similar and identical residues, respectively. Blue lanes indicate the putative M1, M2 and M3 transmembrane domains. Red box indicates the KEV motif, necessary for the formation of the channel.

Generation of knock out fish using the CRISPR/Cas9 gene editing system

The first aim was to generate Osteogenesis Imperfecta (OI) type VII, VIII and XIV zebrafish models using the CRISPR/Cas9 gene editing system.

Targets selection and constructs generation

The identification of the genomic targets in *p3h1*, causative of OI type VIII, in *crtap*, causative of OI type VII and in *tmem38b*, causative of OI type XIV, was obtained using the online software CHOPCHOP. Potential target sequences in *p3h1*, *crtap* and *tmem38b* correspond to stretches of 20-bp, characterized by a 5'-GG dinucleotide, needed to optimize T7 promoter efficiency. A protospacer-adjacent motif (PAM) sequence, NGG, is present in the genome targeted sequence at the 3'-end of the guide for efficient Cas9 binding and cutting. Based on these parameters, the sequences for the targeting were chosen on exon 2 (5069-5091 nt, NC_007122.6) for *p3h1*, on exon 1 (186-208 nt, NC_007130.6) for *crtap* and on exon 7 for *tmem38b* (11391-11416 nt, NC_007132.7). For all guide RNAs (gRNAs), the number of potential off targets was zero and the GC-content was in the accepted range (40-80%), being 57% for *p3h1*, 61% for *crtap* and 52% for *tmem38b* (Figure 11).

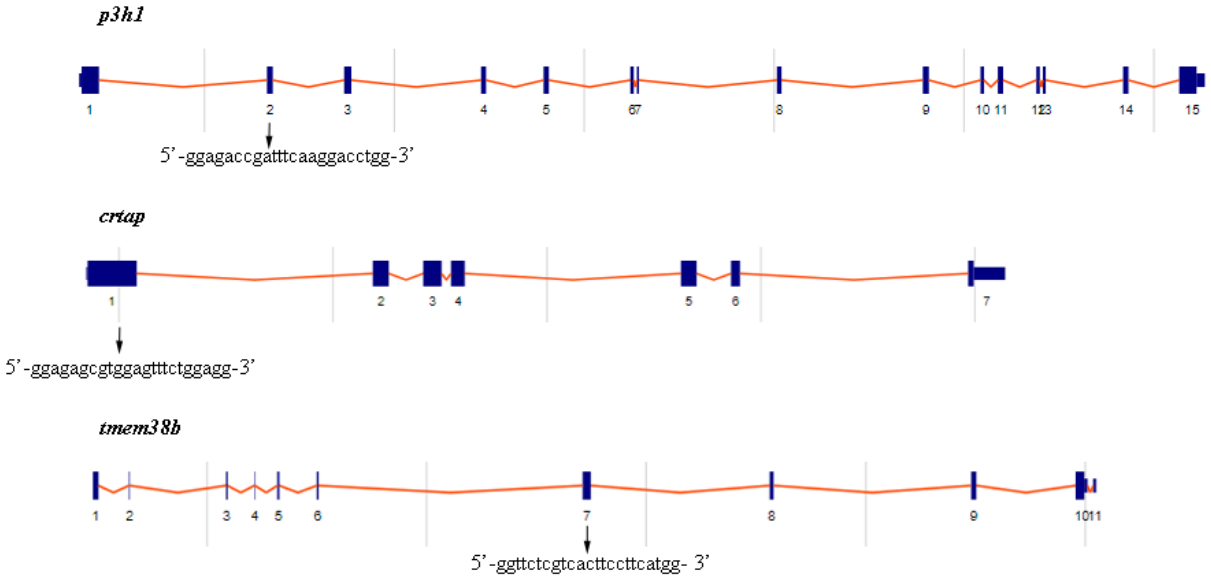

Target sequence	Genomic location	Exon	Strand	GC (%)	Off targets		
					0	1	2
ggagaccgatttcaaggacctgg	chr11:40333817	2	-	57	0	0	0
ggagagcgtggagtttctggagg	chr19:43039880	1	+	61	0	0	0
ggttctcgtcacttccttcatgg	chr21:358634	7	-	52	0	0	0

Figure 11. Selection of genomic target sequences in *p3h1, crtap* and *tmem38b*. Schematic representations of *p3h1, crtap* and *tmem38b* genes with their exons (blue rectangles) and introns (red lines). Target sequences located in exon 2, exon 1 and exon 7 respectively are indicated. Potential off targets, based on the number of mismatches (0, 1 or 2), are shown in the table. GG dinucleotide at the 5' end of the gRNA is indicated in red and PAM sequence is underlined.

The synthesis of the specific gRNAs and of the Cas9 mRNA was performed using a CRISPR/Cas9 system. Two different plasmids commercially available were used. One of them carries a cloning site for the insertion of the gRNA sequence of interest under the control of T7 promoter and the second contains the Cas9 endonuclease coding sequence with nuclear localization signals (nls) at both amino and carboxyl end and codons optimized for zebrafish expression (nls-zCas9-nls) (Jao et al. 2013). The cloning experiment for the gRNAs was performed as described in M&M. All the desired targeting gRNAs and the Cas9 mRNAs were generated by *in vitro* transcription after plasmids linearization.

Microinjection and identification of F0 founders' mutations

p3h1, *crtap* or *tmem38b* gRNA (12.5 ng/µL), respectively and Cas9 mRNA (300 ng/µL) mixed with the red tracer rodhamine, were co-injected into one/two-cell-stage embryos. A successful injection was determined by the visualization at 1 day post injection of the tracer inside the embryo under a fluorescence-dissecting microscope. At 1 dpf around 90% of the survived injected embryos exhibited positive fluorescent signal and were used to assess the efficiency of the targeting. We randomly selected 10 embryos and, after DNA extraction and amplification of the genomic targeted region, we quantified the mutagenesis rate using the T7 endonuclease I (T7EI) assay. Briefly, after denaturation and renaturation, the DNA amplicon should contain heteroduplex only when mutations are present. Being able to recognize and digest heteroduplex, T7 should cut only *heteroduplex* amplicon (Figure 8 A). Taking into account that Cas9 cuts the target DNA 3-5 bp upstream of the PAM, all mutations were expected to occur at the 3' end of the target sequence. Indeed, *mosaic* fish displayed the two bands expected from digestion, 126 bp and 318 bp for *p3h1*, 178 bp and 281 bp for *crtap* and 80 and 132 for *tmem38b*. On the contrary WT fish showed the undigested amplicon of 444 bp for *p3h1*, 459 bp for *crtap* and 212 bp for *tmem38b* (Figure 12 B, C, D). Successfully targeted embryos were *mosaic*, carrying different mutations introduced by the error-prone non-homologous end joining (NHEJ) repair system, which is the mechanism activated after the double-stranded breaks catalysed by the Cas9 endonuclease. Indeed, the electrophoretic signal obtained from some of the sequenced identified mosaic fish appeared disturbed and decreased in the target region due to the presence of more than one mutation in the same *locus* (Figure 12 E). The mutagenesis rate was high for all the targeted genes, 77% for *p3h1*, 92% for *crtap* and 63% for *tmem38b*.

The subcloning in the TA cloning vector of the amplicons containing the targeted sequences obtained from the F0 *mosaic* population and their sequencing were performed to identify the single mutations. The presence of insertions/deletions (indels) in *p3h1*, *crtap* and *tmem38b* F0 fish was detected as expected as consequence of the activation of NHEJ repair (Table 5 and 6).

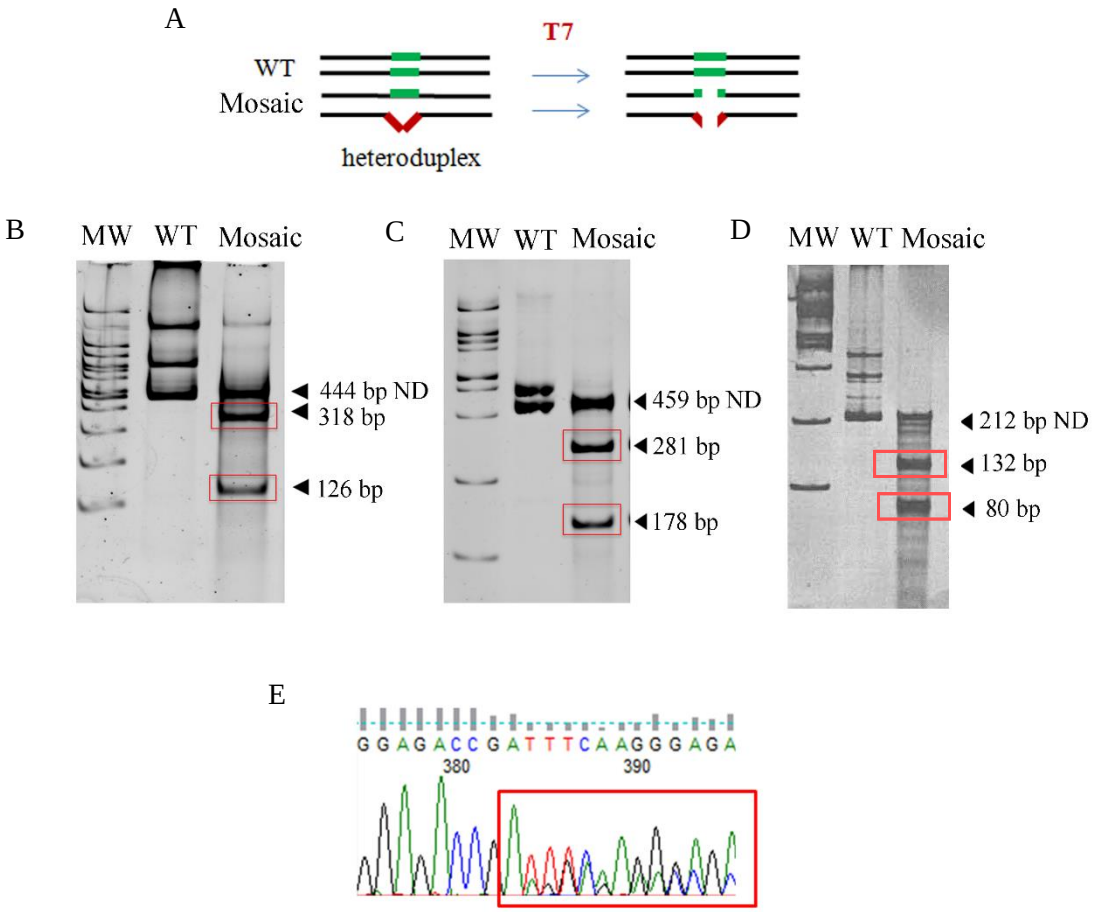

Figure 12. **Screening strategy for the identification of *mosaic* fish. (A)** Schematic screening strategy for the identification of the mutant allele following T7 digestion of the amplicon surrounding the mutation. PCR was performed in the region surrounding the target sites. In red the mutated allele. The amplicons were denatured and renatured and T7 endonuclease digestion was performed. **(B, C, D)** Representative gel images indicating the expected bands after T7 assay, the undigested WT band and the presence of the cleaved bands (red boxes) in *mosaics* resulting from the digestion of *p3h1***(B)**, *crtap* **(C)** and *tmem38b* samples **(D)**. MW: 100 bp molecular weight marker; ND: not digested. **(E)** Representative sequence of the amplicon obtained from a F0 *mosaics* shows the disturbed signal at the level of the target sequence (red box).

Table 5. Mutations identified in *p3h1* and *crtap* F0 fish.

DNA mutation	Protein defect	Frequency
Gene Of Interest (GOI): p3h1		
c.640_645delAAGGAC	p.(Lys195_Asp196del)	7,9% (3/38)
c.644_645delAC	*p.Asp196Argfs*224*	2,6% (1/38)
c.645_650delCCTGGA	p.(Asp196_Leu197del)	23,7% (9/38)
c.638_647delTCAAGGACCTinsACAA	p.Phe194Tyr, p.(Asp196_Leu197del)	2,6% (1/38)
c.636_649delTTTCAAGGACCTGG	*p.Asp193Glufs*220*	2,6% (1/38)
c.641_644delAGGA	*p.Lys195Thrtfs*263*	2,6% (1/38)
c.644_645insGTTGTGTGGGATCCAGGTTTCCCA	p.(Lys195_Asp196del), p.Phe194_Leu195ins9	2,6% (1/38)
c.644_645insGGAGAACCTGGAGGAGACCGATTTCAAGGAGGAGAA	p.(Lys195_Asp196del), p.Phe194_Leu195ins13	2,6% (1/38)
c.644_645insGAAA	*p.Asp196Glufs*226*	2,6% (1/38)
c.642_643delGG	*p.Asp196Pro*224*	10,5% (4/38)
Gene Of Interest (GOI): crtap		
c.183_267delGAAGGAGAGCGTGGAGTTTCTGGAGGTCAGTCTGCGGCTCTACCGGCTGCTCCGGGACAGCGAGGCCTTCTGTAGCCTCAACTG	p.(Trp57_Asn84del)	3,3% (1/30)
c.201_233delTCTGGAGGTCAGTCTGCGGCTCTACCGGCTGCT	p.(Leu64_Leu74del)	3,3% (1/30)
c.199_207delTTTCTGGAG	p.(Phe63_Glu65del)	40% (12/30)
c.202_210delCTGGAGGTC	p.(Leu64_Val66del)	3,3% (1/30)
c.201_209delTCTGGAGGT	p.(Leu64_Val66del)	6,7% (2/30)
c.200_213delTTCTGGAGGTCAGT	*p.Phe63Serfs*77*	3,3% (1/30)
c.199_217delTTTCTGGAGGTCAGTCTGCinsCTTGT	*p.Phe63Leufs*76*	3,3% (1/30)
c.199_202delTTTCinsCG	*p.Phe63Argfs*80*	6,7% (2/30)
c.194T>C, c.201_202delTCinsCAG	p.Val61Ala, p.Leu64Arg	3,3% (1/30)
c.194_218delTGGAGTTTCTGGAGGTCAGTCTGCG	*p.Val61Glyfs*99*	6,7% (2/30)

Table 6. Mutations identified in *tmem38b* F0 fish**.**

DNA mutation	Protein defect	Frequency
	Gene Of Interest (GOI): tmem38b	
c. 529_532delGAAG	P.Glu123*	6 % (1/16)
c. 523_529delATGAAGG	*p.Met121Lysfs*122*	6 % (1/16)
c.525_538delAAGGAAGTGACGA	p.*Lys122Asnfs*150*	6 % (1/16)
c. 524_540delTGAAGGAAGTGACGAGA	*p.Met121Asnfs*149*	6 % (1/16)
c. 528_529insTGACGA	p.Glu123*	6 % (1/16)
c. 524_527delTGAA	*p.Met121Arg*123*	13 % (2/16)
c. 527_539delAAGGAAGTGACGAinsTGACGAGTGACGT	p.Lys122Ser; Glu123Asp; *Val124Glufs*125*	6 % (1/16)
c. 526_540delAAGGAAGTGACGAGA	p.Lys122_Arg126del	6 % (1/16)
c. 523_532 delATGAAGGAAG	p.Met121*	6 % (1/16)
c. 527_528delAGinsTATGAAGCCAT	*p.Lys122Ilefs*123*	6 % (1/16)
c.526_528del AAGinsCACCT	p.Lys122His; Glu123Leu; *Val124Lysfs*125*	6 % (1/16)
c. 524_532delTGAAGGAAG	p. Lys122_Val124del	6 % (1/16)
c. 524_530 del TGAAGGA	*p.Met121Lysfs*122*	6 % (1/16)
c. 526_527insCGAGAACC	p.Lys122Thr; Glu123Arg; Val124Thr; Thr125Arg; *R126Kfs*127*	6 % (1/16)
c. 523_527delATGAA_insT	p.Met121Trp; Glu123*	6 % (1/16)
C. 526_532delAAGGAAG	p.Lys122*	6 % (1/16)
c. 528_531delGGAA	p. Glu123*	13 %(2/16)
c. 529delG	*p.Glu123Lysfs*124*	6 % (1/16)
c. 525_531delGAAGGAAinsTAGGCT	p.Met121Ile; Lys122Arg; *Glu123Leufs*124*	6 % (1/16)
c. 527_533 del AGGAAGTinsCGA	p.Lys123Thr; Glu123Arg; Val124Arg; Thr125Glu; Arg126Pro;Thr127Gly; Trp128Arg; *Lys129Phefs*130*	6 % (1/16)

To determine whether the Cas9-induced mutations were germ line transmitted, the F0 *mosaic* fish were first crossed, upon reaching sexual maturity, with AB wild type (WT) and several pools of embryos were collected at 1 dpf and screened again with T7EI assay. The fish able to generate mutated progeny were used to obtain the F1 founders, with the *p3h1*, *crtap* or *tmem38b loci* carrying a specific mutation in heterozygosis.

Selection of F1 heterozygous and generation of F2 homozygous mutants

The F0 germline mutants were crossed with AB WT and the progeny was grown until it reached the minimum size required for performing the genotyping by tail clipping (about 1 month). The DNA extracted from the tail was used for the T7 endonuclease assay, as described above, in order to discriminate WT from heterozygous fish. Upon denaturation and renaturation of the amplicon of the region surrounding the target site, the samples from WT were not cleaved by T7 enzyme, whereas the ones from heterozygous fish were digested. The sequencing of the identified heterozygous F1 fish allowed us to find several specific mutations mainly responsible for frameshifts, causing the introduction of premature stop codon in the protein (Table 7). Since our final aim was to obtain knock out mutants, more than one line with a stop codon for each target protein was selected and used for the F2 generation. Two mutants carrying a stop codon in position 202 and 266, respectively, were chosen for *p3h1*. On the contrary, two lines with different mutations in the DNA, both causing the formation of a stop codon in the protein at position 80 were chosen for *crtap*. Four lines were obtained for *tmem38b*. The first carries 8 amino acids deletion including the KEV tripeptide, two lines are characterized by premature stop codons in position 122 and one is characterized by premature stop codon in position 124. Among these lines, to generate and deeply characterize the F2 population, we used the *p3h1* carrying the stop codon at amino acid 266 (c.645delCinsGGAGAA), the *crtap* carrying the stop codon at amino acid 80 (c.199_202delTTTCinsAG) and the *tmem38b* carrying a deletion of 8 amino acids in which the KEV motif is contained (c.355_378del24nt).

Table 7. Mutations identified in *p3h1*, *crtap* and *tmem38b* F1 fish population. F1 founders used for F2 generation are indicated by bold edges.

DNA mutation	Protein defect	Frequency
Gene Of Interest (GOI): p3h1		
c.637_643delTTCAAGGinsCAAGGTTTTACCTTGATTTT	*p.Phe194Glnfs*202*	2,6% (1/38)
c.631_651delACCGATTTCAAGGACCTGGAG	p.(Thr192_Glu198del)	5,3% (2/38)
c.645delCinsGGAGAA	*p.Asp196Glufs*266*	5,3% (2/38)
c.644_645insGGAGGAGAAAA	*p.Asp196Glufs*269*	2,6% (1/38)
c.643delG	*p.Asp196Thrfs*264*	5,3% (2/38)
c.643_644delGAinsCCATCT	*p.Asp196Pro*fs*226	2,6% (1/38)
c.645_653delCCTGGAGGA	p.(Asp196_Glu198del)	2,6% (1/38)
c.634_646delGATTTCAAGGACC	*p.Asp193Trpfs*260*	7,9% (3/38)
c.645_648delCCTGinsGGA	*p.Asp196Glufs*264*	2,6% (1/38)
c.631_651delACCGATTTCAAGGACCTGGAG	p.(Thr192_Glu198del)	2,6% (1/38)
c.645_650delCCTGGA	p.(Asp196_Leu197del)	23,7% (9/38)
Gene Of interest (GOI): crtap		
c.199_212delTTTCTGGAGGTCAGinsGTCAA	p.(Phe63_Leu68del), p.Glu62_Arg63insValAsnLeu	3,3% (1/30)
c.203_210delTGGAGGTC	*p.Leu64Glnfs*78*	3,3% (1/30)
c.199_202delTTTCinsAG	*p.Phe63Serfs*80*	6,7% (2/30)
c.199_202delTTTCinsCG	*p.Phe63Serfs*80*	6,7% (2/30)
c.200_209delTTCTGGAGGT	*p.Phe63Serfs*104*	3,3% (1/30)
Gene Of interest (GOI): tmem38b		
c.355_378del24nt	*p.(*Ala120_Thr127*)*	
c.367delG	*p.Glu123Lys*124*	
c.362_368delTGAAGGA	*p.Met121del*122*	
c.360_366ATGAAGG	*p.Met121del*122*	

Male and female heterozygous fish for the same mutation were crossed to obtain the F2 mutants. Since T7 assay specifically recognizes heteroduplex, a second type of screening, based on the use of restriction enzymes, was adopted. Digestion maps allowed us to choose the proper enzyme for *p3h1* and *crtap*, able to recognize a unique cutting site present in the WT sequence, which is removed by the mutation. Following PCR amplification and specific restriction enzyme digestion the cleavage only of the WT allele was expected. For *p3h1*, the restriction enzyme used was Eco0109I (Figure 13 A), while for *crtap* was BpmI (Figure 13 B). For *tmem38b* the 24 nt deletion selected to generate F2

population allows to discriminate the genotype based on the different size of the PCR amplification product (Figure 13 C).

After the identification of *crtap* and *p3h1* homozygous mutants, fish were characterized to validate them as models for OI type VII and VIII. The characterization of *tmem38b* mutants is still ongoing.

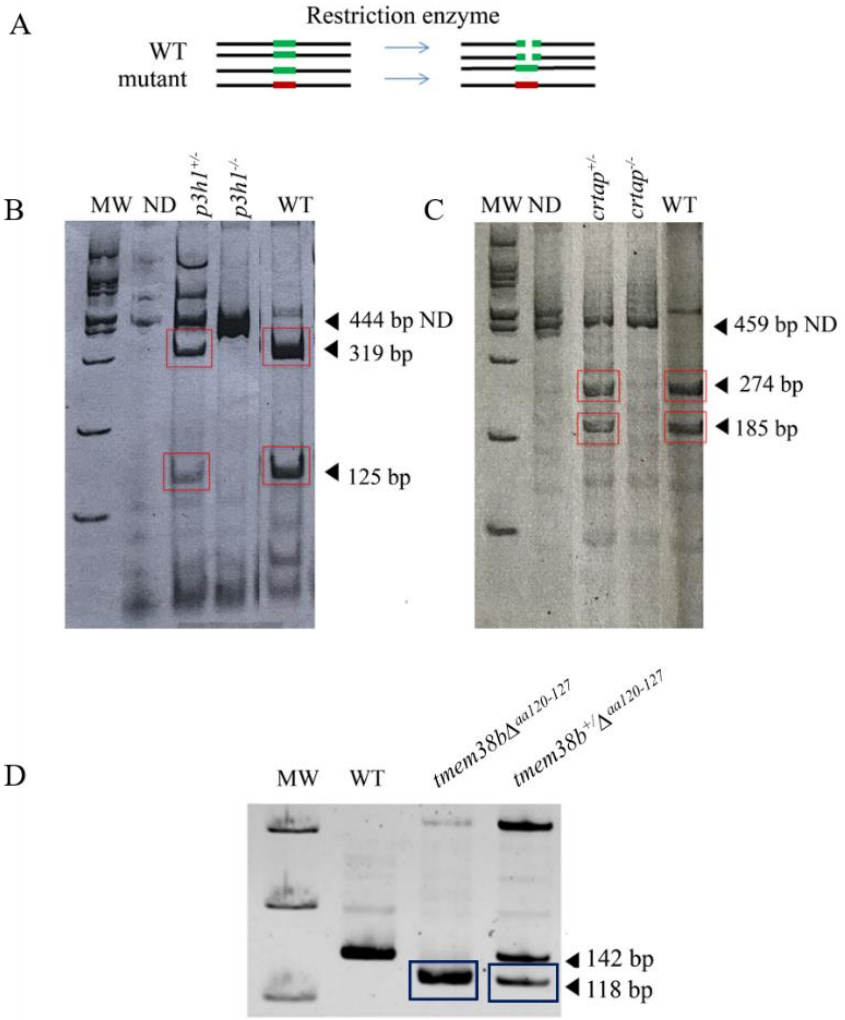

Figure 13. Screening of F2 population. (A) Schematic screening strategy for the identification of the mutant allele following restriction enzyme digestion of the amplicon surrounding the mutation (red lines). **(B, C)** Representative gels with expected bands (red rectangles) after restriction enzyme digestion for *p3h1* and *crtap*. **(D)** PCR amplification product for the genotyping of *tmem38b* mutants. Blue rectangles indicate the presence of deletion. MW: 100 bp molecular weight marker; ND: not digested.

Validation of p3h1 and crtap mutant fish as OI models

In order to validate our mutants as recessive OI models, a deep phenotypic characterization of both larvae and adult fish was performed.

p3h1 and crtap mutants are shorter compared to wild type

The standard length (SL) of homozygous, heterozygous and WT zebrafish was measured, as described in M&M, at 1, 2, 3, 4, 8 and 24 (for *p3h1*) or at 1, 2, 3 and 8 (for *crtap*) weeks post fertilization (wpf) (Supplementary Table 1 and 2). Heterozygous fish displayed a similar length compared to WT at all analysed ages.

The SL of *p3h1* homozygous fish was comparable to WT values at 1 and 3 wpf, with a slight difference at 2 wpf **(p = 0.048)**. It became definitively shorter from 4 wpf (**p = 0.015**) and this difference increased at 8 wpf (**p = 0.009**) and at 24 wpf (**p = 0.004**) (Figure 14 A).

Interestingly, *crtap* homozygous fish were shorter than WT starting from 1 wpf (**p = 0.003**) and consistently remained shorter at 2 wpf (**p = 0.002**), at 3 wpf (**p = 0.001**) and at 8 wpf (**p = 0.002**) (Figure 14 B).

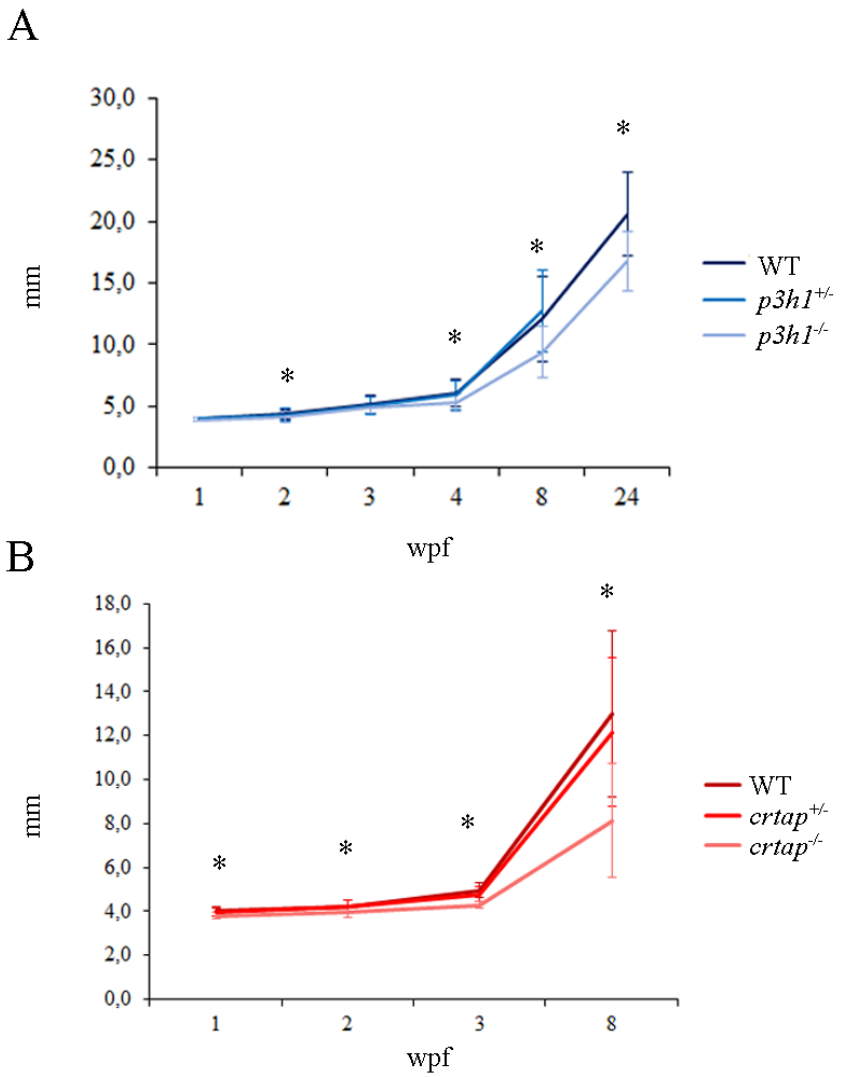

Figure 14. Growth curves of WT and heterozygous and homozygous mutant fish. (A) *p3h1* KO become definitively shorter then WT from 4 wpf. **(B)** *crtap* KO are shorter respect to WT starting from 1 wpf and the difference increases in adulthood. * $p<0.05$

Mutants display reduced bone mineralization and skeletal abnormalities

Whole-mount alizarin red staining was performed to evaluate vertebrae mineralization. The tendency to have a lower number of mineralized vertebrae in mutants compared to WT was detected both in *p3h1*$^{-/-}$and *crtap*$^{-/-}$ at 2 wpf, even if no statistical significance was reached (*p3h1*: **p = 0.206**, *crtap*: **p = 0.149**). This difference was not observed at 3 wpf in *p3h1* mutants, which have the same number of mineralized vertebrae of both WT and heterozygotes (**p = 0.686**), but it was present in *crtap*$^{-/-}$ (**p = 0.007**) (Figure 15A, 15 B) (Supplementary Table 3).

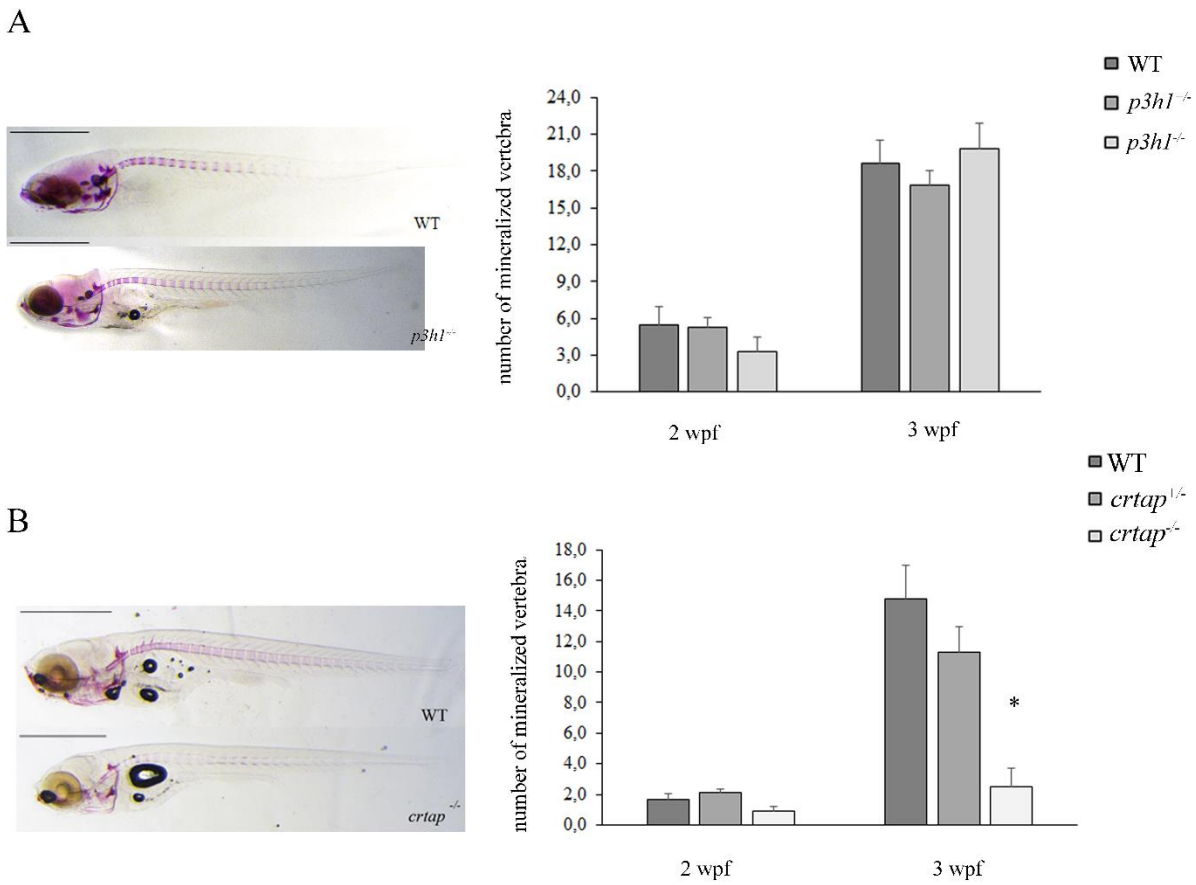

Figure 15. Analysis of vertebrae mineralization. (A) *p3h1* mutants' vertebrae mineralization at 2 (WT: n = 29, *p3h1*$^{+/-}$: n = 84, *p3h1*$^{-/-}$: n = 24) and 3 wpf (WT: n = 22, *p3h1*$^{+/-}$: n = 48, *p3h1*$^{-/-}$: n = 20). Data are expressed as mean ± standard error of the mean (SEM). (B) *crtap* mutants' vertebrae mineralization at 2 (WT: n = 28, *crtap*$^{+/-}$: n = 53, *crtap*$^{-/-}$: n = 19) and 3 wpf (WT: n = 11, *crtap*$^{+/-}$: n = 18, *crtap*$^{-/-}$: n = 5). Data are expressed as mean ± SEM.

Also, the evaluation of the cranial bones of WT and *p3h1*$^{-/-}$ and *crtap*$^{-/-}$ at 1 and at 2 wpf revealed a mineralization delay in mutant fish. We analysed the hyomandibular bone (HM) and the ceratohyal bone (CHB), characterized by endochondral ossification and the notochord (NC), example of perichordal ossification (Figure 16). Three classes of mineralization were identified, namely beginning, incomplete and complete based on the level of alizarin red staining.

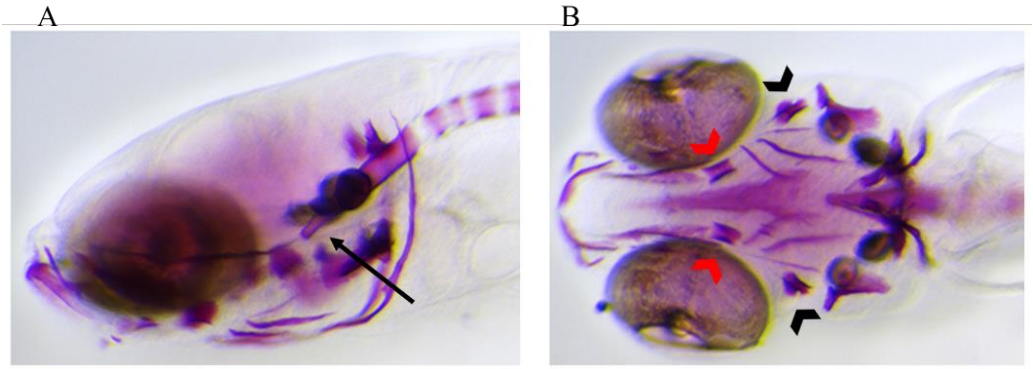

Figure 16. Cranial bones analysed following alizarin red staining. The black arrow in the lateral view **(A)** indicates notochord (NC). The red arrowhead in the ventral view **(B)** indicates ceratohyal bone (CHB) and the black arrowhead indicates hyomandibular bone (HM).

At 1 wpf, a slight delay in the mineralization of the three bones analysed was observed in *p3h1* mutants, compared to controls. *crtap* mutants showed, at 1 wpf, a significant difference in the mineralization of all the three bones analysed, compared to WT (NC: p = 0.043; HM: p = 0.012; CHB: p = 0.03) At 2 wpf this difference was observed also in *p3h1*$^{-/-}$ (NC: p = 0.003; CHB: p = 0.002) and was maintained in *crtap*$^{-/-}$ (NC, HM, CHB: p < 0.001), compared to WT (Figure 17, 18).

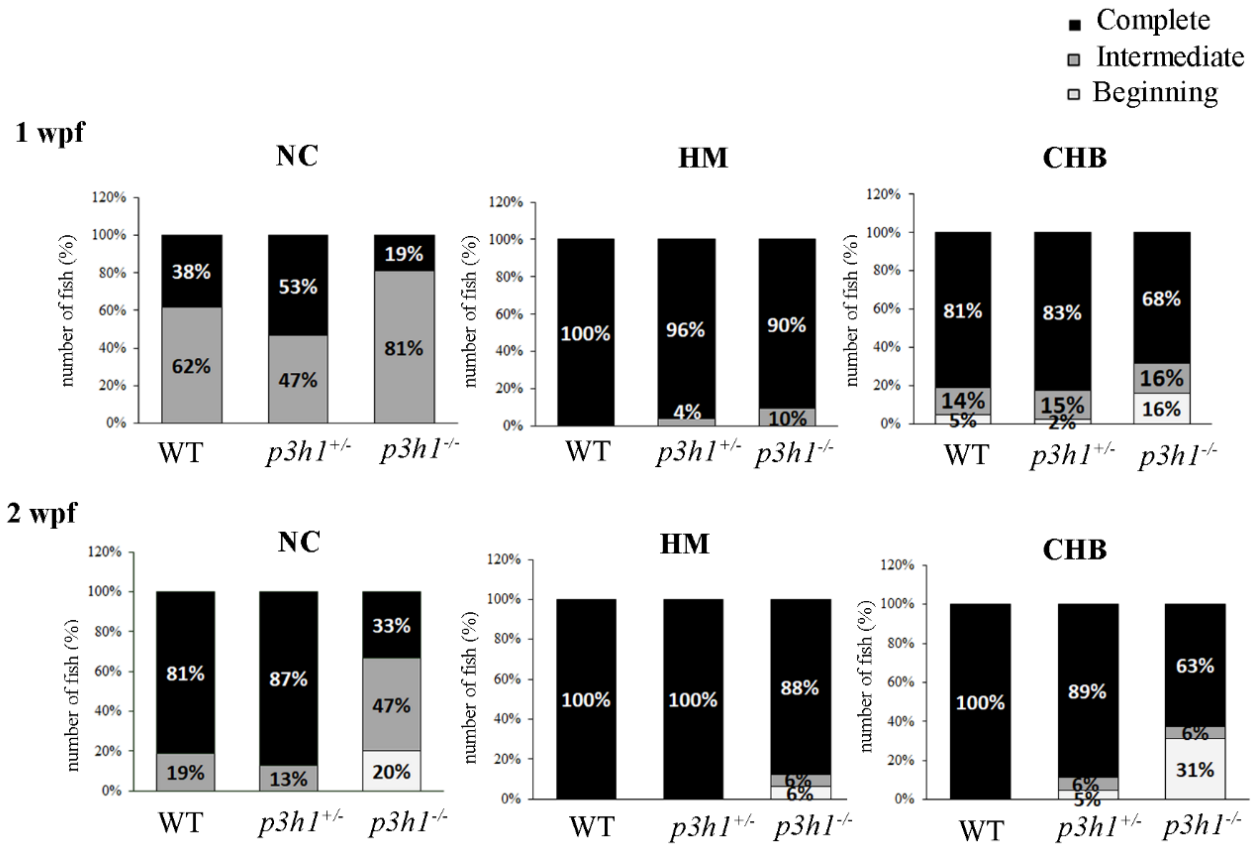

Figure 17. Mineralization level of cranial bones. A mineralization delay in *p3h1* mutants compared to controls at 1 (WT: n = 21, *p3h1*$^{+/-}$: n = 45, *p3h1*$^{-/-}$: n = 21) and at 2 (WT: n = 22, *p3h1*$^{+/-}$: n = 63, *p3h1*$^{-/-}$: n = 16) wpf is evident.

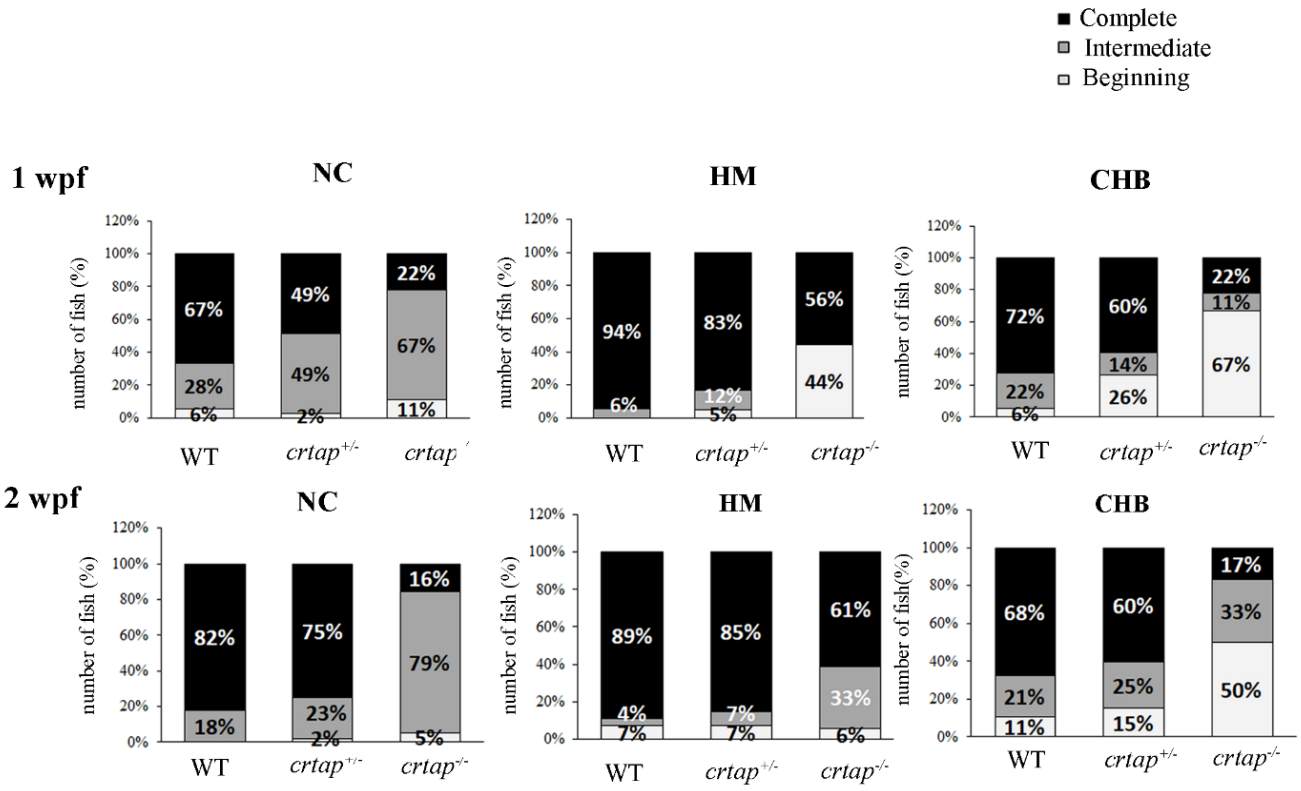

Figure 18. Mineralization level of cranial bones. A mineralization delay in *crtap* mutants compared to controls at 1(WT: n = 18, *crtap* $^{+/-}$: n = 41, *crtap* $^{-/-}$: n = 9) and at 2 wpf is evident (WT: n = 28, *crtap* $^{+/-}$: n = 52, *crtap* $^{-/-}$: n = 19).

A general disorganization of the spine was detected in adult *p3h1*$^{-/-}$ and *crtap*$^{-/-}$ fish by X-Rays at 8 wpf (Figure 19). Mutants were characterized by a deformed vertebral column with vertebrae compression along the antero-posterior axis.

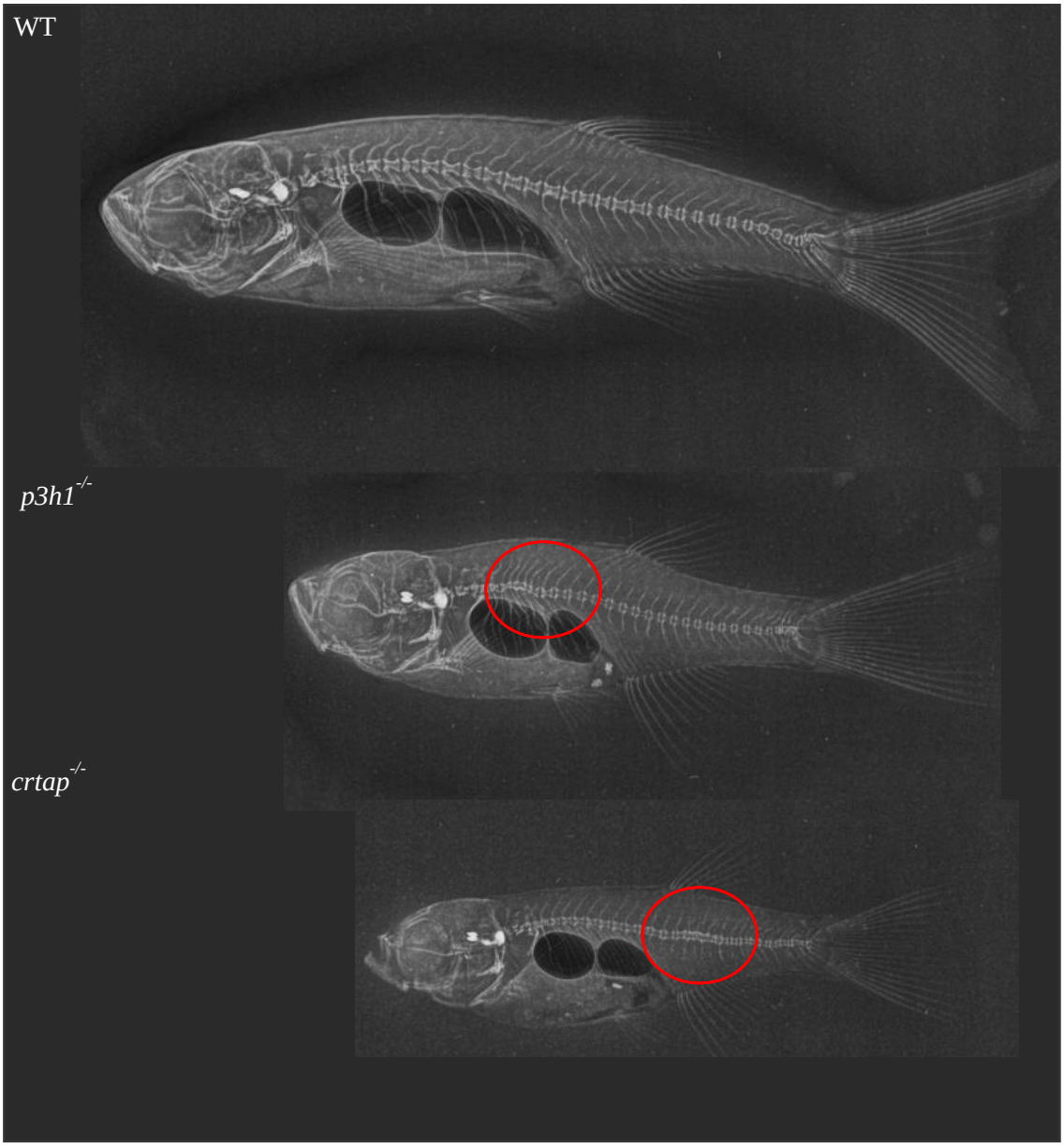

Figure 19. Radiographic analysis on WT and mutant fish. Both *p3h1* and *crtap* homozygous mutants show a general disorganization of the vertebral column compared to WT and reduced length. Vertebral fusions are shown in red circles. Magnification: 5X.

p3h1$^{-/-}$ and *crtap*$^{-/-}$ skeletal phenotype became even worse over time. X-Rays showed increased vertebral malformations (Figure 20 A) both in *crtap*$^{-/-}$ at 16 wpf and in *p3h1*$^{-/-}$ at 24 wpf, when severe vertebral fusions and compressions were detectable. These abnormalities were also evident in µCT scans performed on 10 months old fish (Figure 20 B). Mutant fish showed spine deformities and presence of calli in the ribs. In all mutant samples analysed a certain degree of phenotypical variability was evident.

A

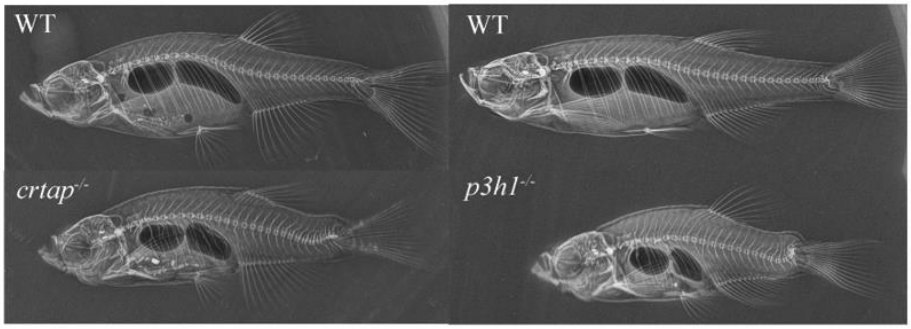

B

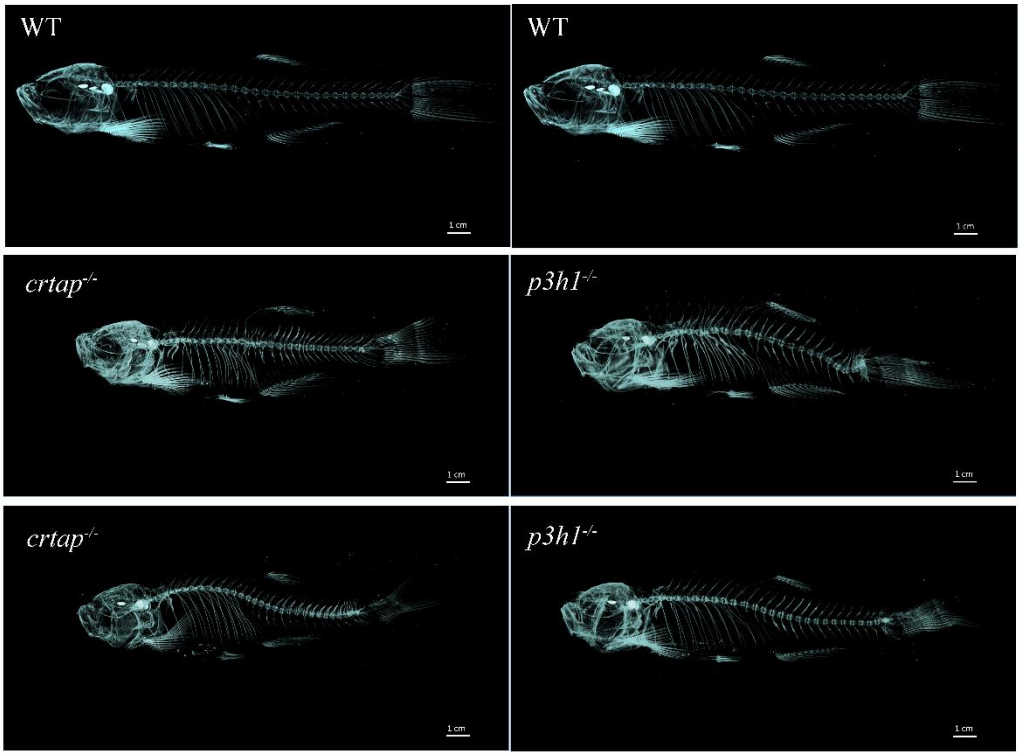

Figure 20.X-Ray and µCT analysis. **(A)** X-Ray images of WT and *crtap*$^{-/-}$ at 16 wpf and WT and *p3h1*$^{-/-}$ at 24 wpf fish. Both mutants show skeletal abnormalities. Magnification: 5X. **(B)** µCT scans of 40 wpf WT and *crtap* and *p3h1* mutant fish. Both mutants show head deformities, disorganization of the spine. Scale bar: 1 cm.

Collagen type I is overmodified in p3h1 and crtap KO mutants

^{3}H-proline labelled type I collagen obtained by pepsin digestion from tail of adult *p3h1*$^{-/-}$ and *crtap*$^{-/-}$ homozygous fish was analysed by SDS-Urea-PAGE. Slower migration of the bands representing the type I collagen α chains was detected in mutant samples with respect to controls, indicating the presence of collagen overmodification, a typical feature of type I collagen in OI patients (Figure 21).

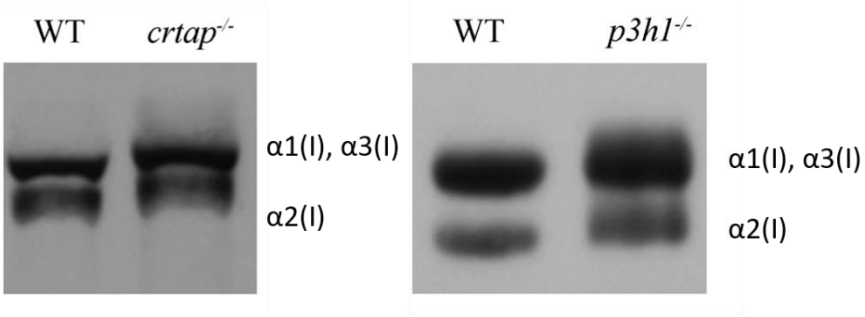

Figure 21. Collagen type I analysis. Representative images of WT, *crtap* and *p3h1* mutants' collagen electrophoretic analysis. Collagen type I is overmodified in both mutants, respect to WT.

Non sense-mediated mRNA decay of p3h1 and crtap mutants

To assess the molecular effect of the mutation on *p3h1* gene expression, qPCR was performed on RNA extracted from skin of *p3h1*$^{-/-}$, *crtap*$^{-/-}$ and WT fish. We observed 80% reduction of the expression of *p3h1* in homozygous mutants compared to WT, and 50% reduction of the expression of *crtap* in homozygous mutants compared to WT suggesting the presence of non sense-mediated mRNA decay (NMD) (Figure 22 A, 22B).

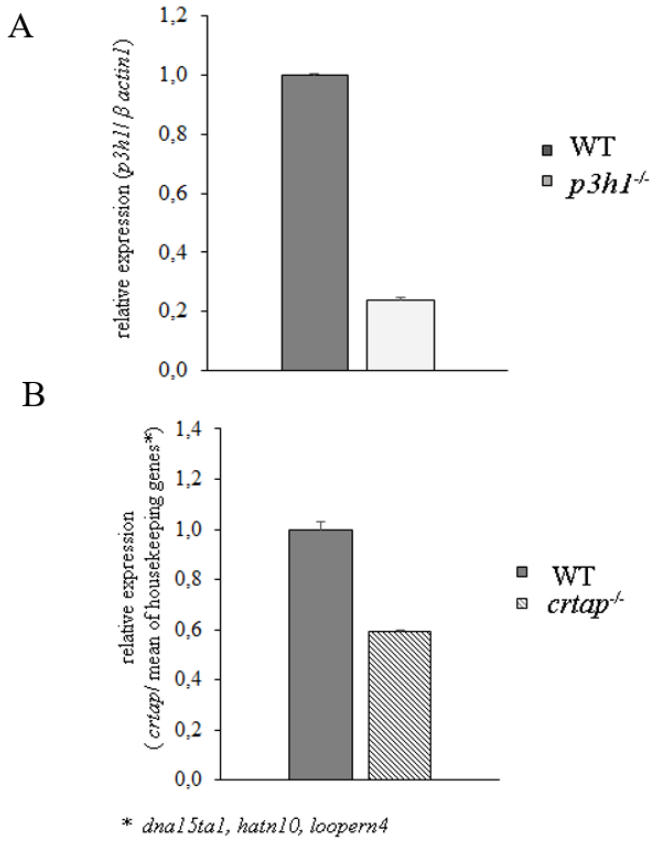

Figure 22. Expression analysis by real time PCR of WT, *p3h1*$^{-/-}$ and *crtap*$^{-/-}$. (A, B) *p3h1* and *crtap* transcripts undergo to non sense-mediated mRNA decay in mutant fish. SD is calculated on technical replicates.

Characterization of p3h1 and crtap zebrafish models

p3h1$^{-/-}$ and crtap$^{-/-}$ display head and vertebral deformities

Morphometric analyses were performed to evaluate differences between WT and mutant body dimensions. Measurements were performed on lateral images of live fish as described in M&M.

At 8 wpf *p3h1* mutants displayed smaller body dimensions compared to WT. The height of the head (HE) was decreased in *p3h1$^{-/-}$* compared to WT, even though it didn't reach statistical significance (**p = 0.078**). The distance from the snout to the most posterior point of operculum (SOL), indicative of the length of the head, was significantly reduced in homozygous *p3h1* mutant compared to WT (**p = 0.032**). The standard length was strongly affected by the presence of the mutation in *p3h1* gene, as already shown by the growth curve (**p = 0.009**). Furthermore, the distance from ventral to dorsal (HAA) was lower in mutants than in WT (**p = 0.025**). However, the ratios SOL/HE (**p = 0.079**) and SL/HAA (**p = 0.776**) were not significantly different between mutants and controls, suggesting that *p3h1$^{-/-}$* are smaller at 8 wpf without any relevant disproportion (Figure 23 A) (Supplementary Table 4).

At 8 wpf *crtap* knock out fish were smaller and thinner than controls (SL: **p = 0.002**, HAA: **p = 0.06**). The head dimension of *crtap* mutants was not significantly reduced with respect to WT (HE: **p = 0.130**, SOL: **p = 0.634**).
SL/HAA tended to be higher in mutants compared to WT, suggesting that *crtap$^{-/-}$* had some body deformities (**p = 0.053**) and the ratio SOL/HE was reduced in mutant compared to controls (**p = 0.04**), denoting the presence of a chunky head (Figure 23 B) (Supplementary Table 5).

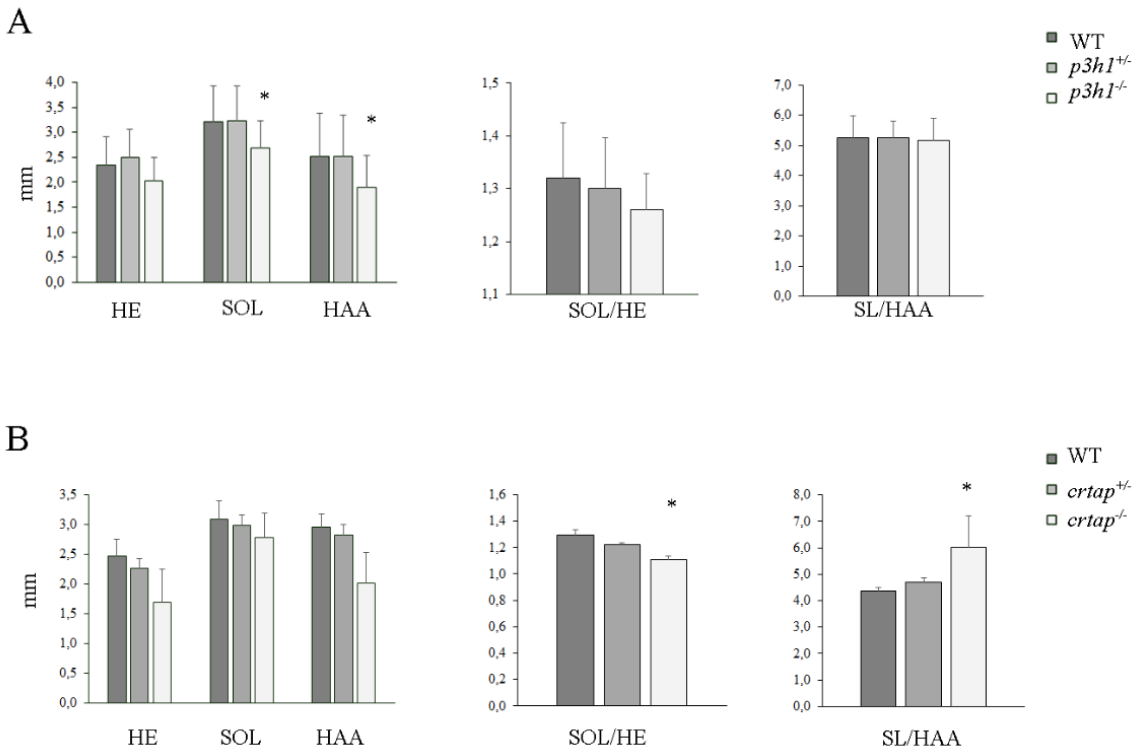

Figure 23. (A) Morphometric analysis of WT and *p3h1*$^{-/-}$ fish at 8 wpf. Statistical analysis reveals a reduction in the body dimensions of *p3h1* mutants compared to WT. However, the ratios of the various analysed parameters do not indicate relevant disproportions both in the head and in the body of the *p3h1* KO model. **(B)** Morphometric analysis of WT and *crtap*$^{-/-}$ fish at 8 wpf. Despite the absence of any difference in body dimensions, *crtap* mutants show disproportions both at the level of the head and at the level of the body, compared to controls. SL: standard length; HE: height at eye; SOL: snout–operculum length; HAA: height at anterior of anal fin. Values are expressed as mean ± standard deviation or SEM. Asterisks indicate the presence of a statistical significance between WT and homozygotes ($p < 0.05$).

p3h1 mutant phenotype became worst over time. At 24 wpf, in fact, *p3h1* KO fish were drastically shorter and they showed disproportions both in the head and in the body (Figure 24) (Supplementary Table 4).

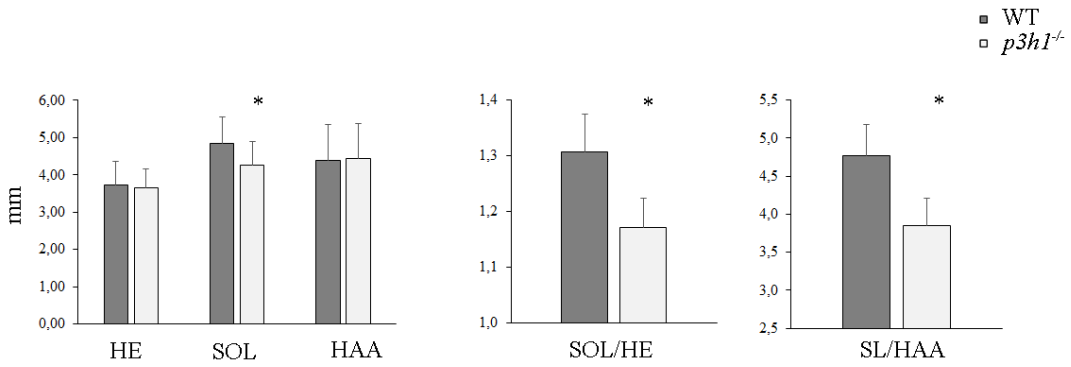

Figure 24. Morphometric analysis of WT and *p3h1*$^{-/-}$ fish at 24 wpf. At this stage disproportions are evident in *p3h1* mutants Asterisks indicate the statistical significance between WT and mutants. The values are expressed as mean ± SD ($p < 0.05$).

Vertebral deformities, already identified by X-Rays, were observed also by alizarin red staining in *p3h1*$^{-/-}$ fish at 4 wpf. The measurements performed on the first 10 vertebrae articulated with the ribs showed that *p3h1* KO have smaller vertebral bodies, characterized by a reduced length (Figure 25) (Supplementary Table 6).

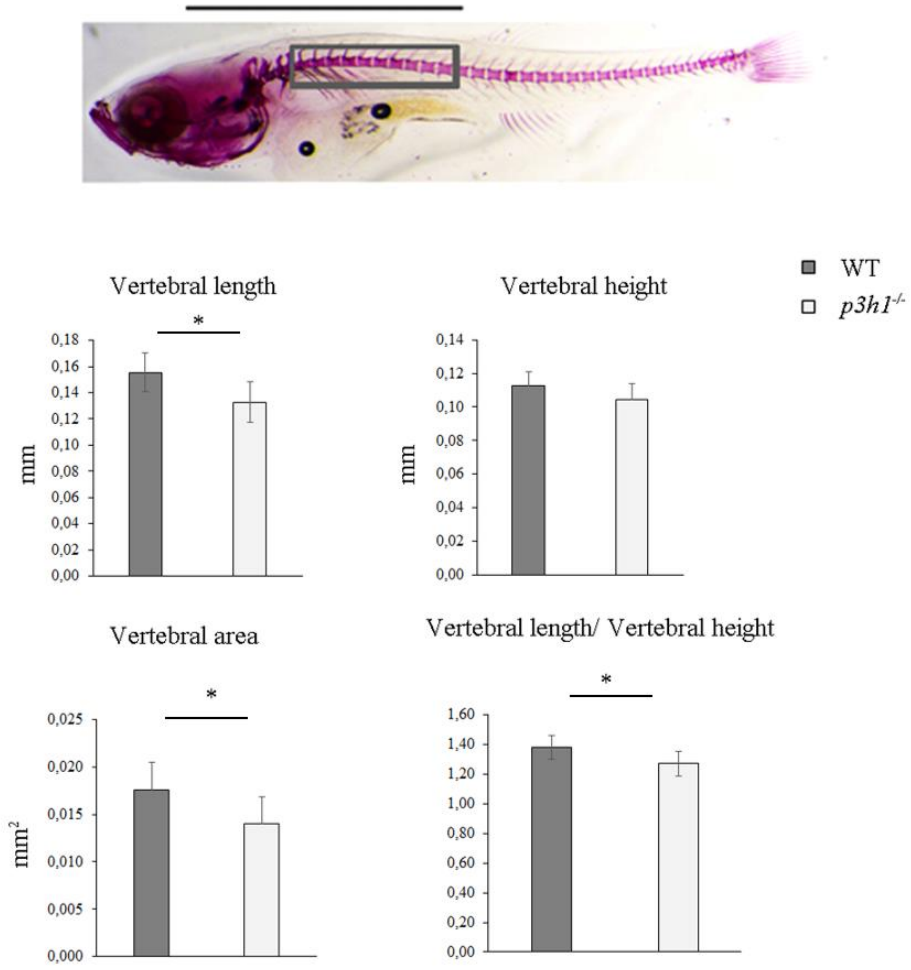

Figure 25. Analysis of vertebral body dimensions. Representative image of 4 wpf fish stained with alizarin red (top). Histograms of the quantification of vertebral length, height, area and ratio of vertebral length and height performed in WT and KO *p3h1*$^{-/-}$ fish. Values are expressed as mean ± standard deviation. Asterisks indicate $p < 0.05$. Scale bar: 2 mm.

Reduced swim bladder insufflation characterizes mutant fish

The teleost swim bladder is located in the dorso-anterior part of the body cavity and it is evolutionary related to the lungs of terrestrial vertebrates. It is composed by a first lobe which appears insufflated at the end of the first week post fertilization. The development of this organ goes on until the second lobe becomes insufflated too, at 3 wpf (Winata et al. 2009). Since in OI type VII lung defects were reported in the KO murine model (Baldridge et al. 2010), we decided to look at the swim bladder insufflation at 1, 2 and 3 wpf (Figure 26 A). We observed a delay in the insufflation of the swim bladder at 1 wpf both in *p3h1* (p = 0.006) and *crtap* (p = 0.002) homozygous mutants compared to WT. At 2 wpf, the first lobe becomes insufflated in all mutants, similarly to what detected in WT and at 3 wpf both WT and mutants present a normal development of the swim bladder (Figure 26 B).

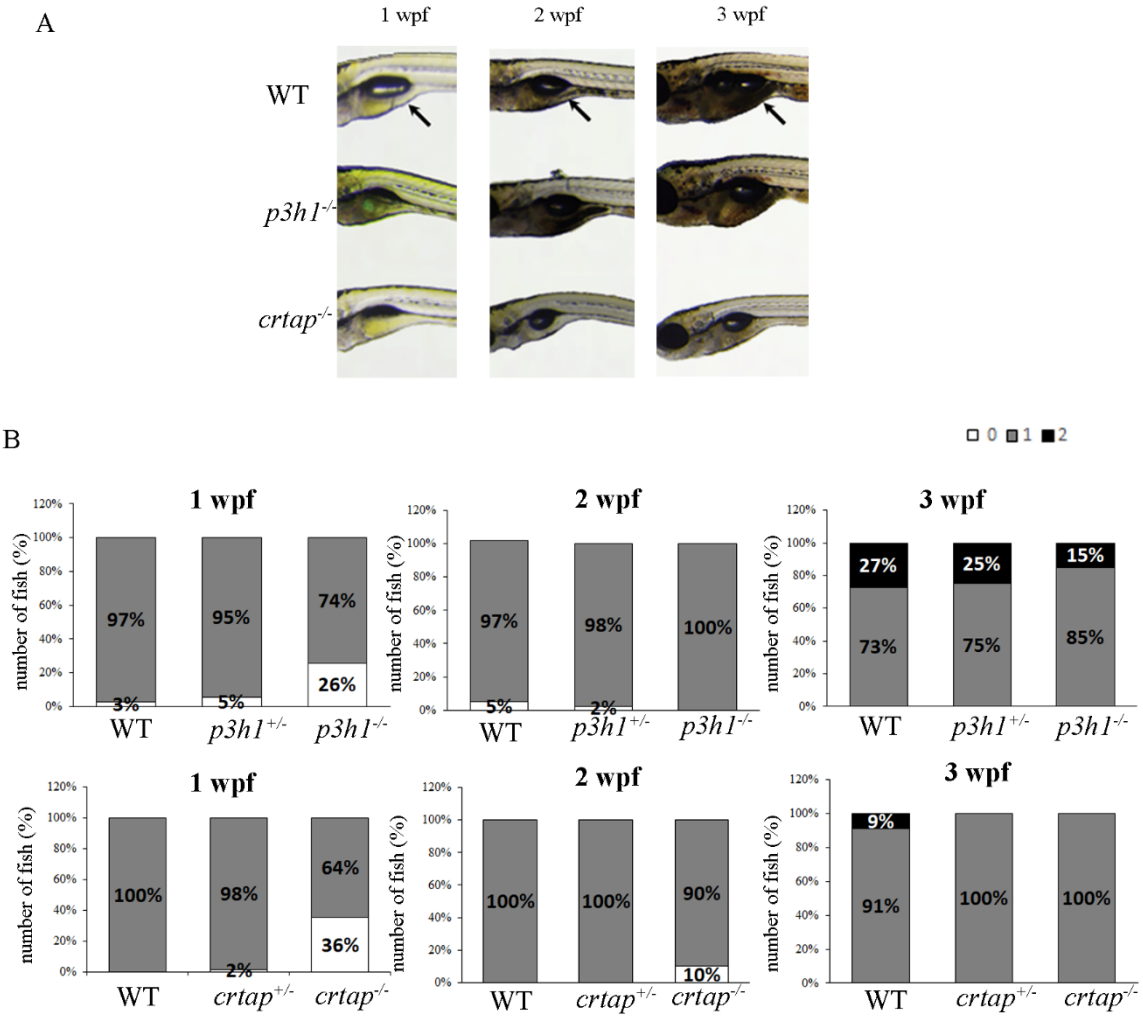

Figure 26. (A) Representative image of 1, 2 wpf WT and mutants with 1 lobe insufflated and 3 wpf WT and mutant fish with the second lobe formed. Scale bar: 1mm. **(B)** Development of swim bladder lobes in both *p3h1* and *crtap* mutants compared to controls. 0, 1 and 2 in the legend refer to swim bladder insufflated lobes.

tmem38b expression in WT zebrafish embryos

tmem38b temporal and spatial expression was evaluated in WT embryos at different developmental stages, since this information was not yet available.

Temporal expression was evaluated by real time PCR performed on RNA extracted from embryos at different stages (from 2-4 cells to 96 hours post fertilization, hpf). We demonstrated that *tmem38b* was expressed early during development and this was confirmed by the presence of the maternal transcript at the 16-32 cells stage. In addition, *tmem38b* levels were high also during somitogenesis. This last result revealed that *tmem38b* is important not only in the first phases of development, but its expression is required also during the zygotic period (Figure 27 A).

To determine the localization of *tmem38b* an *in situ* hybridization on 24, 48, 72, 96 and 120 hpf WT embryos was performed. The presence of the transcript was visible at 120 hpf at the level of the swim bladder (Figure 27 B). Further analysis will be performed after sectioning the hybridized fish.

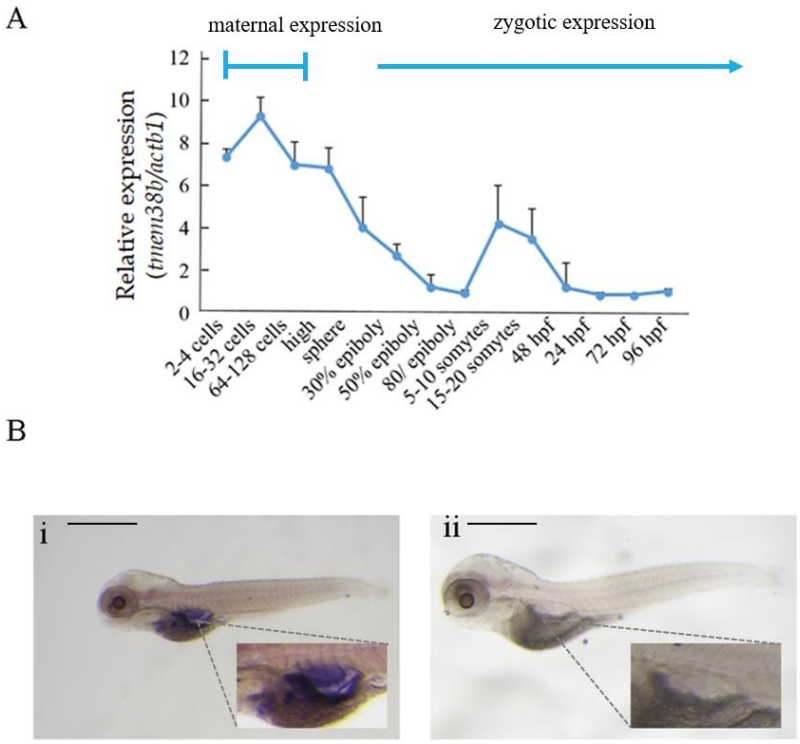

Figure 27. (A) Temporal analysis of *tmem38b* by real time PCR in zebrafish embryos at different developmental stages. Expression both at the maternal and zygotic period are evident. **(B)** *In situ* hybridization in 120 hpf zebrafish embryos. The violet signal **(i)** indicates the presence of *tmem38b* transcript in the swim bladder. In **(ii)** is reported the negative control. Scale bar: 500 µm.

Preliminary characterization on adult tmem38b$^{\Delta aa120\text{-}127}$

In our facility the homozygous mutant *tmem38b*$^{\Delta aa120\text{-}127}$ was the first mutant *tmem38b* fish available to be preliminary characterized. At 8 wpf X-Ray analysis did not allow to observe any differences between the available mutant (n = 2) and WT (n = 2). At 16 wpf the same fish underwent again to X-Ray analysis and morphometric parameters such as SL, vertebral height and length and the angle between vertebral body and neural spine were also evaluated (Figure 28 A, B, C). Considering the very limited number of mutant and WT fish and the variability between the mutants, we didn't observe any differences between them and the WT in the SL as well as in the dimensions of vertebral bodies (Figure 28 C, D). Interestingly, we observed a different slope of the neural spine in WT compared to mutants. The mean of the neural spine slope of the first 10 vertebrae articulated with the ribs was steeper in *tmem38b*$^{\Delta aa120\text{-}127}$ compared to WT (Figure 28 C, D). Only in one *tmem38b* mutant the presence of bone calli at the level of the ribs was detected.

A

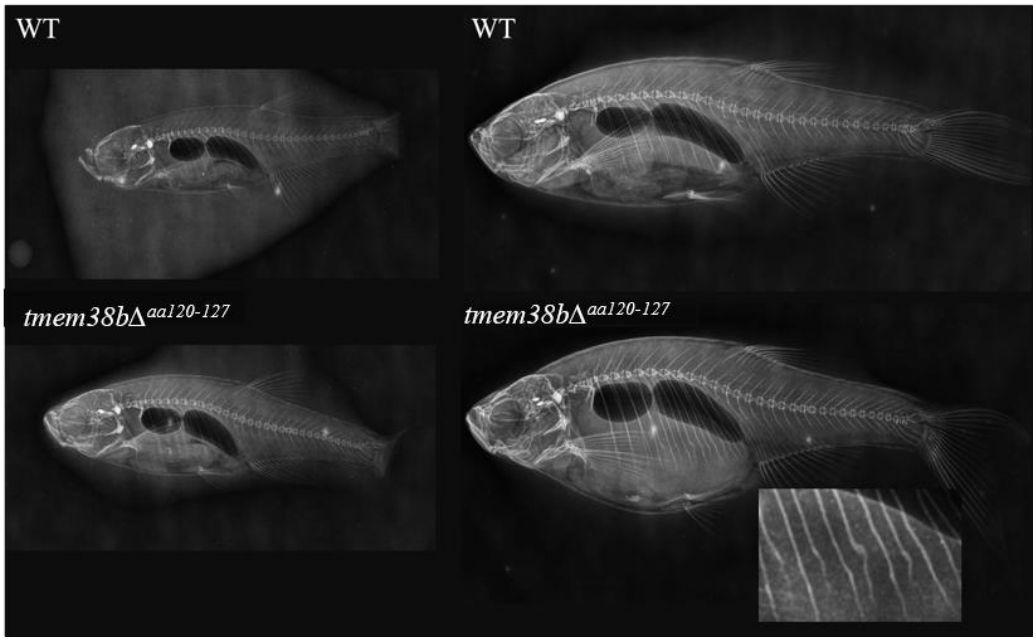

B

C

16 wpf	SL	VL	VH	VL/VH	NSS (°)
WT 1	1750	42.3 ± 4.9	28.6 ± 2.2	1.47 ± 0.09	40.4 ± 3.6
WT 2	1643	40 ± 4.6	27.2 ± 2.0	1.46 ± 0.09	44.3 ± 5.19
tmem38bΔaa120-127 1	1327	30.4 ± 2.4	23.1 ± 0.8	1.32 ± 0.09	47.2 ± 3.3
*tmem38bΔaa120-127*2	1654	40.2 ± 4.3	27.4 ± 1.3	1.47 ± 0.13	47.03 ± 5.0

D

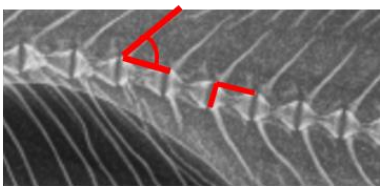

Figure 28. X-Ray images of WT and *tmem38b*$^{\Delta aa120\text{-}127}$ **(A)** At 8 wpf no differences were observed between mutants and controls. **(B)** At 16 wpf few calli at the level of the ribs were present in one *tmem38bΔ*$^{aa120\text{-}127}$ as shown in the magnification. Magnification: 5X. **(C)** Morphometric analysis of *tmem38b*$^{\Delta aa120\text{-}127}$ and WT fish. SL: standard length; VL: vertebral length; VH: vertebral height; NSS: neural spine slope. Numbers are reported as arbitrary unit.

Discussion

I successfully employed the gene editing system CRISPR/Cas9 to generate three zebrafish models for three recessive forms of osteogenesis imperfecta, namely OI type VII, VIII and XIV targeting *crtap*, *p3h1* and *tmem38b* gene, respectively. Using molecular, biochemical, histological and radiographic techniques I demonstrated the goodness of the zebrafish knock out for *crtap* and *p3h1* as valid models for the disease and I started a preliminary analysis of the *tmem38b* mutant.

OI type VII and VIII zebrafish models recapitulate the skeletal phenotype of murine models and human patients

Patients with recessive OI types VII and VIII are clinically indistinguishable at birth. Infants with null defects in *CRTAP* or *P3H1* have lethal to severe osteochondrodysplasias (Marini, Cabral et al. 2007), similar to the lethal OI types II and progressive deforming type III classified by Sillence in 1979 (Sillence and Rimoin1979). However, instead of the blue sclerae, relatively large head and triangular facies of classical OI, these children show white sclerae, relatively small head circumference and a round face. In both cases, the phenotype is characterized by severe rhizomelia, undertubulated long bones and neonatal fractures.

Children with null mutation in *CRTAP* mostly die during infancy. However, a mutation, occurring in an isolated First Nations pedigree in Quebec, which results in partially functional *CRTAP* (IVS1-1021C>G) is compatible with survival (Morello et al. 2006). Affected individuals have a moderately severe skeletal dysplasia, characterized by rhizomelia, coxa vara, and distinct histomorphometry (increased bone formation, decreased mineral apposition rate and very high bone turnover) (Ward et al. 2002).

Infants with mutations in *P3H1* often die in the perinatal period and those who survive have extremely low bone mineral density, severe growth deficiency and bulbous metaphysis. The most common defect, occurring in about half of the OI type VIII patients, is the so-called West African allele carrying a null mutation. The affected patients die in infancy (Marini, Cabral et al. 2007). Other types of mutations allow patients to reach the second decade with severe osteoporosis, growth deficiency and vertebral compression (Marini, Cabral et al. 2007).

Viable knock out murine models for both OI type VII and VIII had been generated (Morello et al. 2006; Vranka et al. 2010). *Crtap* null mice develop progressive and severe kyphoscoliosis over the first 6 months of age and rhizomelia. They exhibit prenatal and postnatal growth delay characterized by shortening of long bone segments (Morello et al. 2006). *P3h1* null mice are significantly smaller, develop kyphoscoliosis which gets progressively worse with age and rhizomelia. In both cases bone density is decreased (Vranka et al. 2010).

Also, the *crtap* and *p3h1* knock out zebrafish survive until adulthood and as expected no phenotype is detectable in heterozygous fish. Interestingly, knock out fish develop a milder phenotype compared to both human patients and mice models. This is not surprising since fish are subjected to a reduced biochemical consequence of gravity, thanks to the swim bladder and the highly sophisticated regulation of its gas content. Anyway, both mutant phenotypes share several common features with OI type VII and VIII patients. Starting from 1 week of life *crtap* knock out fish are shorter then wild type and heterozygous and this difference becomes more evident over time, similarly *p3h1* knock out fish are smaller than WT from 4 wpf and their length differences with the WT is increasing with age. Moreover, at 8 wpf both *crtap* and *p3h1* mutant fish display body and head disproportions and these deformities are accentuated at 24 wpf in *p3h1*$^{-/-}$ fish. Radiographic analysis show altered skeletal organization with deformed vertebral column, vertebral fusions and compressions in both models, approximating the skeletal phenotype described in human patients (Vranka et al. 2010), but not detectable in the OI murine models (Morello et al. 2006; Vranka et al. 2010). Indeed, vertebral compressions together with vertebral fractures are present in human OI and are mainly consequences of poor quality of bones that are unable to sustain the mechanical loading. Interestingly, none of the OI murine models reproduced the vertebral phenotype, mainly because, being quadrupeds, they have a structure of spine and centre of gravity quite different from humans. Zebrafish instead bear cranial-to caudal spinal loads that are originated by swimming forward through water coupled with caudal propulsion and that are quite comparable to the gravitational load to which humans are subjected.

Vertebrae and head bone mineralization is decreased in knock out models compared to WT.

One of the advantages of the zebrafish is the possibility to evaluate bone mineralization very early during development. Thanks to this opportunity we demonstrated that the loss of *p3h1* and *crtap* gene causes a delay in the mineralization of perichondral bones, generally derived from a cartilaginous scaffold (Weigele et al. 2016), without altering the ossification of membranous bones directly

originated from stem cells (Cubbage et al. 1996). Interestingly, a delay in the ossification of the parietal bone of the skull was observed in *P3h1* null mice (Vranka et al. 2010). These features could resemble some clinical findings obtained from X-Ray analysis on a homozygous patient with *P3H1* nonsense codon mutation, characterized by brachycephaly and decreased calvarial thickness, at birth (Baldridge et al. 2008). This result can be related to the role of the prolyl 3-hydroxylation complex on both collagen type I and type II. Indeed, the *crtap* and the *p3h1* knock out murine model showed abnormality not only in bone, but also in the growth plate mainly constituted by type II collagen. In *crtap*$^{-/-}$ the growth plate showed disorganized growth columns of proliferating chondrocytes (Morello et al. 2006), in *P3h1* null mice chondrocytes in the hypertrophic zone appeared less organized than those in the same region in the wild-type (Vranka et al. 2010).

The most common causes of death in individual with severe OI are respiratory problems. Lung stroma is composed by a significant amount of collagen fibrils and hence they may also be affected by mutations in genes involved in collagen biosynthesis. *Crtap*$^{-/-}$ mice showed increased airways space in the lungs, leading to a reduction in the thickness of alveolar walls (Baldridge et al. 2010).

In zebrafish, similarly to mammalian lung, swim bladder derives from an extension of the foregut endoderm and its development is mainly regulated by Hedgehog (Hh) pathway which is involved also in the development of many important events in vertebrates (Winata et al. 2009). Indeed, looking at the inflation of the swim bladder chambers, exploiting the transparency of embryo and larvae, would be the way to gain additional insight into OI pathophysiology. A detectable delay in the inflation of the first lobe of the swim bladder is evident at 7 dpf in both zebrafish mutants compared to WT, suggesting that proline 3-hydroxylation complex can play an essential role also in non-skeletal tissues in zebrafish, as already demonstrated in rats and chick embryos in the late 1979 (Tryggvason et al. 1979) and described in the OI murine models of these OI forms (Baldridge et al. 2010; Pokidysheva et al. 2013).

OI type VII and VIII zebrafish models have overmodified collagen type I

OI type VII and VIII patients are characterized by overmodification of the helical region of type I collagen, easily detected as delayed collagen α chain migration on electrophoretic analysis (Barnes et al. 2006). The absence of the prolyl 3-hydroxylation complex increases the modification of

collagen helix likely as direct consequence of helix folding delay, but the mechanism linking the complex to the delay folding is still poorly understood (Marini, Cabral et al. 2007).

3-Hydroxyproline is an ancient and ubiquitous collagen modification, found throughout as far back as porifera (Hudson and Eyre 2014). At which point in evolution 3-hydroxylation first appeared in fibrillar collagens, and specifically at Pro986 residue, is unknown. Using mass spectrometry several new molecular sites of 3-Hyp along fibrillar collagen chains, in various species, have been discovered. For instance, the 100% of the 3-hydroxylation of the Pro986 in type III collagen from chicken skin is absent in mammalian collagen type III (Weis et al. 2010).
In zebrafish the Pro707 of α2(I) is completely unoccupied by 3-Hyp; in contrast, the prerequisite GPP sequence in the same site, is conserved (Hudson et al. 2011).
Interestingly, in zebrafish type I collagen Pro986 is not hydroxylated (David Eyre personal communication). Despite that, in our mutants the disruption of the complex results in skeletal dysplasia, that resembles human OI patients' phenotype, reproducing also the presence of collagen type I overmodification. In *p3h1* null mice bone an increase in the glycosylation of 5-hydroxylysine (5-Hyl) was hypothesized to have a more severe impact on the tight packing and mineralization of collagen that lack 3-Hyp itself (Pokidysheva et al. 2013). But in the *Lepre1*$^{H662A/H662A}$ knock-in mouse, carrying a mutation in P3H1 catalytic domain affecting enzyme activity, but no complex assembly, no differences in collagen migration were detected indicating normal collagen post translational modification (Homan et al. 2014). This observation, supported by our zebrafish data, shed new light on the function of the 3 hydroxylation in the complex. It seems that the delayed collagen folding, causing excessive glycosylation in OI type VII and VIII, is not likely due to lack of 3-Hyp at Pro986 specific residue, but rather to the impaired chaperone activity of the complex.

p3h1 and crtap mutants show altered transcripts levels

Non sense mediated decay (NMD) is a mRNA surveillance system that degrades transcripts containing premature stop codon preventing translation of unnecessary or aberrant transcripts, reducing the amount of dominant-negative protein that could be produced and resulting in loss-of-function effects (Khajavi et al. 2006). The majority of *CRTAP* and *P3H1* mutations, which lead to the formation of a premature stop codon, trigger NMD (Barnes et al. 2010).

In our OI type VII and VIII mutant zebrafish both mutations lead to the formation of premature stop codon, for *crtap* in position 80 and for *p3h1* in position 266 of the protein. Real time PCR performed on RNA extracted from skin of WT, *p3h1* and *crtap* mutants indicates the presence of NMD, as expected.

OI type VII and VIII zebrafish models as tool to validate chemical chaperones as valid drug for OI

Based on our data the zebrafish *crtap* and *p3h1* knock out well reproduce the phenotype and molecular characteristic of human OI type VII and VIII. Thus, they may represent a valid tool for drug screening focused on identifying new treatment for OI. Indeed, the synthesis in both models of overmodified type I collagen suggests the presence of ER stress due to mutant collagen retention as reported in OI type VII and VIII patients and as we recently demonstrated in the zebrafish *Chihuahua* (Gioia et al. 2017), a model for classical OI. The possibility to validate common target for multiple form of OI will be extremely important for patients' treatment especially considering the rare nature of this disease.

Zebrafish model for OI type XIV: a tool to elucidate OI pathophysiology in vivo.

One of the genes most recently found associated to OI is *TMEM38B* encoding for the ubiquitous endoplasmic reticulum (ER) potassium channel, whose activity is essential for ER calcium release. The exact mechanism linking loss of the activity of this channel to OI has been only partially elucidated through calcium role on collagen intracellular synthesis. The knock out murine model for *Tmem38b* is lethal at birth due to respiratory insufficiency, thus the generation of a different model to investigate the disease may be of great relevance. This motivate us to reproduce OI type XIV in fish, which normally have a less severe bone phenotype due to the less gravity effect in the water environment. We first demonstrated that the gene is expressed in zebrafish through development and we identified its main site of expression in the swim bladder, supporting its predominant expression in non excitable tissues similar to what reported for tetrapods.

We successfully target *tmem38b* in zebrafish by CRISPR/Cas9 editing system. In selecting the guide RNA we chose a region where the highly conserve KEV tripeptide relevant for channel activity is located. Indeed, we were able to obtain not only knock out line reproducing the defect in human OI type XIV patients, but also a line of heterozygous fish carrying a deletion of 8 amino acids including

the tripeptide KEV. Although up to now only two mutant fish have been characterized, interestingly both of them reproduce the steeper slope of the neural arch/vertebral body angle, already described in the mutant *Chihuahua* (Gioia et al. 2017). We believe that these mutants will not only help us to elucidate OI pathophysiology, but also the Tric-B activity *in vivo*.

Supplementary methods

Supplementary tables

Supplementary table 1. Standard length of WT, *p3h1*$^{+/-}$ and *p3h1*$^{-/-}$ fish.

	N	MEAN ± SD (mm)	p.value
1 wpf			
WT	37	3.92 ± 0.17	0.443
p3h1$^{+/-}$	73	3.92 ± 0.15	
p3h1$^{-/-}$	31	3.90 ± 0.15	
2 wpf			
WT	29	4.33 ± 0.40	0.048
p3h1$^{+/-}$	84	4.29 ± 0.48	
p3h1$^{-/-}$	24	4.11 ± 0.40	
3 wpf			
WT	22	5.11 ± 0.73	0.143
p3h1$^{+/-}$	48	5.03 ± 0.66	
p3h1$^{-/-}$	20	4.83 ± 0.43	
4 wpf			
WT	19	6.09 ± 1.11	0.015
p3h1$^{+/-}$	34	5.90 ± 1.19	
p3h1$^{-/-}$	20	5.33 ± 0.72	
8 wpf			
WT	28	12.11 ± 3.46	0.009
p3h1$^{+/-}$	56	12.66 ± 3.34	
p3h1$^{-/-}$	14	9.34 ± 2.08	
24 wpf			
WT	33	20.59 ± 3.34	0.004
p3h1$^{-/-}$	8	16.75 ± 2.40	

The p value was calculated between *p3h1*$^{-/-}$ and WT fish. N: number of fish.

Supplementary table 2. Standard length of WT, *crtap*$^{+/-}$ and *crtap1*$^{-/-}$ fish

	N	MEAN ± SD (mm)	p.value
1 wpf			
WT	24	3.99 ± 0.20	0.003
crtap$^{+/-}$	64	3.94 ± 0.17	
crtap$^{-/-}$	14	3.80 ± 0.13	
2 wpf			
WT	27	4.20 ± 0.28	0.002
crtap$^{+/-}$	55	4.20 ± 0.32	
crtap$^{-/-}$	20	3.95 ± 0.22	
3 wpf			
WT	11	4.94 ± 0.34	0.001
crtap$^{+/-}$	18	4.76 ± 0.34	
crtap$^{-/-}$	5	4.29 ± 0.16	
8 wpf			
WT	13	12.99 ± 3.76	0.002
crtap$^{+/-}$	27	12.14 ± 3.38	
crtap$^{-/-}$	10	8.12 ± 2.58	

The p value was calculated between *crtap*$^{-/-}$ and WT fish. N: number of fish.

Supplementary table 3. Number of mineralized vertebrae in WT, heterozygous and homozygous *p3h1* and *crtap* mutants.

	Number of fish	MEAN ± SEM (number of vertebrae)	p.value
p3h1			
2 wpf			
WT	29	5.50 ± 1.40	0.206
p3h1$^{+/-}$	84	5.30 ± 0.81	
p3h1$^{-/-}$	24	3.30 ± 1.19	
3 wpf			
WT	22	18.59 ± 1.94	0.686
p3h1$^{+/-}$	48	17.21 ± 1.18	
p3h1$^{-/-}$	20	18.45 ± 2.11	
crtap			
2 wpf			
WT	28	1.68 ± 0.36	
crtap$^{+/-}$	53	2.09 ± 0.29	0.149
crtap$^{-/-}$	19	0.89 ± 0.34	
3 wpf			
WT	11	14.82 ± 2.2	0.007
crtap$^{+/-}$	18	11.28 ± 1.66	
crtap$^{-/-}$	5	2.5 ± 1.18	

The p value was calculated between *crtap*$^{-/-}$ or *p3h1*$^{-/-}$ and WT fish.

Supplementary table 4. Morphometric analysis of adult WT, *p3h1*$^{+/-}$ and *p3h1*$^{-/-}$ fish.

p3h1							
8 wpf							
	N	**HE (mm)**	**p.value**	**SOL (mm)**	**p.value**	**SOL/HE**	**p.value**
WT	26	2.34 ± 0.56	0.078	3.21 ± 0.71	0.032	1.32 ± 0.10	0.079
p3h1$^{+/-}$	51	2.50 ± 0.55		3.23 ± 0.69		1.30 ± 0.10	
p3h1$^{-/-}$	13	2.02 ± 0.47		2.68 ± 0.54		1.26 ± 0.07	
	N	**SL (mm)**	**p.value**	**HAA (mm)**	**p.value**	**SL/HAA**	**p.value**
WT	28	12.11 ± 3.46	0.009	2.51± 0.87	0.025	5.54 ± 0.73	0.776
p3h1$^{+/-}$	56	12.66 ± 3.34		2.52 ± 0.82		5.23 ± 0.56	
p3h1$^{-/-}$	14	9.34 ± 2.08		1.89 ± 0.65		5.17 ± 0.73	
24 wpf							
	N	**HE (mm)**	**p.value**	**SOL (mm)**	**p.value**	**SOL/HE**	**p.value**
WT	33	3.73 ± 0.63	0.706	4.84 ± 0.70	0.040	1.31 ± 0.07	7.382E-06
p3h1$^{-/-}$	8	3.64 ± 0.52		4.26 ± 0.64		1.17 ± 0.05	
	N	**SL (mm)**	**p.value**	**HAA (mm)**	**p.value**	**SL/HAA**	**p.value**
WT	33	20.59 ± 3.34	0.004	4.39 ± 0.95	0.910	4.76 ± 0.42	1.289E-06
p3h1$^{-/-}$	8	16.75 ± 2.40		4.43 ± 0.95		3.84 ± 0.37	

The p value was calculated between *p3h1*$^{-/-}$ and WT fish. N: number of fish.

Supplementary table 5. Morphometric analysis of adult WT, *crtap*$^{+/-}$ and *crtap* $^{-/-}$ fish.

crtap							
8 wpf							
	N	**HE (mm)**	**p.value**	**SOL (mm)**	**p.value**	**SOL/HE**	**p.value**
WT	13	2.47 ± 0.27	0.130	3.09 ± 0.31	0.634	1.29 ± 0.04	0.040
crtap$^{+/-}$	24	2.27 ± 0.16		2.99 ± 0.18		1.22 ± 0.01	
crtap$^{-/-}$	4	1.69 ± 0.56		2.79 ± 0.40		1.11 ± 0.02	
	N	**SL (mm)**	**p.value**	**HAA (mm)**	**p.value**	**SL/HAA**	**p.value**
WT	13	12.99 ± 1.04	0.002	2.95 ± 0.22	0.060	4.38 ± 0.12	0.530
crtap$^{+/-}$	23	12.14 ± 0.65		2.83 ± 0.18		4.71 ± 0.14	
crtap$^{-/-}$	6	8.12 ± 0.81		2.02 ± 0.52		6.03 ± 1.18	

The p value was calculated between *crtap*$^{-/-}$ and WT fish. N: number of fish

.

Supplementary table 6. Analysis of vertebral dimensions of 4 wpf WT and *p3h1*$^{-/-}$ fish.

p3h1					
4 wpf					
	N	**LENGTH**	**p.value**	**HEIGHT**	**p.value**
WT	9	0.156 ± 0.015	0.009	0.113 ± 0.008	0.008
p3h1$^{-/-}$	7	0.133 ± 0.015		0.104 ± 0.009	
	N	**AREA**	**p.value**	**LENGTH/HEIGHT**	**p.value**
WT	9	0.018 ± 0.003	0.024	1.381 ± 0.079	0.018
p3h1$^{-/-}$	7	0.014 ± 0.003		1.272 ± 0.084	

The p value was calculated between *p3h1*$^{-/-}$ and WT fish. N: number of fish.

References

Abzhanov A, Rodda SJ, McMahon AP, and Tabin CJ. 2007. “Regulation of Skeletogenic Differentiation in Cranial Dermal Bone.” *Development (Cambridge, England)* 134: 3133–3144.

Akiyama T, Dass CR, Shinoda Y, Kawano H, Tanaka S, Choong PF. 2010. “PEDF Regulates Osteoclasts via Osteoprotegerin and RANKL.” *Biochem Biophys Res Commun* 391: 789–94.

Alanay, Yasemin, Hrispima Avaygan, Natalia Camacho, G Eda Utine, and Boduroglu. 2010. “Mutations in the Gene Encoding the RER Protein FKBP65 Cause Autosomal-Recessive Osteogenesis Imperfecta.” *The American Journal of Human Genetics* 86: 551–59.

Amores, Angel, Julian Catchen, Indrajit Nanda, Wesley Warren, and Ron Walter. 2014. “A RAD-Tag Genetic Map for the Platyfish (Xiphophorus Maculatus) Reveals Mechanisms of Karyotype Evolution among Teleost Fish.” *Genetics* 197: 625–41.

Asharani, Keupp, Semler, Wang, Li, Thiele, Yigit, Pohl, Becker, Frommolt, Sonntag, Altmu¨ller, Zimmermann, Greenspan, Akarsu, Netzer, Scho¨nau, Wirth, Hammerschmidt, Nu¨rnberg, Wollnik and Carney. 2012. “Attenuated BMP1 Function Compromises Osteogenesis, Leading to Bone Fragility in Humans and Zebrafish.” *American Journal of Human Genetics* 90 (4). Elsevier: 661–74.

Auer, Thomas O, Karine Duroure, Anne De Cian, Jean-paul Concordet, and Filippo Del Bene. 2014. “Highly Efficient CRISPR / Cas9-Mediated Knock-in in Zebrafish by Homology-Independent DNA Repair,” *Genom Res* 24: 142–53.

Bächinger HP, Bruckner P, Timpl R, Engel J. 1978. “The Role of Cis-Trans Isomerization of Peptide Bonds in the coil leads to and comes from triple helix conversion of collagen.” *Eur J Biochem* 90: 605–13.

Baldridge, Schwarze, Morello, Lennington, Bertin, Pace, Pepin, Weis, Eyre, Walsh, Lambert, Green, Robinson, Michelson, Houge, Lindman, Martin, Ward, Lemyre, Mitchell, Krakow, Rimoin, Cohn, Byers and Brendan Lee. 2008. “CRTAP and LEPRE1 Mutations in Recessive Osteogenesis Imperfecta.” *Human Mutation* 29 (12): 1435–42.

Baldridge, Lennington, Weis, Homan, Jiang, Munivez, Keene, Hogue, Pyott, Byers, Krakow, Cohn, Eyre, Lee and Morello. 2010. “Generalized Connective Tissue Disease in Crtap- / - Mouse.”

PloS One 5 (5).

Bargman, Renee, Alice Huang, Adele L. Boskey, Cathleen Raggio, and Nancy Pleshko. 2011. "RANKL Inhibition Improves Bone Properties in a Mouse Model of Osteogenesis Imperfecta." *Connective Tissue Research* 51 (2): 123–31.

Barnes, Duncan, Weis, Paton, Cabral, Mertz, Makareeva, Gambello, Lacbawan, Leikin, Fertala, Eyre, Bale and Marini. 2013. "Kuskokwim Syndrome , a Recessive Congenital Contracture Disorder , Extends the Phenotype of FKBP10 Mutations." *Human Mutation* 34 (9): 1279–88.

Barnes, Carter, Cabral, Weis, Chang, Makareeva, Leikin, Rotimi, Eyre, Raggio, and Marini. 2010. "Lack of Cyclophilin B in Osteogenesis Imperfecta with Normal Collagen Folding." *The New England Journal O F Medicine* 362: 521–28.

Barnes, Chang, Morello, Cabral, Weis, Eyre, Leikin, Makareeva, Kuznetsova, E. Uveges, Ashok, Flor, Mulvihill, Wilson, Sundaram, Lee and Marini. 2006. "Deficiency of Cartilage-Associated Protein in Recessive Lethal Osteogenesis Imperfecta." *N Engl J Med* 355: 2757–64.

Baron R, Kneissel M. 2013. "WNT Signaling in Bone Homeostasis and Disease: From Human Mutations to Treatments." *Nat Med* 19: 179–92.

Barrangou, Fremaux, Deveau, Richards, Boyaval, Moineau, Romero, and Philippe Horvath. 2007. "CRISPR Provides Acquired Resistance Against Viruses in Prokaryotes." *Science (New York, N.Y.)* 315: 1709–12.

Becerra SP, Notario V. 2013. "The Effects of PEDF on Cancer Biology: Mechanisms of Action and Therapeutic Potential." *Nat Rev Cancer* 13: 258–71.

Besio, Roberta, and Antonella Forlino. 2015. "Treatment Options for Osteogenesis Imperfecta." *Expert Opinion on Orphan Drugs* 3 (2): 165–81.

Bianchi, Gagliardi, Maruelli, Besio, Landi, Gioia, Kozloff, Khoury, Coucke, Symoens, Marini, Rossi, Bini and Forlino. 2015. "Altered Cytoskeletal Organization Characterized Lethal but Not Surviving Brtl+/− Mice: Insight on Phenotypic Variability in Osteogenesis Imperfecta." *Human Molecular Genetics* 24 (21): 6118–33.

Bishop NJ, Walsh JS. 2014. "Osteogenesis Imperfecta in Adults." *J Clin Invest.* 124: 476–477.

Bolotin, Quinquis, Sorokin, and Ehrlich. 2005. "Clustered Regularly Interspaced Short Palindrome Repeats (CRISPRs) Have Spacers of Extrachromosomal Origin." *Microbiology* 151 (8): 2551–61.

Boudko, Engel, and Bächinger 2012. “The Crucial Role of Trimerization Domains in Collagen Folding.” *International Journal of Biochemistry and Cell Biology* 44 (1): 21–32.

Bourhis, Mariano, Zhao, Harlos, Exposito, Jones, Moali, Aghajari, and Hulmes. 2012. “Structural Basis of Fibrillar Collagen Trimerization and Related Genetic Disorders.” *Nature Structural & Molecular Biology* 19 (10): 1031–36.

Boyde A, Travers R, Glorieux FH, Jones SJ. 1999. “The Mineralization Density of Iliac Crest Bone from Children with Osteogenesis Imperfecta.” *Calcif Tissue Int* 64: 185–190.

Braasch, Ingo, Yann Guiguen, Ryan Loker, John H Letaw, and Allyse Ferrara. 2014. “Connectivity of Vertebrate Genomes: Paired-Related Homeobox (Prrx) Genes in Spotted Gar, Basal Teleosts, and Tetrapods.” *Comp Biochem Physiol C Toxicol Pharmacol.* 163: 24–36.

Bradshaw, Amy D. 2009. “The Role of SPARC in Extracellular Matrix Assembly.” *Journal of Cell Communication and Signaling*.

Brizola, Evelise, and Jay Robert Shapiro. 2015. “Bisphosphonate Treatment of Children and Adults with Osteogenesis Imperfecta: Unanswered Questions.” *Calcified Tissue International*.

Brouns, Stan J J, Matthijs M. Jore, Magnus Lundgren, Edze R. Westra, Rik J H Slijkhuis, Ambrosius P L Snijders, Mark J. Dickman, Kira S. Makarova, Eugene V. Koonin, and John Van Der Oost. 2003. “Small CRISPR RNAs Guide Antiviral Defense in Prokaryotes.” *Science (New York, N.Y.)* 321: 960–64.

Brusilow, S. W.; Maestri, N. E. 1996. “Urea Cycle Disorders: Diagnosis, Pathophysiology, and Therapy.” *Adv Pediatr* 43: 127–70.

Burger, E. H., Klein-Nulend, J. & Smit, T. H. 2003. “Strain Derived Canalicular Fluid Flow Regulates Osteoclast Activity in a Remodelling Osteon – a Proposal.” *Journal of Biomechanics* 36: 1453 –1459.

Cabral, Wayne A., Masaki Ishikawa, Matthias Garten, Elena N. Makareeva, Brandi M. Sargent, Weis, Barnes, Webb, Shaw, Ala-Kokko, Lacbawan, Högler, Leikin, Blank, Zimmerberg, Eyre, Yamada, Marini. 2016. “Absence of the ER Cation Channel TMEM38B/TRIC-B Disrupts Intracellular Calcium Homeostasis and Dysregulates Collagen Synthesis in Recessive Osteogenesis Imperfecta.” Edited by John F Bateman. *PLOS Genetics* 12 (7): e1006156.

Cabral, Barnes, Adeyemo, Cushing, Chitayat, Porter, Panny, Gulamali-Majid, Tishkoff, Rebbeck, Gueye, Bailey-Wilson, Brody, Rotimi and Marini. 2012. “A Founder Mutation in LEPRE1

Carried by 1 . 5 % of West Africans and 0 . 4 % of African Americans Causes Lethal Recessive Osteogenesis Imperfecta." *Genetics in Medicine* 14 (5): 543–51.

Cabral, Perdivara, Weis, Terajima, Blissett, Chang, Perosky, Makareeva, Mertz6 , Leikin, Tomer, Kozloff, Eyre, Yamauchi, Marini. 2014. "Abnormal Type I Collagen Post-Translational Modification and Crosslinking in a Cyclophilin B KO Mouse Model of Recessive Osteogenesis Imperfecta" 10 (6).

Canty, Elizabeth G., and Karl E. Kadler. 2005. "Procollagen Trafficking, Processing and Fibrillogenesis." *Journal of Cell Science* 118 (7): 1341–53.

Castagnola, P, M Gennari, R Morello, L Tonachini, O Marin, A Gaggero, and R Cancedda. 1997. "Cartilage Associated Protein (CASP) Is a Novel Developmentally Regulated Chick Embryo Protein." *J Cell Sci* 110: 1351–59.

Ceasar, S. Antony, Vinothkumar Rajan, Sergey V. Prykhozhij, Jason N. Berman, and S. Ignacimuthu. 2016. "Insert, Remove or Replace: A Highly Advanced Genome Editing System Using CRISPR/Cas9." *Biochimica et Biophysica Acta - Molecular Cell Research*.

Chakrabarti, S., Streisinger, G., Singer, F. &, and C. Walker. 1983. "Frequency of γ-Ray Induced Specific Locus and Recessive Lethal Mutations in Mature Germ Cells of the Zebrafish, Brachydanio Rerio." *Genetics* 103: 109–123.

Chang, Barnes, Cabral, Bodurtha, and Marini. 2009. "Prolyl 3-Hydroxylase 1 and CRTAP Are Mutually Stabilizing in the Endoplasmic Reticulum Collagen Prolyl 3-Hydroxylation Complex." *Human Molecular Genetics* 19 (2): 223–34.

Chen, Yang, Tang. 2018. " Chemical modifications of nucleic acid drugs and their delivery systems for gene-based therapy". *Med Res Rev.*

Christiansen, H.E., Schwarze, U., Pyott, S.M., AlSwaid, A., D. Balwi, A.l.M., Alrasheed, S., Pepin, M.G., Weis, M.A., Eyre, and P.H. R. and Byers. 2010. "Homozygosity for a Missense Mutation in SERPINH1, Which Encodes the Collagen Chaperone Protein HSP47, Results in Severe Recessive Osteogenesis Imperfecta." *Am. J. Hum. Genet.* 86: 389–398.

Cubbage, Carol C., and Paula M. Mabee. 1996. "Development of the Cranium and Paired Fins in the Zebrafish *Danio Rerio* (Ostariophysi, Cyprinidae)." *Journal of Morphology* 229 (May): 121–60.

Currie, P. D., Schilling, T. F., and Ingham, P. W. 1999. "Small-Scale Marker-Based Screening for

Mutations in Zebrafish Development." *Methods Mol. Biol.* 97: 441–460.

Dallas, Park-Snyder, Miyazono, Twardzik, Mundy, Bonewald. 1994. "Characterization and Autoregulation of Latent Transforming Growth Factor β (TGF β) Complexes in Osteoblast-like Cell Lines. Production of a Latent Complex Lacking the Latent TGF B–binding Protein." *J. Biol. Chem.* 269: 6815–6821.

Dean DC, Barr JF, Freytag JW, Hudson BG. 1983. "Isolation of Type IV Procollagen-like Polypeptides from Glomerular Basement Membrane. Characterization of pro-Alpha 1(IV)." *J Biol Chem.* 258: 590– 6.

De Wet WJ, Pihlajaniemi T, Myers J, Kelly TE, Prockop DJ. 1983. "Synthesis of a Shortened pro-Alpha 2(I) Chain and Decreased Synthesis of pro-Alpha 2(I) Chains in a Proband with Osteogenesis Imperfecta." *J Biol Chem* 258: 7721–28.

Doench, John G., Ella Hartenian, Daniel B. Graham, Zuzana Tothova, Mudra Hegde, Ian Smith, Meagan Sullender, Benjamin L. Ebert, Ramnik J. Xavier, and Root. 2014. "Rational Design of Highly Active sgRNAs for CRISPR-Cas9- Mediated Gene Inactivation." *Nature Biotechnology* 32 (12): 1262–67.

Doro, F., P. Cavarzere, E. Monti, G. Venturi, and S. Adami. 2010. "Growth Hormone in Combination with Bisphosphonate Treatment in Osteogenesis Imperfecta." *Bone* 46: S18–19.

Due, Dienhart .2001." Zebrafish tiggy-winkle hedgehog promoter directs notochord and floor plate green fluorescence protein expression in transgenic zebrafish embryos". *Dev Dyn.* 222(4):655-66.

Duran, Ivan, Jorge H Martin, Mary Ann Weis, Pavel Krejci, and Peter Konik. 2017. "A Chaperone Complex Formed by HSP47, FKBP65, and BiP Modulates Telopeptide Lysyl Hydroxylation of Type I Procollagen." *Journal of Bone and Mineral Research* 32 (6): 1309–29.

Eames, Singer, Smith, Wood, Yan, X, Polizzi, Catchen, Rodriguez-Maria, Linbo, Raible, and Postlethwait. 2010. "UDP Xylose Synthase 1 Is Required for Morphogenesis and Histogenesis of the Craniofacial Skeleton." *Dev Biol* 341: 400–15.

Eames, Yan, Swartz, Levic, Knapik, Postlethwait, Kimmel. 2011. "Mutations in fam20b and xylt1 Reveal That Cartilage Matrix Controls Timing of Endochondral Ossification by Inhibiting Chondrocyte Maturation." *PLoS Genet* 7: e1002246.

Eyre, D. R., M. A. Paz, and P. M. Gallop. 1984. "Cross-Linking in Collagen and Elastin." *Annual*

Review of Biochemistry 53: 717–48. doi:10.1146/annurev.biochem.53.1.717.

Eyre DR, Weis M, Hudson DM, Wu JJ, Kim L. 2011. “A Novel 3-Hydroxyproline (3Hyp)-Rich Motif Marks the Triple-Helical C Terminus of Tendon Type I Collagen.” *J Biol Chem* 286: 7732–36.

Eyre, Weis. 2013. “Bone Collagen : New Clues to Its Mineralization Mechanism from Recessive Osteogenesis Imperfecta.” *Calcified Tissue International* 93: 338–47.

Farber, Reich, Barnes, Becerra, Rauch, Cabral, Bae, Quinlan, Glorieux, Clemens and Marini. 2014. “A Novel IFITM5 Mutation in Severe Atypical Osteogenesis Imperfecta Type VI Impairs Osteoblast Production of Pigment Epithelium-Derived Factor.” *J Bone Miner Res* 29: 1402–11.

Fisher, S., and Halpern, M. E. 1999. “Patterning the Zebrafish Axial Skeleton Requires Early Chordin Function.” *Nat. Genet.* 23: 442– 446.

Fisher, Shannon, Pudur Jagadeeswaran, and Marnie E Halpern. 2003. “Radiographic Analysis of Zebrafish Skeletal Defects.” *Developmental Biology* 264 (1): 64–76.

Flanagan-Steet H, Sias C, Steet R. 2009. “Altered Chondrocyte Differentiation and Extracellular Matrix Homeostasis in a Zebrafish Model for Mucolipidosis II.” *Am J Pathol* 175: 2063–75.

Fleming, Sato and Goldsmith. 2005. "High-Throughput In Vivo Screening for Bone Anabolic Compounds with Zebrafish". *Journal of Biomolecular Screening* 10(8).

Force, A., Lynch, M., Pickett, F.B., Amores, A., Yan, Y.L., Postlethwait, J. 1999. “Preservation of Duplicate Genes by Complementary, Degenerative Mutations.” *Genetics* 151: 1531–1545.

Forlino, Cabral, Barnes, and Marini. 2011. “New Perspectives on Osteogenesis Imperfecta.” *Nature Reviews. Endocrinology* 7 (9): 540–57.

Forlino and Marini. 2016. “Osteogenesis Imperfecta.” *The Lancet* 387. Elsevier Ltd: 1657–71.

Forlino, Tani, Rossi, Lupi, Campari, Gualeni, Bianchi, Armini, Cetta, Bini, and Marini. 2007. “Differential Expression of Both Extracellular and Intracellular Proteins Is Involved in the Lethal or Nonlethal Phenotypic Variation of BrtlIV , a Murine Model for Osteogenesis Imperfecta.” *Proteomics* 11: 1877–91.

Fratzl-Zelman, Schmidt, Roschger, Glorieux, Klaushofer, Fratzl, Rauch, Wagermaier. 2014. “Mineral Particle Size in Children with Osteogenesis Imperfecta Type I Is Not Increased Independently of Specific Collagen Mutations.” *Bone* 60: 122–128.

Gavaia, Paulo J, M Leonor Cancela, and Vincent Laize. 2014. “Fish : A Suitable System to Model

Human Bone Disorders and Discover Drugs with Osteogenic or Osteotoxic Activities." *Drug Discovery Today: Disease Models* 13: 29–37.

Gaj T., Charles A. Gersbach and Carlos F. 2011. "Perspective Forward and Reverse Genetic Approaches for the Analysis of Vertebrate Development in the Zebrafish." *Developmental Cell* 21 (1): 48–64.

Gaj, Gersbach, and Barbas III. 2013. "ZFN, TALEN and CRISPR/Cas-Based Methods for Genome Engineering." *Trends Biotechnol.* 31 (7): 397–405.

Gelse, K., E. Pöschl, and T. Aigner. 2003. "Collagens - Structure, Function, and Biosynthesis." *Advanced Drug Delivery Reviews* 55 (12): 1531–46.

Gilles, Anna F, and Michalis Averof. 2014. "Functional Genetics for All: Engineered Nucleases, CRISPR and the Gene Editing Revolution." *EvoDevo* 5 (1): 43.

Gioia, Tonelli, Ceppi, Biggiogera, Leikin, Fisher, Tenedini, Yorgan, Schinke, Tian, Schwartz, Forte, Wagener, Villani, Rossi and Antonella Forlino. 2017. "The Chaperone Activity of 4PBA Ameliorates the Skeletal Phenotype of Chihuahua, a Zebrafish Model for Dominant Osteogenesis Imperfecta." *Human Molecular Genetics* 26: 2897–2911.

Gistelinck, Witten, Huysseune, Symoens, Malfait, Larionova, Simoens, Dierick, Van Hoorebeke, De Paepe, Kwon, Weis, Eyre, Willaert and Paul J Coucke. 2016. "Loss of Type I Collagen Telopeptide Lysyl Hydroxylation Causes Musculoskeletal Abnormalities in a Zebrafish Model of Bruck Syndrome." *Journal of Bone and Mineral Research* 31 (11): 1930–42.

Glorieux, Francis H, Leanne M Ward, Frank Rauch, Ljiljana Lalic, and Peter J Roughley. 2002. "Osteogenesis Imperfecta Type VI : A Form of Brittle Bone Disease with a Mineralization Defect." *J Bone Miner Res* 17: 30–38.

Gorman KF, Tredwell SJ, Breden F. 2007. "The Mutant Guppy Syndrome Curveback as a Model for Human Heritable Spinal Curvature." *Spine (Phila Pa 1976)* 32: 735–41.

Grafe, Ingo, Tao Yang, Stefanie Alexander, Erica P Homan, and Caressa Lietman. 2014. "Excessive Transforming Growth Factor-β Signaling Is a Common Mechanism in Osteogenesis Imperfecta." *Nature Medicine* 20 (6): 670–75.

Green J, Taylor JJ, Hindes A, Johnson SL, Goldsmith MI. 2009. "A Gain of Function Mutation Causing Skeletal Overgrowth in the Rapunzel Mutant." *Dev Biol* 334: 224–34.

Guerreiro, Fuentes, Canario, Power. 2002. "Calcium balance in sea bream (Sparus aurata): the effect of oestradiol-17ß". *Journal of Endocrinology* 173, 377–385.

Guillot, Pascale V, Oyebode Abass, J H Duncan Bassett, Sandra J Shefelbine, and George Bougharios. 2017. "Intrauterine Transplantation of Human Fetal Mesenchymal Stem Cells from First-Trimester Blood Repairs Bone and Reduces Fractures in Osteogenesis Imperfecta Mice." *Transplantation* 111 (3): 1717–26.

Hamilton F. 1822. An account of the fishes found in the river ganges and its branches. Edinburgh: Archibald Constable and Company.

Hering, Isken, Knabbe, Janott, Jost, Pommer, Muhr, Schatz, Pfeiffer. 2001. "TGFβ1 and TGFβ2 mRNA and Protein Expression in Human Bone Samples." *Exp. Clin. Endocrinol. Diabetes* 109: 217–226.

Homan, Erica P, Caressa Lietman, Ingo Grafe, Jennifer Lennington, and Roy Morello. 2014. "Differential Effects of Collagen Prolyl 3-Hydroxylation on Skeletal Tissues." *PLoS Genetics* 10 (1).

Howe, Clark, Torroja, Torrance, Berthelot. 2013. "The Zebrafish Reference Genome Sequence and Its Relationship to the Human Genome." *Nature* 496 (7446): 498–503.

Hoyer-kuhn, Heike, Christian Netzer, Friederike Koerber, Eckhard Schoenau, and Oliver Semler. 2014. "Two Years ' Experience with Denosumab for Children with Osteogenesis Imperfecta Type VI" 9 (1): 1–8.

Hruscha, Krawitz, Rechenberg, Heinrich, Hecht, Haass, Schmid. 2013. "Efficient CRISPR/ Cas9 Genome Editing with Low off-Target Effects in Zebrafish." *Development (Cambridge, England)* 140: 4982–4987.

Hudson, David M, and David R Eyre. 2014. "Collagen prolyl3-Hydroxylation: A Major Role for a Minor Posttranslational Modification?" *Connective tissue research* 54: 245–51.

Hudson, David M, Maryann Weis, and David R Eyre. 2011. "Insights on the Evolution of Prolyl 3-Hydroxylation Sites from Comparative Analysis of Chicken and Xenopus Fibrillar Collagens" 6 (5): 1–7.

Huitema, Apschner, Logister, Spoorendonk, Bussmann, Hammond, and Schulte-Merker. 2012. "Entpd5 Is Essential for Skeletal Mineralization and Regulates Phosphate Homeostasis in Zebrafish." *Proc Natl Acad Sci U S A* 109: 21372–77.

Hulmes, D. J S. 2008. "Collagen Diversity, Synthesis and Assembly." In *Collagen: Structure and*

Mechanics, 15–47.

Hussar DA, Stevenson T. 2003. “New Drugs: Denosumab, Dienogest/estradiol Valerate, and Polidocanol.” *J Am Pharm Assoc.* 50: 658–662.

Huysseune, Ann. 2000. “In the Laboratory Fish.” In *Skeletal System: Microscopic Functional Anatomy*, 307–317.

Ichimura, Atsuhiko, and Hiroshi Takeshima. 2016. “TRIC-B Mutations Causing Osteogenesis Imperfecta.” *Biol. Pharm. Bull.* 39 (11): 1743–47.

Ishikawa, Yoshihiro, and Hans Peter Bächinger. 2013. “A Molecular Ensemble in the rER for Procollagen Maturation.” *BBA - Molecular Cell Research* 1833. 2479–91.

Ishikawa, Yoshihiro, Paul Holden, and Hans Peter Bächinger. 2017. “Heat Shock Protein 47 and 65 KDa FK506 Binding Protein Weakly but Synergistically Interact during Collagen Folding in the Endoplasmic Reticulum,” *J Biol Chem* 292: 1–25.

Ishikawa, Yoshihiro, Shinya Ito, Kazuhiro Nagata, Lynn Y Sakai, and Hans Peter Bächinger. 2016. “Intracellular Mechanisms of Molecular Recognition and Sorting for Transport of Large Extracellular Matrix Molecules.” *Proceedings of the National Academy of Sciences of the United States of America* 113 (41): E6036–44.

Jao, L., Susan R Wente, and Wenbiao Chen. 2013. “Efficient Multiplex Biallelic Zebrafish Genome Editing Using a CRISPR Nuclease System.” *Proceedings of the National Academy of Sciences of the United States of America* 110 (34): 13904–9.

Jinek, Martin, Krzysztof Chylinski, Ines Fonfara, Michael Hauer, Jennifer A Doudna, and Emmanuelle Charpentier. 2012. “A Programmable Dual-RNA – Guided DNA Endonuclease in Adaptice Bacterial Immunity.” *Science (New York, N.Y.)* 337: 816–22.

Kalueff, Gebhardt, Stewart, Cachat, Brimmer, Chawla, Craddock, Kyzar, Roth, Landsman, Gaikwad, Robinson, Baatrup, Tierney, Shamchuk, Norton, Miller, Nicolson, Braubach, Gilman, Pittman, Rosemberg, Gerlai, Echevarria,.Lamb, Neuhauss, Weng, Bally-Cuif, Schneider, and the Zebrafish Neuroscience Research Consortium (ZNRC). 2013. Towards a Comprehensive Catalog of Zebrafish Behavior 1.0 and Beyond, *"Zebrafish"*, 10.

Kasaai B, Gaumond MH, Moffatt P. 2013. “Regulation of the Bone-Restricted IFITM-like (Bril) Gene Transcription by Sp and Gli Family Members and CpG Methylation.” *J Biol Chem* 288: 13278–94.

Keller, Rachel B, Thao T Tran, Shawna M Pyott, Melanie G Pepin, and et al Savarirayan, Ravi. 2017. “Monoallelic and Biallelic CREB3L1 Variant Causes Mild and Severe Osteogenesis Imperfecta , Respectively.” *Genetics in Medicine*

Khajavi, Mehrdad, Ken Inoue, and James R Lupski. 2006. “Nonsense-Mediated mRNA Decay Modulates Clinical Outcome of Genetic Disease.” *European Journal of Human Genetics* 14: 1074-1081.

Khandpur, S., R. Bhat, and M. Ramam. 2005. “Ichthyosis Follicularis, Alopecia and Photophobia (IFAP) Syndrome Treated with Acitretin.” *Journal of the European Academy of Dermatology and Venereology* 19 (6): 759–62.

Kimura, S., Zhu, X.-P., Matsui, R., Shijoh, M. & Takami, and S. Zawa. 1988. “Characterization of Fish Muscle Type I Collagen.” *J.Food Sci.* 53: 1315±1318.

Knapik, Ela W. 2000. “ENU Mutagenesis in Zebrafish — from Genes to Complex Diseases.” *Mamm Genome* 519: 511–19.

Koide, Nishikawa, Asada, Yamazaki, Takahara, Homma, Otaka, Ohtani, Wakamiya, Nagata and Kitagawa. 2006. “Specific Recognition of the Collagen Triple Helix by Chaperone HSP47. II. The HSP47-Binding Structural Motif in Collagens and Related Proteins.” *J Biol Chem* 281: 11177–85.

Kondo, Murakami, Tatsumi, Ogata, Kanemoto, Otori, Iseki, Wanaka and Imaizumi. 2005. “OASIS, a CREB/ATF-Family Member, Modulates UPR Signalling in Astrocytes.” *Nat Cell Biol* 7: 186–94.

Koonin, Eugene V, and Kira S Makarova. 2013. “CRISPR-CAS. Evolution of an RNA-Based Adaptive Immunity System in Prokaryotes.” *RNA Biology* 10 (5): 679–86.

Lall, S. P. & Lewis-Mccrea, L. M. 2007." Role of nutrients in skeletal metabolism and pathology in fish – An overview". *Aquaculture* 267, 3–19.

Lang MR, Lapierre LA, Frotscher M, Goldenring JR, Knapik EW. 2006. “Secretory COPII Coat Component Sec23a Is Essential for Craniofacial Chondrocyte Maturation.” *Nat Genet* 38: 1198–203.

Langheinrich, Ulrike. 2003. *Zebrafish : A New Model on the Pharmaceutical Catwalk*.

Lapunzina, Aglan, Temtamy, Caparros-Martın, Valencia, Leton, Martınez-Glez, Elhossini, Amr, Vilaboa, and Ruiz-Perez. 2010. “Identification of a Frameshift Mutation in Osterix in a Patient

with Recessive Osteogenesis Imperfecta." *Am J Hum Genet* 87: 110–14.

Laue, Pogoda, Daniel, van Haeringen, Alanay, von Ameln, Rachwalski, Morgan, Gray,Breuning, Sawyer, Sutherland-Smith, Nikkels, Kubisch, Bloch, Wollnik, Hammerschmidt and Robertson. 2011. "Craniosynostosis and Multiple Skeletal Anomalies in Humans and Zebrafish Result from a Defect in the Localized Degradation of Retinoic Acid." *Am J Hum Genet* 89: 595–606.

Le Blanc, Gotherstrom, Ringden, Hassan, McMahon, Horwitz. 2005. "Fetal Mesenchymal Stem-Cell Engraftment in Bone after In Utero Transplantation in a Patient with Severe Osteogenesis Imperfecta." *Transplantation* 79 (11): 1607–14.

Li, Zhang, Ren, Gu, Xiang, Du. 2015. "Intron Targeting-Mediated and Endogenous Gene Integrity-Maintaining Knockin in Zebrafish Using the CRISPR/Cas9 System." *Cell Res* 25: 634–637.

Li, Nan, Katharina Felber, Phil Elks, Peter Croucher, and Henry H Roehl. 2009. "Tracking Gene Expression During Zebrafish Osteoblast Differentiation Atypical Gene Expression :," Dev.Dyn 238: 459–66.

Lieschke, Graham J, and Peter D Currie. 2010. "Animal Models of Human Disease : Zebrafish Swim into View" 8: 353–67.

Lieschke GJ, Currie PD. 2007. "Animal Models of Human Disease: Zebrafish Swim into View." *Nat Rev Genet* 8: 353–367.

Lindahl, Katarina, Aileen M Barnes, Nadja Fratzl-zelman, Michael P Whyte, and Theresa E Hefferan. 2011. "COL1 C-Propeptide Cleavage Site Mutations Cause High." *Human Mutation* 2946.

Lindert, Uschi, Wayne A Cabral, Surasawadee Ausavarat, Siraprapa Tongkobpetch, and Katja Ludin. 2016. "MBTPS2 Mutations Cause Defective Regulated Intramembrane Proteolysis in X-Linked Osteogenesis Imperfecta." *Nature Communications.* 7: 11920.

Liu, Jiaqi, Yangzhong Zhou, Xiaolong Qi, Jia Chen, and Weisheng Chen. 2017. "CRISPR / Cas9 in Zebrafish : An Efficient Combination for Human Genetic Diseases Modeling." *Human Genetics* 136 (1): 1–12.

Liu, Song, Ma, Lv, Xu, Wang, Xia, Jiang, Wang, Song, Xing, Asan, Li. 2016. "Genotype-Phenotype Analysis of a Rare Type of Osteogenesis Imperfecta in Four Chinese Families with WNT1 Mutations." *Clinica Chimica Acta* 461: 172–80.

Mackay, Eirinn W, Alexander Apschner, and Stefan Schulte-merker. 2013. "A Bone to Pick with

Zebrafish." *BoneKEy Reports.* 2: 1–5.

Makarova, Haft, Barrangou, Brouns, Charpentier, Horvath, Moineau, Mojica, Wolf, Yakunin, van deer Oost, Koonin. 2011. "Evolution and Classification of the CRISPR-Cas Systems." *Nature Reviews. Microbiology* 9 (6): 467–77.

Malfait, Symoens, Coucke, Nunes, De Almeida, and De Paepe. 2006. "Total Absence of the a 2(I) Chain of Collagen Type I Causes a Rare Form of Ehlers-Danlos Syndrome with Hypermobility and Propensity to Cardiac Valvular Problems." *Journal of Medical Genetics* 2: 2–6.

Malhotra, Vivek, and Patrik Erlmann. 2015. "The Pathway of Collagen Secretion." *Annual Review of Cell and Developmental Biology* 31 (1): 109–24.

Marini, Joan C., Wayne A. Cabral, and Aileen M. Barnes. 2010. "Null Mutations in LEPRE1 and CRTAP Cause Severe Recessive Osteogenesis Imperfecta." *Cell and Tissue Research* 339 (1). 59–70.

Marini, Joan C, Antonella Forlino, Hans Peter Bächinger, Nick J Bishop, and Peter H Byers. 2017. "Osteogenesis Imperfecta." *Nature Reviews Disease Primer* 3: 1–19.

Marini, Joan C, Elizabeth Hopkins, Francis H Glorieux, George P Chrousos, and James C Reynolds. 2003. "Positive Linear Growth and Bone Responses to Growth Hormone Treatment in Children with Types III and IV Osteogenesis Imperfecta: High Predictive Value of the Carboxyterminal Propeptide of Type I Procollagen." *J Bone Miner Res* 18 (2): 237–43.

Marini JC, Cabral WA, Barnes AM, Chang W. 2007. "Components of the Collagen Prolyl 3-Hydroxylation Complex Are Crucial for Normal Bone Development." *Cell Cycle* 6: 1675–81.

Marini JC, Forlino A, Cabral WA, et al. 2007. "Consortium for Osteogenesis Imperfecta Mutations in the Helical Domain of Type I Collagen: Regions Rich in Lethal Mutations Align with Collagen Binding Sites for Integrins and Proteoglycans." *Hum Mutat* 28: 209–21.

Marshall, Charlotte, Jaime Lopez, Laura Crookes, Rebecca C Pollitt, and Meena Balasubramanian. 2016. "A Novel Homozygous Variant in SERPINH1 Associated with a Severe , Lethal Presentation of Osteogenesis Imperfecta with Hydranencephaly." *Gene* 595 (1): 49–52.

Martínez-Glez, Víctor, Maria Valencia, José A. Caparrós-Martín, and Mona Aglan. 2012. "Identification of a Mutation Causing Deficient BMP1/mTLD Proteolytic Activity in Autosomal Recessive Osteogenesis Imperfecta." *Human Mutation* 33 (2): 343–50.

Masic, Bertinetti, Schuetz, Chang, Metzger, Buehler and Fratzl. 2015. "Osmotic Pressure Induced

Tensile Forces in Tendon Collagen." *Nat Commun.* 6: 5942.

Matukas V.J., Miller E.J. 1969. "Chick Cartilage Collagen: A New Type of α1 Chain Not Present in Bone or Skin of the Species." *PNAS* 64: 1264–68.

Mayden, Tang, Conway, Freyhof, Chamberlain, Haskins, Schneider, Sudkamp, Wood, Agnew, Bufalino, Sulaiman, Miya, Saitoh, He. 2007. Phylogenetic relationships of Danio within the order Cypriniformes: a framework for comparative and evolutionary studies of a model species. *Journal of Experimental Zoology Part B, Molecular and Developmental Evolution* 308: 642-654.

Mayne. 1989. "Cartilage Collagens—what Is Their Function, and Are They Involved in Articular Disease?" *Arthritis Rheum.* 32: 241– 246.

Mekahli D, Bultynck G, Parys JB, De Smedt H, Missiaen L. 2011. "Endoplasmic-Reticulum Calcium Depletion and Disease." *Cold Spring Harb Perspect Biol* 3.

Meldolesi J, Pozzan T. 1998. "The Endoplasmic Reticulum Ca2+ Store: A View from the Lumen." *Trends in Biochemical Sciences* 23: 10–14.

Melville, Montero-Balaguer, Levic, Bradley, Smith, Hatzopoulos and Knapik. 2011. "The Feelgood Mutation in Zebrafish Dysregulates COPII-Dependent Secretion of Select Extracellular Matrix Proteins in Skeletal Morphogenesis." *Dis Model Mech* 4: 763–76.

Mendoza-Londono, Roberto, Somayyeh Fahiminiya, and Majewski. 2015. "Recessive Osteogenesis Imperfecta Caused by Missense Mutations in SPARC." *American Journal of Human Genetics* 96 (6): 979–85.

Mimori, S.; Okuma, Y.; Kaneko, M.; Kawada, K.; Hosoi, T.; Ozawa, K.; Nomura Y.; Hamana. 2012. "Protective Effects of 4-Phenylbutyrate Derivatives on the Neuronal Cell Death and Endoplasmic Reticulum Stress." *H. Biol. Pharm. Bull.* 35: 84–90.

Misof, Roschger, Baldini, Raggio, Zraick, Root, Boskey, Klaushofer, Fratzl, Camacho. 2005. "Differential Effects of Alendronate Treatment on Bone from Growing Osteogenesis Imperfecta and Wildtype Mouse." *Bone Jan* 36: 150–8.

Miyauchi, Hruska, Greenfield, Duncan, Alvarez, Barattolo, Colucci, Zambonin-Zallone, Teitelbaum. 1990. "Osteoclast Cytosolic Calcium,regulated by Voltage-Gated Calcium Channels and Extracellular Calcium, Controls Podosome Assembly and Bone Resorption." *J Cell Biol* 111: 2543–2552.

Mojica, F. J M, C. Díez-Villaseñor, J. García-Martínez, and C. Almendros. 2009. “Short Motif Sequences Determine the Targets of the Prokaryotic CRISPR Defence System.” *Microbiology* 155 (3): 733–40.

Montague, Tessa G., José M. Cruz, James A. Gagnon, George M. Church, and Eivind Valen. 2014. “CHOPCHOP: A CRISPR/Cas9 and TALEN Web Tool for Genome Editing.” *Nucleic Acids Research* 42: 401–7.

Monti, Elena, Monica Mottes, Paolo Fraschini, PierCarlo Brunelli, Antonella Forlino, and Giacomo Venturi. 2010. “Current and Emerging Treatments for the Management of Ostegenesis Imperfecta.” *Therapeutics and Clinical Risk Management* 6: 367–81.

Morello, Roy, Terry K. Bertin, Yuqing Chen, Patrizio Castagnola, and Frank Rauch. 2006. “CRTAP Is Required for Prolyl 3- Hydroxylation and Mutations Cause Recessive Osteogenesis Imperfecta.” *Cell* 127 (2): 291–304. doi:10.1016/j.cell.2006.08.039.

Morello, Tonachini, Monticone, Viggiano, Rocchi, Cancedda, Castagnola. 1999. “cDNA Cloning, Characterization and Chromosome Mapping of Crtap Encoding the Mouse Cartilage Associated Protein.” *Matrix Biol* 18: 319–24.

Morvan-Dubois, G., Le Guellec, D., Garrone, R., Zylberberg, L. & Bonnaud, L. 2003. “Phylogenetic Analysis of Vertebrate Fibrillar Collagen Locates the Position of Zebrafish alpha3(I) and Suggests an Evolutionary Link between Collagen Alpha Chains and Hox Clusters.” *J Mol Evol* 57: 501–514.

Murakami T, Saito A, Hino S, Kondo, Kanemoto, Chihara, Sekiya, Tsumagari, Ochiai, Yoshinaga, Saitoh, Nishimura, Yoneda, Kou, Furuichi, Ikegawa, Ikawa, Okabe, Wanaka and Imaizumi. 2009. “Signalling Mediated by the Endoplasmic Reticulum Stress Transducer OASIS Is Involved in Bone Formation.” *Nat Cell Biol* 11: 1205–11.

Naomi, D, Filippo Rossignoli, Giulia Golinelli, Giulia Grisendi, and Carlotta Spano. 2015. “Mesenchymal Stem / Stromal Cells as a Delivery Platform in Cell and Gene Therapies.” *BMC Medicine* 13: 186.

Nasevicius A, Ekker SC. 2000. “Effective Targeted Gene ‘knockdown’ in Zebrafish.” *Nat Genet.* 26: 216–220.

NEB. “CRISPR/Cas9 and Targeted Genome Editing: A New Era in Molecular Biology.”

Neer, Robert M., Claude D. Arnaud, Jose R. Zanchetta, and Richard Prince. 2001. “Effect of

Parathyroid Hormone (1-34) on Fractures and Bone Mineral Density in Postmenopausal Women With Osteoporosis." *The New England Journal of Medicine* 344 (19): 1434–41.

Nicolaou, N., Y. Agrawal, M. Padman, J. A. Fernandes, and M. J. Bell. 2012. "Changing Pattern of Femoral Fractures in Osteogenesis Imperfecta with Prolonged Use of Bisphosphonates." *Journal of Children's Orthopaedics* 6 (1): 21–27.

Nissen RM, Amsterdam A, Hopkins N. 2006. "A Zebrafish Screen for Craniofacial Mutants Identifies wdr68 as a Highly Conserved Gene Required for Endothelin-1 Expression." *BMC Dev Biol,* 6:28.

Obafemi AA, Bulas DI, Troendle J, Marini JC. 2008. "Popcorn Calcification in Osteogenesis Imperfecta: Incidence, Progression, and Molecular Correlation." *Am J Med Genet A* 146: 2725–2732.

Ogle JD, Arlinghaus RB, Logan MA. 1962. "3-Hydroxyproline, a New Amino Acid of Collagen." *J Biol ChemChem.* 237: 3667–73.

Oreffo, R.O., Mundy, G.R., Seyedin, S.M. & Bonewald, L.F. 1989. "Activation of the Bone-Derived Latent TGF β Complex by Isolated Osteoclasts." *Biochem. Biophys. Res. Commun.* 158: 817–823.

Orwoll, Eric S., Jay Shapiro, Sandra Veith, Ying Wang, and Jodi Lapidus. 2014. "Evaluation of Teriparatide Treatment in Adults with Osteogenesis Imperfecta." *Journal of Clinical Investigation* 124 (2). American Society for Clinical Investigation: 491–98.

Ozcan U., Yilmaz, Ozcan L., Furuhashi, Vaillancourt, Smith, Gorgun and Hotamisligil. 2006. "Chemical Chaperones Reduce ER Stress and Restore Glucose Homeostasis in a Mouse Model of Type 2 Diabetes." *Science* 313: 1137–1140.

Papapoulos, Socrates E. 2008. "Bisphosphonates: How Do They Work?" *Best Practice & Research Clinical Endocrinology & Metabolism* 22 (5): 831–47.

Parichy DM. 2015. Advancing biology through a deeper understanding of zebrafish ecology and evolution., eLife 2015, 4.

Parichy, Elizondo, Mills, Gordon, and Engeszer. 2009. "Normal Table of Post-Embryonic Zebrafish Development: Staging by Externally Visible Anatomy of the Living Fish" *Dev Dyn.* 238(12): 2975–3015.

Paschalis, Gamsjaeger, Fratzl-zelman, Roschger, Masic, Brozek, Hassler, Glorieux, Rauch,

Klaushofer, Fratzl. 2016. “Evidence for a Role for Nanoporosity and Pyridinoline Content in Human Mild Osteogenesis Imperfecta.” *JBMR* 31: 1050–59.

Peng, Rongxue, Guigao Lin, and Jinming Li. 2016. “Potential Pitfalls of CRISPR/Cas9-Mediated Genome Editing.” *FEBS Journal* 283 (7): 1218–31.

Perlmutter, David H. 2002. “Chemical Chaperones : A Pharmacological Strategy for Disorders of Protein Folding and Trafficking.” *PEDIATRIC RESEARCH* 52 (6): 832–36.

Piotrowski, Dae-gwon, Schilling, Nair, Ruvinsky, Geisler, Rauch, Haffter, Zon, Zhou, Foott, Dawid and Ho. 2003. “The Zebrafish van Gogh Mutation Disrupts tbx1, Which Is Involved in the DiGeorge Deletion Syndrome in Humans.” *Development* 130: 5043–5052.

Pitt, Park, Nishi, Urashima, Aoki, Yamazaki, Ma, Takeshima and Sitsapesan. 2010. “Charade of the SR K+-Channel: Two Ion-Channels, TRIC-A and TRIC-B, Masquerade as a Single K+-Channel.” *Biophys. J.* 99: 417–426.

Pokidysheva, Zientek, Ishikawa, Mizuno, Vranka, Montgomery, Keene, Kawaguchi, Okuyama , and Bächinger. 2013. “Post Translational Modifications in Type I Collagen from Different Tissues Extracted from Wild Type and Prolyl 3-Hydroxylase 1 Null Mice.” *J Biol Chem* 288: 24742–52.

Poole KES, van Bezooijen RL, Loveridge N, Hamersma H, Papapoulos SE, Löwik CW and Reeve. 2018. “Sclerostin Is a Delayed Secreted Product of Osteocytes That Inhibits Bone Formation.” *FASEB J Nov 2005* 19: 1842–4.

Postlethwait, J., Amores, A., Cresko, W., Singer, A., Yan, Y.L. 2004. “Subfunction Partitioning, the Teleost Radiation and the Annotation of the Human Genome.” *Trends Genet* 20: 481–490.

Postlethwait, Yan, Gates, Hornes, Amores, Brownlie, Donovan, Egan, Force, Gong, Goutel, Fritz, Kelsh, Knapik, Liao, Paw, Ransom, Singer, Thomson, Abduljabbar, Yelick, Beier, Joly, Larhammer, Rosa, Westerfield, Zon, Johnson and Talbot. 1998. “Vertebrate Genome Evolution and the Zebrafish Gene Map.” *Nat. Genet.* 18: 345–9.

Pyott, Schwarze, Christiansen, Pepin, Leistritz, Dineen, Harris, Burton, Angle, Kim, Sussman, Weis, Eyre, Russell, McCarthy, Steiner9 and Peter H. Byers. 2011. “Mutations in PPIB (Cyclophilin B) Delay Type I Procollagen Chain Association and Result in Perinatal Lethal to Moderate Osteogenesis Imperfecta Phenotypes.” *Human Molec Genet.* 20: 1595–609.

Quan, Ojaimi, Li, Kartsogiannis, Zhou, Choong. 2005. “Localization of Pigment Epithelium-

Derived Factor in Growing Mouse Bone." *Calcif Tissue Int* 76: 146–53.

Rauch, Frank, Francis H Glorieux, and Klaus Klaushofer. 2008. "Evidence That Abnormal High Bone Mineralization in Growing Children with Osteogenesis Imperfecta Is Not Associated with Specific Collagen Moutations." *Calcif Tissue Int* 82: 263–70.

Rawson, Robert B. 2004. "S2P Protease." In *Handbook of Proteolytic Enzymes: Second Edition*, 1:985–88.

Renn, J, C Winkler, M Schartl, R Fischer, and R Goerlich. 2006. "Zebrafish and Medaka as Models for Bone Research Including Implications Regarding Space-Related Issues," 209–14.

Ricard-Blum S. 2011. "The Collagen Family." *Cold Spring Harb Perspect Biol* 3 (1): a004978.

Richter, Corinna, James T Chang, and Peter C Fineran. 2012. "Function and Regulation of Clustered Regularly Interspaced Short Palindromic Repeats (CRISPR) / CRISPR Associated (Cas) Systems." *Viruses* 4: 2291–2311.

Ricobaraza, A.; Cuadrado-Tejedor, M.; Pérez-Mediavilla, A.; Frechilla, D.; Del, and A. Rio, J.; García-Osta. 2009. "Phenylbutyrate Ameliorates Cognitive Deficit and Reduces Tau Pathology in an Alzheimer's Disease Mouse Model." *Neuropsychopharmacology* 34: 1721–32.

Risteli, Bachinger, Engel, Furthmayer, Timpl. 1980. "7-S Collagen: Characterization of an Unusual Basement Membrane Structure." *Eur J Biochem/FEBS.* 108: 239–50.

Robu, Larson, Nasevicius, Beiraghi, Brenner, Farber, Ekker. 2007. "p53 Activation by Knockdown Technologies." *PLoS Genet* 3: e78.

Rossert, Jerome, and Benoit de Crombrugghe. 2002. "Type I Collagen: Structure, Synthesis, and Regulation." In *Principles of Bone Biology*, 2:189–210.

Roy, Witten, Hall, Lall, 2002. "Effects of dietary phosphorus on bone growth and mineralisation of vertebrae in haddock (Melanogrammus aeglefinus L.)". *Fish Physiology and Biochemistry* 27, 35–48.

Roy, P.K. and Lall, S. P. 2003. "Dietary phosphorus requirement of juvenile haddock (Melanogrammus aeglefinus L.)". *Aquaculture* 221, 451–468.

Saito, Masataka, Yoshitaka Takenouchi, Naomichi Kunisaki, and Shigeru Kimura. 2001. "Complete Primary Structure of Rainbow Trout Type I Collagen Consisting of a 1 (I) a 2 (I) a 3 (I) Heterotrimers" 2827: 2817–27.

Sakkers, Kok, Engelbert, van Dongen, Jansen, Pruijs, Verbout, Schweitzer, Uiterwaal. 2004.

"Skeletal Effects and Functional Outcome with Olpadronate in Children with Osteogenesis Imperfecta: A 2-Year Randomised Placebo-Controlled Study." *Lancet* 363: 1427–31.

Sampson, Timothy R, and David S Weiss. 2014. "CRISPR-Cas Systems: New Players in Gene Regulation and Bacterial Physiology." *Frontiers in Cellular and Infection Microbiology* 4: 37.

Sarmah S, Barrallo-Gimeno A, Melville DB, Topczewski J, Solnica-Krezel L, and Knapik EW. 2010. "Sec24D-Dependent Transport of Extracellular Matrix Proteins Is Required for Zebrafish Skeletal Morphogenesis." *PLoS ONE* 5: e10367.

Schartl, M. 2013. "Beyond the Zebrafish: Diverse Fish Species for Modeling Human Disease." *Dis Model. Mech.* 7: 181–92.

Schauerte HE, van Eeden FJM, Fricke C, Odenthal J, Stra¨hle U, Haffter P. 1998. "Sonic Hedgehog Is Not Required for the Induction of Medial Floor Plate Cells in the Zebrafish." *Development* 125: 2983–93.

Schilling, Piotrowski, Grandel, Brand, Heisenberg, Jiang, Beuchle, Hammerschmidt, Kane, Mullins, van Eeden, Kelsh, Furutani-Seiki, Granato, Haffter, Odenthal, Warga, Trowe and Nüsslein-Volhard. 1996. "Jaw and Branchial Arch Mutants in Zebrafish. I. Brachial Arches." *Development* 123: 329–344.

Schwarze U, Cundy T, Pyott SM, Christiansen, Hegde, Bank, Pals, Ankala, Conneely, Seaver, Yandow, Raney, Babovic-Vuksanovic, Stoler, BenNeriah, Segel, Lieberman, Siderius, Al-Aqeel, Hannibal, Hudgins, McPherson Clemens, Sussman, Steiner, Mahan, Smith, Anyane-Yeboa, Wynn, Chong, Uster, Aftimos, Sutton, Davis, Kim, Weis, Eyre and Byers. 2013. "Mutations in FKBP10, Whichresult in Bruck Syndrome and Recessive Forms of Osteogenesis Imperfecta, Inhibit the Hydroxylation of Telopeptide Lysines in Bone Collagen." *Hum Mol Genet* 22: 1–17.

Semler O, Garbes L, Keupp K. 2012. "A Mutation in the 5′-UTR of IFITM5 Creates an in-Frame Start Codon and Causes Autosomaldominant Osteogenesis Imperfecta Type V with Hyperplastic Callus." *Am J Hum Genet* 91: 349–57.

Shah, Shiraz A, Susanne Erdmann, Francisco J M Mojica, and Roger A Garrett. 2013. "Protospacer Recognition Motifs: Mixed Identities and Functional Diversity." *RNA Biology* 10 (5): 891–99.

Shaheen, Ranad, Anas M Alazami, Muneera J Alshammari, Eissa Faqeih, Nadia Alhashmi, Noon Mousa, Aisha Alsinani, Ansari, Alzahrani, Al-Owain, Alzayed and Alkuraya. 2012. "Study of

Autosomal Recessive Osteogenesis Imperfecta in Arabia Reveals a Novel Locus Defined by *TMEM38B* Mutation." *Journal of Medical Genetics* 49 (10): 630–35.

Shoulders, Matthew D., and Ronald T. Raines. 2009. "Collagen Structure and Stability." *Annu Rev Biochem* 78: 929–58.

Sillence DO, Rimoin DL. 1979. "Clinical Variability in Osteogenesis Imperfecta-Variable Expressivity or Genetic Heterogeneity." *Birth Defects Orig Artic Ser* 15: 113–29.

Sinder, Benjamin P., Mary M. Eddy, Michael S. Ominsky, Michelle S. Caird, and Joan C. Marini. 2013. "Sclerostin Antibody Improves Skeletal Parameters in a Brtl/+ Mouse Model of Osteogenesis Imperfecta." *Journal of Bone and Mineral Research* 28 (1): 73–80.

Singer, Richard B, Simon A Ogston, and Colin R Paterson. 2001. "Mortality in Various Types of Osteogenesis Imperfecta" 33: 216–20.

Stankiewicz P, Lupski JR. 2010. "Structural Variation in the Human Genome and Its Role in Disease." *Annu Rev Med* 61: 437–455.

Streisinger, G., Singer, F., Walker, C., Knauber, D and N. Dower. 1986. "Segregation Analyses and Gene-Centromere Distances in Zebrafish." *Genetics* 112: 311–319.

Streisinger, G., Walker, C., Dower, N., Knauber, D. 1981. "Production of Clones of Homozygous Diploid Zebra Fish (Brachydanio Rerio)." *Nature* 291: 293–96.

Stuart, G. W., McMurray, J. V., Westerfield, M. 1988. "Replication, Integration and Stable Germ-Line Transmission of Foreign Sequences Injected into Early Zebrafish Embryos." *Development (Cambridge, England)* 103: 403–412.

Suh, B. C. and Hille, B. 2008. "PIP2 Is a Necessary Cofactor for Ion Channel Function: How and Why?" *Annu. Rev. Biophys.* 37: 175–95.

Symoens, Malfait, D'hondt, Callewaert, Dheedene, Steyaert, Bächinger, De Paepe, Kayserili and Coucke. 2013. "Deficiency for the ER-Stress Transducer OASIS Causes Severe Recessive Osteogenesis Imperfecta in Humans." *Orphanet J Rare Dis* 8: e154.

Tang, Xiangwei, Weiqi, Lijuan, Chao, Shi, Zhao, Nagy, Peng, Hu, Feng, Van Hul, Wan and Cao. 2009. "TGF-β1–induced Migration of Bone Mesenchymal Stem Cells Couples Bone Resorption with Formation." *Nat. Med.* 15: 757–765.

Tasab, M, M R Batten, and N J Bulleid. 2000. "Hsp47: A Molecular Chaperone That Interacts with and Stabilizes Correctly-Folded Procollagen." *The EMBO Journal* 19 (10): 2204–11.

Tryggvason, Karl, Kari Majamaa, Juha Risteli, and Kari I Kivirikko. 1979. “Partial Purification and Characterization of Chick-Embryo Prolyl 3-Hydroxylase,” 303–7.

Tsukamoto T, Li X, Morita H, Minowa, Aizawa, Hanagata, Demura. 2013. “Role of S-Palmitoylation on IFITM5 for the Interaction with FKBP11 in Osteoblast Cells.” *PLoS One* 8: e75831.

Tveten, K.; Holla, Ø. L.; Ranheim, T.; Berge, K. E.; Leren, T. P.; Kulseth, M. A. 2007. “4-Phenylbutyrate Restores the Functionality of a Misfolded Mutant Low-Density Lipoprotein Receptor.” *FEBS J. 1881* 274: 1881–93.

Udvadia, A. J. and Linney, E. 2003. “Windows into Development: Historic, Current, and Future Perspectives on Transgenic Zebrafish.” *Dev. Biol.* 256: 1–17.

Uehara, Masashi, Yukio Nakamura, Jun Takahashi, Mikio Kamimura, and Shota Ikegami. 2017. “Efficacy of Denosumab for Osteoporosis in Three Female Patients with Osteogenesis Imperfecta.” *Tohoku J Exp Med.* 242: 115–20.

Uveges, Kozloff, Ty, Ledgard, Raggio, Gronowicz, Goldstein, and Marini. 2009. “Alendronate Treatment of the Brtl Osteogenesis Imperfecta Mouse Improves Femoral Geometry and Load Response before Fracture but Decreases Predicted Material Properties and Has Detrimental Effects on Osteoblasts and Bone Formation.” *J Bone Miner Res May* 24: 849–59.

Van Dijk, F. S. Van, J. M. Cobben, A. Kariminejad, A. Maugeri, and P. G J Nikkels. 2011. “Osteogenesis Imperfecta: A Review with Clinical Examples.” *Molecular Syndromology* 2 (1): 1–20.

Van Dijk, Nesbitt, Zwikstra, Nikkels, Piersma, Fratantoni, Jimenez, Huizer, Morsman, Cobben, van Roij, Elting, Verbeke, Wijnaendts, Shaw, Hogler, McKeown, Sistermans, Dalton, Meijers-Heijboer and Pals .2009. “PPIB Mutations Cause Severe Osteogenesis Imperfecta.” *American Journal of Human Genetics* 85 (4): 521–27.

Van Eeden, Granato, Schach, Brand, Furutani-Seiki, Haffter, Hammerschmidt, Heisenberg, Jiang, Kane, Kelsh, Mullins, Odenthal, Warga and Nüsslein-Volhard.1996. “Genetic Analysis of Fin Formation in the Zebrafish, Danio Rerio.” *Development (Cambridge, England)* 123: 255–262.

Van’t Padje, van Swieten, Oostra. 2010. “Zebrafish (Danio Rerio) as a Model Organism for Dementia. ” *Neuromethods, Animal Models of Dementia* 48: 255-269.

Vanhauwaert, Van Peer, Rihani, Janssens, Rondou, Lefever, De Paepe, Coucke, Speleman,

Vandesompele and Willaert. 2014. “Expressed Repeat Elements Improve RT-qPCR Normalization across a Wide Range of Zebrafish Gene Expression Studies.” *PloS One* 9 (10): e109091.

Vanleene, Porter, Guillot, Boyde, Oyen, Shefelbine. 2012. “Ultra-Structural Defects Cause Low Bone Matrix Stiffness despite High Mineralization in Osteogenesis Imperfecta Mice.” *Bone* 50: 1317–1323.

Venturi, Elisa, Rebecca Sitsapesan, and Daiju Yamazaki. 2012. “TRIC Channels Supporting Efficient Ca2 + Release from Intracellular Stores TRIC Channels Supporting Efficient Ca 2 + Release from Intracellular Stores.” *European Journal of Physiology* 465 (December): 187–95.

Vranka, Janice A., Lynn Y. Sakai, and Hans Peter Bächinger. 2004. “Prolyl 3-Hydroxylase 1, Enzyme Characterization and Identification of a Novel Family of Enzymes.” *Journal of Biological Chemistry* 279 (22): 23615–21.

Vranka, Janice A, Elena Pokidysheva, Lauren Hayashi, Keith Zientek, and et al Mizuno, Kazunori. 2010. “Prolyl 3-Hydroxylase 1 Null Mice Display Abnormalities in Fibrillar Collagen-Rich Tissues Such as Tendons , Skin and Bone.” *J Biol Chem.* 285 (22): 17253–62.

Wang, Ruiying, Gan Preamplume, Michael P. Terns, Rebecca M. Terns, and Hong Li. 2011. “Interaction of the Cas6 Riboendonuclease with CRISPR RNAs: Recognition and Cleavage.” *Structure* 19 (2): 257–64.

Ward LM, Rauch F, Travers R, Chabot G, Azouz EM, Lalic L, Roughley PJ, Glorieux FH. 2002. “Osteogenesis Imperfecta Type VII: An Autosomal Recessive Form of Brittle Bone Disease.” *Bone* 31: 12-8.

Ward, Rauch, Whyte, D’Astous, Gates, Grogan, Lester, McCall, Pressly, Sanders, Smith, Steiner, Sullivan, Tyerman, Smith-Wright, Verbruggen, Heyden, Lombardi, and Glorieux. 2011. “Alendronate for the Treatment of Pediatric Osteogenesis Imperfecta: A Randomized Placebocontrolled Study.” *J Clin Endocrinol Metab* 96: 355–64.

Webb, Balasubramanian, Fratzl-Zelman, Cabral, Titheradge. 2017. “Phenotypic Spectrum in Osteogenesis Imperfecta Due to Mutations in TMEM38B: Unraveling a Complex Cellular Defect.” *The Journal of Clinical Endocrinology & Metabolism* 102 (6): 2019–28.

Weber M, Roschger P, Fratzl-Zelman N, Schoberl T, Rauch F, and Klaushofer K Glorieux FH, Fratzl P. 2006. “Pamidronate Does Not Adversely Affect Bone Intrinsic Material Properties in

Children with Osteogenesis Imperfecta." *Bone* 39: 616–622.

Weigele, Jochen, and Tamara A. Franz-Odendaal. 2016. "Functional Bone Histology of Zebrafish Reveals Two Types of Endochondral Ossification, Different Types of Osteoblast Clusters and a New Bone Type." *Journal of Anatomy* 229 (1): 92–103.

Weis, Hudson, Kim, Scott, Wu and Eyre. 2010. "Location of 3-Hydroxyproline Residues in Collagen Types I, II, III, and V/XI Implies a Role in Fibril Supramolecular Assembly." *J Biol Chem.* 285: 2580–90.

Winata, Cecilia Lanny, Svetlana Korzh, Igor Kondrychyn, Weiling Zheng, Vladimir Korzh, and Zhiyuan Gong. 2009. "Development of Zebrafish Swimbladder : The Requirement of Hedgehog Signaling in Specification and Organization of the Three Tissue Layers." *Developmental Biology* 331 (2): 222–36.

Witten, P Eckhard, and Ann Huysseune. 2009. "A Comparative View on Mechanisms and Functions of Skeletal Remodelling in Teleost Fish , with Special Emphasis on Osteoclasts and Their Function" 84: 315–46.

Xie, Khaoustov, Chung, Sohn, Krishnan, Lewis, Yoffe. 2002. "Effect of Tauroursodeoxycholic Acid on Endoplasmic Reticulum Stress-Induced Caspase-12 Activation." *Hepatology* 36: 592–601.

Xi Y, Chen D, Sun L, Li Y, Li L. 2013. "Characterization of Zebrafish Mutants with Defects in Bone Calcification during Development." *Biochem Biophys Res Commun* 440: 132–6.

Yamauchi, Mitsuo, and Marnisa Sricholpech. 2012. "Lysine Post-Translational Modifications of Collagen." *Essays Biochem.* 52: 113–33.

Yamazaki, Daiju, Shinji Komazaki, Hiroki Nakanishi, Aya Mishima, Miyuki Nishi, Masayuki Yazawa, Tetsuo Yamazaki, Ryo Taguchi, and Hiroshi Takeshima. 2009. "Essential Role of the TRIC-B Channel in Ca2+ Handling of Alveolar Epithelial Cells and in Perinatal Lung Maturation." *Development (Cambridge, England)* 136 (14): 2355–61.

Yan Y, Miller CT, Nissen RM, Singer A, Liu D, Kirn, Draper, Willoughby, Morcos, Amsterdam, Chung, Westerfield, Haffter, Hopkins, Kimmel and Postlethwait. 2002. "A Zebrafish sox9 Gene Required for Cartilage Morphogenesis." *Development* 129: 5065–79.

Yang, Grafe, Bae, Chen S., Chen Y., Bertin, Jiang, Ambrose, and Brendan Lee. 2013. "E-Selectin Ligand 1 Regulates Bone Remodeling by Limiting Bioactive TGF-β in the Bone

Microenvironment." *Proc. Natl. Acad. Sci. USA* 110: 7336–7341.

Yang, Hanting, Miaohui Hu, Jianli Guo, Xiaomin Ou, and Tanxi Cai. 2016. "Pore Architecture of TRIC Channels and Insights into Their Gating Mechanism." *Nature* 538 (7626): 537–41.

Yazawa, Ferrante, Feng, Mio, Ogura, Zhang, Lin, Pan, Komazaki, Kato, Nishi, Zhao, Weisleder, Sato, Ma and Takeshima. 2007. "TRIC Channels Are Essential for Ca2+ Handling in Intracellular Stores." *Nature* 448: 78–82.

Zhao, Ichimura, Qian, Iida, Yamazaki, Noma, Asagiri, Yamamoto, Komazaki, Sato, Aoyama, Sawaguchi, Kakizawa, Nishi, Takeshima. 2016. "Mice Lacking the Intracellular Cation Channel TRIC-B Have Compromised Collagen Production and Impaired Bone Mineralization." *Science Signaling* 9 (428): ra49.

Zhou X., Zhang Z., Feng, Dusevich, Sinha, Zhang H., Darnay, de Crombrugghe. 2010. "Multiple Functions of Osterix Are Required for Bone Growth and Homeostasis in Postnatal Mice." *Proc Natl Acad Sci U S A* 107 (29): 12919–24.

Zhou, Xinyu, Peihui Lin, Daiju Yamazaki, Ki Ho Park, and Shinji Komazaki. 2014. "Trimeric Intracellular Cation Channels and Sarcoplasmic/endoplasmic Reticulum Calcium Homeostasis." *Circulation Research* 114 (4): 706–16.